Phononic crystal-based devices for improving the accuracy of ultrasonic flowmeters

Valiya Valappil, S.

DOI
10.4233/uuid:4a6506fb-3f7d-4a21-8d7c-d75990448786

Publication date
2024

Document Version
Final published version

Citation (APA)
Valiya Valappil, S. (2024). *Phononic crystal-based devices for improving the accuracy of ultrasonic flowmeters*. [Dissertation (TU Delft), Delft University of Technology]. https://doi.org/10.4233/uuid:4a6506fb-3f7d-4a21-8d7c-d75990448786

Important note
To cite this publication, please use the final published version (if applicable).
Please check the document version above.

Phononic crystal-based devices for improving the accuracy of ultrasonic flowmeters

Phononic crystal-based devices for improving the accuracy of ultrasonic flowmeters

Dissertation

for the purpose of obtaining the degree of doctor
at Delft University of Technology,
by the authority of the Rector Magnificus Prof. Dr. Ir. T.H.J.J. van der Hagen,
chair of the Board for Doctorates,
to be defended publicly on
Wednesday 4 September 2024 at 15:00 o'clock

by

Sabiju VALIYA VALAPPIL

Master of Technology in Mechanical Systems Design,
Indian Institute of Technology, Kharagpur, India,
born in Taliparamba, Kerala, India.

This dissertation has been approved by the promotors.

Composition of the doctoral committee:

Rector Magnificus,	chairman
Prof. dr. ir. A. van Keulen,	Delft University of Technology, promotor
Dr. A.M. Aragón,	Delft University of Technology, promotor
Dr. ir. J.F.L. Goosen,	Delft University of Technology, copromotor
Dr. ir. J. Hogendoorn,	Krohne Technologies
Independent members:	
Prof. dr. M. Hussein,	University of Colorado
Prof. dr. C. Yilmaz,	Bogazici University
Prof. dr. ir. P. J. Steeneken,	Delft University of Technology
Dr. O. Bilal,	University of Connecticut
Prof. dr. ir. J. L. Herder,	Delft University of Technology, reserve member

This work was part of the Topconsortia voor Kennis en Innovatie (TKI) program, which was partly financed by the industrial partner KROHNE.

Keywords: Phononic crystals, ultrasonic flowmeters, wave manipulation, crosstalk reduction, design optimization, numerical modeling.

Printed by: IPSKAMP printing

Front & Back: Sabiju Valiya Valappil.

ISBN 978-94-6384-621-9

An electronic version of this dissertation is available at
http://repository.tudelft.nl/.

To Namitha and Sanvi.

Contents

Summary

Acoustic waves due to their non-destructive and non-reactive nature, have been extensively used as information carriers in various applications including, medical imaging, material characterization, distance and velocity measurement, and flow rate measurement, among others. In an ultrasonic flowmeter (UF), the upstream and downstream travel times of ultrasound pulses across the fluid are measured, whose difference is directly related to the flow rate. However, during the measurement, a significant amount of the pulse's energy leaks through the solid pipe (parasitic signal) and interferes with the fluid signal (working signal) known as crosstalk. Since crosstalk can lead to measurement errors and in extreme cases complete signal losses, we explore possibilities of phononic crystals (PnCs) to mitigate crosstalk from UFs.

PnCs are periodic structures possessing unusual dynamic characteristics due to the presence of band gaps (BGs)—frequency ranges where elastic and acoustic waves are attenuated. Because of BGs, they are explored in several applications, including vibration isolation, energy harvesting, acoustic wave steering, super/hyperlens, wave focusing, and cloaking. However, extending the PnCs to real applications such as the crosstalk reduction in UFs, is still very challenging since the application has multiple requirements and can be subjected to extreme environmental conditions. We design PnC waveguides to possess BGs in the UF's operating frequencies, thereby acting as wave filters to alleviate crosstalk.

The thesis is separated into two parts: The first part deals with developing rigorous analysis tools and design methods to generate intricate PnC designs. We start by exploring the use of complex material behavior, such as viscoelastic damping, in the PnC analysis. This involves developing low-cost analytical models based on the spectral element method (SEM) to characterize wave propagation through viscoelastic phononic crystals. The model results are then verified experimentally. Since SEM has difficulty in dealing with intricate geometries, we further develop 3D PnC models via the finite element method (FEM). We also propose an approach to design PnCs with particular BG behaviors, such as partial BGs that are present only in specific wave propagation directions. The BGs can be manipulated by tuning the displacement modes of the bounding wavebands using concepts from mechanics.

The second part involves applying the aforementioned tools to develop PnC structures capable of mitigating crosstalk from UFs. To that end, we design a 3D PnC waveguide possessing a broad BG centered around 1 MHz, which is fabricated via metal additive manufacturing using selective laser sintering (SLS). This device is then integrated into an inline UF, and by ultrasonic experiments, we validate its BG predicted numerically. We extend the PnC design to incorporate additional objectives, such as preventing fluid leakage and withstanding a high hydrostatic pressure. To that end, we propose a design procedure to maximize the BG and

minimize the stress induced due to the fluid pressure. This design is also fabricated via SLS, and its parameters are verified using computed tomography.

We further explore the capabilities of PnCs in alleviating crosstalk in a clamp-on UF. Unlike an inline UF, the working and parasitic signals arrive at the receiver from the same interface, making it challenging to filter the latter. Since both signals have similar frequency ranges and arrival times, conventional frequency- or time-based filters cannot separate them. Thus, we develop a frequency-steering mechanism based on partial BG PnCs to guide the working signal while attenuating the parasitic signals, thereby avoiding crosstalk. Since characterizing a clamp-on UF requires a time-domain analysis, which is computationally very intensive when using FEM at high frequencies in 3D, we develop a semi-analytical approach that combines 2D FEM, ray tracing, geometric projection, and 3D FEM (only for the fluid domain). We show that the method can capture the 3D effects, such as wave-focusing, and provide a detailed description of the wave propagation via the clamp-on flowmeter.

From the findings presented in the thesis, we can conclude that to apply PnCs in real-world applications several challenges need to be addressed. The foremost difficulty is the lack of adequate manufacturing processes to fabricate intricate PnC structures, which prevents several designs from realization. Another challenge is the vast computational cost of PnC analyses that require surrogate modeling or other forms of simplification such as a domain separation. It is expected that the outcome of this thesis will take PnCs one step closer to applying them to more real-world scenarios.

Samenvatting

Akoestische golven worden gebruikt als informatiedrager in verschillende applicaties omdat ze niet-destructief en niet-reactief zijn. Onder deze applicaties vallen medische beeldvorming, materiaal karakterisatie, afstandsmetingen en stromingsmetingen. In de laatst genoemde toepassingen wordt een ultrasone flowmeter (UF) gebruikt die door middel van het verschil in doorlooptijd de stroming kan meten. Het verschil in doorlooptijd tussen een golf met de stroming mee en tegen is een directe maatstaaf voor de stroomsnelheid. Dit principe is alleen niet foutvrij. Tijdens een meting lekt een groot gedeelte van golfenergie weg via de pijp rond de vloeistof en dit parasitaire signaal interfereert met het signaal door de vloeistof zelf. Dit effect wordt crosstalk genoemd en kan zorgen voor meetfouten of in extreme gevallen zelfs tot een compleet verlies van signaal. In deze proefschrift onderzoeken we daarom de mogelijkheden van fononische kristallen, afgekort als PnCs in het Engels, om de negatieve effecten van crosstalk te voorkomen.

PnCs zijn periodische structuren die zich ongebruikelijk gedragen door de aanwezigheid van band gaps (BGs), een band van frequenties waarin elastische en akoestische golven worden verzwakt. Door deze BGs worden PnCs in verschillende applicaties toegepast zoals het isolatie tegen vibraties, sturen van akoestische golven, superlenzen en cloaking. Daarentegen is het toepassen van PnCs in de praktijk, zoals voor het reduceren van crosstalk in flowmetingen, niet vanzelfsprekend. Voor het toepassen tijdens flowmetingen moet een PnC voldoen aan velen velen vereisten en moet het apparaat kunnen werken onder extreme werkomstandigheden. Dit weerhoud ons er niet van om PnCs golfgeleiders te ontwerpen die een BG in het frequentiebereik van een UF heeft, zodat ze zich als een golffilter kunnen gedragen en het effect van crosstalk kunnen verminderen.

Deze proefschrift is opgedeeld in twee delen. In het eerste deel is de focus op het ontwikkelen van rigoureuze analyse- en ontwikkelingsmethodes om PnCs te ontwerpen. De eerste stap hierin is het verkennen van hoe complex materiaal gedrag, zoals de visco-elastische demping, de werking van PnCs beïnvloed. Hiervoor hebben we een analytisch model die weinig rekenkracht vergt ontwikkeld gebaseerd op de spectral element method (SEM) om de golf propagatie door visco-elatische PnCs te karakteriseren. Dit doel is hierna experimenteel geverifieerd. Omdat SEM niet goed om kan gaan met complexe geometrieën hebben we ook 3D finite element method (FEM) model van PnCs ontwikkeld. Hiernaast hebben we ook ontwerp procedure voorgesteld om PnCs te ontwikkelen met een bepaald BG gedrag, zoals een gedeeltelijke BG die alleen voorkomt in een bepaalde propagatie richting. De BGs kunnen worden gemanipuleerd door de verplaatsingsmodi van de begrenzende golfbanden af te stemmen met behulp van concepten uit de mechanica.

In het tweede deel van de proefschrift passen we de ontwikkelde procedures en modellen toe om PnCs te ontwerpen die crosstalk kunnen voorkomen in ultrasone

flowmetingen. De eerste toepassing is voor een inline UF. Het gemaakte ontwerp van de PnC golfgeleider bevat brede BG rond de 1 MHz en is gefabriceerd door middel selective laser sintering (SLS). Om het ontwerp te verifiëren is het geïntegreerd in een inline ultrasone flowmeter en zijn er ultrasone metingen gedaan. De volgende stap is het aanpassen van het PnC ontwerp om aan additionele doelen te voldoen, zoals het voorkomen van lekkages en om bestand te zijn tegen een hoge hydrostatische druk. Met dat doel voor ogen stellen we een ontwerp procedure voor om de BG te maximaliseren en om de stress veroorzaakt door de hydrostatische druk te minimaliseren. Dit ontwerp is ook gefabriceerd doormiddel van SLS, en de paramaters zijn geverifieerd doormiddel van computertomografie.

In het tweede deel onderzoeken we ook de mogelijkheden van PnCs om crosstalk te verminderen in een clamp-on UF. In tegenstelling tot een inline UF arriveert het parasitaire signaal via dezelfde interface bij de ontvanger als het flowsignaal, waardoor het separeren van de signalen. Omdat beide signalen een vergelijkbare frequentieband en aankomsttijd hebben is het niet mogelijk de signalen te scheiden doormiddel van traditionele frequentie- of tijdsfilters. Om die reden ontwerpen we een frequency-steering mechanisme gebaseerd op gedeeltelijke BG PnCs om het flowsignaal te sturen en tegelijkertijd het parasitaire signaal te verzwakken, zodoende crosstalk te voorkomen. Omdat clamp-on UF alleen te analyseren zijn in het tijdsdomein en aangezien dit niet effectief gedaan kan worden met een combinatie 3D FEM en hoge frequenties, hebben we een semi-analytische benadering ontwikkeld die 2D FEM combineert met ray tracing, geometrische projectie en 3D FEM voor alleen het vloeistof domein. We laten zien dat deze methode de 3D effecten kan weergeven, zoals het focusseren van golven, en dat deze methode een gedetailleerde beschrijving geeft van golfpropagatie door de clamp-on flowmeter.

De resultaten in deze proefschrift laten zien dat er nog meerdere uitdagingen zijn voordat PnCs kunnen worden toegepast in de praktijk. Het grootste probleem is het ontbreken van productieprocessen die de gecompliceerde PnC structuren kunnen produceren, waardoor meerdere ontwerpen gepresenteerd in deze proefschrift niet kunnen worden gefabriceerd. Een andere probleem is dat het simuleren van PnCs een enorme rekenkracht vereist, waardoor in de praktijd simulaties alleen mogelijk zijn via een surrogaat model of andere vormen van simplificatie zoals het apart simuleren van verschillende domeinen. We verwachten dat de resultaten in deze proefschrift het gebruik van PnCs in de praktijk een stap dichter bij de werkelijkheid brengen.

1

Introduction

The propagation of mechanical disturbances through solids and fluids is of great importance in several industries since these waves can be used to characterize various properties of a system. For instance, mechanical waves in the form of ultrasound greatly aid fault diagnostics to identify cracks or other potential failures in dynamic systems such as rotating shafts [1]. Additionally, these waves are commonly used in medical imaging to study the anatomy of humans [2] and other animals [3]. However, in many situations, waves adversely affect the performance of precision instruments [4], hinder human health [5], and harm large structures [6], among others.

One application is ultrasonic flowmeters (UFs), which are often used in various industries, such as pharma [7], water treatment [8], aerospace [9], automotive [10], oil and natural gas [11], medical [12], and nuclear power plants [13]. In transit-time UFs, an ultrasonic pulse generated by a transducer is transmitted through the measured fluid and is received by another transducer, which provides its travel time (upstream measurement). The same process is repeated in the opposite direction to obtain the travel time in that direction (downstream measurement). The difference between upstream and downstream measurements is directly related to the flow rate. UFs are further classified as inline and clamp-on transit-time UFs depending on their operation. In an inline UF, the ultrasonic transducers (generally six to twelve) are inserted into a pipe section, which is then connected to the required pipeline. Figure 1.1 shows a schematic of the inline UF, where the green arrows between transducers T_1 and T_2 show the upstream and downstream signal paths. Since the flow needs to be temporally interrupted to install these UFs, this may lead to pressure drops, fouling, and leakage [14]. On the contrary, clamp-on UFs do not have these limitations and are portable devices that can be attached (temporarily) to the pipe wall without disrupting the flow to measure the flow rate as shown in Figure 1.2. Additionally, they are less expensive than their inline counterparts and provide measurement across a wide flow range [15].

1

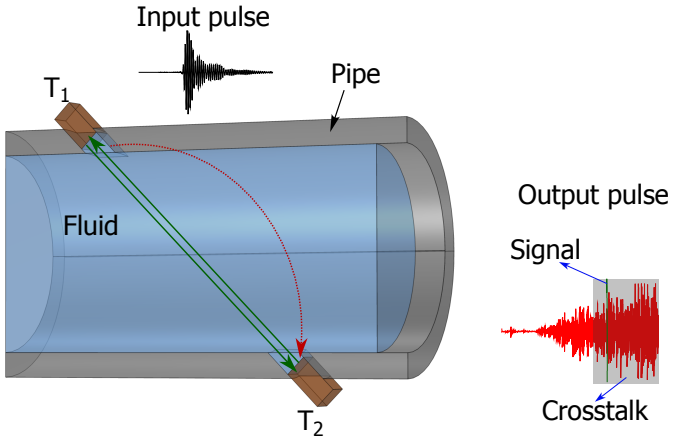

Figure 1.1: Schematic of an inline UF where T_1 and T_2, respectively, represent the ultrasound transducers used to send and receive the acoustic signals. The green arrow is the required signal (traveling through the fluid) while the red arrow is the parasitic wave traveling via the solid portion.

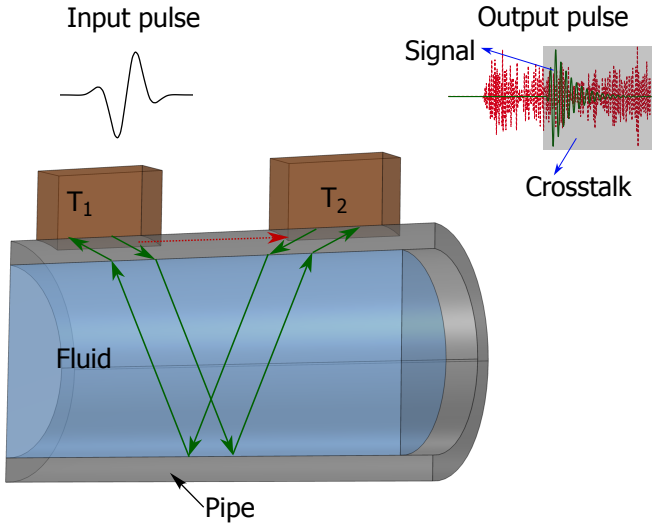

Figure 1.2: Schematic of a clamp-on UF where transducers T_1 and T_2 are placed along the same side of the pipe wall. The required signal and parasitic waves reach the receiver from the same interface.

1.1. Crosstalk in ultrasonic flowmeters

The ultrasound transducers in an inline UF are directly in contact with the fluid medium, and the acoustic pulse transmits through the fluid from the transmitter to the receiver (and vice versa) via a metallic window. Due to the immense acoustic impedance mismatch between this window and the adjacent fluid, a significant portion of the supplied energy reflects back to the solid. It then travels through the

pipe wall to the receiver as shown by the dotted red arrow from Figure 1.1. This results in crosstalk—interference between the waves traveling through the fluid region (required/fluid signal) with that of the solid region (parasitic/solid signal) as described in the output pulse from the same figure. Similar to the inline UF, the clamp-on UF also suffers from crosstalk. However, since the transducers only interact with the pipe wall both fluid and solid signals arrive at the receiver from the same interface as shown in Figure 1.2. The figure also shows the output pulse where crosstalk is shown using the shaded region. In both cases, crosstalk results in a reduction in measurement accuracy or the complete loss of the required signal; thus crosstalk mitigation is quintessential for the smooth operation of these UFs.

Several methods have been proposed to mitigate crosstalk in inline UFs such as isolating the ultrasonic transducer from the solid signal path [16, 17]. However, this approach is challenging in high-pressure situations, since a heavy casing is required to withstand high pressures, which increases the crosstalk by allowing more waves to pass through the solid region [18]. Another approach is to create time delays between the required and parasitic signals [19]. To that end, transducers with protrusions that would increase the solid signal path and thereby its travel time were used [20]. They enable the fluid signal to arrive at the receiver earlier than the parasitic signal preventing the crosstalk [20]. However, this depends on the distance between the transducers. If the pipe has a large diameter, then the parasitic signal can arrive along with the fluid signal resulting in the crosstalk [21]. A third method is to localize the energy transmitted by the solid region using resonators and damping systems attached to the transducer [22, 23]. However, resonators and damping systems are limited to low frequencies (a few hundred kHz) since it is challenging to construct a MHz-range oscillator in macro-scale. Additionally, dampers with constant dissipation are also less effective at high frequencies as the energy increases with frequency but the dissipation stays constant. Thus, it is essential to have a wave filter that eliminates the crosstalk with a significant operating frequency range (in MHz) and is least influenced by pressure and temperature.

Similar to the case of inline UFs, various approaches have been used to alleviate crosstalk from clamp-on UFs, such as using absorbing layers between the transducers to attenuate the solid signals [14]. This method is less feasible, though, since the pipe is often covered in materials meant to prevent heat transfer, thus restricting access to the pipe wall. Another method is to modify the incident angle of the pulse to reduce the signal generation in the solid region [24]. However, this requires manual adjustment of the transducers, thereby making the process operator-dependent. A third solution based on ultrasound transducer arrays can avoid manual calibrations and suppress multiple wave interactions to improve the measurement accuracy [25]. Further, a matrix transducer array can manipulate the beam angle and the wavefront shape allowing them to produce multiple beams in different directions, thereby achieving high accuracy [26–28]. However, they suffer from electric crosstalk because of the deficiency of electromagnetic shielding and close electric connections [29]. This crosstalk can adversely affect the directivity of the pulse and can accidentally excite the adjacent piezoelectric element reducing the capacity to control the beam. Consequently, a solution to reduce the interfer-

1

ence of waves from the pipe and the fluid without introducing additional crosstalk is needed to improve the measurement accuracy of clamp-on UFs.

1.2. Crosstalk mitigation using phononic crystals

A potential solution to alleviate crosstalk in UFs can be based on phononic crystals (PnCs) [30] possessing frequency-dependent wave manipulation capabilities. PnCs are periodic structures with unusual dynamic characteristics due to band gaps (BGs)—frequency ranges where elastic/acoustic waves attenuate—due to destructive interference (Bragg scattering) [31]. Figure 1.3 shows a schematic of a one-

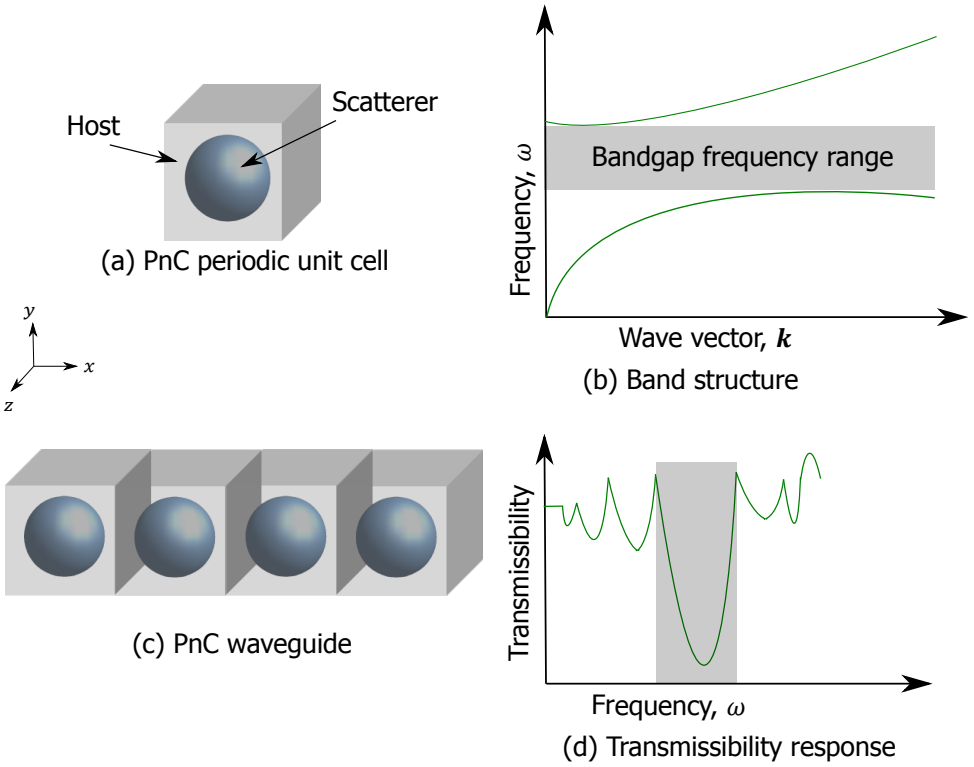

Figure 1.3: Schematic of (a) PnC PUC and (c) waveguide. (b) and (d), respectively, are the band structure and transmissibility responses, which are used to characterize the PnC's performance.

dimensional PnC structure composed of scatterers embedded in a host material. Figure 1.3(a) is the PnC's periodic unit cell (PUC)—smallest repeating element—, whose wave propagation behavior can be revealed by means of its band structure, as shown in Figure 1.3(b). The band structure is obtained by sweeping the wave vector (reciprocal of wavelength directed towards the wavefront) along the irreducible Brillouin zone—the smallest section of the Brillouin zone (representation of the PUC in the reciprocal lattice)—of the PUC after applying Bloch-Floquet periodic boundary conditions. The band structure relates the frequency with the wave vector, where

the slopes of the wavebands provide the wave speed. The shaded region in the figure, where no wavebands are present and hence no waves propagate is the BG. Since the band structure assumes a periodic boundary condition and thus considers an infinite number of PUCs, it cannot provide the actual attenuation behavior. To that end, a finite PnC waveguide (one-dimensional PnC waveguide) as shown in Figure 1.3(c) is used, which is obtained by replicating the PUC in the x direction. The waveguide's dynamic response is now characterized via a transmissibility relation (see Figure 1.3(d)), which is the ratio of the output displacement to the prescribed displacement for the frequency range of interest. The transmissibility within the BG frequency range will be considerably lower than outside the BG, as shown by the gray-shaded region in the figure. Because of BGs, PnCs show potential applications in several fields, including vibration isolation [32], energy harvesting [33], super/hyper lens [34, 35], acoustic antennas [36], frequency steering [37, 38], and acoustic cloaking [39, 40].

PnCs have been previously employed within ultrasonic transducers to optimize the piezoelectric coefficient [41–44], while PnCs were also used to improve the measurement accuracy of transducers for non-destructive evaluation [45, 46]. Other similar applications include improving acousto-ultrasonic-based devices' sensitivity for structural health monitoring [47], enhancing crack detection ability of the acoustic emission method [48], and reducing nonlinearities in ultrasonic damage detection [49]. PnCs have also been used in non-invasive applications such as in ultrasonic transducers to enhance the sensitivity of liquid sensors [50, 51]. Other applications of PnCs in a clamp-on setting include enhancing sensing capabilities of gasoline property detection systems [52, 53], improving transducer's accuracy during non-destructive evaluation [45, 46], and aiding in structural health monitoring [47, 49, 54].

1.3. Research scope and outline

Using the two case studies we formulate the research question as:

How can PnCs be used to mitigate crosstalk from both inline and clamp-on UFs?

In this thesis, wave manipulation mechanisms are developed for mitigating crosstalk from both inline and clamp-on UFs. In the case of the inline UF, a PnC-based broadband acoustic wave filter operating around 1 MHz is developed, which can suppress the parasitic signals, alleviating the crosstalk. In the clamp-on UF case, a wave steering mechanism based on PnCs is developed that can guide the required signal to the receiver while isolating/redirecting the parasitic signals, thereby preventing crosstalk.

We explore various aspects of PnCs, as discussed in subsequent chapters.

In Chapter 2, a feasibility study is performed to investigate whether PnCs can be used for the indented applications. To that end, the finite element method (FEM) and spectral element method(SEM) are explored to design PnCs with broad BGs. Additionally, since wave isolation has been carried out predominantly by exploiting damping, we incorporate damping in our analysis by studying PnCs with viscoelastic

material behavior. Thus, in the same chapter, we propose an SEM-based inexpensive analytical model to characterize the dynamic response of viscoelastic PnCs and verify it experimentally. However, the ultrasonic device deals with wave propagation in 3D, and hence it is necessary to develop the crosstalk rejection system also in 3D, which is not possible using SEM, and instead, FEM is used hereafter. However, the PnC's analyses of band structure and transmissibility remain unchanged.

Chapter 3 proposes, for the first time, a 3D single-phase PnC design based on cubic lattice arrangement to mitigate crosstalk from inline UFs. This design is analyzed using FEM and fabricated in stainless steel 316 via metal additive manufacturing. The device is then attached to an inline UF and its wave attenuation performance is validated using ultrasonic experiments.

Since in an inline UF, the transducers are immersed in the fluid, this could adversely affect the performance of the PnC wave filter. This is because the fluid seepage into the PnC waveguide (the PnC waveguide from Chapter 3 is an open structure) would severely reduce its wave attenuation performance. To address this, the PnC waveguide needs to be enclosed, which leads to the damage of the delicate structures within the waveguide due to the high hydrostatic pressure (approximately 15 MPa) exerted by the surrounding fluid. To incorporate these conditions, in Chapter 4 additional requirements are added to the PnC design, thereby increasing the complexity. A multi-objective design problem is solved for maximizing the wave attenuation behavior and mechanical strength. The obtained PnC design is also realized via metal 3D printing, whose parameters' dimensions are verified by micro-computed tomography techniques.

A similar wave filter is inadequate for mitigating crosstalk in clamp-on UFs since, as mentioned already, the working signal from the fluid and the signals from the solid (parasitic signal) arrive at the receiver from the same interface. Thus, a directional waveguide that can separate the required signal from the parasitic signal is necessary, for which the PnC waveguide should possess a partial BG (BG present in specific wave propagation directions). This requires breaking the symmetry of the unit cell, which introduces many additional design parameters. Thus, Chapter 5 introduces an approach for designing PnCs for specific requirements by correlating various displacement modes of the wavebands with the design parameters. The band structure can then be tuned iteratively to achieve a PnC geometry for particular BG behavior such as a PnC with a PBG.

In Chapter 6 a directional waveguide based on PnCs with PBGs is designed using the method from Chapter 5. This waveguide can steer the working signal from the transmitter to the receiver while attenuating the parasitic signals from the solid, thereby preventing the crosstalk generation. To ensure that the required signal is not filtered out from the output signal, a time-domain analysis of the complete clamp-on UF is performed in addition to the band structure and transmissibility analyses of the PnC. To that end, the discontinuous Galerkin (DG) method is adopted as DG possesses higher accuracy than standard FEM in simulating traveling waves at high frequencies.

Chapter 7 is built on the concepts from Chapter 6 in analyzing traveling waves in complex media. Since high-fidelity wave propagation models are costly to simulate

at MHz frequencies, this chapter proposes an efficient wave analysis approach based on combinations of DG, ray tracing, and geometric projection methods. Here the clamp-on measurement system is subdivided into fluid and solid domains, where the former is analyzed using DG and ray tracing, while the latter is characterized via geometric projection.

Chapter 8 discusses the manufacturing aspects of various PnC structures fabricated via additive manufacturing techniques. Here a detailed discussion is provided on different 3D printing processes (both metal and plastic) used for devices discussed in Chapters 3, 4, and 6.

Chapter 9 concludes the investigation of applications of PnCs in crosstalk mitigation from both inline and clamp-on UFs with recommendations for further research.

Bibliography

[1] Ikgeun Jeon et al. "Fatigue crack detection in rotating steel shafts using non-contact ultrasonic modulation measurements". In: *Engineering Structures* 196 (2019), p. 109293. ISSN: 0141-0296. DOI: https://doi.org/10.1016/j.engstruct.2019.109293. URL: https://www.sciencedirect.com/science/article/pii/S0141029619306728.

[2] K Kirk Shung, Michael Smith, and Benjamin MW Tsui. *Principles of medical imaging*. Academic Press, 2012.

[3] A.M. King. "Development, advances and applications of diagnostic ultrasound in animals". In: *The Veterinary Journal* 171.3 (2006), pp. 408–420. ISSN: 1090-0233. DOI: https://doi.org/10.1016/j.tvjl.2004.10.014. URL: https://www.sciencedirect.com/science/article/pii/S109002330400231X.

[4] Eugene I. Rivin. "Vibration isolation of precision equipment". In: *Precision Engineering* 17.1 (1995), pp. 41–56. ISSN: 0141-6359. DOI: https://doi.org/10.1016/0141-6359(94)00006-L. URL: https://www.sciencedirect.com/science/article/pii/014163599400006L.

[5] Bożena Smagowska and Małgorzata Pawlaczyk-Łuszczyńska. "Effects of Ultrasonic Noise on the Human Body—A Bibliographic Review". In: *International Journal of Occupational Safety and Ergonomics* 19.2 (2013). PMID: 23759188, pp. 195–202. DOI: 10.1080/10803548.2013.11076978. eprint: https://doi.org/10.1080/10803548.2013.11076978. URL: https://doi.org/10.1080/10803548.2013.11076978.

[6] Hugo Bachmann. *Vibration problems in structures: practical guidelines*. Springer Science & Business Media, 1995.

[7] Richard Smith et al. "A MEMS-Based Coriolis Mass Flow Sensor for Industrial Applications". In: *IEEE Transactions on Industrial Electronics* 56.4 (2009), pp. 1066–1071. DOI: 10.1109/TIE.2008.926703.

[8] David Lozano and Luciano Mateos. "Field evaluation of ultrasonic flowmeters for measuring water discharge in irrigation canals". In: *Irrigation and Drainage* 58.2 (2009), pp. 189–198. DOI: https://doi.org/10.1002/ird.404. eprint: https://onlinelibrary.wiley.com/doi/pdf/10.1002/ird.404. URL: https://onlinelibrary.wiley.com/doi/abs/10.1002/ird.404.

[9] Yong Chen, Yiyong Huang, and Xiaoqian Chen. "Acoustic propagation in viscous fluid with uniform flow and a novel design methodology for ultrasonic flow meter". In: *Ultrasonics* 53.2 (2013), pp. 595–606. ISSN: 0041-624X. DOI: https://doi.org/10.1016/j.ultras.2012.10.005. URL: https://www.sciencedirect.com/science/article/pii/S0041624X12002016.

[10] M. Kupnik et al. "Adaptive Pulse Repetition Frequency Technique for an Ultrasonic Transit-Time Gas Flowmeter for Hot Pulsating Gases". In: *IEEE Sensors Journal* 6.4 (2006), pp. 906–915. DOI: 10.1109/JSEN.2006.876042.

[11] Mahmoud Meribout et al. "Multiphase Flow Meters Targeting Oil & Gas Industries". In: *Measurement* 165 (2020), p. 108111. ISSN: 0263-2241. DOI: https://doi.org/10.1016/j.measurement.2020.108111. URL: https://shorturl.at/KauuH.

[12] H.-H. Eckstein et al. "Improvement of carotid blood flow after carotid endarterectomy Evaluation using intraoperative ultrasound flow measurement". In: *European Journal of Vascular and Endovascular Surgery* 25.2 (2003), pp. 168–174. ISSN: 1078-5884. DOI: https://doi.org/10.1053/ejvs.2002.1820. URL: https://www.sciencedirect.com/science/article/pii/S1078588402918204.

[13] Jae Cheon Jung and Poong Hyun Seong. "Estimation of the flow profile correction factor of a transit-time ultrasonic flow meter for the feedwater flow measurement in a nuclear power plant". In: *IEEE Transactions on Nuclear Science* 52.3 (2005), pp. 714–718. DOI: 10.1109/TNS.2005.846879.

[14] M.L Sanderson and H Yeung. "Guidelines for the use of ultrasonic non-invasive metering techniques". In: *Flow Measurement and Instrumentation* 13.4 (2002), pp. 125–142. ISSN: 0955-5986. DOI: https://doi.org/10.1016/S0955-5986(02)00043-2. URL: https://www.sciencedirect.com/science/article/pii/S0955598602000432.

[15] Furio Cascetta. "Application of a portable clamp-on ultrasonic flowmeter in the water industry". In: *Flow Measurement and Instrumentation* 5.3 (1994), pp. 191–194. ISSN: 0955-5986. DOI: https://doi.org/10.1016/0955-5986(94)90019-1. URL: https://www.sciencedirect.com/science/article/pii/0955598694900191.

[16] Pierre Ueberschlag, Andreas Berger, and Michal Bezdek. *Ultrasonic transducer for application in an ultrasonic, flow measuring device or in an ultrasonic, fill-level measuring device*. US Patent 10,620,026. Apr. 2020.

[17] Emanuel J Gottlieb et al. *Acoustically isolated ultrasonic transducer housing and flow meter*. US Patent 9,506,789. Nov. 2016.

[18] Lawrence C Lynnworth. *Ultrasonic transducer system with crosstalk isolation*. US Patent 5,515,733. May 1996.

[19] Jeroen Martin Van Klooster. *Flowmeter*. US Patent 6,799,475. Oct. 2004.

[20] Søren Tønnes Nielsen, Peter Schmidt Laursen, and Jens Lykke Sørensen. *Flow meter with protruding transducers*. US Patent 9,182,260. Nov. 2015.

[21] Dandan Zheng, Pengyong Zhang, and Tianshi Xu. "Study of acoustic transducer protrusion and recess effects on ultrasonic flowmeter measurement by numerical simulation". In: *Flow Measurement and Instrumentation* 22.5 (2011), pp. 488–493. ISSN: 0955-5986. DOI: https://doi.org/10.1016/j.flowmeasinst.2011.08.003. URL: https://shorturl.at/cFrSW.

[22] A. Ramos, J.L. San Emeterio, and P.T. Sanz. "Improvement in transient piezoelectric responses of NDE transceivers using selective damping and tuning networks". In: *IEEE Transactions on Ultrasonics, Ferroelectrics, and Frequency Control* 47.4 (2000), pp. 826–835. DOI: 10.1109/58.852064.

[23] Jereon Martin Van Klooster and Arie Huijzer. *Ultrasonic transducer*. US Patent **8**,127,613. Mar. 2012.

[24] Kenichi TEZUKA et al. "Analysis of Ultrasound Propagation in High-Temperature Nuclear Reactor Feedwater to Investigate a Clamp-on Ultrasonic Pulse Doppler Flowmeter". In: *Journal of Nuclear Science and Technology* 45.8 (2008), pp. 752–762. DOI: 10.1080/18811248.2008.9711476. eprint: https://www.tandfonline.com/doi/pdf/10.1080/18811248.2008.9711476. URL: https://www.tandfonline.com/doi/abs/10.1080/18811248.2008.9711476.

[25] Americo Zuzunaga and Bob Maron. "A survey of non-invasive and semiinvasive flow meters for mining applications: Understanding and selecting the right technology for the application". In: *CiDRA Minerals Processing, Wallingford, USA* (2013).

[26] Jack Massaad et al. "Suppression of Lamb wave excitation via aperture control of a transducer array for ultrasonic clamp-on flow metering". In: *The Journal of the Acoustical Society of America* 147.4 (2020), pp. 2670–2681. DOI: 10.1121/10.0001135. eprint: https://doi.org/10.1121/10.0001135. URL: https://doi.org/10.1121/10.0001135.

[27] Jack Massaad et al. "Design and Proof-of-Concept of a Matrix Transducer Array for Clamp-On Ultrasonic Flow Measurements". In: *IEEE Transactions on Ultrasonics, Ferroelectrics, and Frequency Control* 69.8 (2022), pp. 2555–2568. DOI: 10.1109/TUFFC.2022.3186170.

[28] Jack Massaad et al. "Acoustic Design of a Transducer Array for Ultrasonic Clamp-on Flow Metering". In: *2019 IEEE International Ultrasonics Symposium (IUS)*. 2019, pp. 1133–1136. DOI: 10.1109/ULTSYM.2019.8925680.

[29] A. Bybi et al. "Reducing crosstalk in array structures by controlling the excitation voltage of individual elements: A feasibility study". In: *Ultrasonics* 53.6 (2013), pp. 1135–1140. ISSN: 0041-624X. DOI: https://doi.org/10.1016/j.ultras.2013.02.009. URL: https://www.sciencedirect.com/science/article/pii/S0041624X13000553.

[30] P.A. Deymier. *Acoustic Metamaterials and Phononic Crystals*. Springer Series in Solid-State Sciences. Springer Berlin Heidelberg, 2013. ISBN: 9783642312328. URL: https://books.google.nl/books?id=8eg%5C_AAAAQBAJ.

[31] W. L. Bragg. "The Diffraction of Short Electromagnetic Waves by a Crystal". In: *Scientia* 23.45 (1929), p. 153.

[32] Matthew Reynolds and Stephen Daley. "An active viscoelastic metamaterial for isolation applications". In: *Smart Materials and Structures* 23.4 (2014), p. 045030.

[33] Kyung Ho Sun et al. "Sound energy harvesting using a doubly coiled-up acoustic metamaterial cavity". In: *Smart Materials and Structures* 26.7 (2017), p. 075011.

[34] Shu Zhang, Leilei Yin, and Nicholas Fang. "Focusing ultrasound with an acoustic metamaterial network". In: *Physical review letters* 102.19 (2009), p. 194301.

[35] Jong Jin Park et al. "Acoustic superlens using membrane-based metamaterials". In: *Applied Physics Letters* 106.5 (2015), p. 051901.

[36] Chengrong Ma et al. "Acoustic metamaterial antennas for combined highly directive-sensitive detection". In: *Applied Physics Letters* 115.5 (2019), p. 053501.

[37] J Xu and J Tang. "Tunable prism based on piezoelectric metamaterial for acoustic beam steering". In: *Applied Physics Letters* 110.18 (2017), p. 181902.

[38] Hyuk Lee et al. "Mass-Stiffness substructuring of an elastic metasurface for full transmission beam steering". In: *Journal of the Mechanics and Physics of Solids* 112 (2018), pp. 577–593.

[39] Mohamed Farhat, Sebastien Guenneau, and Stefan Enoch. "Ultrabroadband elastic cloaking in thin plates". In: *Physical review letters* 103.2 (2009), p. 024301.

[40] Nicolas Stenger, Manfred Wilhelm, and Martin Wegener. "Experiments on elastic cloaking in thin plates". In: *Physical Review Letters* 108.1 (2012), p. 014301.

[41] Wallace Arden Smith, Avner Shaulov, and BA Auld. "Tailoring the properties of composite piezoelectric materials for medical ultrasonic transducers". In: *IEEE 1985 Ultrasonics Symposium*. IEEE. 1985, pp. 642–647.

[42] W.A. Smith and B.A. Auld. "Modeling 1-3 composite piezoelectrics: thickness-mode oscillations". In: *IEEE Transactions on Ultrasonics, Ferroelectrics, and Frequency Control* 38.1 (1991), pp. 40–47. DOI: 10.1109/58.67833.

[43] W.A. Smith. "The role of piezocomposites in ultrasonic transducers". In: *Proceedings., IEEE Ultrasonics Symposium,* 1989, 755–766 vol.2. DOI: 10.1109/ULTSYM.1989.67088.

[44] Wallace Arden Smith and Avner A. Shaulov. "Composite piezoelectrics: Basic research to a practical device". In: *Ferroelectrics* 87.1 (1988), pp. 309–320. DOI: 10.1080/00150198808201393. eprint: https://doi.org/10.1080/00150198808201393. URL: https://doi.org/10.1080/00150198808201393.

[45] M. Miniaci et al. "Proof of Concept for an Ultrasensitive Technique to Detect and Localize Sources of Elastic Nonlinearity Using Phononic Crystals". In: *Phys. Rev. Lett.* 118 (21 May 2017), p. 214301. DOI: 10.1103/PhysRevLett.118.214301. URL: https://link.aps.org/doi/10.1103/PhysRevLett.118.214301.

[46] Elizabeth J. Smith and Kathryn H. Matlack. "Metal additively manufactured phononic materials as ultrasonic filters in nonlinear ultrasound measurements". In: *The Journal of the Acoustical Society of America* 149.6 (2021), pp. 3739–3750. DOI: 10.1121/10.0004995. eprint: https://doi.org/10.1121/10.0004995. URL: https://doi.org/10.1121/10.0004995.

[47] Menglong Liu et al. "Applications of a nanocomposite-inspired in-situ broadband ultrasonic sensor to acousto-ultrasonics-based passive and active structural health monitoring". In: *Ultrasonics* 78 (2017), pp. 166–174. ISSN: 0041-624X. DOI: https://doi.org/10.1016/j.ultras.2017.03.007. URL: https://www.sciencedirect.com/science/article/pii/S0041624X16302414.

[48] Xiaoli Li. "A brief review: acoustic emission method for tool wear monitoring during turning". In: *International Journal of Machine Tools and Manufacture* 42.2 (2002), pp. 157–165. ISSN: 0890-6955. DOI: https://doi.org/10.1016/S0890-6955(01)00108-0. URL: https://www.sciencedirect.com/science/article/pii/S0890695501001080.

[49] Geoffrey Roger Sherwood et al. "3D-printed phononic crystal waveguide transducers for nonlinear ultrasonic damage detection". In: *NDT & E International* 121 (2021), p. 102456. ISSN: 0963-8695. DOI: https://doi.org/10.1016/j.ndteint.2021.102456. URL: https://www.sciencedirect.com/science/article/pii/S0963869521000554.

[50] Ralf Lucklum and Nikolay Mukhin. "Enhanced sensitivity of resonant liquid sensors by phononic crystals". In: *Journal of Applied Physics* 130.2 (2021), p. 024508. DOI: 10.1063/5.0046847. eprint: https://doi.org/10.1063/5.0046847. URL: https://doi.org/10.1063/5.0046847.

[51] Nikolay Mukhin et al. "Narrow Band Solid-Liquid Composite Arrangements: Alternative Solutions for Phononic Crystal-Based Liquid Sensors". In: *Sensors* 19.17 (2019). ISSN: 1424-8220. DOI: 10.3390/s19173743. URL: https://www.mdpi.com/1424-8220/19/17/3743.

[52] A. Oseev, M. Zubtsov, and R. Lucklum. "Octane Number Determination of Gasoline with a Phononic Crystal Sensor". In: *Procedia Engineering* 47 (2012). 26th European Conference on Solid-State Transducers, EUROSENSOR 2012, pp. 1382–1385. ISSN: 1877-7058. DOI: https://doi.org/10.1016/j.proeng.2012.09.414. URL: https://www.sciencedirect.com/science/article/pii/S1877705812044773.

[53] A. Oseev, M. Zubtsov, and R. Lucklum. "Gasoline properties determination with phononic crystal cavity sensor". In: *Sensors and Actuators B: Chemical* 189 (2013). Selected Papers from the 26th European Conference on Solid-State Transducers, pp. 208–212. ISSN: 0925-4005. DOI: https://doi.org/10.1016/j.snb.2013.03.072. URL: https://www.sciencedirect.com/science/article/pii/S0925400513003535.

[54] Minoo Kabir, Amir Mostavi, and Didem Ozevin. "Noise isolation with phononic crystals to enhance fatigue crack growth detection using acoustic emission". In: *Journal of Civil Structural Health Monitoring* 8.3 (July 2018), pp. 529–542.

2

Analytical characterization of the dynamic response of viscoelastic metamaterials

The band gap frequencies of elastic metamaterials are ideally determined by a metamaterial architecture; yet, in practical situations, are often dependent on the material damping in their constituent(s). The analysis of viscoelastic metamaterials requires however substantial computational resources and, except for oversimplified cases, is solely done numerically. Here, we propose an analytical procedure based on the spectral element method (SEM) to analyze bulk metamaterials with viscoelastic damping as continuous systems. Due to the intrinsic limitations of the SEM to deal with complex geometries, we develop a procedure to build an approximate model based on SEM frame elements. The viscoelastic behavior is included by means of complex viscoelasticity moduli expressed by the generalized Maxwell mechanical model. We validate this approach by analyzing metamaterial plates and verify the findings experimentally. We demonstrate that our SEM-based analytical model can accurately capture wave transmission around the first band gap frequencies. Therefore, our extension of the SEM approach to analyze three-dimensional meta-structures is promising to characterize wave propagation in realistic viscoelastic structures (with any type of linear viscoelastic behavior) in an accurate and computationally efficient way.

2.1. Introduction

Damping is an intrinsic property of real-world dynamic systems that reduces, restricts, and even prevents oscillations [1]. Although damping is beneficial in vehicle

Parts of this chapter have been published in Computational Materials Science **229**, p. 112385 (2023).

suspension systems [2], seismic isolation [3], and sound or vibration mitigation [4], among others, high damping values can detrimentally amplify higher-frequency resonance modes [5], decrease the quality factor of resonators [6], and generate heat in high-speed systems [7, 8]. Damping has a complex nature and different origins. Material damping is caused, for example, by internal losses due to defects and impurities at the microstructural level. Structural damping is due to friction in joints and semi-rigid connections. Other forms of damping are thermoelastic damping, where a gradient in local temperature leads to energy dissipation, and fluid damping, where energy loss is due to drag resistance in a fluid. In this study, we consider damping due to viscoelastic material behavior, which can be represented by the imaginary components of complex-values elasticity moduli [9]. Viscoelastic damping, being an intricate subject in material science and rheology by itself [10], becomes even more challenging to analyze when superimposed on the dynamic effects governed by the material architecture. This occurs in elastic metamaterials.

Elastic metamaterials are architected materials with frequency band gaps where the propagation of mechanical waves is forbidden. This peculiar functionality, not typical for most conventional engineering materials, is achieved due to destructive interference of waves at material interfaces or boundaries [11]. In periodic structures, this process is similar to the Bragg scattering of electromagnetic waves [12] and occurs at frequencies when the corresponding wavelength is comparable with a characteristic dimension of a lattice. Alternatively, destructive interference can be induced by Mie (resonance-type) scattering near a resonance frequency of embedded resonators enabling the break of the periodicity restriction [13].

Large application potential of elastic metamaterials, including vibration isolation [14], acoustic diodes and transistors [15, 16], energy harvesting [17], acoustic lenses [18, 19], acoustic antennas [20], frequency steering [21, 22], acoustic cloaking [23–26], and other acoustic devices [27], requires accurate prediction of their wave propagation characteristics. This implies considering realistic material behavior while analyzing the dynamics of elastic metamaterials. For intrinsically viscoelastic polymer meta-structures, the dynamic analysis is not straightforward due to the complexity of lossy material behavior and the abundance of viscoelastic models with not readily available parameters. These complications are further aggravated by high computational costs due to doubled size of the stiffness and mass matrices in finite-element simulations. Additionally, the frequency-dependent viscoelasticity can drastically alter the dynamic response of viscoelastic metamaterials by changing the positions of pass and stop bands thus modifying the width and frequencies of band gaps [28, 29]. Therefore, proper analysis of viscoelastic metamaterials requires the knowledge of viscoelastic models, time- and resource-efficient approaches, and, simultaneously, should be accurate enough to reliably predict experimentally observed dynamics.

Currently available models to study the wave dynamics in viscoelastic metamaterials can be loosely classified into discrete lumped-mass [30], discretized distributed-mass [31], and continuous distributed-mass models [32]. The discrete lumped-mass models, in which a host medium and scatterers/resonators are represented as interconnected springs, dashpots, and point masses, can capture the viscoelas-

tic damping. They are straightforward to implement and computationally inexpensive [33–36], can be extended to include nonlinear behavior [37] or multiple resonators/scatterers [38], and have been used to model damped metamaterials in various applications [39–41]. However, the accuracy of these models is inherently limited to a low-frequency range, *i.e.,* to frequencies below the first band gap. Distributed-mass models (discretized and continuous) consider the geometry of viscoelastic metamaterials as is that allows adequate capturing of the wave dynamics at various frequency ranges. A representative example is the finite element method (FEM) [42] that has been extensively used to analyze damped metamaterials of complex geometries [43–49]. The finite element models are though computationally expensive as they require—as a rule of thumb—more than six linear elements to represent the wavelength accurately [50], and thus the degrees of freedom (DOFs) drastically increase with frequency and because of the complex-valued problem formulation. As a result, finite-element simulations are incredibly costly in terms of memory and computational time. To overcome this, Shi *et al.* [51, 52] proposed the time-dependent spectral element method (*t*-SEM), whereby using high-order polynomials (Gauss-Lobatto-Legendre basis functions) to define the approximation that greatly improved computational efficiency [53, 54]. For the same target frequency, *t*-SEM shows a significant reduction in the number of finite elements when compared to standard finite element formulation based on linear shape functions.

The two discussed classes of analysis approaches imply the discretization of the equations of motion. This step is however not needed (or at least not entirely) in continuous distributed-mass methods, including the spectral element method (SEM) [55]. The SEM, which is completely unrelated to *t*-SEM, is an analytical method based on fast or discrete Fourier transform techniques (FFT/DFT) [56] that has mainly been used to solve wave propagation problems. It does not have a limitation with respect to frequency because the employed shape functions are solutions to the wave equations. Because of this, SEM has been applied in analyses of flow-induced vibrations in pipes [57], axially moving structures [58], dynamics of multi-layer and smart structures [59], and the identification of cracks and joints [59], among others. The viscoelasticity can easily be incorporated into an SEM model by means of complex-valued elasticity moduli. SEM has the potential to predict the dynamics of viscoelastic metamaterials accurately with low computational cost, as has been successfully shown for 1D meta-structures [60–65]. However, the extension to two- or three-dimensional structures is not straightforward as the SEM cannot directly solve nonlinear problems [59] and deal with complex geometries due to the unavailability of corresponding solutions to the wave equations. To the best of our knowledge, nowadays there are no studies on the dynamics of viscoelastic metamaterials of complex geometries by means of SEM or any other similar techniques that can provide reliable predictions.

In this work, we extend SEM to study the dynamics of bulk and plate-like viscoelastic meta-structures and prove that it accurately predicts the wave dynamics below and above the first band gap with little to no computational costs. Our approach relies on approximating the geometry of a representative unit cell of a viscoelastic metamaterial by a combination of the SEM frame elements and incorpo-

rating the viscoelastic behavior by a generalized Maxwell model, which fits experimentally measured master curves of a viscoelastic polymer. The predicted results are validated in transmission experiments performed on polycarbonate metamaterial plates.

2.2. Spectral element method for wave propagation analysis of viscoelastic systems

We begin by describing the steps of the general procedure to study the wave propagation by means of the SEM as also outlined in the flowchart in Figure 2.1. First, one needs to represent (approximate) the geometry of an analyzed structure by means of *spectral elements* such as bars, beams, plates, or other elements, for which solutions to the wave equations are available (or can be derived). Next, the equations of motion are transformed from the time domain to the frequency domain using FFT/DFT. These equations are formulated in terms of complex-valued elastic moduli in order to describe the viscoelastic material behavior and then solved to obtain the shape functions. Using these functions, one can derive the dynamic stiffness matrix (DSM) for each spectral element, which enters a global DSM. The assembly process of the global DSM is similar to that in the standard FEM. Further, one can solve the system equations under appropriate boundary conditions to obtain the required response. In the case of a linear viscoelastic behavior, such as the one described in the present study, the viscoelastic model can be introduced after deriving the shape functions and only then incorporated into the DSM.

2.2.1. SEM model for 3D viscoelastic metamaterials

In this section, we apply the described procedure to study the dynamics of bulk elastic metamaterials. For this, we consider a general elastic metamaterial configuration shown in Figure 2.2. The constituent cylinders can be considered as frame elements with 12 DOFs responsible for axial, bending, and torsional deformations as indicated in the inset of Figure 2.2. The dynamics of these elements can be approximated by that of the Euler-Bernoulli beam, with the viscoelastic behavior incorporated in the complex-valued elasticity moduli [66].

The equations of motion that govern the wave propagation in a corresponding 1D viscoelastic frame element in the absence of a source term are those that represent the propagation of longitudinal (axial component), flexural (bending component), and twisting (torsional component) waves, respectively:

$$\begin{aligned} \hat{E}(\iota\omega) A \frac{\partial^2 u}{\partial x^2} - \rho A \frac{\partial^2 u}{\partial t^2} &= 0, \\ \hat{E}(\iota\omega) I_{xx} \frac{\partial^4 w}{\partial x^4} - \rho A \frac{\partial^2 w}{\partial t^2} &= 0, \\ \hat{G}(\iota\omega) J \frac{\partial^2 \theta}{\partial x^2} - \rho J \frac{\partial^2 \theta}{\partial t^2} &= 0. \end{aligned} \tag{2.1}$$

Here u, w, and θ are the axial, flexural, and torsional DOFs of the frame element; x and t are the spatial coordinate and time; ρ is the density, $\hat{E}(\iota\omega)$ and $\hat{G}(\iota\omega)$

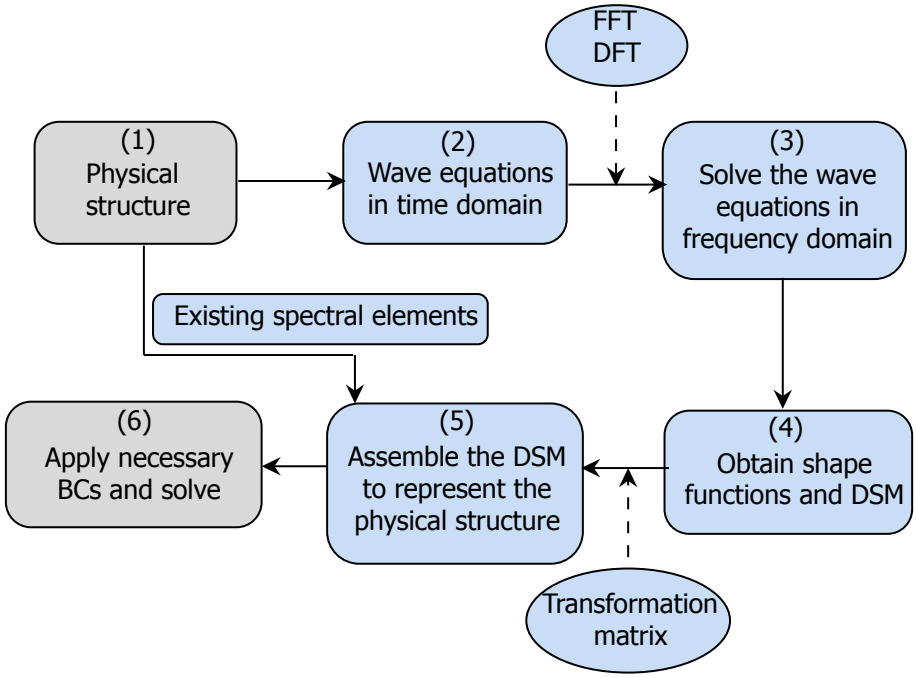

Figure 2.1: Flowchart representing the general SEM process for analyzing wave propagation through a structure starting from the physical structure till solving the DSM after applying BCs. The viscoelastic model can either be introduced in step 3 before solving the EOM or, in the case of a linear viscoelastic system, during step 4 after obtaining the shape functions.

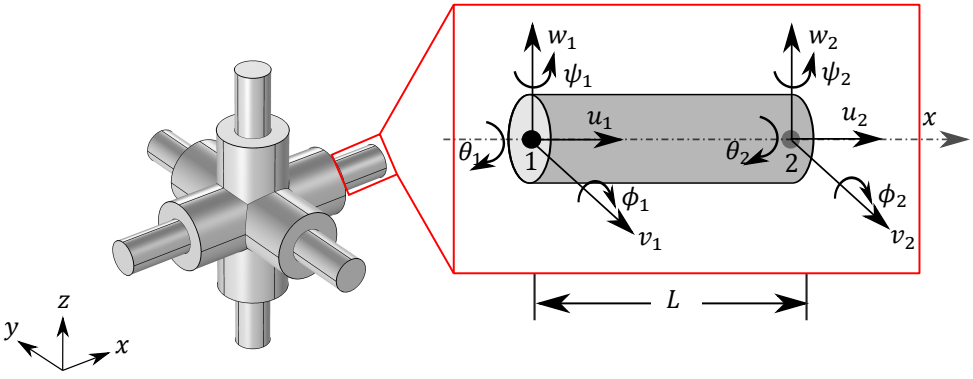

Figure 2.2: A three-dimensional metamaterial unit cell that can be represented by a collection of a two-node frame element shown in the inset. The frame element of length L has 6 DOFs per node corresponding to axial, bending, and torsional deformations.

are the complex-valued Young's and shear moduli with ι denoting the imaginary number; ω is frequency; A is the cross-sectional area; I_{xx} is the second moment of area w.r.t. x axis, and J is the second polar moment of area of the frame element.

Note that w represents the flexural displacement that can capture only bending with respect to the x axis. A similar equation to capture the bending with respect to the y axis can be obtained by replacing w, x, and I_{xx} in the second equation of Eqs. (2.1) with v, y, and I_{yy}, respectively. The complex Young's modulus and shear modulus are represented as [47]:

$$\hat{E}(\iota\omega) = E_\infty + \sum_{i=1}^{n} \frac{\iota\omega E_i}{\iota\omega\tau_i + 1}, \qquad \hat{G}(\iota\omega) = \frac{\hat{E}(\iota\omega)}{2(1+\nu)} \tag{2.2}$$

where $\tau_i = \eta_i / E_i$ and E_i denote, respectively, the i^{th} Maxwell element's relaxation time and relaxation modulus, η_i is the dynamic viscosity, E_∞ is Young's modulus at equilibrium, and ν is the Poisson's ratio, which is assumed to be constant. The number n is usually chosen to ensure adequate fit with experimental data.

We consider two boundary-value problems (BVPs) corresponding to the following analysis cases:

1. **BVP 1: Band structure analysis** implies the study of the dispersion relation. This relation is obtained by solving an eigenvalue problem for a metamaterial unit cell subject to Bloch-Floquet boundary conditions with the wave vector values restricted to the irreducible Brillouin zone [67]. These boundary conditions in our case take the following form:

$$\boldsymbol{u}(\underline{x} + \boldsymbol{a}_i, t) = e^{i(\boldsymbol{k}.\boldsymbol{a}_i)}\boldsymbol{u}(\underline{x}, t), \tag{2.3}$$

   where $\boldsymbol{u}$ is the DOF vector that includes all displacements and rotations, $\underline{x}$ is the position vector, and $\boldsymbol{a}_i$ is the lattice vector along the i^{th} coordinate. For the band structure analysis, we use the $\omega(\boldsymbol{k})$ approach that implies calculating frequencies for a fixed $\boldsymbol{k}$.

2. **BVP 2: Transmission analysis** allows studying wave characteristics in finite-size structures by performing the steady-state dynamic analysis of a metamaterial waveguide under the Dirichlet boundary conditions [68]:

$$\boldsymbol{u}(\underline{l}, t) = \tilde{\boldsymbol{u}} e^{i\omega t}, \tag{2.4}$$

   where $\tilde{\boldsymbol{u}}$ is the prescribed displacement amplitude at location $\underline{x} = \underline{l}$. The wave transmission can be estimated as a ratio of the output displacement to the input displacement for the frequency range of interest.

The shape functions satisfying Eq. (2.1) for longitudinal waves can be represented as follows [59]:

$$\boldsymbol{N}_L(x, \omega) = \left[\csc(k_L L)\sin[k_L(L-x)] \quad \csc(k_L L)\sin(k_L x)\right], \tag{2.5}$$

where $k_L = \|\boldsymbol{k}_L\| = \omega / C_L$ is the magnitude of the longitudinal wave vector along the wave propagation direction and $C_L = \sqrt{\hat{E}(\iota\omega)/\rho}$ is the longitudinal wave velocity.

For flexural waves, the shape functions can be represented as follows:

$$
\begin{aligned}
\boldsymbol{N}_B(x,\omega) &= [N_{B1} \quad N_{B2} \quad N_{B3} \quad N_{B4}],\\
N_{B1}(x,\omega) &= \eta^{-1}k_{Fx}[\cos\bar{x} - \cos(\bar{L}_x - \bar{x})\cosh\bar{L}_x - \cos\bar{L}_x\cosh(\bar{L}_x - \bar{x})\\
&\quad + \cosh\bar{x} + \sin(\bar{L}_x - \bar{x})\sinh\bar{L}_x - \sin\bar{L}_x\sinh(\bar{L}_x - \bar{x})],\\
N_{B2}(x,\omega) &= \eta^{-1}[-\cosh(\bar{L}_x - \bar{x})\sin\bar{L}_x + \cosh\bar{L}_x\sin(\bar{L}_x - \bar{x}) + \sin\bar{x}\\
&\quad - \cos(\bar{L}_x - \bar{x})\sinh\bar{L}_x + \cos\bar{L}_x\sinh(\bar{L}_x - \bar{x}) + \sinh\bar{x}],\\
N_{B3}(x,\omega) &= \eta^{-1}k_{Fx}[\cos(\bar{L}_x - \bar{x}) - \cos\bar{x}\cosh\bar{L}_x - \cos\bar{L}_x\cosh\bar{x}\\
&\quad + \cosh(\bar{L}_x - \bar{x}) + \sin\bar{x}\sinh\bar{L}_x - \sin\bar{L}_x\sinh\bar{x}],\\
N_{B4}(x,\omega) &= -\eta^{-1}[-\cosh\bar{x}\sin\bar{L}_x + \cosh\bar{L}_x\sin\bar{x} + \sin(\bar{L}_x - \bar{x})\\
&\quad - \cos\bar{x}\sinh\bar{L}_x + \cos\bar{L}_x\sinh\bar{x} + \sinh(\bar{L}_x - \bar{x})].
\end{aligned}
\tag{2.6}
$$

where $\eta = 2k_{Fx}(1 - \cos\bar{L}_x\cosh\bar{L}_x)$, $\bar{x} = k_{Fx}x$, and $\bar{L}_x = k_{Fx}L$ are introduced for brevity, $k_{Fx} = \|\boldsymbol{k}_{Fx}\| = \sqrt{\omega}\left(\frac{\rho A}{\hat{E}(\iota\omega)I_{xx}}\right)^{1/4}$ is the magnitude of the flexural wave vector along the x axis, $C_{Fx} = \left(\frac{\hat{E}(\iota\omega)I_{xx}}{\rho A}\right)^{1/4}$ is the velocity of flexural waves. The shape functions for bending waves along the y axis can be obtained from Eq. (2.6) by replacing x with y, I_{xx} with I_{yy}, and $\boldsymbol{k}_{Fx}$ with $\boldsymbol{k}_{Fy}$. For torsional waves, the shape functions take the form:

$$
\boldsymbol{N}_T(x,\omega) = \begin{bmatrix}\csc(k_TL)\sin[k_T(L-x)] & \csc(k_TL)\sin(k_Tx)\end{bmatrix}, \tag{2.7}
$$

where $k_T = \|\boldsymbol{k}_T\| = \omega/C_T$ is the magnitude of the torsional wave vector and $C_T = \sqrt{\hat{G}(\iota\omega)/\rho}$ is the torsional wave velocity. Note that wave velocities C_L, C_F, and C_T are functions of frequency and thus correspond to dispersive waves, in contrast to the undamped situation when C_L and C_T are constants. Since the shape functions implicitly contain these wave velocities, the dispersive behavior is accurately captured by SEM.

The DSM for a single frame element can then be obtained by using the derived shape functions as follows (see [59] for more details):

$$
\boldsymbol{s} = \begin{bmatrix}
s_{A11} & 0 & 0 & 0 & 0 & 0 & s_{A12} & 0 & 0 & 0 & 0 & 0\\
0 & s_{Bx11} & 0 & 0 & s_{Bx12} & 0 & 0 & s_{Bx13} & 0 & 0 & s_{Bx14} & 0\\
0 & 0 & s_{By11} & 0 & 0 & s_{By12} & 0 & 0 & s_{By13} & 0 & 0 & s_{By14}\\
0 & 0 & 0 & s_{T11} & 0 & 0 & 0 & 0 & 0 & s_{T12} & 0 & 0\\
0 & s_{Bx12} & 0 & 0 & s_{Bx22} & 0 & 0 & s_{Bx23} & 0 & 0 & s_{Bx24} & 0\\
0 & 0 & s_{By12} & 0 & 0 & s_{By22} & 0 & 0 & s_{By23} & 0 & 0 & s_{By24}\\
s_{A12} & 0 & 0 & 0 & 0 & 0 & s_{A22} & 0 & 0 & 0 & 0 & 0\\
0 & s_{Bx13} & 0 & 0 & s_{Bx23} & 0 & 0 & s_{Bx33} & 0 & 0 & s_{Bx34} & 0\\
0 & 0 & s_{By13} & 0 & 0 & s_{By23} & 0 & 0 & s_{By33} & 0 & 0 & s_{By34}\\
0 & 0 & 0 & s_{T12} & 0 & 0 & 0 & 0 & 0 & s_{T22} & 0 & 0\\
0 & s_{Bx14} & 0 & 0 & s_{Bx24} & 0 & 0 & s_{Bx34} & 0 & 0 & s_{Bx44} & 0\\
0 & 0 & s_{By14} & 0 & 0 & s_{By24} & 0 & 0 & s_{By34} & 0 & 0 & s_{By44}
\end{bmatrix}, \tag{2.8}
$$

where the longitudinal waves are described by the following stiffness components:

$$\begin{aligned} s_{A11} &= s_{A22} = \hat{E}\,(\mathrm{i}\omega)\,Ak_A \cot(k_A L), \\ s_{A12} &= -\hat{E}\,(\mathrm{i}\omega)\,Ak_A \csc(k_A L). \end{aligned} \tag{2.9}$$

The flexural x-polarized waves are described by the other set of stiffness components:

$$\begin{aligned} s_{Bx11} &= s_{Bx33} = \Delta_{Bx}\bar{L}_x^3(\cos\bar{L}_x \sinh\bar{L}_x + \sin\bar{L}_x \cosh\bar{L}_x), \\ s_{Bx22} &= s_{Bx44} = \Delta_{Bx}\bar{L}_x^3 k_{Fx}^{-2}(-\cos\bar{L}_x \sinh\bar{L}_x + \sin\bar{L}_x \cosh\bar{L}_x), \\ s_{Bx12} &= -s_{Bx34} = \Delta_{Bx}\bar{L}_x^3 k_{Fx}^{-1} \sin\bar{L}_x \sinh\bar{L}_x, \\ s_{Bx13} &= -\Delta_{Bx}\bar{L}_x^3(\sin\bar{L}_x + \sinh\bar{L}_x), \\ s_{Bx14} &= -s_{B23} = \Delta_B\bar{L}_x^3 k_F^{-1}(-\cos\bar{L}_x + \cosh\bar{L}_x), \\ s_{Bx24} &= \Delta_B\bar{L}_x^3 k_F^{-2}(-\sin\bar{L}_x + \sinh\bar{L}_x), \end{aligned} \tag{2.10}$$

with $\Delta_{Bx} = \frac{1}{1-\cos\bar{L}_x \cosh\bar{L}_x}$. The corresponding stiffness components for flexural y-polarized waves are obtained from Eq. (2.10) by replacing $\bar{L}_x$ with $\bar{L}_y$, $\boldsymbol{k}_{Fx}$ with $\boldsymbol{k}_{Fy}$, and Δ_{Bx} with Δ_{By}. Finally, the torsional stiffness components are:

$$\begin{aligned} s_{T11} &= s_{T22} = \hat{G}\,(\mathrm{i}\omega)\,Jk_T \cot(k_T L), \\ s_{T12} &= -\hat{G}\,(\mathrm{i}\omega)\,Jk_T \csc(k_T L). \end{aligned} \tag{2.11}$$

Dynamic stiffness matrix of the 3D viscoelastic metamaterial

The global DSM is obtained by assembling individual DSMs of each frame element considering its orientation. To that end, we use the following rotation matrices [69]:

$$\boldsymbol{T} = \begin{bmatrix} \boldsymbol{Q} & 0 & 0 & 0 \\ 0 & \boldsymbol{Q} & 0 & 0 \\ 0 & 0 & \boldsymbol{Q} & 0 \\ 0 & 0 & 0 & \boldsymbol{Q} \end{bmatrix}, \qquad \boldsymbol{Q} = \begin{bmatrix} \boldsymbol{n}_{x1} & \boldsymbol{n}_{x2} & \boldsymbol{n}_{x3} \\ \boldsymbol{n}_{y1} & \boldsymbol{n}_{y2} & \boldsymbol{n}_{y3} \\ \boldsymbol{n}_{z1} & \boldsymbol{n}_{z2} & \boldsymbol{n}_{z3} \end{bmatrix}, \qquad \bar{\boldsymbol{s}}_1 = \boldsymbol{T}^{\mathsf{T}} \times \boldsymbol{s}_1 \times \boldsymbol{T}, \tag{2.12}$$

where $\boldsymbol{n}_x = \frac{1}{L}\{x_2 - x_1 \quad y_2 - y_1 \quad z_2 - z_1\}$, $\boldsymbol{n}_y = \frac{1}{\sqrt{n_{x1}^2 + n_{x2}^2}}\{-n_{x2} \quad n_{x1} \quad 0\}$, and $\boldsymbol{n}_z = \boldsymbol{n}_x \times \boldsymbol{n}_y$ are directional cosines and $\{x, y, z\}$ is the coordinate system of the frame element's node (see Figure 2.2). The global DSM for the unit cell shown in Figure 2.2 has thus 78 DOFs (12 frame elements) and can be used to estimate the band structure when combined with Eq. (2.3) or to estimate wave transmission using Eq. (2.4).

To analyze the dynamics of a viscoelastic metamaterial, one needs to introduce an appropriate damping model into the DSM. In the next section, we discuss how it can be done.

Viscoelastic mechanical models

Complex elastic moduli describing viscoelastic behavior have the real part – storage modulus – representing elastic behavior and the imaginary part – loss modulus –

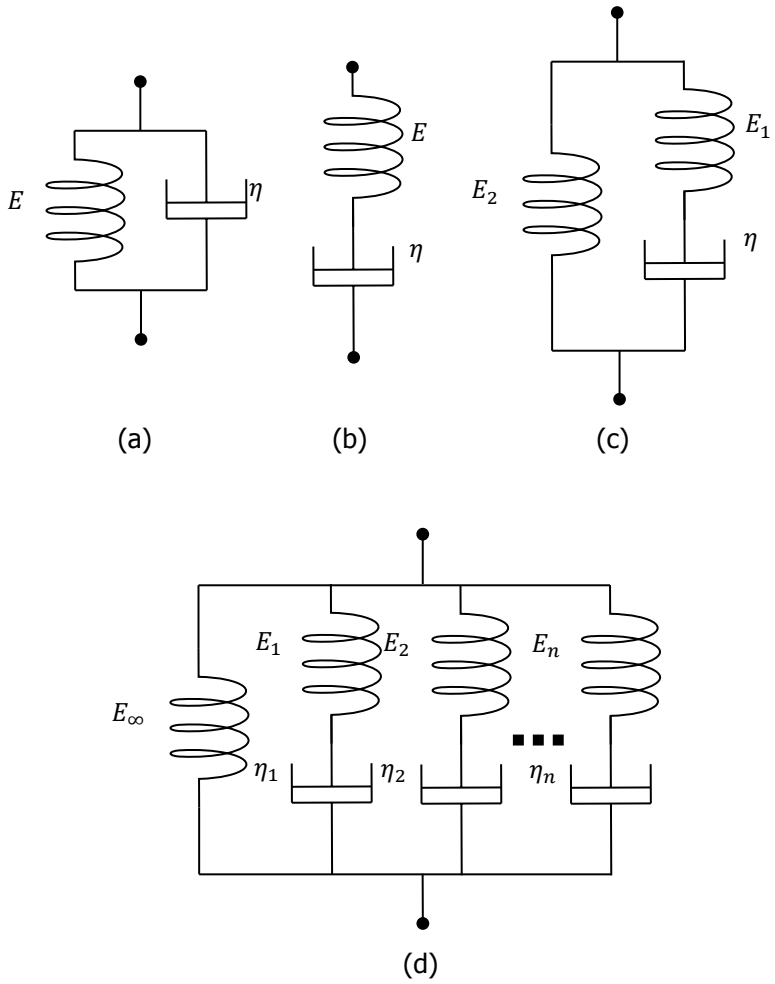

Figure 2.3: Linear viscoelastic models with their parameters. (a) Kelvin-Voigt, (b) Maxwell, (c) Zener, and (d) generalized Maxwell models. E_i and η_i, respectively, represent the relaxation modulus and damping factor of the i^{th} Maxwell element, while E_∞ is the elastic modulus at equilibrium.

describing viscous losses. The ratio of the loss modulus to the storage modulus is known as the loss factor (or loss tangent) and provides a measure of energy dissipation in a material. The dependence of the viscoelastic properties (storage modulus, loss modulus, and loss factor) on frequency, temperature, strain-rate, creep, pre-load [70], and aging [71] complicates the material characterization and quantification of the moduli. To address this challenge, it was proposed to use several simplified models, *e.g.*, Kelvin-Voigt [72], Zener [73], and Maxwell [74] models as shown in Figure 2.3. The Kelvin-Voigt and Maxwell models represented by a spring and a dashpot connected in parallel and in series, respectively, are widely used [75], but cannot capture the viscoelastic behavior of any real material.

The Zener model is an extension of the Kelvin-Voigt model with an added spring to represent the elastic behavior at equilibrium. Despite being more accurate, this model is still oversimplified for practical situations. More accurate approximations of viscoelastic material response can be obtained by combining several Maxwell or Kelvin-Voigt elements together that result in generalized models, for instance, the generalized Maxwell model shown in Figure 2.3(d), which are typically used to fit experimentally measured values of the storage and loss moduli [76].

2.2.2. SEM *vs.* FEM for viscoelastic problems

Here, we incorporate the generalized Maxwell viscoelastic model into the DSM by replacing elastic moduli in (2.8)—(2.11) with Eqs. (2.2). As explained, the values of the relaxation moduli and relaxation times for the Maxwell elements in Eqs. (2.2) can be obtained by fitting them into experimentally measured master curves [76]. Since in SEM, the wave vector is a function of the material moduli, variations in the moduli values are immediately reflected in the wave vector and, thus, in the elements of the DSM. Therefore, at every analyzed frequency, the constituents of the DSM change according to the viscoelastic behavior reflected by the viscoelastic moduli values, ensuring accurate predictions. This is in contrast to the FEM analysis, where the viscoelastic moduli do not enter the interpolation functions, and thus the variations of the moduli values are not considered. This highlights The advantage of SEM in analyzing wave dynamics in viscoelastic media as compared to the standard FEM.

Another advantage of SEM follows from the fact that the SEM shape functions are the solutions to the wave equations, so the viscoelastic moduli entering these functions can provide accurate responses instantly. In the FEM, the viscoelastic moduli only appear in the constitutive matrix that requires updating this matrix at each step of the solution procedure and results in vastly increased computational costs [77]. These differences are especially pronounced in dynamic problems. Figure 2.4 illustrates the variation of the SEM shape functions with frequency (Figure 2.4(b)) in comparison with the FEM shape functions that remain unchanged, enabling thus to accurately capture only static behavior 2.4(d). To overcome this issue, the FEM requires a sufficiently large number of elements to resolve the dynamic response governed by the frequency. This puts strict requirements on the mesh density (the mesh should properly resolve the waves at the highest analyzed frequency) resulting in (extremely) fine-meshed models in a high-frequency range. This is not the case for the SEM models.

2.3. The SEM procedure for a viscoelastic metamaterial plate

In this section, we apply the proposed SEM formulation to model the wave dynamics in a polymer metamaterial plate. The metamaterial unit cell is shown in Figure 6.4, where four rods of 1 mm thick with rectangular cross-sections are connected to a central cylindrical disc of 28 mm diameter. The height in the vertical direction is 10 mm. The lattice vectors $\boldsymbol{a}_1$ and $\boldsymbol{a}_2$ ($\|\boldsymbol{a}_1\| = \|\boldsymbol{a}_2\| = a = 40$ mm) are aligned with

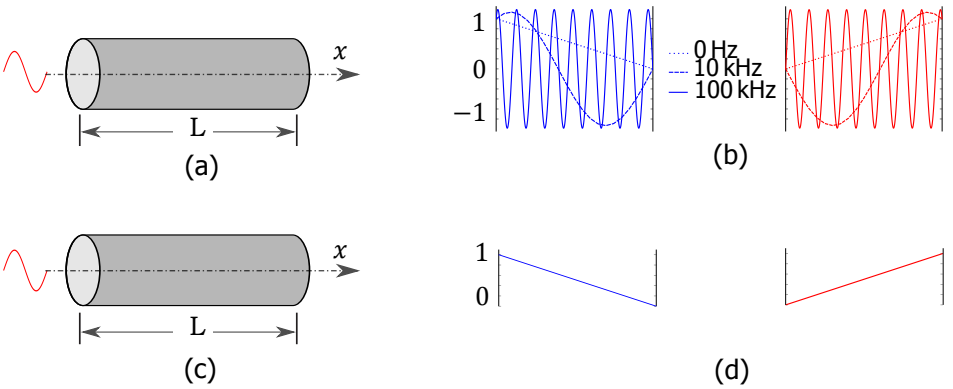

Figure 2.4: Comparison of SEM and FEM shape functions at different frequencies: (a), (c) schematics of a traveling wave through a cylindrical rod for both methods; (b) SEM shape functions at the indicated frequencies; (d) FEM linear shape functions.

x and y directions, respectively. For the square lattice of the unit cells we use a triangular IBZ for the band structure analysis [78] as shown in Figure 2.5b.

The host material is polycarbonate, which is a durable and tough thermoplastic with a glass transition temperature above 150 °C. Polycarbonate shows viscoelastic properties at room temperature due to secondary transitions in the glassy state [79]. To estimate the effects of the secondary viscous losses, which are often neglected, we model the plate as an elastic and viscoelastic solid. Polycarbonate has a material density of 1185 kg/m^3, elastic modulus 2.17 GPa, and a Poisson's ratio of 0.375. Its viscoelastic behavior can be represented by Prony series (2.2) with the two sets of values for the relaxation modulus and relaxation time: (0.356 GPa, 0.618 s) and (0.15 GPa, 0.0996 s). Noteworthy, as the Poisson's ratio is also a time (or frequency)-dependent material function in the case of the viscoelastic material, its constant approximation could introduce variations in the dynamic behavior. Although in this study, we have selected a constant Poisson's ratio for polycarbonate [80], it is possible to account for its variability via Equation (2.2).

According to the formulation of the SEM procedure (Fig. 1), we need to represent the plate geometry by means of the SEM frame elements. For this, we note that the stiffness of the central disc is considerably higher than that of the surrounding rods meaning that the eigenfrequencies of the disc should also be high. At low frequencies, *i.e.,* around the first band gap, the dynamics of the metamaterial is thus governed by wave scattering in the thin ligaments [76, 81], and we can assume that the geometry of the disc is not relevant. The 28 mm diameter disc can then be replaced with a square prism shown in Figure 2.5b, one side of which has a dimension of $b = 20$ mm and the length of the side at the four corners reduces to $b - 2d$ with $d = 2.7$ mm; the height of the unit cell is preserved.

Eventual discrepancies due to the modification of the unit-cell geometry can be estimated by comparing band structure diagrams for the original and modified unit cells given in Figures 2.5c and 2.5d, respectively, under the assumption of lossless (elastic) material behavior. The two band structures have a band gap (shaded re-

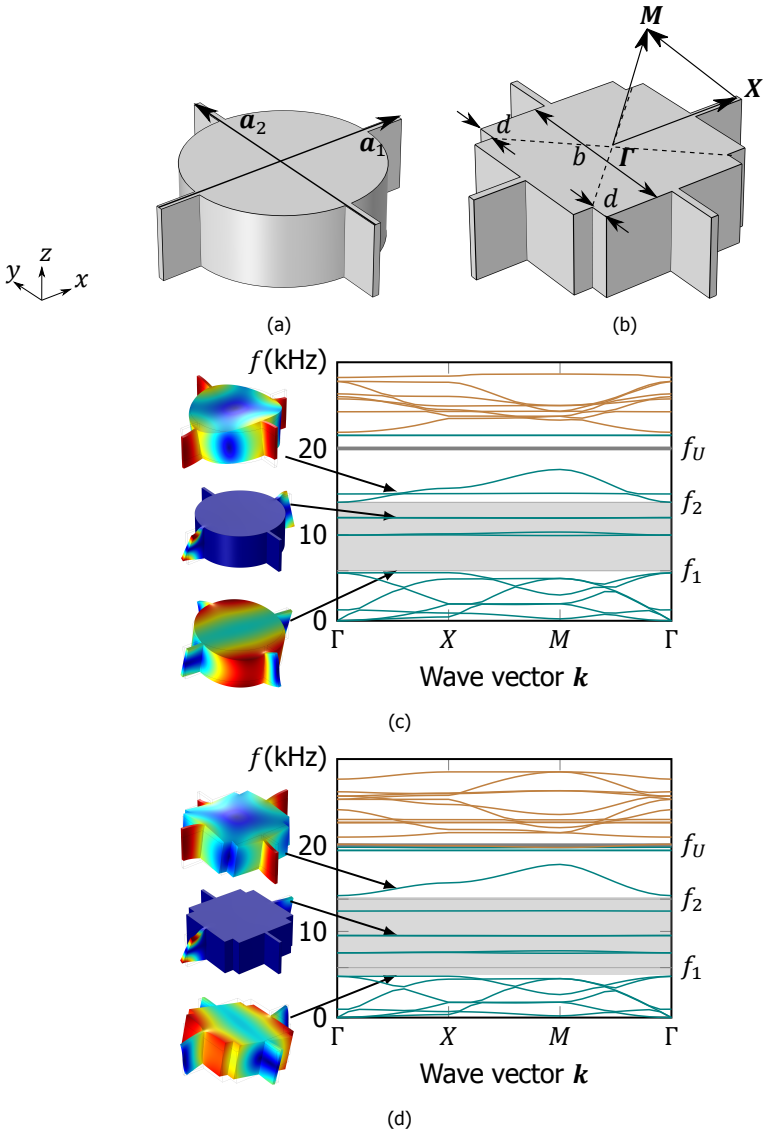

Figure 2.5: (a) Unit cell of the metamaterial plate with lattice vectors $\boldsymbol{a}_1$ and $\boldsymbol{a}_2$ aligned to x and y directions. (b) The modified unit cell, where the central disc is replaced with a square prism, and the corresponding IBZ is marked with arrows. The dashed lines separate the prism into four identical parts that can be represented by SEM frame elements. (c-d) Band structures and selected eigenmodes for the two unit cells. As can be seen, the two structures are identical below the first band gap indicated by the shaded region between f_1 = 5.8 kHz and f_2 = 13.75 kHz. The frequency range of interest is marked by gray solid lines and reached f_U = 20 kHz in both band structures. The displacement modes correspond to f_1, f_2, and a localized mode within the band gap are similar for the two unit cells. The bands with the similar dynamics for both models are marked in teal, the other bands are depicted in brown.

gion) that spans from $f_1 = 5.8\,\text{kHz}$ to $f_2 = 13.75\,\text{kHz}$ with some localized modes in between. The eigenmodes at f_1 are similar for the two geometries and governed by the bending of the ligaments with no contribution from the disk. The localized modes within the first band gap are also governed by the bending of the ligaments. These modes, however, have negligible influence on the wave propagation characteristics in the plate and are thus not considered further. Note that the frequencies and curvature of the passbands up to 20 kHz (marked as f_U) are almost identical in the two diagrams with some differences appearing at higher frequencies. The high-frequency variations are due to the interaction of the higher-order eigenmodes of the disk (prism) with those of the ligaments as can already be seen for the mode at f_2. The latter mode is governed by the bending of the disk (prism), but since the mass of the central elements is identical, the variations in the corresponding wavebands are negligible. Therefore, the proposed approximation of the original unit cell geometry is appropriate to analyze the wave dynamics, *i.e.,* up to 20 kHz (which includes the first band gap).

Next, the central square (bulk portion) is converted to four SEM frame elements joined at the center with the separation shown by the dashed lines in Figure 2.5b. This is necessary because the SEM frame element cannot represent a bulk geometry by a two-node one-dimensional element shown in Fig. 2.2. After the separation, the four frame elements can capture most of the modes of the central bulk region due to a large number of the available DOFs (3 translation and 3 rotation DOFs per each frame element). Further, we represent the four ligaments in the original unit cell with the rod frame elements and finally obtain an equivalent SEM model of the unit cell. The SEM unit cell is tessellated to form an equivalent metamaterial plate (Figure 2.6(b)) representing the original plate design (Figure 2.6(a)).

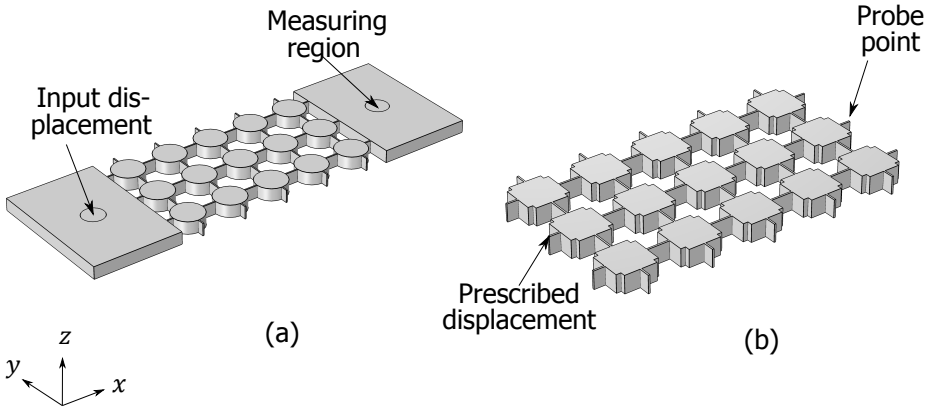

Figure 2.6: (a) The model of the metamaterial plate for the transmission analysis with indicated excitation and output regions, (b) The generated SEM model of the plate with equivalent boundary conditions.

The derived SEM model of the metamaterial plate has only 120 frame elements (8 elements per unit cell $\times 15$ unit cells). For comparison, we developed an FEM model that has 168519 tetrahedral elements required to analyze the target frequency range. Hence, the computational advantage of the SEM model is obvious.

As explained, the wave dynamics of the viscoelastic plate is analyzed by replacing the elastic moduli with their complex-valued counterparts expressed by Prony series [82]. Note that despite one typically requires a large number of the elements in the Prony series to properly capture the material viscoelasticity [83], this is not the case for the SEM model. It is because the 3D structural viscoelasticity allowing all types of modes and their interactions is replaced by considering 1D elements that restrict the motion to specific modes corresponding to the allowed DOFs.

2.3.1. Experimental setup for transmission experiments

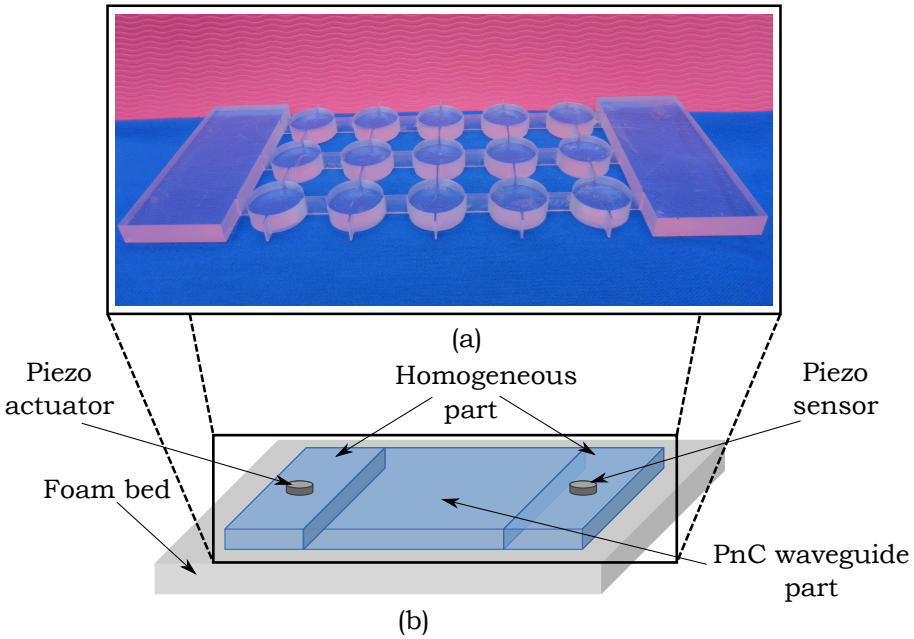

Figure 2.7: Schematic of the experimental setup to measure the transmission in the metamaterial plate: (a) the photograph of the plate placed on a foam bed to isolate it from environmental vibrations; (b) schematics of the experimental setup with the piezo-actuator to apply harmonic excitation and the piezo-sensor to detect transmitted waves.

The metamaterial plate is fabricated from a transparent polycarbonate sheet of 10 mm thickness. The pattern was introduced via milling (Benchman VMC 4000). The final configuration of the plate specimen has a metamaterial part with 3×5 unit cells and two homogeneous parts with dimensions 120 mm $\times$ 200 mm.

The experimental setup to measure wave transmission in the plate includes a bi-morphic piezoelectric PZT disc of 10 mm diameter glued to a surface of a homogeneous part of the plate (Figure 2.7) that acts as an actuator. The actuator connected to the signal generator and high-voltage amplifier (OPA547-TI) applies vertical excitation in the target frequency range (Figure 2.6). Another PZT disk of the same diameter is glued symmetrically at the opposite side of the meta-structure,

on the other homogeneous part, and acts as a sensor. This sensor is connected to oscilloscope RTM3000 with a sample rate of 5G samples/s for acquiring the transmitted signal. The sample is placed on a foam bed to isolate it from environmental vibrations without affecting its dynamic response.

2.4. Results and discussion

2.4.1. Numerical *vs.* experimental viscoelastic response

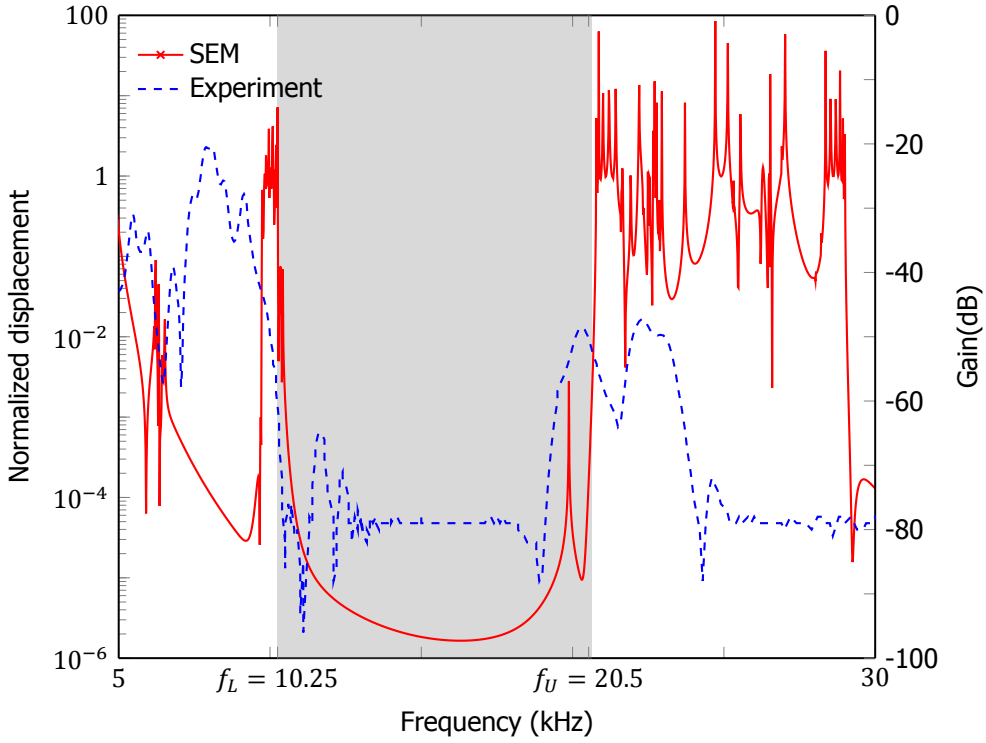

Figure 2.8: SEM (red) and experimental (dashed blue) transmission values for the polycarbonate metamaterial plate. The theoretical data are represented using normalized displacement ((the left y-axis), while the experimental data is plotted by using a gain function (the right y-axis). The shaded region is the predicted band gap bounded by frequencies f_L and f_U.

Figure 2.8 shows the comparison between the calculated (SEM) and measured transmission response with the predicted band gap shaded in gray. The experimental transmission is estimated as the ratio of voltages between the piezo sensor (V_{out}) and the piezo actuator (V_{in}) obtained using the gain function:

$$\text{Gain} = 20 \times \log_{10}\left(\frac{V_{out}}{V_{in}}\right). \tag{2.13}$$

Comparing the theoretical and experimental data, we see that SEM can adequately

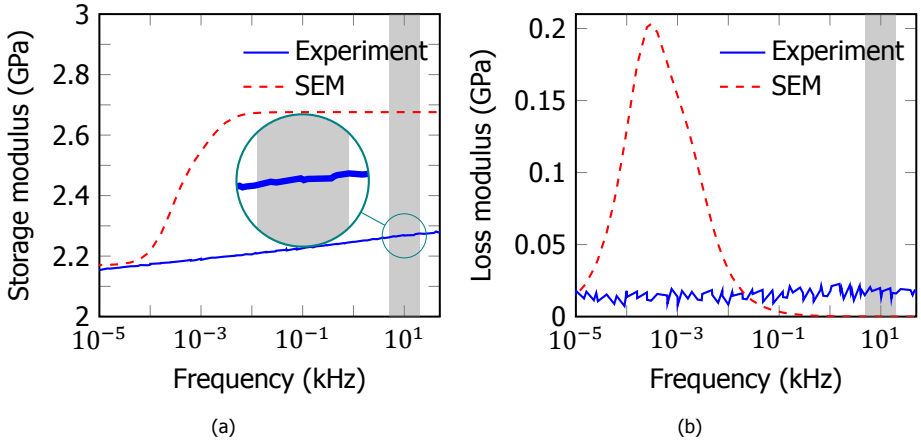

Figure 2.9: SEM and experimental master curve at room temperature (20 °C) with the shaded region indicating the target frequency range: (a) storage modulus and (b) loss modulus. The inset in (a) shows the presence of localized peaks and dips in the experimentally measured storage modulus.

predict the transmission around the first band gap that spans from $f_L = 10.25$ kHz to $f_U = 20.5$ kHz. This frequency range significantly differs from that for the undamped case shown in Figure 2.5c. Therefore, we can state that the material viscoelasticity shifts the first band gap to higher frequencies (the lower band-gap band is moved from 7 kHz to 10.25 kHz) and increases its width (the upper band-gap bound is shifted from 13.75 kHz to 20.5 kHz). At frequencies above 20 kHz, the variation between the SEM and experimental results increases due to the contribution of the disc's eigenmodes, which are not properly captured by the SEM frame elements. Another limitation of the SEM approximation is the impossibility of predicting experimentally observed transmission peaks and dips because the three-dimensional dynamics of the plate are modeled by one-dimensional elements and due to the complexity of the viscoelastic material behavior, as discussed below. Note that FEM models also suffer from a similar drawback [76]. Additionally, as described in Section 2.2.2, the variations in the viscoelastic moduli are not accounted for by the interpolation functions in FEM models, which further increases the number of evaluation steps and hence the computational cost compared to the SEM counterpart.

The dynamic behavior of viscoelastic (meta)material can be accurately predicted provided the viscoelastic moduli adequately capture experimental master curves that typically require many elements in the corresponding Prony series (2.2) depending on the target frequency range and its proximity to the primary and secondary transition zones [76]. In our case, the difference in the storage and loss moduli values between the approximated and experimental master curves are significant (Figure 2.9). The theoretical master curves are constructed by using two elements of the series, while the experimental curves are generated via the dynamic temperature-mechanical analysis (DMTA) [76]. As a result, the storage modulus curves match only at low frequencies (close to 0.0001 kHz) and strongly deviate

from each other at higher frequencies. In the target frequency range (the shaded region: 5 kHz-20 kHz), the theoretical storage modulus is about 18% higher as compared to the experimental value. Besides, the theoretical storage modulus remains constant, while the experimental one increases with frequency in a non-uniform way (see the inset in Figure 2.9a). The experimental loss modulus shows negligible variation with the frequency with close to zero values at room temperature. In contrast, the theoretical loss modulus has a Gaussian-type shape with a peak around 0.001 kHz. However, the loss modulus values remain very small at the target frequencies implying an insignificant effect on the dynamic response of the plate. Additionally, as described in Subsection 2.3, the Poisson's ratio is assumed as a constant value corresponding to the metamaterial plate's equilibrium behavior, which introduces further error in estimating its transmission peaks response.

The discussed differences between the theoretical and experimental master curves and the use of 1D frame elements to approximate the 3D geometry hinder the SEM model from accurately predicting the wave transmission in the considered plate. However, increasing the number of the components in the Prony series in order to improve the match with the experimental master curves might not necessarily improve the performance of the SEM model due to its intrinsic one-dimensional nature. Nevertheless, despite this restriction, the SEM model provides surprisingly accurate predictions around the first band gap that can be challenging even for the computationally expensive FEM models [76]. Therefore, we conclude that this model can be successfully used as a first-hand approximation to design and optimize viscoelastic metamaterial structures at frequencies close to the first band gap.

2.5. Summary and Conclusions

In this work, we proposed an analytical procedure based on the spectral element method (SEM) to characterize the wave dynamics of bulk (3D) and plate-like (2D) viscoelastic metamaterials. We discussed how to approximate a metamaterial's 3D geometry by means of 1D SEM frame elements. The accuracy of the approximation was estimated by studying the band structures of both the original and simplified unit cells, and such accuracy was shown to be adequate at frequencies around the first band gap. The wave transmission predicted by the SEM model was also validated experimentally for a polycarbonate metamaterial plate. The obtained results allow us to draw the following conclusions:

- The dynamic analysis of dissipative metamaterials is intricate due to frequency-dependent viscoelastic effects that increase the computational costs when employing standard computational tools such as finite element analysis. Analytical models, such as the proposed extension of SEM, can partially solve this issue depending on the target frequency range. Since SEM incorporates frequency dependence in its shape functions, fine meshes are not required. Additionally, linear viscoelastic behavior can easily be introduced into the SEM elements by modifying the shape functions, which further simplifies the analysis and reduces the computational costs;

- The obtained accurate match between the SEM and experimental results for the wave transmission in the plate suggests that SEM models can provide reliable approximations by significantly reducing the simulation time for plate-like viscoelastic metamaterials at frequencies around the first band gap at the cost of introducing a simplified geometry for a plate;
- The limitation of SEM, *i.e.*, its inability to deal with complex geometries, can be overcome in practice by developing approximate models in 2D and 3D by assembling 1D (beam/frame) elements, which would be accurate for specific frequency ranges. Moreover, depending on complexities in the geometry, the number and arrangement of 1D elements can be defined. This approach provides the designer with a back-of-envelope method/tool for quick analysis of these structures, which is otherwise very tedious. SEM models are very effective in determining accurately the first band gap. This allows us to easily test many materials (changing the properties of the base material) and any number of the metamaterial's unit cells. This can therefore make SEM the methodology of choice to quickly prototype new metamaterials irrespective of their field of application.

As a future direction, complex structural elements such as plates/shells can be incorporated into the SEM-based viscoelastic model to represent the behavior of intricate geometries accurately. This modification will also aid in incorporating more Maxwell elements into the Prony series as plates/shells possess complex displacement modes allowing them to accurately mimic the response from DMTA. Additionally, an SEM-FEM *hybrid* method [59] that leverages both advantages can be used to model viscoelastic metamaterials with complex geometries.

Bibliography

[1] Stephen H Crandall. "The role of damping in vibration theory". In: *Journal of sound and vibration* 11.1 (1970), 3–IN1.

[2] DH Wang and WH Liao. "Semi-active suspension systems for railway vehicles using magnetorheological dampers. Part I: system integration and modelling". In: *Vehicle System Dynamics* 47.11 (2009), pp. 1305–1325.

[3] Feilong Xu et al. "Decorated membrane resonators as underground seismic wave barriers against high magnitude earthquakes". In: *Journal of Applied Physics* 128.8 (2020), p. 084902. DOI: 10.1063/5.0013234. eprint: https://doi.org/10.1063/5.0013234. URL: https://doi.org/10.1063/5.0013234.

[4] S. S. Iyer et al. "Nonlinear damping for vibration isolation of microsystems using shear thickening fluid". In: *Applied Physics Letters* 102.25 (2013), p. 251902. DOI: 10.1063/1.4812192. eprint: https://doi.org/10.1063/1.4812192. URL: https://doi.org/10.1063/1.4812192.

[5] Ioannis Politopoulos. "A review of adverse effects of damping in seismic isolation". In: *Earthquake Engineering & Structural Dynamics* 37.3 (2008), pp. 447–465. DOI: https://doi.org/10.1002/eqe.763. eprint: https://onlinelibrary.wiley.com/doi/pdf/10.1002/eqe.763. URL: https://onlinelibrary.wiley.com/doi/abs/10.1002/eqe.763.

[6] Hadi Najar et al. "High quality factor nanocrystalline diamond micromechanical resonators limited by thermoelastic damping". In: *Applied Physics Letters* 104.15 (2014), p. 151903. DOI: 10.1063/1.4871803. eprint: https://doi.org/10.1063/1.4871803. URL: https://doi.org/10.1063/1.4871803.

[7] Marko Mihalec et al. "Damping heat coefficient–theoretical and experimental research on a vibrating beam". In: *Journal of Sound and Vibration* 400 (2017), pp. 13–21.

[8] Thomas H. Metcalf et al. "Thermoelastic damping in micromechanical resonators". In: *Applied Physics Letters* 95.6 (2009), p. 061903. DOI: 10.1063/1.3190509. eprint: https://doi.org/10.1063/1.3190509. URL: https://doi.org/10.1063/1.3190509.

[9] F. R. Schwarzl. "Numerical calculation of storage and loss modulus from stress relaxation data for linear viscoelastic materials". In: *Rheologica Acta* 10.2 (June 1971), pp. 165–173. ISSN: 1435-1528. DOI: 10.1007/BF02040437. URL: https://doi.org/10.1007/BF02040437.

[10] Roderic Lakes and Roderic S Lakes. *Viscoelastic materials*. Cambridge university press, 2009.

[11] M. S. Kushwaha et al. "Acoustic band structure of periodic elastic composites". In: *Physical Review Letters* 71 (13 Sept. 1993), pp. 2022–2025. DOI: 10.1103/PhysRevLett.71.2022. URL: https://link.aps.org/doi/10.1103/PhysRevLett.71.2022.

[12] W. L. Bragg. "The Diffraction of Short Electromagnetic Waves by a Crystal". In: *Scientia* 23.45 (1929), p. 153.

[13] Steven A Cummer, Johan Christensen, and Andrea Alù. "Controlling sound with acoustic metamaterials". In: *Nature Reviews Materials* 1.3 (2016), p. 16001.

[14] Matthew Reynolds and Stephen Daley. "An active viscoelastic metamaterial for isolation applications". In: *Smart Materials and Structures* 23.4 (2014), p. 045030.

[15] AA Maznev, AG Every, and OB Wright. "Reciprocity in reflection and transmission: What is a 'phonon diode'?" In: *Wave Motion* 50.4 (2013), pp. 776–784.

[16] Osama R. Bilal, André Foehr, and Chiara Daraio. "Bistable metamaterial for switching and cascading elastic vibrations". In: *Proceedings of the National Academy of Sciences* 114.18 (2017), pp. 4603–4606. ISSN: 0027-8424. DOI: 10.1073/pnas.1618314114. eprint: https://www.pnas.org/content/114/18/4603.full.pdf. URL: https://www.pnas.org/content/114/18/4603.

[17] Kyung Ho Sun et al. "Sound energy harvesting using a doubly coiled-up acoustic metamaterial cavity". In: *Smart Materials and Structures* 26.7 (2017), p. 075011.

[18] Shu Zhang, Leilei Yin, and Nicholas Fang. "Focusing ultrasound with an acoustic metamaterial network". In: *Physical review letters* 102.19 (2009), p. 194301.

[19] Choon Mahn Park et al. "Amplification of Acoustic Evanescent Waves Using Metamaterial Slabs". In: *Phys. Rev. Lett.* 107 (19 Nov. 2011), p. 194301. DOI: 10.1103/PhysRevLett.107.194301. URL: https://link.aps.org/doi/10.1103/PhysRevLett.107.194301.

[20] Chengrong Ma et al. "Acoustic metamaterial antennas for combined highly directive-sensitive detection". In: *Applied Physics Letters* 115.5 (2019), p. 053501.

[21] J Xu and J Tang. "Tunable prism based on piezoelectric metamaterial for acoustic beam steering". In: *Applied Physics Letters* 110.18 (2017), p. 181902.

[22] Hyuk Lee et al. "Mass-Stiffness substructuring of an elastic metasurface for full transmission beam steering". In: *Journal of the Mechanics and Physics of Solids* 112 (2018), pp. 577–593.

[23] Shu Zhang, Chunguang Xia, and Nicholas Fang. "Broadband acoustic cloak for ultrasound waves". In: *Physical Review Letters* 106.2 (2011), p. 024301.

[24] Mohamed Farhat, Sebastien Guenneau, and Stefan Enoch. "Ultrabroadband elastic cloaking in thin plates". In: *Physical review letters* 103.2 (2009), p. 024301.

[25] Nicolas Stenger, Manfred Wilhelm, and Martin Wegener. "Experiments on elastic cloaking in thin plates". In: *Physical Review Letters* 108.1 (2012), p. 014301.

[26] HK Zhang et al. "An asymmetric elastic metamaterial model for elastic wave cloaking". In: *Journal of the Mechanics and Physics of Solids* 135 (2020), p. 103796.

[27] Fabrice Lemoult, Mathias Fink, and Geoffroy Lerosey. "Acoustic resonators for far-field control of sound on a subwavelength scale". In: *Physical Review Letters* 107.6 (2011), p. 064301.

[28] Y.P. Zhao and P.J. Wei. "The band gap of 1D viscoelastic phononic crystal". In: *Computational Materials Science* 46.3 (2009). Proceedings of the 18th International Workshop on Computational Mechanics of Materials, pp. 603–606. ISSN: 0927-0256. DOI: https://doi.org/10.1016/j.commatsci.2009.03.040. URL: https://www.sciencedirect.com/science/article/pii/S0927025609001657.

[29] Joo Hwan Oh, Yoon Jae Kim, and Yoon Young Kim. "Wave attenuation and dissipation mechanisms in viscoelastic phononic crystals". In: *Journal of Applied Physics* 113.10 (2013), p. 106101. DOI: 10.1063/1.4795285. eprint: https://doi.org/10.1063/1.4795285. URL: https://doi.org/10.1063/1.4795285.

[30] Gang Wang et al. "Lumped-mass method for the study of band structure in two-dimensional phononic crystals". In: *Phys. Rev. B* 69 (18 May 2004), p. 184302. DOI: 10.1103/PhysRevB.69.184302. URL: https://link.aps.org/doi/10.1103/PhysRevB.69.184302.

[31] Jianbao Li, Yue-Sheng Wang, and Chuanzeng Zhang. "Finite element method for analysis of band structures of three dimensonal phononic crystals". In: *2008 IEEE Ultrasonics Symposium*. 2008, pp. 1468–1471. DOI: 10.1109/ULTSYM.2008.0357.

[32] Yong Xiao et al. "Theoretical and Experimental Study of Locally Resonant and Bragg Band Gaps in Flexural Beams Carrying Periodic Arrays of Beam-Like Resonators". In: *Journal of Vibration and Acoustics* 135.4 (June 2013). 041006. ISSN: 1048-9002. DOI: 10.1115/1.4024214. eprint: https://asmedigitalcollection.asme.org/vibrationacoustics/article-pdf/135/4/041006/6340170/vib_135_4_041006.pdf. URL: https://doi.org/10.1115/1.4024214.

[33] Mahmoud I Hussein and Michael J Frazier. "Band structure of phononic crystals with general damping". In: *Journal of Applied Physics* 108.9 (2010), p. 093506.

[34] Mahmoud I Hussein and Michael J Frazier. "Metadamping: An emergent phenomenon in dissipative metamaterials". In: *Journal of Sound and Vibration* 332.20 (2013), pp. 4767–4774.

[35] Michael J Frazier and Mahmoud I Hussein. "Viscous-to-viscoelastic transition in phononic crystal and metamaterial band structures". In: *The Journal of the Acoustical Society of America* 138.5 (2015), pp. 3169–3180.

[36] Michael J Frazier and Mahmoud I Hussein. "Generalized Bloch's theorem for viscous metamaterials: Dispersion and effective properties based on frequencies and wavenumbers that are simultaneously complex". In: *Comptes Rendus Physique* 17.5 (2016), pp. 565–577.

[37] Raj K Narisetti, Massimo Ruzzene, and Michael J Leamy. "Study of wave propagation in strongly nonlinear periodic lattices using a harmonic balance approach". In: *Wave Motion* 49.2 (2012), pp. 394–410.

[38] GL Huang and CT Sun. "Band gaps in a multiresonator acoustic metamaterial". In: *Journal of Vibration and Acoustics* 132.3 (2010), p. 031003.

[39] P Frank Pai. "Metamaterial-based broadband elastic wave absorber". In: *Journal of Intelligent Material Systems and Structures* 21.5 (2010), pp. 517–528.

[40] YY Chen, GL Huang, and CT Sun. "Band gap control in an active elastic metamaterial with negative capacitance piezoelectric shunting". In: *Journal of Vibration and Acoustics* 136.6 (2014).

[41] Kwek Tze Tan, HH Huang, and CT Sun. "Blast-wave impact mitigation using negative effective mass density concept of elastic metamaterials". In: *International Journal of Impact Engineering* 64 (2014), pp. 20–29.

[42] Dongwoo Lee, Minkyung Kim, and Junsuk Rho. "A finite element method towards acoustic phononic crystals by weak formulation". In: *Journal of Physics: Condensed Matter* 31.37 (June 2019), p. 375901. DOI: 10.1088/1361-648x/ab2700. URL: https://doi.org/10.1088/1361-648x/ab2700.

[43] Rixin Cui, Jinsong Zhou, and Dao Gong. "Band Gap and Vibration Reduction Properties of Damped Rail with Two-Dimensional Honeycomb Phononic Crystals". In: *Shock and Vibration* 2021 (Feb. 2021), p. 8814962. ISSN: 1070-9622. DOI: 10.1155/2021/8814962. URL: https://doi.org/10.1155/2021/8814962.

[44] K Billon et al. "Design and experimental validation of a temperature-driven adaptive phononic crystal slab". In: *Smart Materials and Structures* 28.3 (Feb. 2019), p. 035007. DOI: 10.1088/1361-665x/aaf670. URL: https://doi.org/10.1088/1361-665x/aaf670.

[45] Yuanchao Zhang et al. "Modeling and experimental analysis of particle damping phononic crystal plate". In: *AIP Advances* 11.10 (2021), p. 105202. DOI: 10.1063/5.0069603. eprint: https://doi.org/10.1063/5.0069603. URL: https://doi.org/10.1063/5.0069603.

[46] Romik Khajehtourian and Dennis M Kochmann. "A continuum description of substrate-free dissipative reconfigurable metamaterials". In: *Journal of the Mechanics and Physics of Solids* (2020), p. 104217.

[47] AO Krushynska, VG Kouznetsova, and MGD Geers. "Visco-elastic effects on wave dispersion in three-phase acoustic metamaterials". In: *Journal of the Mechanics and Physics of Solids* 96 (2016), pp. 29–47.

[48] MA Lewińska et al. "The attenuation performance of locally resonant acoustic metamaterials based on generalised viscoelastic modelling". In: *International Journal of Solids and Structures* 126 (2017), pp. 163–174.

[49] Yan-Feng Wang, Yue-Sheng Wang, and Vincent Laude. "Wave propagation in two-dimensional viscoelastic metamaterials". In: *Physical Review B* 92.10 (2015), p. 104110.

[50] P. Langer et al. "More Than Six Elements Per Wavelength: The Practical Use of Structural Finite Element Models and Their Accuracy in Comparison with Experimental Results". In: *Journal of Computational Acoustics* 25.04 (2017), p. 1750025. DOI: 10.1142/S0218396X17500254. eprint: https://doi.org/10.1142/S0218396X17500254. URL: https://doi.org/10.1142/S0218396X17500254.

[51] Linlin Shi et al. "Spectral element method for elastic and acoustic waves in frequency domain". In: *Journal of Computational Physics* 327 (2016), pp. 19–38.

[52] Linlin Shi et al. "Spectral element method for band-structure calculations of 3D phononic crystals". In: *Journal of Physics D: Applied Physics* 49.45 (2016), p. 455102.

[53] Anthony T Patera. "A spectral element method for fluid dynamics: laminar flow in a channel expansion". In: *Journal of computational Physics* 54.3 (1984), pp. 468–488.

[54] Dimitri Komatitsch and Jean-Pierre Vilotte. "The spectral element method: an efficient tool to simulate the seismic response of 2D and 3D geological structures". In: *Bulletin of the seismological society of America* 88.2 (1998), pp. 368–392.

[55] James F Doyle. "Wave propagation in structures". In: *Wave Propagation in Structures*. Springer, 1989, pp. 126–156.

[56] Henri J. Nussbaumer. "The Fast Fourier Transform". In: *Fast Fourier Transform and Convolution Algorithms*. Berlin, Heidelberg: Springer Berlin Heidelberg, 1981, pp. 80–111. ISBN: 978-3-662-00551-4. DOI: 10.1007/978-3-662-00551-4_4. URL: https://doi.org/10.1007/978-3-662-00551-4_4.

[57] Usik Lee and Hyuckjin Oh. "The spectral element model for pipelines conveying internal steady flow". In: *Engineering Structures* 25.8 (2003), pp. 1045–1055. ISSN: 0141-0296. DOI: https://doi.org/10.1016/S0141-0296(03)00047-6. URL: https://www.sciencedirect.com/science/article/pii/S0141029603000476.

[58] Usik Lee and Hyungmi Oh. "Dynamics of an axially moving viscoelastic beam subject to axial tension". In: *International Journal of Solids and Structures* 42.8 (2005), pp. 2381–2398. ISSN: 0020-7683. DOI: https://doi.org/10.1016/j.ijsolstr.2004.09.026. URL: https://shorturl.at/FxC12.

[59] Usik Lee. *Spectral element method in structural dynamics*. John Wiley & Sons, 2009.

[60] Yong Xiao, Jihong Wen, and Xisen Wen. "Longitudinal wave band gaps in metamaterial-based elastic rods containing multi-degree-of-freedom resonators". In: *New Journal of Physics* 14.3 (2012), p. 033042.

[61] Yong Xiao et al. "Theoretical and experimental study of locally resonant and Bragg band gaps in flexural beams carrying periodic arrays of beam-like resonators". In: *Journal of Vibration and Acoustics* 135.4 (2013).

[62] Filippo Casadei and Katia Bertoldi. "Wave propagation in beams with periodic arrays of airfoil-shaped resonating units". In: *Journal of Sound and Vibration* 333.24 (2014), pp. 6532–6547.

[63] ED Nobrega et al. "Vibration band gaps for elastic metamaterial rods using wave finite element method". In: *Mechanical Systems and Signal Processing* 79 (2016), pp. 192–202.

[64] Muhammad, Weijian Zhou, and C.W. Lim. "Topological edge modeling and localization of protected interface modes in 1D phononic crystals for longitudinal and bending elastic waves". In: *International Journal of Mechanical Sciences* 159 (2019), pp. 359–372. ISSN: 0020-7403. DOI: https://doi.org/10.1016/j.ijmecsci.2019.05.020. URL: https://www.sciencedirect.com/science/article/pii/S0020740319306617.

[65] CW Lim et al. "Analytical modeling and computational analysis on topological properties of 1-D phononic crystals in elastic media". In: *Journal of Mechanics of Materials and Structures* 15.1 (2020), pp. 15–35.

[66] Richard Christensen. *Theory of viscoelasticity: an introduction*. Elsevier, 2012.

[67] Felix Bloch. "Über die quantenmechanik der elektronen in kristallgittern". In: *Zeitschrift für physik* 52.7-8 (1929), pp. 555–600.

[68] Thomas JR Hughes. *The finite element method: linear static and dynamic finite element analysis*. Courier Corporation, 2012.

[69] Jean H Prévost and Serguei Bagrianski. *An introduction to matrix structural analysis and finite element methods*. World Scientific, 2017.

[70] Yudong Zhang, Leiying He, and Chuanyu Wu. "The effect of preload force on damping in tendon-driven manipulator". In: *Industrial Robot: the international journal of robotics research and application* 48.3 (Jan. 2021), pp. 454–462. ISSN: 0143-991X. DOI: 10.1108/IR-10-2020-0232. URL: https://doi.org/10.1108/IR-10-2020-0232.

[71] Paul Macioce. "Viscoelastic damping 101". In: *Sound and Vibration Magazine* 4 (2003), pp. 4–5.

[72] R. Lewandowski and B. Chorążyczewski. "Identification of the parameters of the Kelvin–Voigt and the Maxwell fractional models, used to modeling of viscoelastic dampers". In: *Computers & Structures* 88.1 (2010), pp. 1–17. ISSN: 0045-7949. DOI: https://doi.org/10.1016/j.compstruc.2009.09.001. URL: https://www.sciencedirect.com/science/article/pii/S0045794909002314.

[73] Émilie Blanc et al. "Highly accurate stability-preserving optimization of the Zener viscoelastic model, with application to wave propagation in the presence of strong attenuation". In: *Geophysical Journal International* 205.1 (Feb. 2016), pp. 427–439. ISSN: 0956-540X. DOI: 10.1093/gji/ggw024. eprint: https://academic.oup.com/gji/article-pdf/205/1/427/8036946/ggw024.pdf. URL: https://doi.org/10.1093/gji/ggw024.

[74] Franck Renaud et al. "A new identification method of viscoelastic behavior: Application to the generalized Maxwell model". In: *Mechanical Systems and Signal Processing* 25.3 (2011), pp. 991–1010. ISSN: 0888-3270. DOI: https://doi.org/10.1016/j.ymssp.2010.09.002. URL: https://www.sciencedirect.com/science/article/pii/S0888327010003079.

[75] G Casula, JM Carcione, et al. "Generalized mechanical model analogies of linear viscoelastic behaviour". In: *Bollettino di geofisica teorica ed applicata* 34.136 (1992), pp. 235–256.

[76] Anastasiia O. Krushynska et al. "Arbitrary-curved waveguiding and broadband attenuation in additively manufactured lattice phononic media". In: *Materials & Design* 205 (2021), p. 109714. ISSN: 0264-1275. DOI: https://doi.org/10.1016/j.matdes.2021.109714. URL: https://www.sciencedirect.com/science/article/pii/S0264127521002665.

[77] Bruno Jurkiewiez, Jean-François Destrebecq, and Alain Vergne. "Incremental analysis of time-dependent effects in composite structures". In: *Computers & Structures* 73.1 (1999), pp. 425–435. ISSN: 0045-7949. DOI: https://doi.org/10.1016/S0045-7949(98)00269-7. URL: https://www.sciencedirect.com/science/article/pii/S0045794998002697.

[78] Fengfeng Shu et al. "Band gap in tubular pillar phononic crystal plate". In: *Ultrasonics* 71 (2016), pp. 172–176. ISSN: 0041-624X. DOI: https://doi.org/10.1016/j.ultras.2016.06.011. URL: https://www.sciencedirect.com/science/article/pii/S0041624X16300956.

[79] Anastasiia O. Krushynska et al. "Dissipative Dynamics of Polymer Phononic Materials". English. In: *Advanced Functional Materials* 31.30 (July 2021). ISSN: 1616-301X. DOI: 10.1002/adfm.202103424.

[80] A.H. Tsou, J. Greener, and G.D. Smith. "Stress relaxation of polymer films in bending". In: *Polymer* 36.5 (1995), pp. 949–954. ISSN: 0032-3861. DOI: https://doi.org/10.1016/0032-3861(95)93593-B. URL: https://shorturl.at/feM7F.

[81] A.O. Krushynska et al. "Coupling local resonance with Bragg band gaps in single-phase mechanical metamaterials". In: *Extreme Mechanics Letters* 12 (2017). Frontiers in Mechanical Metamaterials, pp. 30–36. ISSN: 2352-4316. DOI: https://doi.org/10.1016/j.eml.2016.10.004. URL: https://shorturl.at/kKQdG.

[82] D. Jalocha, A. Constantinescu, and R. Neviere. "Revisiting the identification of generalized Maxwell models from experimental results". In: *International Journal of Solids and Structures* 67-68 (2015), pp. 169–181. ISSN: 0020-7683. DOI: https://doi.org/10.1016/j.ijsolstr.2015.04.018. URL: https://www.sciencedirect.com/science/article/pii/S0020768315001894.

[83] J. E. Soussou, F. Moavenzadeh, and M. H. Gradowczyk. "Application of Prony Series to Linear Viscoelasticity". In: *Transactions of the Society of Rheology* 14.4 (1970), pp. 573–584. DOI: 10.1122/1.549179. eprint: https://doi.org/10.1122/1.549179. URL: https://doi.org/10.1122/1.549179.

3

Phononic crystals for suppressing crosstalk in ultrasonic flowmeters

*Ultrasonic flowmeters that use transit-time ultrasonic transducers face measurement errors due to "crosstalk," whereby the working signal travels through the pipe wall and couplings, interfering with the signal from the fluid. Although various procedures have been proposed to solve the issue of crosstalk, they're limited to low-frequency ranges, or they are not effective in high-pressure environments. We propose a mounting mechanism based on a single-phase 3D phononic crystal (PnC) waveguide that can mitigate crosstalk at high frequencies (*MHz *range) and thus improve the flowmeters' measurement accuracy. PnCs are artificial materials consisting of periodically arranged scatterers thereby showing bandgaps (BGs)—ranges of frequencies where elastic/acoustic waves are attenuated— due to Bragg scattering. We design PnC wave filters by engineering the BG frequency range to the working signal of the ultrasonic flowmeter. We then fabricate the waveguide using additive manufacturing and connect it between the transducer and the pipe wall. Transient ultrasonic experiments show that transducers with PnC mountings attain a* 40 dB *crosstalk reduction in comparison with a standard transducer mounting configuration.*

3.1. Introduction

Ultrasonic transducers, due to their versatility and non-destructive nature, are extensively used in various measurement systems, including ultrasonic flowmeters [1–4],

Parts of this chapter have been published in IEEE Transactions on Instrumentation and Measurement **72**, pp. 1-11, (2023).

non-destructive testing devices [5–7], and medical imaging systems [8–10]. These transducers convert electrical input signals to ultrasound waves (and vice versa), which interact with the desired media to provide the required measurement. However, ultrasonic flowmeters that use transit-time ultrasonic transducers to measure flow rates through pipes face accuracy issues due to "crosstalk," which is caused by the interference of signals traveling through the solid region (solid/pipe signal) with the fluid region (fluid signal). Additionally, the solid signal contains more energy than the required signal due to the often unavoidable large impedance mismatch between the transducer, pipe wall, and the measuring fluid, leading to an immense reflection of waves in the solid portion. Hence, crosstalk makes it difficult to identify the required signal [11].

Various solutions have been proposed to mitigate crosstalk in ultrasonic flowmeters. For instance, crosstalk has been minimized by isolating the sensor from the solid signal path [12]. For example, enclosing the acoustic transducer and the surrounding housing in a sheath also aids in isolating the housing from the rest of the solid region, thereby minimizing the interaction between the solid and fluid signals [13]. Another approach is to create time delays between the required and the pipe signals [14]. For instance, applying protrusions to transducers increases the solid wave path so that the solid signal arrives at the receiving transducer after the fluid signal, thus avoiding the crosstalk [15]. A third approach is by localizing the energy transmitted from the pipe signal [16]. To that end, resonators and damping systems are attached to the transducer [17], where resonators aid in localizing the energy while damping systems reduce the energy of solid waves by converting the wave energy to heat.

All these methods, however, have drawbacks. In the case of the protruded design, the distance between the transducers determines the generation of the crosstalk. *i.e.,* if the transducers are far away, as in the case of a large-diameter pipe, then the solid signal could arrive at the receiver along with the required signal resulting in crosstalk. This distance limitation imposes restrictions on the pipe diameter, flow velocity, and sound velocity of the fluid medium, among others [18, 19]. Resonators and damping systems are limited to relatively low frequencies (a few hundred kHz) because it is difficult to construct an oscillator that has resonance frequencies in the MHz-range at the macro-scale. Similarly, damping systems with constant dissipation are also less effective at high frequencies because, although energy increases with the frequency, the dissipation remains the same. Acoustic insulation becomes an issue in high-pressure environments since a heavy casing is needed to withstand high pressures, which increases the crosstalk by allowing more solid waves to pass through the casing [20]. Consequently, for the smooth operation of the flowmeter, it is necessary to have a wave filtering mechanism that removes the crosstalk, which has a substantial operational frequency range (at MHz level) and has a limited influence from pressure and temperature.

A potential solution could be based on frequency-dependent insulation by exploiting the properties of phononic crystals (PnCs) [21–23]. PnCs are man-made periodic media that exhibit Bragg scattering [24] type band gaps (BGs)—ranges of frequencies where elastic/acoustic waves are attenuated. Because of BGs, PnCs

have been explored in many applications, including vibration isolation [25], energy harvesting [26], acoustic cloaking [27], super/hyper lens [28, 29], frequency steering [30], among others. PnCs (or similar periodic structures) have previously been used inside the piezoelectric component of transducers to optimize the piezoelectric coefficient [31–34]. Another related application of PnCs in ultrasonic transducers is to improve the measurement accuracy of the transducers in non-destructive evaluation [35, 36]. Liu *et al.* [37] used PnCs to improve the sensitivity of acousto-ultrasonic-based devices for structural health monitoring, thereby improving their performance for a broad frequency range. By blocking unwanted signals using PnCs, Kabir *et al.* [38] were able to enhance the crack detection ability of the acoustic emission method [39]. Other applications of PnCs in ultrasonic transducers include enhancing sound receiving accuracy of parametric loudspeakers [40], and reducing nonlinearities in ultrasonic damage detection [41]. Still, to the best of our knowledge, PnC structures have not been used as mountings on the transducer of ultrasonic flowmeters to mitigate crosstalk.

In this paper, we investigate the use of PnC structures as wave filters to mitigate crosstalk in ultrasonic flowmeters (Figure 3.1). A PnC-embedded wave filter is designed, realized, and connected between the piezo and the back of the transducer that is attached to the pipe wall such that the PnC waveguide filters the signal arriving from the pipe wall to the piezo. We explore various practical aspects, such as selecting the geometry and arrangement of the PUCs for the best performance within a limited space and choosing a suitable material for the mounting. Additionally, we incorporate manufacturing aspects and industrial standards in the design process. We fabricate two different designs of PnC waveguides via additive manufacturing, where one has a broad BG frequency, and the other possesses greater manufacturability. For comparison purposes, we also construct a dummy block with the exact outer dimensions as the PnC waveguide via the same manufacturing process (additive manufacturing). We validate the performance of the PnC-embedded ultrasonic transducer via transient ultrasonic experiments and compare them against a standard transducer.

3.2. Theoretical aspects of ultrasonic transducers and phononic crystals

3.2.1. Challenges in the flow measurement through a pipe using an ultrasonic flowmeter

The flow rate through a pipe can be measured by various methods such as pressure-based meters, variable-area type measurement systems, optical systems, magnetic flowmeters, Coriolis devices, and ultrasonic flowmeters [42]. Among them, ultrasonic flowmeters are of great interest because of their high accuracy and low maintenance cost [43]. In an ultrasonic flowmeter, a high-frequency ultrasound pulse generated using an ultrasonic transducer (based on piezoelectric effect [44]) is transmitted through the moving media at an angle. An ultrasonic receiver receives this signal on the opposite side, which provides the travel time. The exact process is repeated in the reverse direction resulting in an upstream and downstream mea-

surement. The difference between these two signals' travel times is directly related to the flow rate through the pipe. Several transmitters and receivers can be placed along the circumference of the pipe to further improve the measurement accuracy, which, in addition, also aids in obtaining a flow profile through the pipe. The layout and operation of the ultrasonic flowmeter are provided in Figure 3.1.

Figure shows the cross-sectional (Figure 3.1(a)) and longitudinal-sectional (Figure 3.1(c)) views of the pipe with ultrasonic transducers, along with a photograph of the transducer (Figure 3.1(b)). The ultrasonic transducer mainly comprises a piezoceramic material (Piezo) for converting electric pulse to ultrasound and vice versa and a window (a structural element usually constructed of the same material as the pipe that is in contact with the fluid, which is marked in Figure 3.1(b)) for transmitting this pulse to the fluid and receiving it at the opposite side. The transducer also possesses electrical components for supplying and receiving electric signals. A metallic casing (stainless steel in the present case) encloses the transducer for protection. Due to its complex construction and the presence of multiple materials, various challenges may occur during the flow measurement that could hinder the flowmeter's accuracy.

The 1 MHz input pulse (refer to Figure 3.1(a)) generated at the transmitter arrives at the window-fluid interface and experiences an immense reflection due to the considerable mismatch in the impedance (density × speed of sound) between the window and the fluid layer (refer Table 3.1 for the material properties of the pipe and the fluid). This reflected signal travels through the solid portion (red signal

Material	Density (kg/m^3)	Pressure wave speed, C_P (m/s)	Shear wave speed, C_S (m/s)
Stainless steel	7800	4935.5	3102.9
Water	998.2	1481.4	–

Table 3.1: Material properties of the pipe and fluid

path in Figure 3.1) to reach the receiver, thus interfering with the required signal (green signal path). This interaction of the two signals (crosstalk) is a complex phenomenon because it comprises pressure waves (P waves) from the fluid region and pressure and shear waves (S waves) from the solid region. Due to crosstalk, the measured signal experiences a reduction in accuracy or even the complete loss of the working signal [45]. Thus, to avert crosstalk, a mechanism is necessary that prevents both P and S wave propagation in the solid region from reaching the receiving transducer. Additionally, as the flowmeter (and the transducer) will be exposed to high pressure and temperature environments, the mounting mechanism should be able to prevent or reduce crosstalk under these conditions.

3.2.2. Design requirements for the mounting structure

Since crosstalk is a significant issue in an ultrasonic flowmeter, we would like to address it by filtering out the solid (pipe wall) signal. As mentioned already, by attaching a mounting structure in the solid wave path that would act as a mechanical

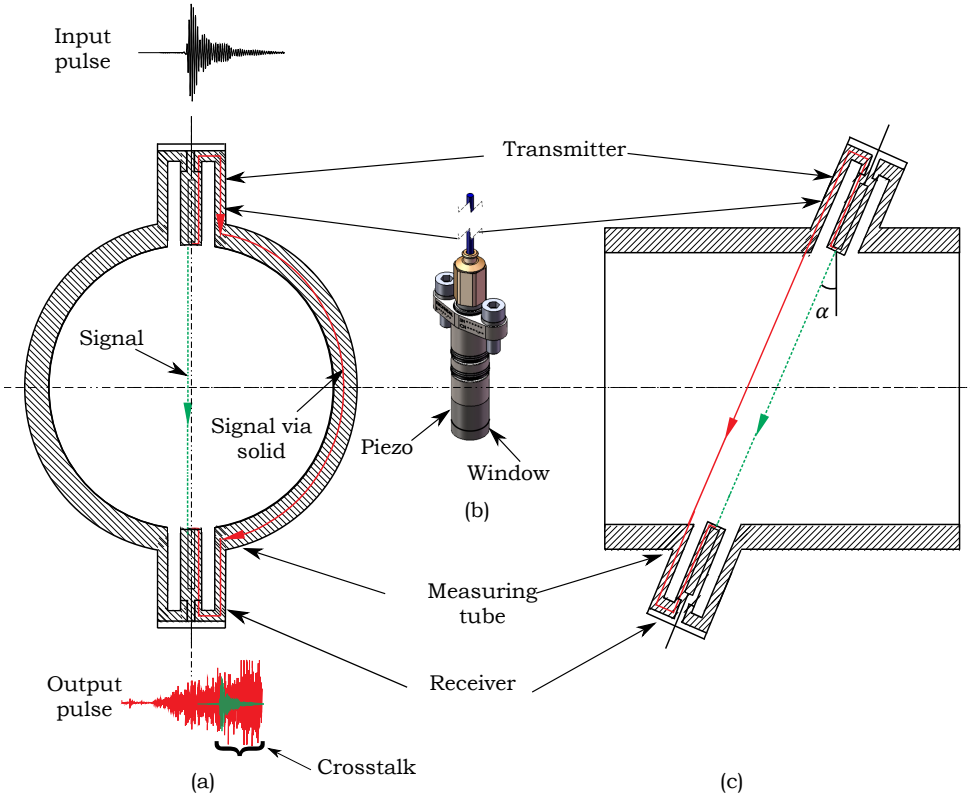

Figure 3.1: Schematic of the ultrasonic flowmeter, where (a) shows its cross-sectional view highlighting the signal paths through the fluid and the solid media. Input pulse and output pulse with crosstalk are also shown here, where the signal through the solid region (red plot) arrives much earlier than the signal through the fluid (green plot), resulting in the crosstalk between these signals (marked using a curly bracket in the output pulse). (b) shows the photograph of an actual ultrasonic transducer where the Piezo that generates the pulse and the window that transmits the signal to the fluid are marked using arrows. (c) displays the longitudinal section of the flowmeter with transmitting and receiving transducers and signal and noise paths. The transmitter and receiver are oriented at an angle α to enable the flow measurement.

wave filter, we might be able to remove the solid signals for the desired frequency range. Since the ultrasonic transducer is composed of stainless steel 316 (SS316), we could fabricate the mounting system from the same material, ensuring a smooth contact and energy transfer between the transducer and the mounting. As the transducer signal is broadband (1 MHz central frequency with a bandwidth of 600 kHz), it is also necessary for the mounting structure to possess a wide operating frequency range with its central frequency close to 1 MHz. Moreover, the lateral dimension of the mounting structure should be in a similar range to that of the outer diameter of the transducer (18 mm). Finally, the structure should be manufacturable at a reasonable cost.

3.2.3. Phononic crystal-based mounting mechanism

As PnCs possess BGs that can attenuate incoming waves for particular frequency ranges, we design a mounting mechanism based on a single-phase 3D PnC waveguide. To investigate the wave propagation through the 3D PnC structure we need the corresponding wave equation. Since the PnC waveguide is entirely composed of solid material, the wave propagation is governed by the 3D elastic wave equation:

$$\rho \ddot{\boldsymbol{u}} = (\lambda + 2\mu)\Delta \boldsymbol{u} - \mu \nabla \times \nabla \times \boldsymbol{u}, \tag{3.1}$$

where, $\boldsymbol{u}$ and $\ddot{\boldsymbol{u}}$ respectively are the spatial displacement and the acceleration. ρ represents the density of the material, λ, and μ are the Lamé coefficients, whereas Δ and $\nabla\times$ respectively represent Laplacian and vector curl operators.

We still need to provide the necessary boundary conditions to fully define the boundary value problem (BVP). We study two BVPs, for which the BCs are:

1. **BVP1: Band structure analysis** (or dispersion analysis) [46] establishes the relationship between the applied frequency ω and the wave vector $\boldsymbol{k}$ that provides the BG frequency range (if any) and speeds of different wave modes. The magnitude of the wave vector $\boldsymbol{k}$ is the reciprocal of the wavelength and it is directed towards the direction of the wave propagation (*i.e.,* in the direction of the phase velocity) [47]. The dispersion relation is obtained by conducting a set of eigenvalue analyses of the periodic unit cell (PUC) after applying Bloch-Floquet periodic boundary conditions (BFPBC) [48] through the irreducible Brillouin zone (IBZ) [49]. The Brillouin zone (BZ) is derived by transforming the PUC from the direct lattice (Bravais lattice [50]) to its reciprocal lattice [51]. The IBZ is the smallest section of the BZ that can capture the wave dynamics of the PUC. We consider a simple cubic PUC (as shown in Figure 3.2(a), (b), (d), and (e)) with a 32-fold symmetry, thus the BZ could be reduced to a tetrahedron (as shown in Figure 3.2(c) [52]. The number of eigenvalue analyses conducted depends on the sampling of the wave vector through the IBZ, as we need one analysis per wave vector step. Similarly, the number of eigenmodes selected for the analysis depends on the frequency range of interest. Since we are interested in the MHz range, we started with 30 eigenmodes. The BFPBC used in these analyses takes the form:

$$\boldsymbol{u}(\boldsymbol{r} + \boldsymbol{a}_i, t) = e^{\iota \boldsymbol{k}.\boldsymbol{a}_i} \boldsymbol{u}(\boldsymbol{r}, t), \tag{3.2}$$

where $\boldsymbol{r}$ is the position vector and $\boldsymbol{a}_i$ is the lattice vector in 3D, *i.e.,* $\boldsymbol{a}_i = \{\boldsymbol{a}_1, \boldsymbol{a}_2, \boldsymbol{a}_3\}$ (refer Figure 3.2(a)). For the cubic geometry, magnitudes of lattice parameters are the same in all three directions, *i.e.,*

$$\|\boldsymbol{a}_1\| = \|\boldsymbol{a}_2\| = \|\boldsymbol{a}_3\| = a, \tag{3.3}$$

where a is the magnitude of the lattice vector (in any of the three directions). If no wave vectors are present for a range of frequencies implying no wave propagation for that frequency range, we get a BG. Additionally, we can obtain wave speeds for various wavebands by taking slopes of the dispersion relation

corresponding to those wavebands. Although less expensive (due to operating on one PUC), the band structure analysis assumes an infinite medium by prescribing BFPBC. Thus, it cannot provide an actual attenuation rate for a finite PnC structure, so we need a transmissibility analysis.

2. **BVP2: Transmissibility analysis** (or harmonic frequency sweep analysis) [53] is the steady-state dynamic analysis of the finite PnC waveguide after applying the essential (Dirichlet) boundary condition [54].

$$\boldsymbol{u}(\boldsymbol{l}, t) = \bar{\boldsymbol{u}} e^{\iota \omega t}, \tag{3.4}$$

where $\bar{\boldsymbol{u}}$ is the constant displacement amplitude applied at one end (left end) of the PnC waveguide (at $\boldsymbol{r} = \boldsymbol{l}$), (shown in Figure 3.2(f) and (g)) and ω is the applied frequency. For a given frequency, the transmissibility response provides the reduction in amplitude of the input signal for a given number of PUCs arranged in space.

3.3. Design and analysis of phononic crystal-based wave filter

Using the band structure and transmissibility analyses, we can start the design process of PnC's periodic unit cell and waveguide. Since the BGs in PnCs are generated due to Bragg scattering, we can use Bragg's law of diffraction to obtain the size of the PUC as follows [24]:

$$n\bar{\lambda} = 2a\cos\theta, \tag{3.5}$$

where n is an integer, $\bar{\lambda}$ is the wavelength in the material, and θ is the angle of incident of the wave to the normal of the surface. At $n = 1$, for a normal incident wave, the magnitude of the lattice parameter can be half of the wavelength in the medium. We can obtain the wavelength in the material from the following expression:

$$\bar{\lambda} = C/f, \tag{3.6}$$

where f is the applied frequency and C is the wave speed. $C = C_P$ for pressure waves and $C = C_S$ for shear waves. For our material choice, SS316, the wave speed values are provided in Table 3.1. To design a PUC possessing a BG with a central frequency of 1 MHz, we can use Equations 3.5 and 3.6 to obtain the magnitude of the lattice parameter, which is estimated to be 2 mm. To accommodate a broad operational frequency range (600 kHz), the PnC should possess a broad BG. We know that the BG width is directly related to the contrast in adjacent phases' impedances within the PUC [55]. Since we have a single-phase PUC, to maximize the impedance mismatch within the elements of the PUC, we need to maximize the contrast in their masses and stiffnesses [56]. Thus we use large spheres separated by small rods as shown in Figure 3.2(a) and (b) to construct the PUC. There is about an order difference in the cross-sectional area of the sphere to the rod. On the contrary, while the second one (refer to Figure 3.2(d) and (e)) has triangular features instead of spherical ones that offer lower contrast in the properties than the former—resulting

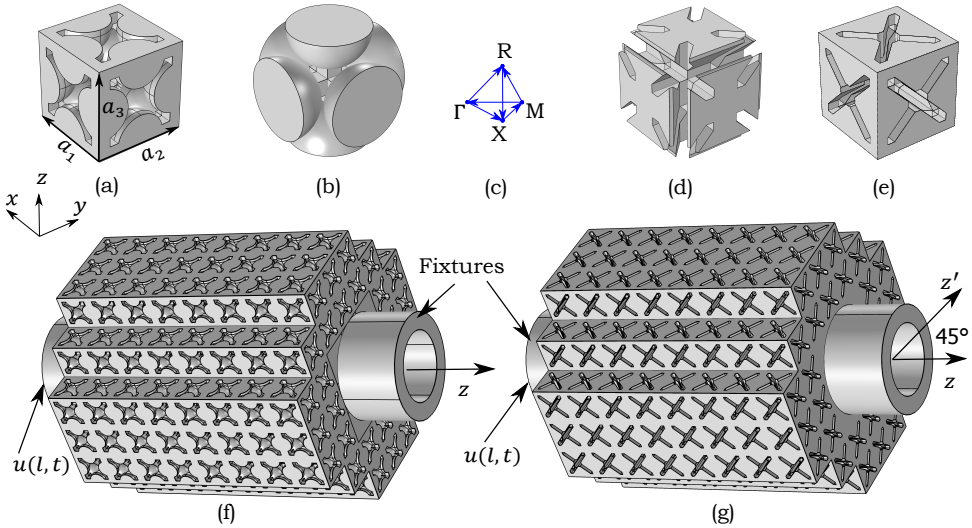

Figure 3.2: 3D phononic crystal PUCs and waveguides where (a) and (b) show different views of the cubic PUC with spherical features where a_i (i = 1 to 3) defines its lattice parameter. (c) shows the IBZ of the cubic PUC. (d) and (e) represent different views of the PUC with triangular features whose lattice parameter is the same as in the previous case. (f) and (g) display PnC waveguides with spherical and triangular features, where z is the principal wave propagation direction, and z' is a direction obtained by rotating z to 45°. The fixtures that connect the waveguides with the rest of the transducer are also shown here. $u(l,t)$ is the Dirichlet BC applied to these PnC waveguides at the location $\boldsymbol{l}$.

in narrower BG—the manufacturability is greatly improved by minimizing overhang angles in additive manufacturing. By populating these PUCs in three dimensions, we arrive at PnC waveguide designs that are shown in Figure 3.2(f) and (g). We also add two hollow cylindrical fixtures to connect them to the transducer from Figure 3.1(b). To verify the performance of these PUCs and waveguides we perform band structure and transmissibility analyses.

3.3.1. Band structure response

The band structure of the cubic PnC is obtained through finite element analysis (FEA) by following the $\omega(\boldsymbol{k})$ approach [56], *i.e.,* by sweeping the wave vector along the vertices of the IBZ and calculating the set of eigenfrequencies corresponding to a fixed number of wavebands. Figures 3.3a and 3.3b respectively represent the band structures of PUCs with spherical and triangular features (their geometries are shown in Figure 3.2). These figures show frequency as a function of wave vector sampled along the IBZ, where $\boldsymbol{\Gamma}$ corresponds to the center of the BZ where the IBZ begins, *i.e.,* at $\boldsymbol{k} = 0.\ 85$ eigenvalue analyses were used to represent 7 IBZ branches. We analyzed 30 wavebands in the case of the PUC with spherical features where the required BG is present between 18^{th} and 19^{th} bands (refer to Figure 3.3a). Conversely, we considered 63 bands in the case of the PUC with triangular features because of the presence of multiple BGs (refer to Figure 3.3b),

where the first BG is also between 18th and 19th bands.

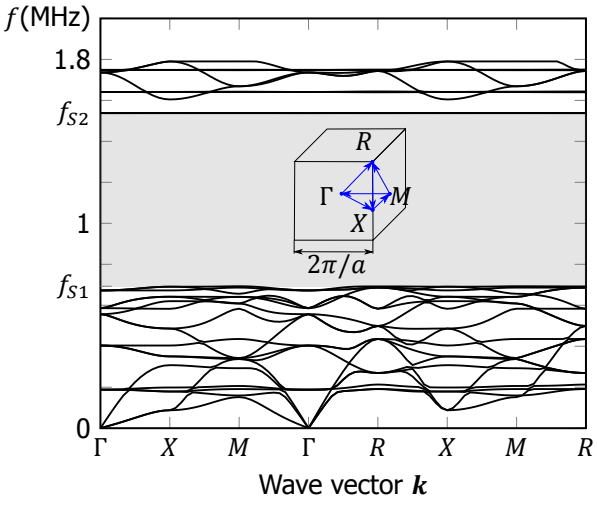

(a)

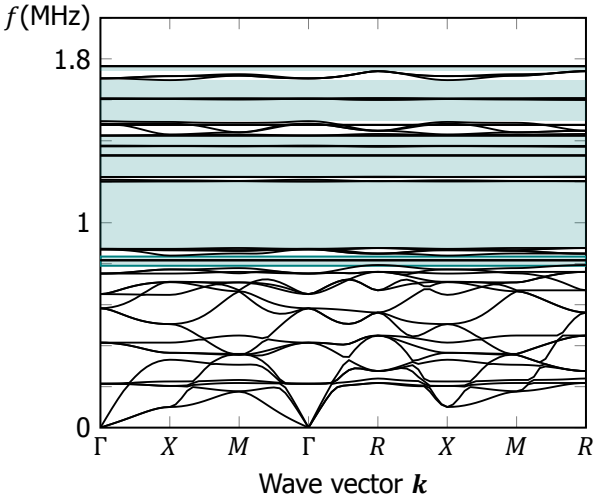

(b)

Figure 3.3: Frequency as a function of wave vector (band structure) for PnCs with (a) spherical and (b) triangular internal features, where the shaded regions show corresponding BGs. f_{S1} = 0.7 MHz and f_{S2} = 1.5 MHz from (a), respectively represent the lower and upper bound of the BG frequency ranges of the PnC with spherical features. The inset in (a) shows the Brillouin zone and its tetrahedral IBZ with its vertices.

Figure 3.3a shows that by connecting spheres with rods, we can produce a wide BG of 800 kHz that spans from f_{S1} = 700 kHz to f_{S2} = 1.5 MHz, which is more than the required operating frequency range of 600 kHz. However, since the maximum overhang angle is higher than the allowable limit (45°) of 3D printing, we could

expect some variations in features (size and shape) as shown in Figure 3.5(b). As all the angles in the design with triangular features are close to 45°, it is easier to fabricate with fewer variations. However, the PnC with triangular features possesses multiple narrow BGs within the operating frequency range instead of a single broad BG. The first BG of the triangular design starts at 780 kHz but only spans up to 835 kHz. The following BG spans from 880 kHz to 1.2 MHz. Nonetheless, the stacking of narrow BGs and flat modes (standing waves) goes up to 1.8 MHz with some low-slope modes present in between.

3.3.2. Transmissibility relations

Following the band structure analysis, we study the transmissibility response of the finite PnC waveguides shown in Figure 3.2. We supplied a harmonic displacement of 1 µm amplitude at the left end of each of the waveguides (as shown in Figure 3.2(f) and (g)) for the frequency range from 600 kHz to 1.8 MHz with a step of 10 kHz. Figure 3.4 shows transmissibility relations of waveguides obtained by taking the ratio of output displacement (right side) to the input displacement for the applied frequency range, where shaded regions represent the triangular PnC's BGs. In the same figure, the BG of the PnC with spherical features is bounded by thick black lines. As the figure shows, the BG frequency ranges are consistent with those dictated by band structure analyses. However, several peaks are present in the transmissibility relations of both designs due to the reflections from the free surfaces and sub-system resonances (*i.e.,* the resonant modes of the finite structure within the bandgap frequency range). Band structure analysis will not capture them since the analysis is operating on a single PUC and assumes infinite material with Bloch-Floquet periodic boundary conditions. Although the band structure analysis report that the PnC with spherical features has a broader BG frequency range than that of the PnC with triangular features, the latter possesses multiple narrow BGs bounded by f_1 through f_{13} spanning almost the same frequency range as the former—and also outperforming the former in the 1.5 MHz to 1.8 MHz range. However, there are still certain frequency bounds (between f_2 & f_3, f_4 & f_5, and f_8 & f_9) within the operational frequency range, where PnC waveguide with triangular features shows higher transmission compared to the spherical featured PnC due to the lack of BGs in those ranges. Both PnC waveguides are nevertheless manufactured since close to 1 MHz (marked as f_C in Figure 3.4) their transmissibilities are in the range of −60 dB, which is desirable for the actual application.

3.4. Fabrication and testing of PnC waveguides

3.4.1. Fabrication of PnC wave filters

Since the dimensions of the PUC are in mm ranges with internal features in the sub-millimeter length scales, the manufacturing processes are significantly limited as mesoscale fabrication is challenging [57]. The two suitable fabrication methods are wire electric discharge machining (wire-EDM) [58] and metal additive manufacturing [59]. Although the former can produce accurate geometry, it can only remove materials from a solid block (subtractive manufacturing), limiting its applications to

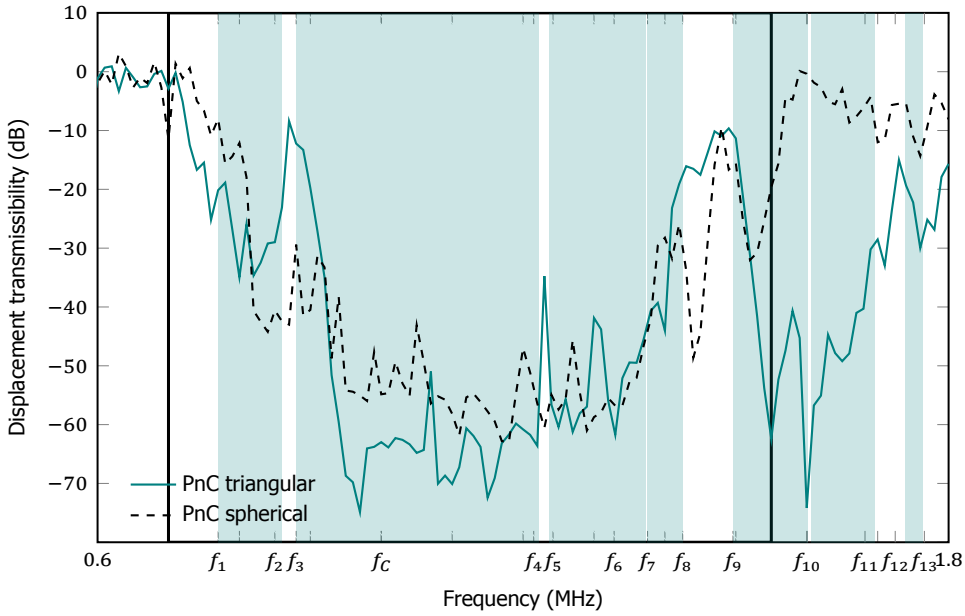

Figure 3.4: Transmissibility relations of cubic PnC waveguides from Figure 3.2 attained through FEM. The BG predicted by the band structure of the PnC with spherical features is bounded by thick black lines, whereas shaded regions represent the BG of the PnC with triangular features. The total frequency range spans from 0.6 MHz to 1.8 MHz, where $f_C = 1$ MHz is the required central frequency, and f_1 through f_{13} are frequency bounds of BGs of PnC with triangular features.

simpler geometries. Even though we can manufacture the PnC design from Figure 3.2(g), we cannot fabricate the design from Figure 3.2(f) using wire-EDM.

Metal additive manufacturing based on selective laser sintering uses laser beams to melt the metallic powder in multiple passes transforming the powder into the desired geometry. After melting every layer, more powder is added, allowing the method to generate complex designs. Additionally, this method is very inexpensive compared to wire-EDM (almost two orders of magnitude). However, the accuracy of the fabrication depends on several factors, such as the overhang constraint, which determines the projection angle of the subsequent layer compared to the previous one, hence determining the printability and dimensional accuracy. The maximum allowable overhang angle in the metal additive manufacturing process is 45° [60]. Since the design with spherical features exceeds this angle, the surface quality, feature sizes, and shapes of the features could be adversely affected. We modified the design as described in Figure 3.2(g) to minimize the overhang angles by keeping all the angles close to 45°, thereby revising the shape of the internal features (from spherical to triangular) and the printing orientation of the PnC waveguide (from aligning towards the z-direction to 45° inclination to the same direction.)

3.4.2. Fabricated PnC specimens' variations from the design

We decided to fabricate both the designs via additive manufacturing. As shown in

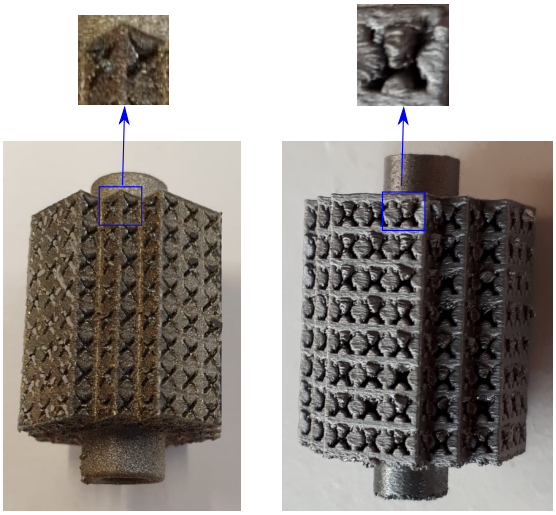

Figure 3.5: Photographs of 3D printed PnC waveguides with (a) triangular and (b) spherical features. The expanded views show the corresponding PUCs, where the latter shows more variation from the model than the former.

Figure 3.5, 3D-printed PnC specimens show certain variations from their designs. One reason is the sticking of powder particles to the sample's lower and side edges with the melt pool, thus distorting the shape. The second is because of residual support structures added to aid the printing process, which could not be removed during the post-processing stage. The PnC with spherical features also faces issues due to large overhang angles. The specimen in Figure 3.5(b) has been printed by aligning the printing axis to the z-axis (refer Figure 3.2(f)), whereas the specimen in Figure 3.5(a) is printed by aligning the printing axis to z' by rotating it 45° from z-axis (refer Figure 3.2(g)), thus keeping all the overhang angles $\leq 45°$. Consequently, the latter is more repeatable and is closer to the model.

One may wonder whether variations from the numerical model introduced by 3D printing affect the performance of the PnC waveguide. Minor variations in feature size have insignificant effects on performance since the BG width is controlled by the mass and stiffness contrast within the PUC, which is not highly affected by slight geometric variations. Similarly, the surface roughness (as seen significantly in Figure 3.5(b)) also has a minor influence on the wave attenuation behavior of the PnC waveguide as we deal with bulk waves instead of surface waves. On the contrary, if the sub-unit cell features (*e.g.,* spheres) experience significant variations leading to connections between those spheres, and if there are a significant number of them, then these connection points could transmit waves leading to changes in

the BG range, shifting of BG center frequency, or reduction in attenuation rate. However, as we can see in Figures 3.5(a) and 3.5(b), this kind of distortion has not happened. As discussed, incorporating process parameters such as overhang angle greatly improves the manufacturability, as seen in the PnC with triangular features. To further improve printing accuracy, other process parameters such as layer thickness, and powder characteristics (particle size, surface tension, feed rate, *etc.*), among others, can be optimized [61]; this is beyond the scope of this paper. We connect both PnC waveguides with existing ultrasonic transducers and test their behavior via transient experiments. To that end, an experimental setup is built.

3.4.3. Experimental setup to measure the required signal and crosstalk levels of ultrasonic flowmeter with and without PnC

The experimental setup for verifying the performance of the PnC waveguide is composed of PnC-mounted transducers, a signal generator for sending the desired signal, the data acquisition system (DAQ) for collecting, converting, and displaying readable data, and transducers with dummy mountings to compare the response with PnC mounted transducers to obtain the effects of the PnC. The dummy block has cross-sectional dimensions of 14 mm $\times$ 14 mm with a height of 16 mm. The dimensions are kept the same as that of the PnC waveguide; otherwise, the signal traveling time through the fluid would vary between those two transducers. It should be noted that the dummy block has a higher mass than the PnC waveguide since the former is a block of material, whereas the latter is a porous structure. This variation in mass will have an insignificant influence on the response of the transducer since the purpose of the dummy waveguide is to transmit the incoming elastic wave to the rest of the structure while maintaining the same construction. Both transducers (with PnC and dummy blocks) are used in pairs; one acts as a transmitter and the other as a receiver (and vice versa). The fabricated PnC waveguides (and dummy blocks) are connected to the ultrasonic transducer between the Piezo element and the transducer-wall coupling by hot pressing and welding to ensure adequate contact (Figure 3.6(a)). A rectangular broadband pulse with a central frequency of 1 MHz and peak-to-peak voltage of 200 V is used as the input signal for the excitation. The receiving signal is amplified using a low-noise amplifier (LNA) and visualized using an oscilloscope (Yokogawa DL160) with a sampling rate of 50 MS s^{-1} and a frequency step of 500 Hz.

Calculation of solid and fluid signal levels

Two sets of experiments are conducted to obtain the solid and fluid signal levels. The first one is performed by attaching PnC-mounted transducers to a fluid-filled chamber (as shown in Figure 3.6(b)). As the chamber walls are very thin, the energy transmitted to the solid region will also be less. Additionally, since the fluid is static, the travel time for the signal through the fluid region is already known, allowing us to identify the fluid signal from the output signal, thereby measuring the required signal strength. The second one is conducted in an empty flowmeter (refer to Figure 3.6(c)). This flowmeter has a very thick solid wall, and almost all

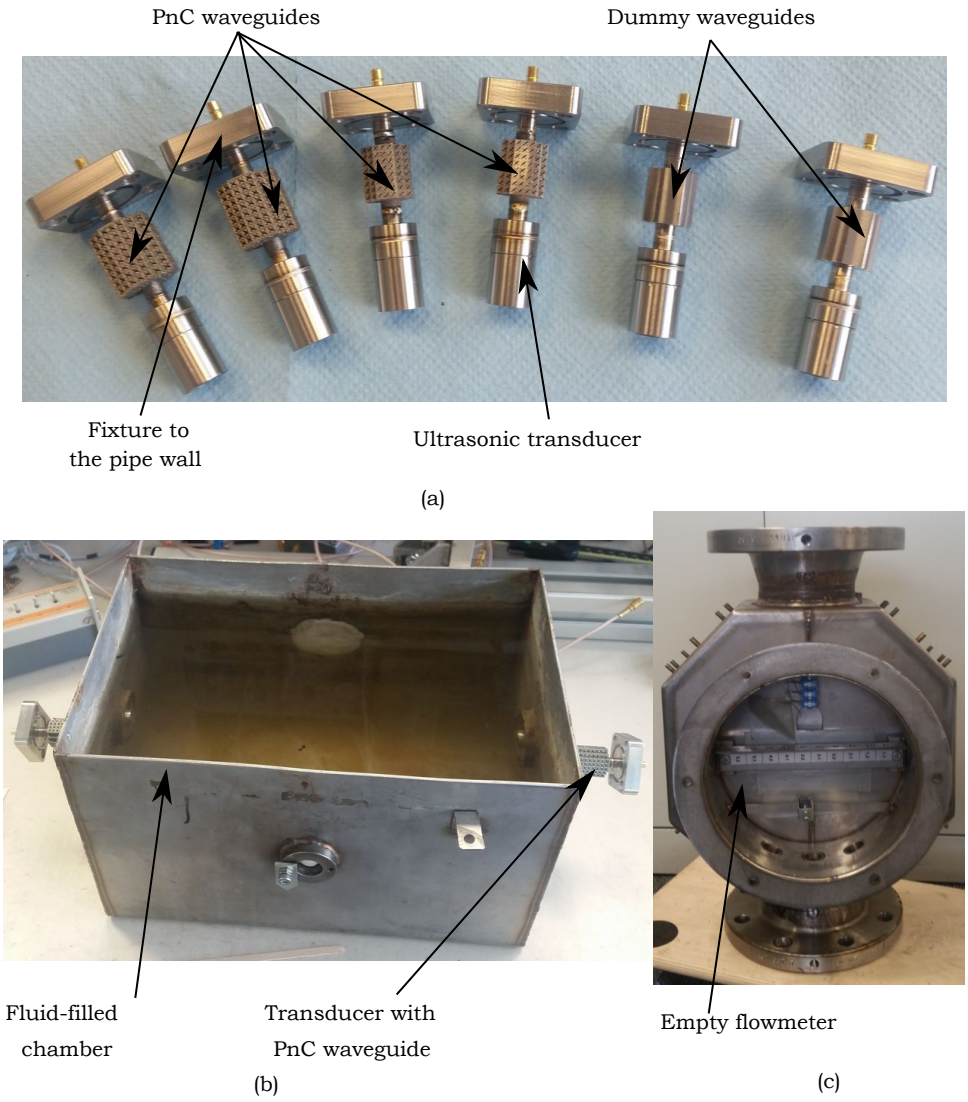

Figure 3.6: Photographs of the assembled specimen and experimental setup. (a) shows the assembled specimens that include transducers connected with two types of PnC waveguides (PnC with spherical and triangular features) and transducers with dummy waveguides. (b) represents the fluid-filled chamber connected with transducers to measure the signal strength in the fluid portion, whereas (c) displays the assembly of an empty flowmeter with the transducers, which is used to measure the signal levels in the solid region.

the energy from the input acoustic signal is reflected back to the solid region as there is no liquid inside. Thus the output signal can be regarded as the wall (solid)

signal. The ratio of the latter signal to the former provides us with the solid-to-fluid signal ratio. The experiments are repeated with transducers possessing dummy mountings for comparison.

3.4.4. Transient experimental results of 3D PnC mounted ultrasonic transducers

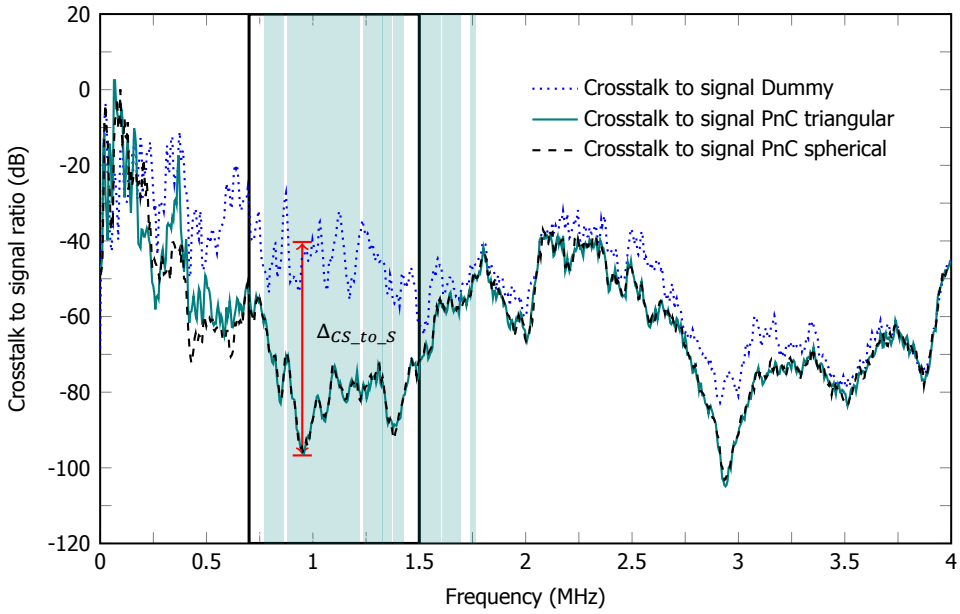

Figure 3.7: Transmissibility relation of different specimens obtained via experiments. The figure includes transmissibilities of a transducer with a dummy block and transducers with triangular and spherical featured PnCs. The spherical PnC's BG is bounded by thick black lines while the triangular PnC's BG is shown using the shaded region (both predicted by analyses). $\Delta_{CS\_to\_S} \approx 60$ dB represents the highest variation in the crosstalk-to-signal ratio between the transducers with and without the PnC mountings, which is observed close to the required central frequency (1 MHz).

We compare the performance of transducers with PnC wave filters against the transducer with a dummy block. Figure 3.7 shows the transmissibility relations obtained by experiments. The PnC mounted transducer shows a considerable reduction in the crosstalk level (*i.e.,* signals traveling through the solid region are greatly attenuated) within the BG frequency range. There is an average crosstalk reduction of 40 dB (within the BG range) and a maximum reduction of 60 dB (close to the required central frequency of 1 MHz marked as $\Delta_{CS\_to\_S}$ in Figure 3.7). In fact, except for 500 kHz to 550 kHz (range outside the BG), both the PnC waveguides show similar performances.

From band structure analyses (refer to Figure 3.3a and 3.3b), we have seen that the PnC with spherical features outperforms the PnC with triangular features due to the former's broad BG as compared to a set of narrow and moderate BGs of

the latter. Transmissibility analyses (refer to Figure 3.4) show that the attenuation rates are closer for both the waveguides till 1.5 MHz, and the PnC with triangular features performs better than the PnC with spherical features from 1.5 MHz to 1.8 MHz. The experiments reveal that the transmissibilities of both PnCs are very similar throughout the frequency range. The minor variations in the BG ranges and propagating modes within the operating frequency range have negligible influence on the response of wave filters. Additionally, we can also observe that, even outside the BG frequency range (*e.g.,* around 0.5 MHz, 2 MHz, 2.5 MHz, and 3 MHz), PnC-embedded transducers outperform the standard one (not as significantly as within the BG range) because of the difference in their dispersion characteristics. Especially close to 3 MHz, we can observe a sharp decrease in solid-to-fluid signal levels (about 20 dB) because of a combination of the higher-order BG generated by Bragg scattering and the high signal strength due to the presence of an actuator displacement mode at that frequency. The analysis details are discussed in the supplementary material, Section 1, while the output fluid signals are provided in the supplementary material, Section 2. In addition, as PnC waveguides are connected in the solid wave path, they do not influence the waves traveling through the measuring fluid; thus, the fluid signal of the PnC-embedded transducer is similar to the standard transducer (refer to supplementary material, Section 2 for details).

3.5. Conclusions

In order to improve the performance of transducers used in ultrasonic flowmeters, we proposed a mounting mechanism based on 3D PnC waveguides. We designed two PnC wave filters, one with spherical features and the other with triangular features that facilitate additive manufacturing. While the former possesses a broad BG around the required frequency, the latter has multiple moderate and small BGs. Both were analyzed using FEA, realized via metal additive manufacturing, and mounted to the transducer by hot pressing and welding. The transient experiments showed a considerable reduction in the crosstalk level within the BG frequency range (40 dB on average with a maximum of 60 dB close to 1 MHz). Thus we conclude that PnC-inspired mountings can drastically improve the measurement accuracy of ultrasonic transducers by mitigating crosstalk when connected to the solid wave path, provided the waveguides are not directly exposed to the surrounding fluid media.

Additional concluding observations are:

- Both PnC waveguides possess a frequency range of attenuation that is broader than dictated by the analysis, which implies that other factors are affecting the wave attenuation, which may be fabrication aspects (surface roughness, material constitution, variations in feature size and shape) and structural damping;

- Other than for a narrow frequency range, both PnC waveguides show similar transmissibility responses throughout the spectrum. Hence, it is not required to have a single broad BG, but combinations of narrow BGs, flat wave modes, and shallow-slope wave modes can add to a moderate BG to create a cumu-

lative wave attenuation region similar to the response of a PnC with a single broad BG;

- Throughout the frequency range except close to 100 kHz, both PnC-embedded transducers show lower crosstalk levels compared to the standard one. This behavior could be due to the complex dispersion characteristics (varying wave speeds and combinations of different wave modes throughout the frequency range) of PnC wave filters augmented by imperfections in their manufacturing;
- Since both spherical and triangular PnC waveguides show similar performances, we can select the latter for practical applications since they are more amenable to additive manufacturing than the former. Additionally, triangular PnC waveguides can be fabricated via multiple processes (3D printing and EDM), further improving their applicability.

PnC waveguides in real applications of ultrasonic flowmeters introduce environmental conditions such as the effects of surrounding fluid media, pressure, and temperature. Thus, a future direction could be to perform an optimization of PnC-inspired mountings incorporating multiple environmental aspects.

3.6. Appendix

3.6.1. Wave propagation of the PnC waveguide around 3 MHz

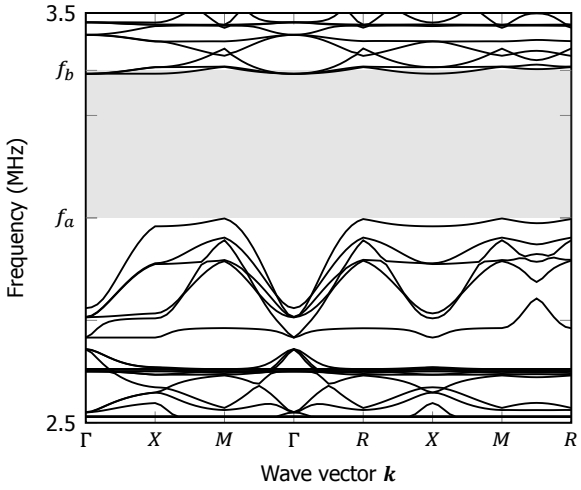

Figure 3.8: Band structure of spherical PnC PUC from Figure 7(a) calculated from 2.5 MHz to 3.5 MHz, where the BG is shaded, which is bounded by f_a = 3 MHz and f_b = 3.36 MHz.

Since the experimental transmissibility from Figure 3.7 of the main document shows a wave attenuation region close to 3 MHz, we investigated the response of the PnC PUC and waveguide in that frequency range along with studying the signal response from experiments. We performed the band structure of the spherical PnC

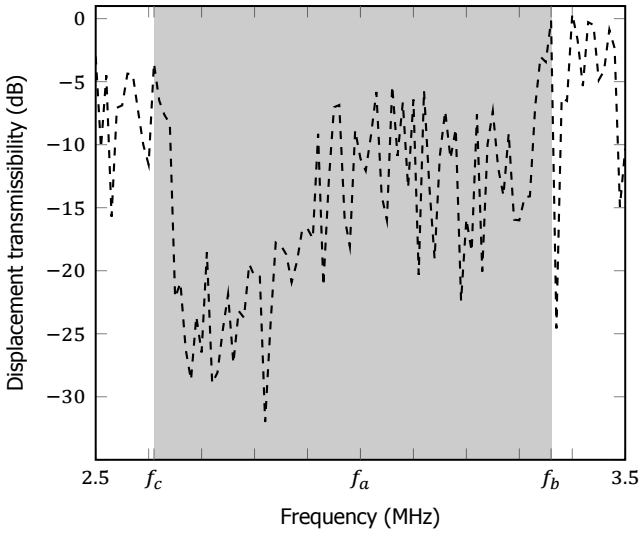

Figure 3.9: Transmissibility relations of the spherical PnC waveguide from Figure 2 of the main document for a range of frequency from 2.5 MHz to 3.5 MHz. The BG bounds from the band structure are marked in the abscissa as f_a and f_b. The complete attenuation region is shaded and is bounded by f_c = 2.62 MHz and f_b.

PUC and the transmissibility response of the corresponding waveguide (Figure 2 of the main document) from 2.5 MHz to 3.5 MHz. The simulation is performed as described in Section 2 of the main document. The resulting band structure and transmissibility relations are shown in Fig. 3.8 and Fig. 3.9, respectively. The BG frequency range is shaded in Fig. 3.8, while the frequency range with attenuation is shaded in Fig. 3.9. The obtained BG frequency range is from 3 MHz to 3.36 MHz, while the frequency range of attenuation obtained via the transmissibility analysis is broader (from 2.62 MHz to 3.36 MHz). This variation in the frequency range is due to the finite nature of the waveguide, which enables the interactions of additional eigenmodes that are dissipative (complex-valued), leading to wave attenuation. By investigating the signal amplitude as shown in Fig. 3.10 at 3 MHz, we can see that the signal strength is very high; thus, it is evident that the piezoceramic disc, which is tuned for 1 MHz pulse also possesses a strong mode around 3 MHz. This high-amplitude signal (from the fluid) further reduces the solid-to-fluid signal ratio, as shown in Figure 3.7 of the main document. The frequency range of attenuation obtained by the analysis matches the corresponding values from the experiments (2.62 MHz to 3.4 MHz, as shown in Figure 3.7 of the main document). Although the PnC structures are designed for 1 MHz operating frequency range, they can exhibit wave attenuation at higher frequencies due to higher-order BGs generated due to Bragg scattering (refer to Equation (3.5) of the main document for Bragg's law of diffraction). and because of the strong displacement mode of the piezoceramic disc. Since this BG width is considerably lower than the BG around 1 MHz, the attenuation rate would also be lower.

3.7. Signal level comparison between different transducers

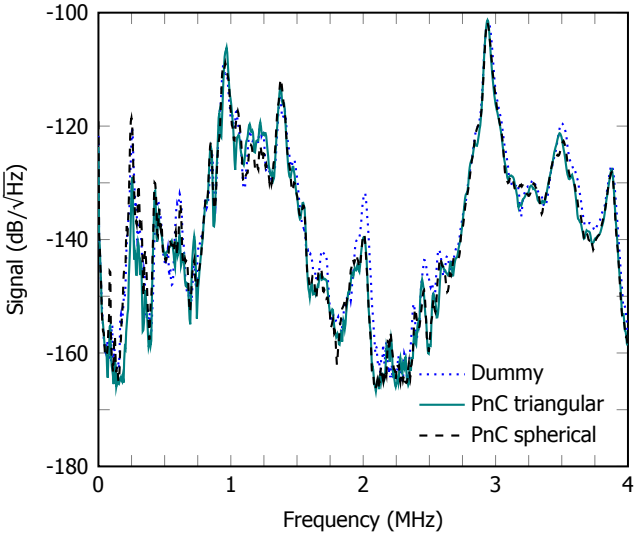

Figure 3.10: Signal amplitudes of transducers with a dummy block, triangular PnC waveguide, and spherical PnC waveguide represented using dB/$\sqrt{\text{Hz}}$ plotted for a range of applied frequencies obtained via experiments conducted on the fluid-filled chamber.

To investigate the influence of the wave filter in the required signal traveling through the fluid region, we compare output signals obtained via the fluid-filled chamber from Figure 3.5(b) of the main document. As mentioned in the main document, Section 3.3, since the chamber is very thin, most of the energy will travel through the fluid region, and as the fluid is static, we can estimate the signal's arrival time (traveling via fluid). Figure 3.10 shows the output signal obtained from the transducer with a dummy block, the triangular PnC waveguide, and the spherical PnC waveguide. The signal amplitudes are represented in dB/$\sqrt{\text{Hz}}$, and all three signals are similar throughout the frequency spectrum. Thus we can infer that the addition of the PnC wave filter has an insignificant influence on the amplitude and arrival time of the required signal through the fluid region. Additionally, we can also state that since the receiving signals with and without PnC waveguides have very similar waveforms, the crosstalk generated in the fluid-filled chamber is minimal and our assumption of considering the signal from the fluid-filled chamber to be the required signal is valid.

Bibliography

[1] L.C. Lynnworth and Yi Liu. "Ultrasonic flowmeters: Half-century progress report, 1955–2005". In: *Ultrasonics* 44 (2006). Proceedings of Ultrasonics International (UI'05) and World Congress on Ultrasonics (WCU), e1371–e1378. ISSN: 0041-624X. DOI: https://doi.org/10.1016/j.ultras.2006.05.046. URL: https://www.sciencedirect.com/science/article/pii/S0041624X06000849.

[2] D. L. Franklin et al. "A Pulsed Ultrasonic Flowmeter". In: *IRE Transactions on Medical Electronics* ME-6.4 (1959), pp. 204–206. DOI: 10.1109/IRETME.1959.5007965.

[3] Pamela I Moore, Gregor J Brown, and Brian P Stimpson. "Ultrasonic transit-time flowmeters modelled with theoretical velocity profiles: methodology". In: *Measurement Science and Technology* 11.12 (Nov. 2000), pp. 1802–1811. DOI: 10.1088/0957-0233/11/12/321. URL: https://doi.org/10.1088/0957-0233/11/12/321.

[4] G. Rajita and Nirupama Mandal. "Review on transit time ultrasonic flowmeter". In: *2016 2nd International Conference on Control, Instrumentation, Energy Communication (CIEC)*. 2016, pp. 88–92. DOI: 10.1109/CIEC.2016.7513740.

[5] Jack Blitz and Geoff Simpson. *Ultrasonic methods of non-destructive testing*. Vol. 2. Springer Science & Business Media, 1995.

[6] James Helal, Massoud Sofi, and Priyan Mendis. "Non-destructive testing of concrete: A review of methods". In: *Electronic Journal of Structural Engineering* 14.1 (2015), pp. 97–105.

[7] Sylvain Chatillon et al. "Ultrasonic non-destructive testing of pieces of complex geometry with a flexible phased array transducer". In: *Ultrasonics* 38.1 (2000), pp. 131–134. ISSN: 0041-624X. DOI: https://doi.org/10.1016/S0041-624X(99)00181-X. URL: https://www.sciencedirect.com/science/article/pii/S0041624X9900181X.

[8] J.F. Havlice and J.C. Taenzer. "Medical ultrasonic imaging: An overview of principles and instrumentation". In: *Proceedings of the IEEE* 67.4 (1979), pp. 620–641. DOI: 10.1109/PROC.1979.11287.

[9] P. Abolmaesumi et al. "Image-guided control of a robot for medical ultrasound". In: *IEEE Transactions on Robotics and Automation* 18.1 (2002), pp. 11–23. DOI: 10.1109/70.988970.

[10] Jeff Powers and Frederick Kremkau. "Medical ultrasound systems". In: *Interface focus* 1.4 (2011), pp. 477–489.

[11] Jankees Hogendoorn et al. "High viscosity hydrocarbon flow measurement: A challenge for Ultrasonic Flow Meters?" In: *27 th International North Sea Flow Measurement Workshop*. 2009.

[12] Pierre Ueberschlag, Andreas Berger, and Michal Bezdek. *Ultrasonic transducer for application in an ultrasonic, flow measuring device or in an ultrasonic, fill-level measuring device*. US Patent 10,620,026. Apr. 2020.

[13] Emanuel J Gottlieb et al. *Acoustically isolated ultrasonic transducer housing and flow meter*. US Patent 9,506,789. Nov. 2016.

[14] Jeroen Martin Van Klooster. *Flowmeter*. US Patent 6,799,475. Oct. 2004.

[15] Søren Tønnes Nielsen, Peter Schmidt Laursen, and Jens Lykke Sørensen. *Flow meter with protruding transducers*. US Patent 9,182,260. Nov. 2015.

[16] A. Ramos, J.L. San Emeterio, and P.T. Sanz. "Improvement in transient piezoelectric responses of NDE transceivers using selective damping and tuning networks". In: *IEEE Transactions on Ultrasonics, Ferroelectrics, and Frequency Control* 47.4 (2000), pp. 826–835. DOI: 10.1109/58.852064.

[17] Jereon Martin Van Klooster and Arie Huijzer. *Ultrasonic transducer*. US Patent **8**,127,613. Mar. 2012.

[18] Dandan Zheng, Pengyong Zhang, and Tianshi Xu. "Study of acoustic transducer protrusion and recess effects on ultrasonic flowmeter measurement by numerical simulation". In: *Flow Measurement and Instrumentation* 22.5 (2011), pp. 488–493. ISSN: 0955-5986. DOI: https://doi.org/10.1016/j.flowmeasinst.2011.08.003. URL: https://shorturl.at/cFrSW.

[19] Y Hu, T Zhang, and DD Zheng. "Estimation on influence of probe protrusion length of ultrasonic flowmeter on measurement". In: *Journal of Tianjin University* 46.9 (2013), pp. 776–783.

[20] Lawrence C Lynnworth. *Ultrasonic transducer system with crosstalk isolation*. US Patent 5,515,733. May 1996.

[21] M. S. Kushwaha et al. "Acoustic band structure of periodic elastic composites". In: *Physical Review Letters* 71 (13 Sept. 1993), pp. 2022–2025. DOI: 10.1103/PhysRevLett.71.2022. URL: https://link.aps.org/doi/10.1103/PhysRevLett.71.2022.

[22] M. S. Kushwaha et al. "Theory of acoustic band structure of periodic elastic composites". In: *Phys. Rev. B* 49 (4 Jan. 1994), pp. 2313–2322. DOI: 10.1103/PhysRevB.49.2313. URL: https://link.aps.org/doi/10.1103/PhysRevB.49.2313.

[23] P.A. Deymier. *Acoustic Metamaterials and Phononic Crystals*. Springer Series in Solid-State Sciences. Springer Berlin Heidelberg, 2013. ISBN: 9783642312328. URL: https://books.google.nl/books?id=8eg%5C_AAAAQBAJ.

[24] W. L. Bragg. "The Diffraction of Short Electromagnetic Waves by a Crystal". In: *Scientia* 23.45 (1929), p. 153.

[25] Matthew Reynolds and Stephen Daley. "An active viscoelastic metamaterial for isolation applications". In: *Smart Materials and Structures* 23.4 (2014), p. 045030.

[26] Kyung Ho Sun et al. "Sound energy harvesting using a doubly coiled-up acoustic metamaterial cavity". In: *Smart Materials and Structures* 26.7 (2017), p. 075011.

[27] Shu Zhang, Chunguang Xia, and Nicholas Fang. "Broadband acoustic cloak for ultrasound waves". In: *Physical Review Letters* 106.2 (2011), p. 024301.

[28] Choon Mahn Park et al. "Amplification of Acoustic Evanescent Waves Using Metamaterial Slabs". In: *Phys. Rev. Lett.* 107 (19 Nov. 2011), p. 194301. DOI: 10.1103/PhysRevLett.107.194301. URL: https://link.aps.org/doi/10.1103/PhysRevLett.107.194301.

[29] Gang Yong Song et al. "Broadband focusing acoustic lens based on fractal metamaterials". In: *Scientific reports* 6 (2016), p. 35929.

[30] J Xu and J Tang. "Tunable prism based on piezoelectric metamaterial for acoustic beam steering". In: *Applied Physics Letters* 110.18 (2017), p. 181902.

[31] Wallace Arden Smith, Avner Shaulov, and BA Auld. "Tailoring the properties of composite piezoelectric materials for medical ultrasonic transducers". In: *IEEE 1985 Ultrasonics Symposium*. IEEE. 1985, pp. 642–647.

[32] W.A. Smith and B.A. Auld. "Modeling 1-3 composite piezoelectrics: thickness-mode oscillations". In: *IEEE Transactions on Ultrasonics, Ferroelectrics, and Frequency Control* 38.1 (1991), pp. 40–47. DOI: 10.1109/58.67833.

[33] W.A. Smith. "The role of piezocomposites in ultrasonic transducers". In: *Proceedings., IEEE Ultrasonics Symposium,* 1989, 755–766 vol.2. DOI: 10.1109/ULTSYM.1989.67088.

[34] Wallace Arden Smith and Avner A. Shaulov. "Composite piezoelectrics: Basic research to a practical device". In: *Ferroelectrics* 87.1 (1988), pp. 309–320. DOI: 10.1080/00150198808201393. eprint: https://doi.org/10.1080/00150198808201393. URL: https://doi.org/10.1080/00150198808201393.

[35] M. Miniaci et al. "Proof of Concept for an Ultrasensitive Technique to Detect and Localize Sources of Elastic Nonlinearity Using Phononic Crystals". In: *Phys. Rev. Lett.* 118 (21 May 2017), p. 214301. DOI: 10.1103/PhysRevLett.118.214301. URL: https://link.aps.org/doi/10.1103/PhysRevLett.118.214301.

[36] Elizabeth J. Smith and Kathryn H. Matlack. "Metal additively manufactured phononic materials as ultrasonic filters in nonlinear ultrasound measurements". In: *The Journal of the Acoustical Society of America* 149.6 (2021), pp. 3739–3750. DOI: 10.1121/10.0004995. eprint: https://doi.org/10.1121/10.0004995. URL: https://doi.org/10.1121/10.0004995.

[37] Menglong Liu et al. "Applications of a nanocomposite-inspired in-situ broadband ultrasonic sensor to acousto-ultrasonics-based passive and active structural health monitoring". In: *Ultrasonics* 78 (2017), pp. 166–174. ISSN: 0041-624X. DOI: https://doi.org/10.1016/j.ultras.2017.03.007. URL: https://www.sciencedirect.com/science/article/pii/S0041624X16302414.

[38] Minoo Kabir, Amir Mostavi, and Didem Ozevin. "Noise isolation with phononic crystals to enhance fatigue crack growth detection using acoustic emission". In: *Journal of Civil Structural Health Monitoring* 8.3 (July 2018), pp. 529–542.

[39] Xiaoli Li. "A brief review: acoustic emission method for tool wear monitoring during turning". In: *International Journal of Machine Tools and Manufacture* 42.2 (2002), pp. 157–165. ISSN: 0890-6955. DOI: https://doi.org/10.1016/S0890-6955(01)00108-0. URL: https://www.sciencedirect.com/science/article/pii/S0890695501001080.

[40] Peifeng Ji, Wenlin Hu, and Jun Yang. "Development of an acoustic filter for parametric loudspeaker using phononic crystals". In: *Ultrasonics* 67 (2016), pp. 160–167. ISSN: 0041-624X. DOI: https://doi.org/10.1016/j.ultras.2016.01.013. URL: https://www.sciencedirect.com/science/article/pii/S0041624X16000147.

[41] Geoffrey Roger Sherwood et al. "3D-printed phononic crystal waveguide transducers for nonlinear ultrasonic damage detection". In: *NDT & E International* 121 (2021), p. 102456. ISSN: 0963-8695. DOI: https://doi.org/10.1016/j.ndteint.2021.102456. URL: https://www.sciencedirect.com/science/article/pii/S0963869521000554.

[42] R.C. Baker. *Flow Measurement Handbook*. Flow Measurement Handbook: Industrial Designs, Operating Principles, Performance, and Applications. Cambridge University Press, 2016. ISBN: 9781107045866. URL: https://books.google.nl/books?id=D4-5DAAAQBAJ.

[43] Jon S Wilson. *Sensor technology handbook*. Elsevier, 2004.

[44] Richard M. Martin. "Piezoelectricity". In: *Phys. Rev. B* 5 (4 Feb. 1972), pp. 1607–1613. DOI: 10.1103/PhysRevB.5.1607. URL: https://link.aps.org/doi/10.1103/PhysRevB.5.1607.

[45] N Roosnek. "Novel digital signal processing techniques for ultrasonic gas flow measurements". In: *Flow Measurement and Instrumentation* 11.2 (2000), pp. 89–99. ISSN: 0955-5986. DOI: https://doi.org/10.1016/S0955-5986(00)00008-X. URL: https://www.sciencedirect.com/science/article/pii/S095559860000008X.

[46] Karl F Graff. *Wave motion in elastic solids*. Courier Corporation, 2012.

[47] A Bedford and DS Drumheller. "Elastic wave propagation". In: *John Wileg g Sons* (1994), pp. 151–165.

[48] Felix Bloch. "Quantum mechanics of electrons in crystal lattices". In: *Z. Phys* 52 (1928), pp. 555–600.

[49] Hendrik J. Monkhorst and James D. Pack. "Special points for Brillouin-zone integrations". In: *Phys. Rev. B* 13 (12 June 1976), pp. 5188–5192. DOI: 10.1103/PhysRevB.13.5188. URL: https://link.aps.org/doi/10.1103/PhysRevB.13.5188.

[50] Charles Kittel and Paul McEuen. *Introduction to solid state physics*. John Wiley & Sons, 2018.

[51] L. P. Bouckaert, R. Smoluchowski, and E. Wigner. "Theory of Brillouin Zones and Symmetry Properties of Wave Functions in Crystals". In: *Phys. Rev.* 50 (1 July 1936), pp. 58–67. DOI: 10.1103/PhysRev.50.58. URL: https://link.aps.org/doi/10.1103/PhysRev.50.58.

[52] Yanyu Chen, Haimin Yao, and Lifeng Wang. "Acoustic band gaps of three-dimensional periodic polymer cellular solids with cubic symmetry". In: *Journal of Applied Physics* 114.4 (2013), p. 043521. DOI: 10.1063/1.4817168. eprint: https://doi.org/10.1063/1.4817168. URL: https://doi.org/10.1063/1.4817168.

[53] István L Vér and Leo L Beranek. *Noise and vibration control engineering: principles and applications*. John Wiley & Sons, 2005.

[54] Thomas JR Hughes. *The finite element method: linear static and dynamic finite element analysis*. Courier Corporation, 2012.

[55] M Hirsekorn et al. "Modelling and simulation of acoustic wave propagation in locally resonant sonic materials". In: *Ultrasonics* 42.1 (2004). Proceedings of Ultrasonics International 2003, pp. 231–235. ISSN: 0041-624X. DOI: https://doi.org/10.1016/j.ultras.2004.01.014. URL: https://www.sciencedirect.com/science/article/pii/S0041624X04000216.

[56] L. D'Alessandro et al. "Modeling and experimental verification of an ultra-wide bandgap in 3D phononic crystal". In: *Applied Physics Letters* 109.22 (2016), p. 221907. DOI: 10.1063/1.4971290. eprint: https://doi.org/10.1063/1.4971290. URL: https://doi.org/10.1063/1.4971290.

[57] Gilbert L Benavides, David P Adams, and Pin Yang. "Meso-machining capabilities". In: *Sandia National Laboratories, Albuquerque, New Mexico* 87185 (2001).

[58] Y.S Liao, J.T Huang, and Y.H Chen. "A study to achieve a fine surface finish in Wire-EDM". In: *Journal of Materials Processing Technology* 149.1 (2004). 14th Interntaional Symposium on Electromachining (ISEM XIV), pp. 165–171. ISSN: 0924-0136. DOI: https://doi.org/10.1016/j.jmatprotec.2003.10.034. URL: https://www.sciencedirect.com/science/article/pii/S0924013604001463,%20keywords%20=%20%7BWire-EDM,%20Finish,%20Pulse-generating%20circuit,%20Surface%20roughness%7D,.

[59] William E Frazier. "Metal additive manufacturing: a review". In: *Journal of Materials Engineering and performance* 23.6 (2014), pp. 1917–1928.

[60] Shaochuan Feng et al. "Experimental and numerical investigation of the origin of surface roughness in laser powder bed fused overhang regions". In: *Virtual and Physical Prototyping* 16.sup1 (2021), S66–S84. DOI: 10.1080/17452759.2021.1896970. eprint: https://doi.org/10.1080/17452759.2021.1896970. URL: https://doi.org/10.1080/17452759.2021.1896970.

[61] Haniyeh Fayazfar et al. "A critical review of powder-based additive manufacturing of ferrous alloys: Process parameters, microstructure and mechanical properties". In: *Materials & Design* 144 (2018), pp. 98–128. ISSN: 0264-1275. DOI: https://doi.org/10.1016/j.matdes.2018.02.018. URL: https://www.sciencedirect.com/science/article/pii/S0264127518300972.

4

Multi-objective design of 3D phononic crystal waveguide by design space trimming

Ultrasonic flowmeters face unique challenges since, in addition to withstanding high fluid pressures, they have to avoid crosstalk, which is the interaction of the signals traveling through the fluid and the solid pipe. To avoid the crosstalk, which leads to poor accuracy or complete loss of the required signal, we develop a mounting mechanism based on phononic crystals (PnCs), which are artificial periodic materials possessing band gaps (BGs) due to Bragg scattering. These PnC structures should also possess high mechanical strength to sustain the fluid pressure. Designing PnCs for such applications is challenging as the BG width and the resistance to mechanical loading are conflicting objectives. To circumvent this, we propose a step-by-step design procedure to optimize both mechanical strength and wave attenuation performance of a single-phase 3D PnC waveguide using parametric sweeping and sensitivity analysis. We use finite element analysis (FEA) to characterize the behavior of the periodic unit cell and the waveguide. Since accurate dynamic FEA at high frequencies is computationally demanding, we develop surrogate models at different levels of the design process. We also consider additive manufacturing aspects in the design procedure, which we validate by 3D-printing the final design and measuring the parameters via computed tomography.

Parts of this chapter have been published in Materials & Design **237**, p. 112594 (2024).

4.1. Introduction

Ultrasonic flowmeters are extensively used in industries such as oil and gas [1], aerospace [2], automotive [3], medical [4], and pharmaceutical [5], among others. One such instrument, an in-line transit-time flowmeter, measures the flow rate via ultrasonic transducers that are in contact with the fluid. An ultrasound signal generated by a piezoelectric element of the transmitter travels through the fluid and arrives at the receiver. This is repeated in the opposite direction, and the time difference between these signals is directly related to the flow rate. Since the flow is not disrupted during the measurement process, ultrasonic flowmeters possess high accuracy. Nevertheless, when the signal is sent, a significant part of it leaks through the solid pipe and interferes with the working signal from the fluid interface, known as crosstalk. Since crosstalk makes it hard to discriminate the required signal traveling through the fluid [6], several solutions have been proposed for crosstalk mitigation [7–10]. However, these approaches are limited by specific ranges of flow velocity, pipe diameter, and sound velocity of the medium [9]. Additionally, many of them operate at relatively low frequencies (approximately 100 kHz range [8]), which limits their applicability to high-frequency situations (for instance, at MHz frequencies).

Phononic crystals (PnCs) present a viable solution to mitigate crosstalk at high frequencies. PnCs are artificial materials consisting of periodically arranged unit cells possessing unusual dynamic characteristics due to band gaps (BGs) [11]. BGs are frequency ranges where elastic/acoustic waves are attenuated or propagate evanescently. These BGs are generated due to the destructive interference of waves because of the impedance mismatch at material interfaces within a periodic unit cell (PUC), similar to Bragg scattering in electromagnetic waves [12]. Because of BGs, PnCs have been explored in many applications, including vibration isolation [13], acoustic diodes and transistors [14, 15], energy harvesting [16], super/hyper acoustic lenses [17, 18], acoustic antennas [19], frequency steering [20], acoustic cloaking [21–23], metasurfaces for phase manipulation [24, 25], acoustic communication devices [26, 27], and high-resolution acoustic devices [28].

BGs in PnCs are typically determined using a dispersion relation (band structure) [29], which is the relation between frequency and wave vector. The wave vector's magnitude is the wavelength's reciprocal, and its direction is towards the phase velocity [30]. The band structure provides the BG frequency range (if any) and the wave speeds. Nevertheless, since the band structure assumes infinite structure—i.e., a PUC repeated *ad infinitum*—it cannot capture the attenuation behavior of a finite system. A displacement transmissibility analysis is therefore necessary [31], which relates the amplitudes of the transmitted displacement (measured at one end of the waveguide) to the input displacement (at the opposite side where the essential boundary condition (BC) is prescribed), as a function of frequency. Systematic computational tools such as topology optimization have been used to design PnCs for maximizing BGs [32–41]. Topology optimization is an iterative procedure where forward analysis is used to analyze the design and sensitivity analysis is used to improve the design for the next iteration; this process continues until some measure of convergence is achieved. For instance, Sharma et al. used gradient-based

topology optimization to maximize the BG width of electrostatically tunable dielectric PnCs [33]. A similar approach was used by Wu et al. to design PnCs with prescribed BG behavior [34]. Zhang et al. used topology optimization with a non-gradient-based algorithm to design a multi-channel narrow-band PnC filter [35]. A density-based topology optimization was used by Dalklint et al. to design PnCs with tunable BGs [36]. Zhang et al. designed a multi-functional metamaterial with tunable thermal expansion and BG through topology optimization and surrogate modeling [37]. van den Boom et al. used a level-set-based topology optimization to design 3D PnCs with smooth boundaries [38]. However, these approaches are computationally demanding since we may need several numbers of iterations to arrive at an optimized design. In addition, numerous issues are present while translating these designs to functional devices that can be used in ultrasonic flowmeters. The main challenge is with the fabrication as the feature size of the PnC's PUC can be in mesoscale (hundreds of microns to a few centimeters), which is challenging to manufacture [42]. Another difficulty is with scaling since the structure and the PUC the structure is made of have orders of magnitude differences in scale, requiring the manufacturing process to deal with both meso- and macro-scales. Additionally, for the ultrasound flowmeter under a high fluid pressure situation, the device must possess a broad BG and high resistance against mechanical loading, further complicating the design process.

The primary objective of the PnC is to mitigate crosstalk, i.e., to filter out elastic waves traveling through the solid region for specific frequency ranges (in the MHz range). In our previous work, we developed a PnC wave filter to mitigate crosstalk from an ultrasonic flowmeter at high frequencies [43]. However, we did not optimize its performance, which requires several iterations of the complete waveguide's transmissibility analysis. This optimization is challenging since dynamic analyses of PnCs at high frequencies are computationally demanding while using standard computational approaches such as finite element analysis (FEA). This is because the PUC's complex geometry and the waveguide's large domain size (comprised of several PUCs) lead to a large number of degrees of freedom (DOFs). Moreover, the computational cost is further aggravated at high frequencies because a small finite element mesh size is required to maintain spatial and temporal accuracy [44]. Although optimization of PnCs' PUCs for BG maximization via band structure is feasible [38–41], it is nearly impossible to perform optimization of the complete model of a finite PnC structure using the transmissibility analysis due to the associated enormous computational cost. Thus, to efficiently optimize the performance of the PnC waveguide at high frequencies, a surrogate model—i.e., an approximate model that is computationally less expensive than the complete model but which captures its behavior with sufficient accuracy—is required. For instance, Yin et al. applied dynamic condensation for band structure and transmission analysis of PnCs, where they reduced the computational cost by condensing internal DOFs to the boundary [45]. Similarly, Aumann et al. reduced the computational cost of the dynamic analysis of acoustic metamaterials by using a parametric model order reduction approach based on Krylov's subspaces' moment-matching methods [46]. However, no surrogate models have been developed to analyze 3D PnCs with applications in ul-

trasonic flowmeters. In addition to the aforementioned challenges associated with computational demands, the PnC design process is further complicated by environmental conditions such as the surrounding fluid pressure, which impose additional requirements and constraints.

One such requirement for the PnC structure is to have a fully closed construction. This is important because transducers, where these waveguides are connected, are immersed in fluid; thus, any fluid leakage into these structures could reduce their performance. Additionally, the pressure from the surrounding fluid (approximately 15 MPa) also imposes an immense mechanical load on the PnC waveguide, and thus an additional objective for the design process. Designing a PnC waveguide with a broad BG and appropriate mechanical strength is challenging since they are both conflicting objectives. High contrast in mass densities and/or stiffnesses between adjacent constituents of the PUC is needed for a wide BG [47], which creates weak members within the PUC. The high-pressure load surrounding the PnC waveguide induces tremendous stress in these thin members, which are likely to undergo yielding. The effects of hydrostatic loading on 1D PnCs were explored by Mehaney and Elsayed [48], who found a shift in BG frequency with increased pressure. However, works that study the effect of hydrostatic pressure on 3D complex PnC structures are still lacking. To the best of our knowledge, no studies have addressed the multi-objective design of PnCs for maximizing the BG width and mechanical strength, incorporating additional aspects such as manufacturing processes and industrial standards.

In this study, we introduce for the first time a 3D PnC waveguide capable of mitigating high-frequency broad-band acoustic noise at MHz ranges under high hydrostatic pressure. To that end, we propose a design procedure to maximize the wave attenuation and minimize the stresses due to high fluid pressure. We also consider manufacturability, domain-size considerations, and industrial standards in the design process. We divide the problem into independent and dependent sub-problems. Independent problems, such as the design of the PUC and the waveguide, are performed separately, while dependent portions, such as different analyses of the waveguide, are solved simultaneously. We also develop a surrogate model to reduce the computational cost of the waveguide's static and dynamic analyses. Since this is a multi-objective design problem, there will be a Pareto set of optimal designs, and our objective is to move towards such a front with our designs. To that end, we use the parametric sweep to move towards optimum designs by design space trimming. Further, we use sensitivity analysis to arrive at an optimized design that satisfies all constraints, which is fabricated via metal additive manufacturing. We then evaluate the quality of the fabrication process by measuring the different parameters of the PnC waveguide using computer tomography. The various steps in the proposed methodology can be applied as a whole or in parts to other multi-objective challenging design problems (e.g., periodic structures with time-consuming conflicting objectives) with appropriate modifications in the design steps.

4.2. Problem statement

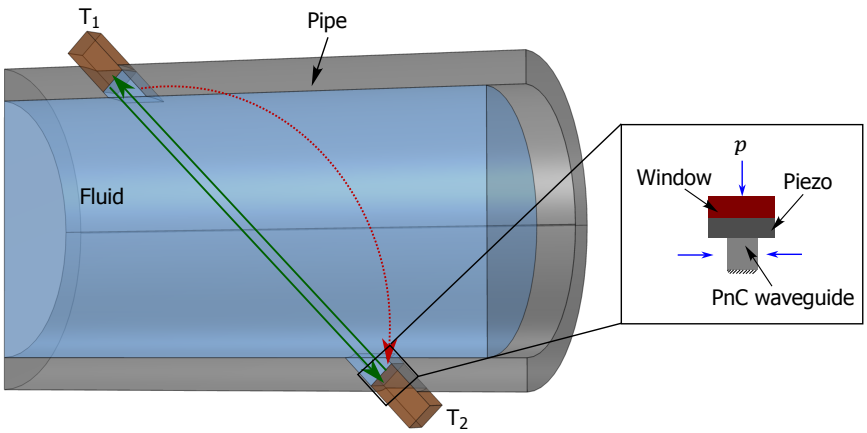

Figure 4.1: Schematics of in-line ultrasonic flowmeter: (a) is a fluid-filled pipe with two ultrasound transducers T_1 and T_2 where the working signal (green arrows) and the signal via the solid region (dotted red arrow) are provided. The inset in (b) shows the portion of the ultrasonic transducer with a window (to transmit the acoustic energy to the fluid) and a PnC waveguide loaded by a hydrostatic pressure load of magnitude p.

Figure 4.1 shows the schematic representation of an in-line ultrasonic flowmeter where the working signal traveling through the fluid is marked using green arrows while the signal traveling via the solid region is represented using a dotted red arrow. Since we want to avoid their crosstalk, a PnC waveguide is placed between the piezoelectric crystal and the adjacent pipe wall as shown in Figure 4.1(b). The surrounding fluid exerts a high pressure p on the transducer and the associated PnC waveguide.

1. The ultrasonic transducer uses a pulse with a central frequency of 1 MHz, which should be the input signal for the PnC waveguide, and hence, the waveguide should possess a BG with its central frequency close to 1 MHz, and a width at least 600 kHz;

2. Fluid seepage into the waveguide should be prevented, causing a reduction in impedance contrast within the PnC, which leads to a reduction in performance. Thus, the PnC device should be closed entirely from the outside;

3. As the flowmeter is exposed to a high-pressure environment, the waveguide should be able to withstand a pressure load of up to 15 MPa. Because the high pressure could be detrimental to the internal features of the PUC, the enclosure should have the additional function of withstanding the high-pressure load;

4. The device should be designed to operate in a wide range of temperatures, from −150 °C till 600 °C, and the material should have a melting point beyond 600 °C;

5. The waveguide should be able to fit within the flowmeter (cylindrical shape), for which the lateral dimension of the PnC waveguide should be less than 18 mm;

6. Finally, the PnC device should be manufacturable with considerable accuracy and precision (repeatability) at a reasonable cost.

We then derive the following objectives:

Objective 1: Maximize the PnC waveguide's wave attenuation performance in the frequency range from 700 kHz to 1.3 MHz with the highest attenuation close to 1 MHz;

Objective 2: Minimize stress throughout the PnC structure when subjected to the pressure load of 15 MPa. Thus, the maximum stress developed in the structure should be less than the allowable stress, $\sigma_A = \sigma_Y/\gamma$, where σ_A is the allowable stress, σ_Y is the yield strength, and γ is the safety factor of the material.

To satisfy some of the design requirements in order to reduce the design space, we take the following design decisions:

- We select stainless steel 316 (SS316) as the preferred material for the PnC waveguide since it has low thermal expansion (17.2×10^{-6}/°C) and a high melting point (1375 °C) to address the thermal requirements. Additionally, since the transducer and associated structures are usually composed of SS316, using the same material for the PnC structure would minimize the thermal stress generation at interfaces;

- We consider a hexagonal PUC for the 3D PnC since it can be arranged close to a cylindrical shape to satisfy the 5^{th} design requirement above, i.e., to have a diameter less than 18 mm;

- Since the waveguide needs to be connected to the ultrasonic transducer, two hollow-cylindrical fixtures are included in the design, which would ensure adequate contact between the transducer and the waveguides;

- As BGs in PnCs are generated via Bragg scattering, we can estimate the outer dimension of the PUC from Bragg's law of diffraction by using the sound speed in the material and the required central frequency as follows:

$$n\bar{\lambda} = 2d\cos\theta \qquad \bar{\lambda} = c/f, \tag{4.1}$$

where n is an integer generally considered to be unity, $\bar{\lambda}$ is the wavelength of the traveling wave in the material, θ is the angle the wave creates with the normal of the incidence surface, d is the periodicity of the scatterer (in the

case of a PnC, it is equivalent to the distance between the PUCs), c is the wave speed of the material, and f is the applied frequency. For SS316, the wave speeds are $c_P = 4935.5\,\text{m/s}$ for pressure wave and $c_S = 3102.9\,\text{m/s}$ for shear wave. For a normal incident wave, at 1 MHz, d is approximately 2 mm, which is selected as the outer dimension of the PUC;

- The PUC's length scale greatly influences the PnC waveguide's manufacturing process. Since the outer dimension of the PUC is 2 mm with a possibility to have even smaller (sub-millimeter) internal features, the available fabrication methods for SS316 are additive manufacturing [49] and wire electric discharge machining [50]. Since, at a prototype stage, the latter is more expensive than the former (two orders of magnitude), we select additive manufacturing as the preferred manufacturing process.

4.3. Design process

To design a PnC waveguide that can satisfy the design requirements, we describe the design process through various steps, as shown in Figure 4.2.

Step-1: We define various building blocks that will be used throughout the process;

Step-2: To design the PUCs, we perform different analyses of the building blocks;

Step-3: Using the build blocks, we design the complete waveguide, which is also characterized using several analyses;

Step-4: To find an optimized design satisfying the objectives, we conduct design space survey for adequate designs, followed by parametric sweeping;

Step-5: In the final step, we fine-tune the design using sensitivity analysis.

4.3.1. **Step-1** – Conceptual building blocks

We need appropriate 3D PnC PUC that would provide adequate BG frequency range as required by **Objective 1**. Additionally, we also select an outer wall to enclose the waveguide and a slab to increase the strength in order to satisfy the design requirements (**Objective 2**). **Step-1** of the Figure 4.2 shows the schematics of all these building blocks (3D PUC, wall, and slab). Since these schematics do not show the exact building blocks, we proceed to Figure 4.3 for a detailed description; however, we will come back to Figure 4.2 when discussing the different design stages. Previously, van den Boom et al. used topology optimization to maximize the BG of a 3D PUC, showing that a spherical cavity maximized the width of the band gap [38]. Since the primary objective of our PnC-based waveguide is to have a broad BG, we design a hexagonal PUC possessing spherical features as shown in Figure 4.3(a). This PUC is designed by connecting spheres with cylindrical rods since this combination provides a wide BG [43] and is a single-phase component. In other words, the BG is generated because of the mismatch in the mass and stiffness between the adjacent sphere and the rod, i.e., dissimilarity in the mechanical impedance, unlike due to the acoustic impedance mismatch in multi-phase PnCs. A similar PUC

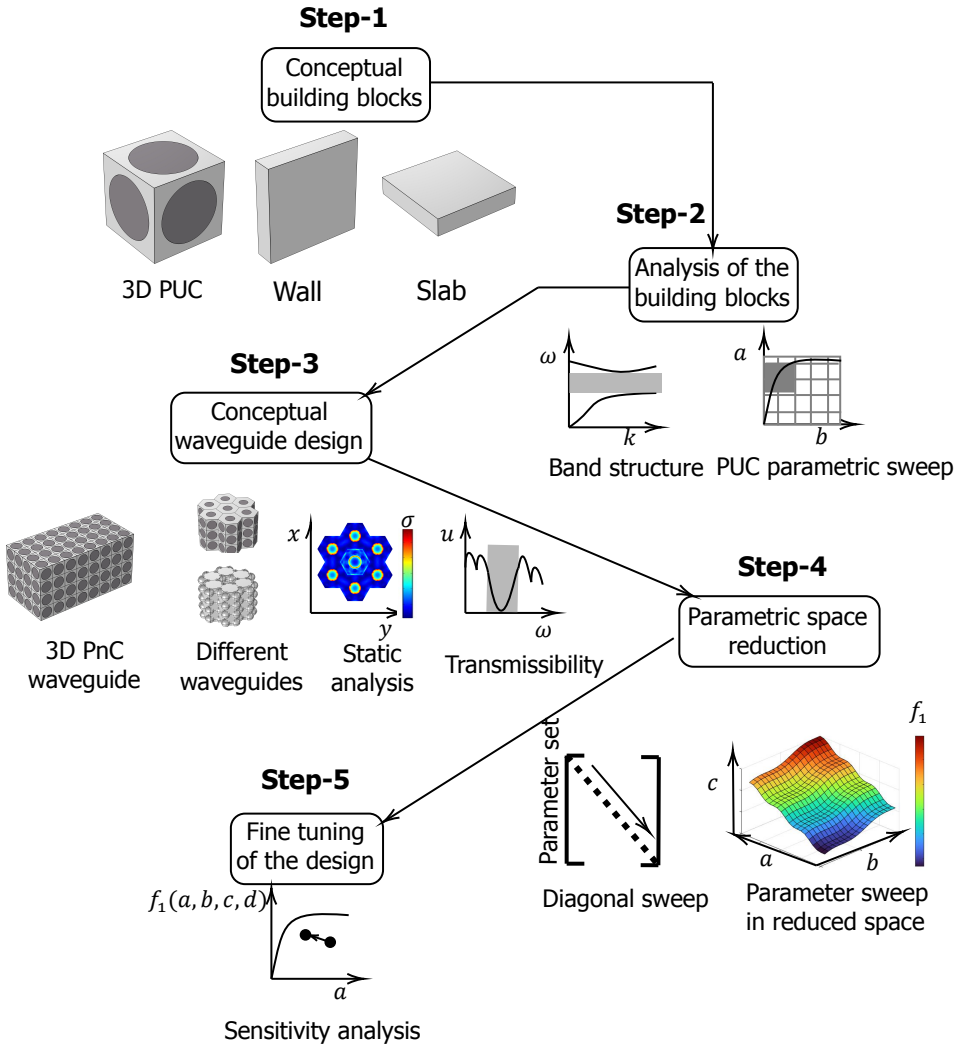

Figure 4.2: Schematic of the design process with individual steps providing a global picture. Step-1 includes all the building blocks that constitute the design, whereas Step-2 describes the analysis of the building blocks. Step-3 consists of different waveguide designs and their analyses, while Step 4 encompasses the parametric space, the design space reduction method, and the parametric sweep to obtain nominal designs. Finally, Step-5 explains the fine-tuning process to attain optimal designs for the required problem.

composed of spheres and ribs with the cubic arrangement was used in our previous work, which also possessed a broad BG [43]. We also performed experiments on this earlier prototype (fabricated via metal additive manufacturing) to characterize the 3D PnC waveguide's performance at MHz frequency ranges, and thus validated the BG predicted numerically. There the spheres were in the middle of the ribs,

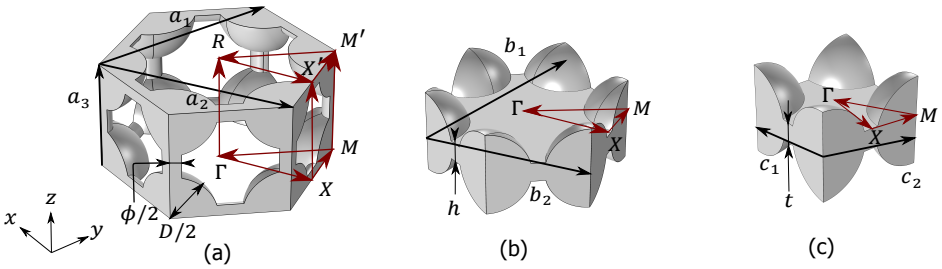

Figure 4.3: Schematics of different PnC's PUC and their corresponding irreducible Brillouin zones. (a) a 3D hexagonal PUC, where $\boldsymbol{a}_i$ (i=1 to 3) defines its lattice vector. We have translated $\boldsymbol{a}_1$ and $\boldsymbol{a}_2$ along the z-axis for visibility; however, this operation does not change the magnitude of these parameters. (b) and (c), respectively, are the 2.5D hexagonal and square PUCs with corresponding lattice vectors, i.e., $\boldsymbol{b}_i$ (i=1 to 2) for hexagonal and $\boldsymbol{c}_i$ (i=1 to 2) for square PUCs. (d) the IBZ of the 3D hexagonal PUC (triangular prism), while (e) and (f), respectively, the IBZs of 2.5D hexagonal and square PUCs (both are triangles). Additionally, we have marked the design parameters: rib diameter ϕ and sphere diameter D in (a), slab thickness h in (b), and wall thickness t in (c), respectively.

resulting in challenges during fabrication using additive manufacturing due to the large overhang angles. We address that problem in this work by positioning the spheres at the intersections of the ribs, thereby reducing the overhang angles (see Figure 4.3(a)). We define two design parameters for the PUC: the sphere diameter D and the rib diameter ϕ, which are later used in a parametric sweep to obtain the widest BG frequency range. Figure 4.3(a) also shows the lattice vectors $\boldsymbol{a}_1$, $\boldsymbol{a}_2$, and $\boldsymbol{a}_3$, although for visualization $\boldsymbol{a}_2$ and $\boldsymbol{a}_3$ have been translated to the top of the PUC. Figure 4.3(b) and 4.3(c), respectively, represent the 2.5D hexagonal and square PUCs that are used to design the outer wall and the internal slabs. These structures are called 2.5D PnCs because they lack the periodicity in the third direction (z-direction), although they are 3D structures. We have also marked lattice vectors in the corresponding PUCs ($\boldsymbol{b}_1$ and $\boldsymbol{b}_2$ in Figure 4.3(b) and $\boldsymbol{c}_1$ and $\boldsymbol{c}_2$ in Figure 4.3(c), respectively.) Since 2.5D PUCs are also made of the same material (SS316) as that of the 3D PUC, their lattice parameters' magnitudes are also the same for the 1 MHz BG central frequency. Thus $\|\boldsymbol{b}_1\| = \|\boldsymbol{a}_1\|$, $\|\boldsymbol{b}_2\| = \|\boldsymbol{a}_2\|$, and $\|\boldsymbol{c}_1\| = \|\boldsymbol{c}_2\| = \|\boldsymbol{a}_3\|$. Two additional design parameters, the slab thickness h and the wall thickness t, are defined and later used in the parametric sweeping of the complete waveguide design in **Step-4**.

To obtain the BG behavior of the aforementioned PUCs, we need to perform the dispersion analysis as mentioned in the introduction. To that end, we transform the PUCs from the Bravais lattice to the reciprocal lattice, where they are represented using Brillouin zones (BZs) [51]. The smallest section of the Brillouin zone that can accurately capture the band structure of the PUC is called the irreducible Brillouin zone (IBZ) [51]; the more symmetries the PUC possesses, the smaller the IBZ. Since the 3D hexagonal PUC has 24-fold symmetry, the resulting IBZ is a triangular prism (marked using maroon arrows in Figure 4.3(a)). Similarly, the 2.5D hexagonal and square PUCs, respectively, possess 12- and 8-fold symmetries; thus, they have triangular IBZs, which are also marked using maroon arrows in Figure 4.3(b) and

4.3(c). To design these PUCs for broad BGs centered around 1 MHz, we carry out their analysis using the band structure analysis as described next.

4.3.2. **Step-2** – Analysis of the building blocks

Since both the 3D and 2.5D PnC structures are solely composed of solid material, the wave propagation is governed by the elastic wave equation:

$$\rho\ddot{\boldsymbol{u}} = (\lambda + 2\mu)\Delta\boldsymbol{u} - \mu\nabla \times \nabla \times \boldsymbol{u}, \tag{4.2}$$

where $\boldsymbol{u}(\boldsymbol{x}, t)$ and $\ddot{\boldsymbol{u}}(\boldsymbol{x}, t)$, respectively, are the spatial displacement and acceleration as functions of position $\boldsymbol{x}$ and time t. ρ is the density of the material, and λ and μ are the Lamé coefficients; Δ and $\nabla\times$ are, respectively, the 3D Laplacian and curl operators. To fully define the boundary value problem, Equation 4.2 needs to be supplemented by appropriate boundary conditions (BCs).

4

Band structure analysis

The band structure analysis is performed by applying Bloch-Floquet periodic boundary conditions [52] along the boundaries of the PUC where the wave vector values are restricted to the IBZ, as follows:

$$\boldsymbol{u}(\boldsymbol{x} + \boldsymbol{a}_i, t) = e^{i\boldsymbol{k}\cdot\boldsymbol{a}_i}\boldsymbol{u}(\boldsymbol{x}, t), \tag{4.3}$$

where $\boldsymbol{k} = \left(k_x, k_y, k_z\right)$ is the 3D wave vector [53] and $\boldsymbol{a}_i, i = \{1 \dots 3\}$ are lattice vectors as shown in Figure 4.3(a). By using FEA via the $\omega(\boldsymbol{k})$ approach – calculating frequencies for given values of wave vectors [54], we obtain the band structure of both 3D and 2.5D PUCs. Figure 4.4a represents the band structure of 3D hexagonal PUC obtained for the design parameters $\phi = 0.4$ mm and $D = 1.6$ mm (not the optimal case with respect to the BG width), with the shaded region showing the BG, while the BZ and IBZ are shown in the inset. We calculate 40 wavebands through 8 branches of the IBZ, with a total of 96 wave vector steps (12 steps per branch) to obtain the dispersion relation up to 2 MHz. We observe a BG between the 11^{th} and 12^{th} wavebands that spans for 815.6 kHz ($f_{H2} - f_{H1}$). Note that this PUC design satisfies the BG requirement; however, the remaining requirements still need to be satisfied.

We also investigate the dispersion relation of the 2.5D square (Figure 4.3(b)) and hexagonal (Figure 4.3(c)) PUCs by the same approach. Here we use corresponding lattice vectors ($\boldsymbol{c}_i$ for square and $\boldsymbol{b}_i$ for hexagonal) and IBZs (Figure 4.3(c) for square and 4.3(b) for hexagonal, respectively). Figures 4.4b and 4.4c represent band structures of square and hexagonal lattices, respectively, where shaded regions represent corresponding BGs. In the case of the square lattice, we calculate 30 wavebands through 3 branches of the IBZ with 36 wave vector steps in total (12 steps per branch) to get the dispersion relation till 1.6 MHz. For the square PUC, two BGs are present, out of which, the first one is between 12^{th} and 13^{th} branches, and spans for 215.8 kHz ($f'_{S2} - f'_{S1}$). The second BG is present between 14^{th} and 15^{th} branches, and has a frequency range of 153 kHz ($f'_{S4} - f'_{S3}$). In the case of the hexagonal lattice, 50 wavebands are calculated through 3 branches of the IBZ with

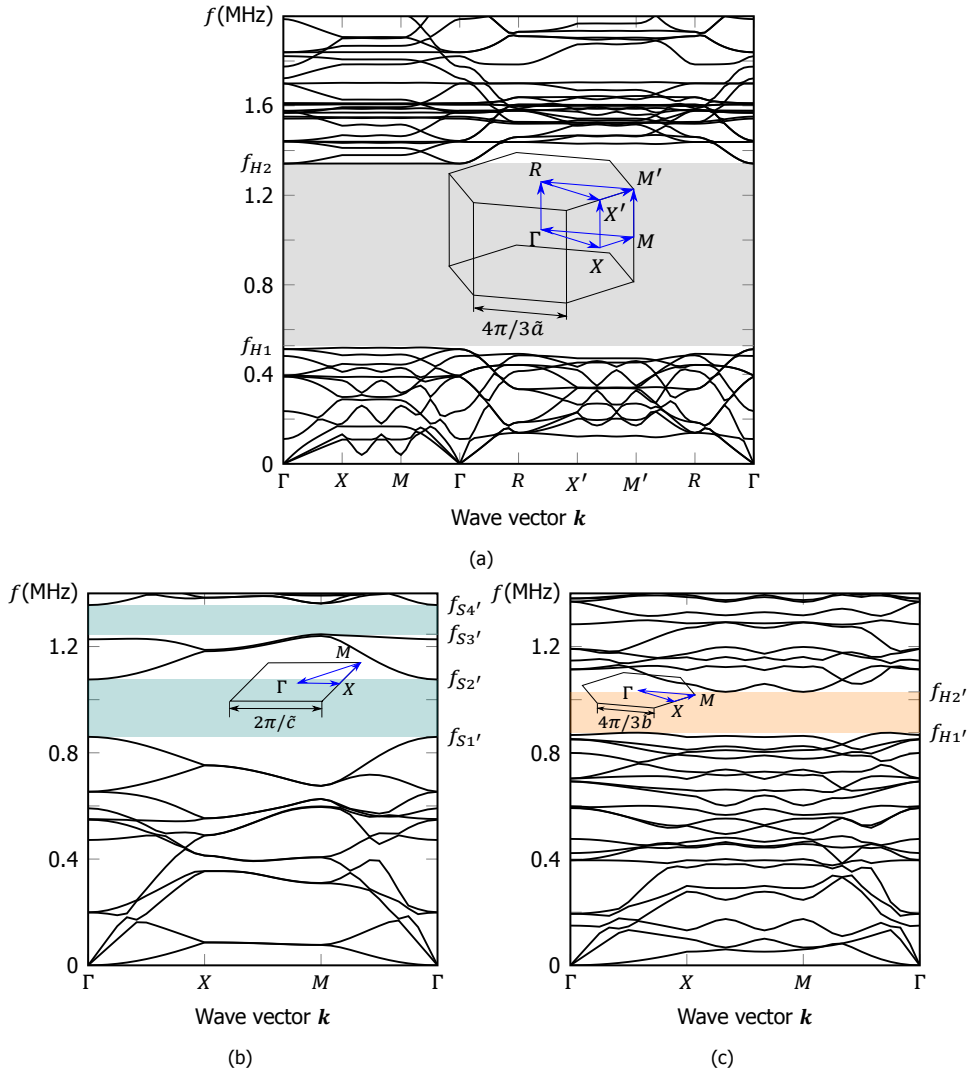

Figure 4.4: (a) Band structure of the 3D PUC hexagonal lattice of Figure 4.3(a) calculated up to 2 MHz, where the shaded region represents the BG. f_{H_1} = 0.53 MHz and f_{H_2} = 1.34 MHz define the extent of the hexagonal PUC's BG frequency range. The inset shows the hexagonal BZ with its IBZ (triangular prism), where $\tilde{a} = \|\boldsymbol{a}_3\| = 2\,\text{mm}$. Similarly, (b) and (c) are, respectively, the band structures of 2.5D PnCs with square and hexagonal PUCs, where the shaded regions represent corresponding BGs. The BG near 1 MHz in the square PUC is bounded by $f_{S1'}$ = 0.86 MHz and $f_{S2'}$ = 1.08 MHz, while $f_{H1'}$ = 0.87 MHz and $f_{H2'}$ = 1.03 MHz are the bounding frequencies of the hexagonal PUC. Additionally, as shown in (b), the second BG in the square PUC is between $f_{S3'}$ = 1.24 MHz and $f_{S4'}$ = 1.36 MHz. The insets in (b) and (c), respectively, show the square BZ with its IBZ (triangular) and the hexagonal BZ with its IBZ (also triangular), where $\tilde{c} = \tilde{b} = 2\,\text{mm}$.

the same number of wave vector steps as in the square lattice to obtain the band structure up to the same frequency (1.6 MHz). We can see a BG between the 21^{st} and 22^{nd} branches, which is 154 kHz wide. Notably, although the 2.5D PUCs' BGs are considerably narrower than that of the 3D PUC, the formers' primary functions are to prevent fluid leakage and provide structural strength to the waveguide. Thus, a narrow BG close to 1 MHz would be sufficient for the 2.5D PUCs since the frequencies containing the largest energy contributions are close to 1 MHz. Moreover, since the waveguides have to mostly deal with bulk waves rather than surface waves, the influence of 2.5D PnCs on the wave attenuation would be low. We now perform a parametric sweep to obtain optimum ranges for the design parameters ϕ and D and remove part of the design space that does not produce any BG.

3D PUC's Parametric sweep

We identified the relevant design parameters from the building blocks as the sphere diameter D, the rib diameter ϕ, the wall thickness t, and the slab thickness h. The lower bound of these parameters is provided by the resolution of the manufacturing process, for which additive manufacturing was selected in the decision phase. Their upper bound is limited by the outer dimension of the PUC (see Table 4.1). Here

Parameters	Min. (mm)	Max. (mm)	range in ξ (0 to 1)
Rib diameter ϕ	0.2	1.5	$0.2 + 1.3 \times \xi$
Sphere diameter D	0.2	2	$2 - 1.8 \times \xi$
Wall thickness t	0.2	1.5	$0.2 + 1.3 \times \xi$
Slab thickness h	0.2	1.5	$0.2 + 1.3 \times \xi$

Table 4.1: Global ranges of design parameters subjected to manufacturing constraints and domain limitations. All parameters are represented in terms of a dimensionless parameter ξ, so we can vary them simultaneously during the diagonal sweeping.

we perform a parametric sweep over D and ϕ in order to identify the parameter combinations that produce a desirable BG width greater than 600 kHz, and in the process, we trim the remaining design space of ϕ and D as shown in Figure 4.5. To that end, we step through the design space with a step size of 0.05 mm and calculate the BG width in every configuration of parameters. Since we need to conduct several band structure analyses, we have to minimize the computational cost per analysis. Thus, we limit the calculations to the 12^{th} waveband and restrict the eigenvalue analysis to four points per IBZ branch (a total of 32 points instead of 96). These modifications result in a tremendous decrease in the computational cost, from 50 min to 45 s per band structure. Figure 4.6 shows the results of this parametric study. The figure shows the BG width as a function of the design parameters ϕ and D. Noteworthy, regions of the design space that do not produce any BG are trimmed from the design space and excluded from this plot. Additionally, the dimensions that are too close to the lower bound are also eliminated because of difficulty in manufacturing. Thus the parameter ranges shown in Figure 4.6 are: ϕ from 0.3 mm

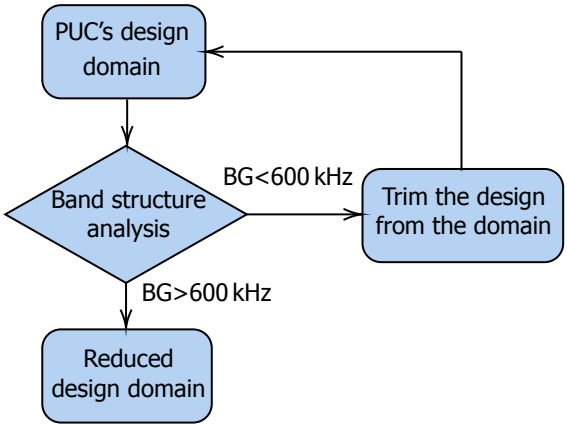

Figure 4.5: The flowchart showing the PUC's parametric sweep, where band structure analysis is performed while stepping through the PUC's design domain (ϕ and D). The designs with narrow BG width (BG<600 kHz) are removed from the domain.

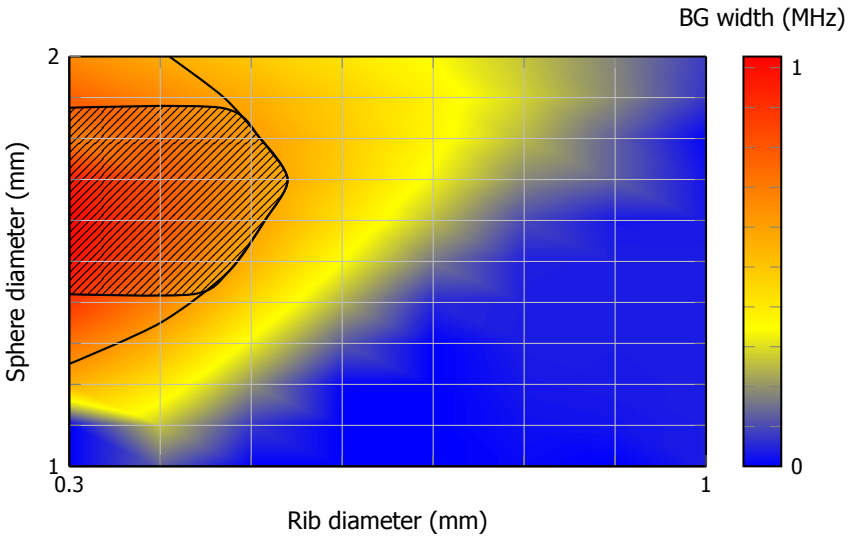

Figure 4.6: Surface plot showing the BG width (in MHz) as a function of rib and sphere diameters, where the isoline represents a BG width of 600 kHz. The rib diameter, ϕ varies from 0.3 mm till 1 mm, whereas the sphere diameter, D varies from 1 mm to 2 mm. Although the BG width increases with an increase in D and a decrease in ϕ, it starts to reduce beyond $D \approx 1.6$ mm. This is because large spheres reduce the length of the interconnecting ribs, resulting in increased rib stiffness and, consequently, decreased stiffness contrast between spheres and ribs. The hatched region (ϕ from 0.3 mm to 0.54 mm and D from 1.42 mm to 1.875 mm) in the plot shows parameter ranges corresponding to the acceptable BG width.

to 1 mm and D from 1 mm to 2 mm. The figure shows that the BG width increases with a decrease in ϕ and an increase in D as this combination increases the variation

in the mass and stiffness and, thus, the mechanical impedance contrast between the rib and the sphere. However, the BG starts to decrease after $D = 1.6\,\text{mm}$ (see Figure 4.6) as a further increase in D results in a decrease in the stiffness contrast. This is because the adjacent spheres become very close, resulting in short connecting ribs, thus increasing the rib stiffness and eventually reducing the BG width. Figure 4.6 also provides information about the parameter combinations that produce narrow BGs ($< 600\,\text{kHz}$), which are excluded hereafter from further analysis (refer to the non-shaded regions from Figure 4.6). Thus we select ranges of ϕ from 0.3 mm to 0.54 mm and D from 1.42 mm to 1.875 mm (refer to the hatched region in Figure 4.6). After trimming the PUC's design space, we move towards PnC waveguide design.

4.3.3. Step-3 – Conceptual waveguide design

3D PnC waveguides are formed by stacking the PUCs in all three directions as shown in the schematic of **Step-3** in Figure 4.2. To create the waveguide design, we arrange seven 3D hexagonal PUCs in one layer ($x-y$ plane), which is then stacked (ten layers) in the out-of-plane (z) direction as shown in Figure 4.7(c). The enclosure is then added by using the 2.5D square (Figure 4.7(b)) and hexagonal (Figure 4.7(a)) waveguides covering the entire outer surface. Furthermore, as described in Figure 4.7(c), two cylindrical fixtures of diameter 4 mm, height 4 mm, and wall thickness 0.5 mm are added at both ends (perpendicular to the $x-y$ plane) to connect to the transducers. This waveguide's wave propagation performance and the resistance against mechanical loading are characterized by means of transmissibility and static analysis, respectively.

Transmissibility analysis of the PnC waveguide with enclosure

The transmissibility analysis provides us with the attenuation rate of the supplied elastic wave for a certain number of spatially arranged PUCs at a particular frequency. This analysis can be used to design the total number of PUCs and their orientation in space corresponding to a required attenuation rate. Thus, transmissibility analysis adds an additional design parameter, the number of layers n, to the parameters from Table 4.1, which we can use to tune the wave attenuation performance of the waveguide.

The displacement transmissibility analysis is carried out by prescribing essential (Dirichlet) BCs [55] $\bar{\boldsymbol{u}}$ at one end of the waveguide as shown in the hatched pattern in Figure 4.7(c). The Dirichlet BC takes the form:

$$\boldsymbol{u}(\boldsymbol{l}, t) = \bar{\boldsymbol{u}} e^{i\omega t}, \tag{4.4}$$

where $\bar{\boldsymbol{u}}$ is the constant displacement imposed at one end (left end), ω is the applied frequency in rad/s, and $\boldsymbol{l}$ represents position vectors of the ring-shaped hatched surface of the waveguide's left fixture (marked in Figure 4.7(c)). For this analysis, the remaining boundaries of the waveguide are free from traction. As the transmissibility analysis is computationally expensive due to the large number of DOFs and many frequency steps, we need to reduce its computational cost to perform several transmissibility analyses. To that end, we generate a minimalistic model that

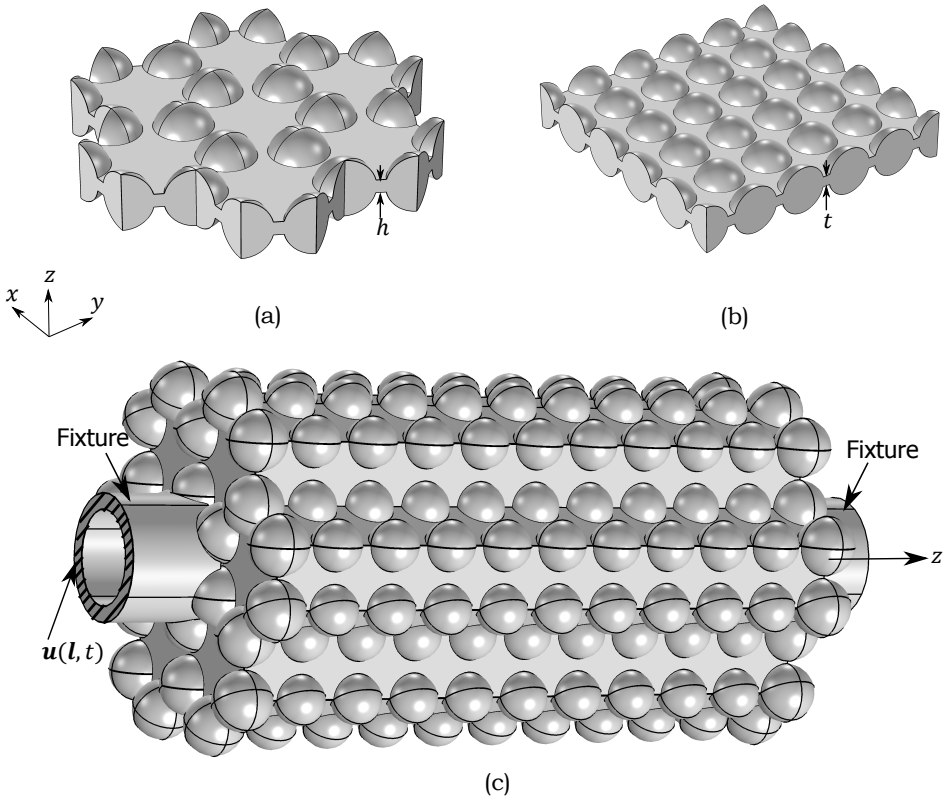

Figure 4.7: Geometries of 2.5D PnCs' waveguides and the enclosed PnC waveguide. (a) and (b) are 2.5D hexagonal and cubic PnC waveguides. (c) the complete PnC waveguide consisting of 3D hexagonal PUCs as internal structures, while 2.5D cubic PUCs are used to close the side walls. Moreover, 2.5D hexagonal PUCs are applied to the top and bottom faces to close the PnC structure entirely. (c) also contains two fixtures (marked using arrows) for connecting the waveguide to the rest of the transducer. The Dirichlet BC is also provided in (c) on the hatched region.

can capture the dynamic response of the complete PnC waveguide while minimizing the computational cost. Thus, we perform the transmissibility analysis on PnC waveguides with different numbers of layers while preserving their cross-sectional topologies. Since a one-layer waveguide does not provide the attenuation rate due to the lack of interfaces (between layers) to generate the BG, we investigate the transmissibility of waveguides with 2, 4, 6, 8, and 10 layers. All these designs look similar to the design from Figure 4.7(c) with varying heights (towards $z-$direction). This approach allows us to compare their dynamic responses since the geometric variation only occurs in one direction, and thus, the attenuation rate varies with a single spatial coordinate (z).

To compare the BG width between the band structure and transmissibility analysis, we select the same values for the design parameters from the band structure study, i.e., $\phi = 0.4\,\text{mm}$ and $D = 1.6\,\text{mm}$. Additionally, here we select the wall

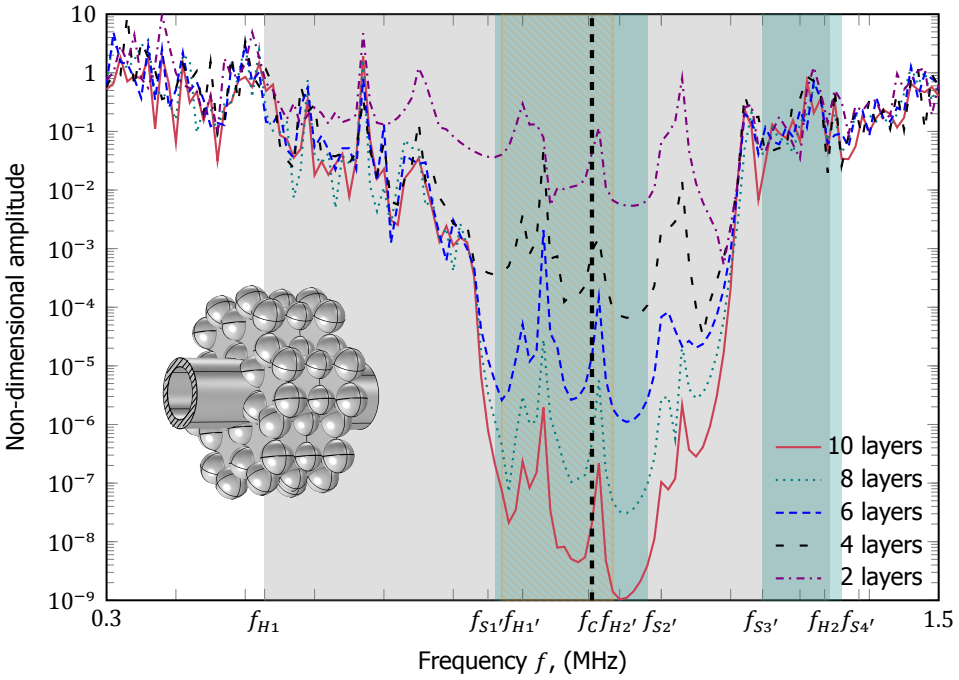

Figure 4.8: Transmissibility responses of hexagonal PnC waveguides with the different number of layers calculated from 0.3 MHz to 1.5 MHz with a frequency step of 10 kHz. The shaded (and hatched) regions represent BGs predicted by the 3D hexagonal (f_{H1} to f_{H2}), 2.5D square ($f_{S1'}$ to $f_{S2'}$ and $f_{S3'}$ to $f_{S4'}$), and 2.5D hexagonal ($f_{H1'}$ to $f_{H2'}$) PUCs with parameters $\phi = 0.4\,\text{mm}, D = 1.6\,\text{mm}$, and $t = 0.4\,\text{mm}$. A 2-layer PnC waveguide with the Dirichlet BC is shown in the inset. The accuracy in capturing the dynamic response of the complete waveguide (10 layers) decreases with a decrease in the number of layers; thus, the model with six layers is selected since it captures most of the dynamic behavior of the complete model.

thickness, $t = 0.4\,\text{mm}$ to be consistent with the rib diameter, which would reduce complexities during finite element meshing. The analyses are performed by providing a continuous harmonic displacement of 1 µm amplitude for a frequency range from 0.3 MHz to 1.5 MHz with a step of 10 kHz. The resulting transmissibility relations for waveguides with different number of layers (2, 4, 6, 8, and 10) are plotted in Figure 4.8, where the BGs predicted by band structure analyses of 3D PUC is shown using gray shaded region, while the blue shaded and orange hatched regions are, respectively, BGs of 2.5D cubic and hex PUCs. The geometry, along with the Dirichlet BC of the 2-layer PnC waveguide, is also shown in the inset of Figure 4.8. As shown in the figure, the waveguide with ten layers captures the attenuation response (BG) predicted by the band structure analysis of the 3D PUC, with the highest attenuation rate at 1.04 MHz. We can also observe that the highest attenuation region is where the BG from the 3D PUC overlaps with 2.5D PUCs because, in the remaining frequency ranges, the enclosure does not possess a BG, which reduces the attenuation rate. Additionally, several peaks are present within

the BG due to reflections from the free surfaces (outer surfaces of the enclosure), which the band structure analysis cannot capture. However, in actual applications, the PnC waveguides are connected to the transducer (via the fixtures), and part of the energy is transmitted through these interfaces, reducing the reflection peaks. Additionally, these peaks are further reduced by the influence of the surrounding fluid, which channels the wave energy through the waveguide-fluid interface. Moreover, the targeted application involves a pulse instead of a continuous signal (as mentioned in the problem statement), further reducing the reflections. Since accommodating all these conditions is practically impossible during parametric sweeping in the later stage, we then apply low-reflection BCs around the waveguide (all outer surfaces except for the hatched region from Figure 4.7(c)).

In addition to checking the attenuation response of the PnC waveguide, as discussed before, the transmissibility study in this section is used to determine a minimalistic model of the complete waveguide. As evident from Figure 4.8, designs with two and four layers fail to capture the actual trend of the waveguide's dynamic behavior of the complete model. In other words, they could not represent the changes in attenuation rate with respect to frequency and the peaks of the 10-layer PnC waveguide. The six-layer model, however, shows the dynamic response of the entire model more accurately with a nominal computational cost, so it is selected for further transmissibility analyses. After selecting this model and obtaining the transmissibility response, we proceed with the static stress analysis of the PnC waveguide.

Static stress analysis

To check the performance of the enclosed PnC waveguide against a fluid pressure load (as required in **Objective 2**), we conduct static analysis. This analysis is carried out after fixing the hatched region, where previously a harmonic displacement was prescribed for the transmissibility analysis (refer Figure 4.7(c)) and by applying a uniform pressure load of 15 MPa on all its remaining outer surfaces, since the entire waveguide is immersed in the fluid. The required BCs can be written as a combination of Dirichlet and Neumann BCs as follows:

$$\boldsymbol{u}(\boldsymbol{l}) = 0; \tag{4.5}$$

and,

$$\boldsymbol{\sigma} \cdot \boldsymbol{n} = \bar{\boldsymbol{t}} = -p\boldsymbol{n}, \tag{4.6}$$

where $\boldsymbol{\sigma}$ represents Cauchy's stress tensor, and $\boldsymbol{n}$ is the outward normal evaluated on the entire waveguide boundary. $\bar{\boldsymbol{t}}$ is the traction generated due to the applied pressure load p. We use von Mises stress throughout the structure as a measure of stress [56] since it correlates with the yield criteria of ductile materials such as SS316. The maximum stress obtained by the static analysis, $\sigma_{\max}$ is compared against the allowable stress of the material to evaluate the mechanical performance as described in **Objective 2**:

$$\sigma_A = \frac{\sigma_Y}{\gamma} = \frac{400\,\text{MPa}}{2} = 200\,\text{MPa}, \tag{4.7}$$

where σ_Y is the yield stress for a SS316 structure fabricated via additive manufacturing [57] and $\gamma = 2$ is the safety factor selected from international standard ISO 2531 [58].

Figures 4.9(a) and 4.9(b), respectively, show the cross-sectional (CS) and longitudinal sectional (LS) views of von Mises stress distribution of the 10-layer PnC waveguide with the same design parameters as the transmissibility analysis ($\phi = 0.4\,\text{mm}$, $D = 1.6\,\text{mm}$, and $t = 0.4\,\text{mm}$). It is noteworthy that since static analysis is not computationally as expensive as transmissibility, we do not need to consider a minimalistic model, and thus, we retain the 10-layer PnC waveguide during the static analysis step. The highest stress region is encircled in Figures 4.9(b), which

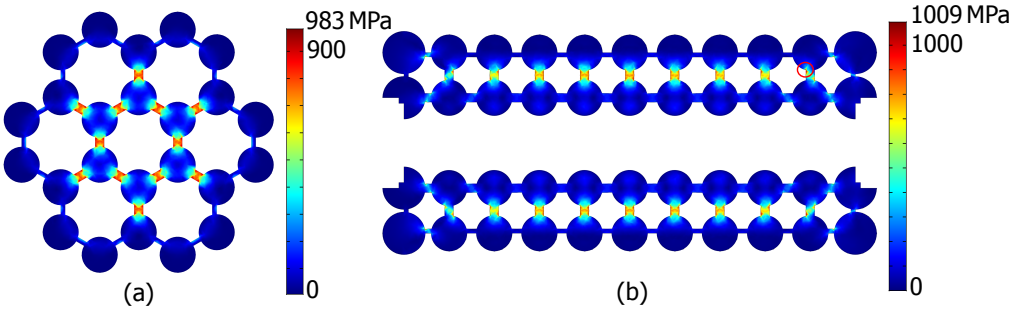

Figure 4.9: von Mises stress distributions of the PnC waveguide subjected to a pressure loading, where (a) and (b), respectively, show the cross-sectional (CS) and longitudinal-sectional (LS) views. The maximum stress in LS is a localized value (encircled in (b)), whereas, in CS, it is distributed through internal ribs.

is 1009 MPa. This value is significantly higher than the allowable stress provided in Equation (4.7). However, this stress is present in a very localized region, and thus, the structure would try to cope with it by redistributing stress to the rest of the regions after creating localized plastic deformations. On the contrary, the maximum stress in the CS (983 MPa) is distributed through the center of all internal ribs (see Figure 4.9(a)). Since the whole member (rib) is affected, this stress is more severe than the former. Thus, the waveguide would likely fail if the cross-sectional stress exceeds the allowable limit. Hence, the design in Figure 4.7(c), although it possesses a broad BG, is not a desirable design from the mechanical loading perspective. Thus, we need to expand our design space further to obtain designs that satisfy all the requirements. Therefore, we perform a design space survey by testing various waveguide designs against the two objectives.

Design space survey: identification of desirable waveguide designs

We modified the waveguide design to improve the mechanical strength, resulting in ten new designs. They are checked for maximum von Mises stress due to the loading and transmissibility area (TA), which is the area under the transmissibility curve between the required frequency bounds (from 400 kHz to 1.4 MHz, which is the bandwidth of the ultrasound transducer).

Figure 4.10 shows different views of these ten designs and compares their performances. The design shown earlier in Figure 4.7(c), which was used in both

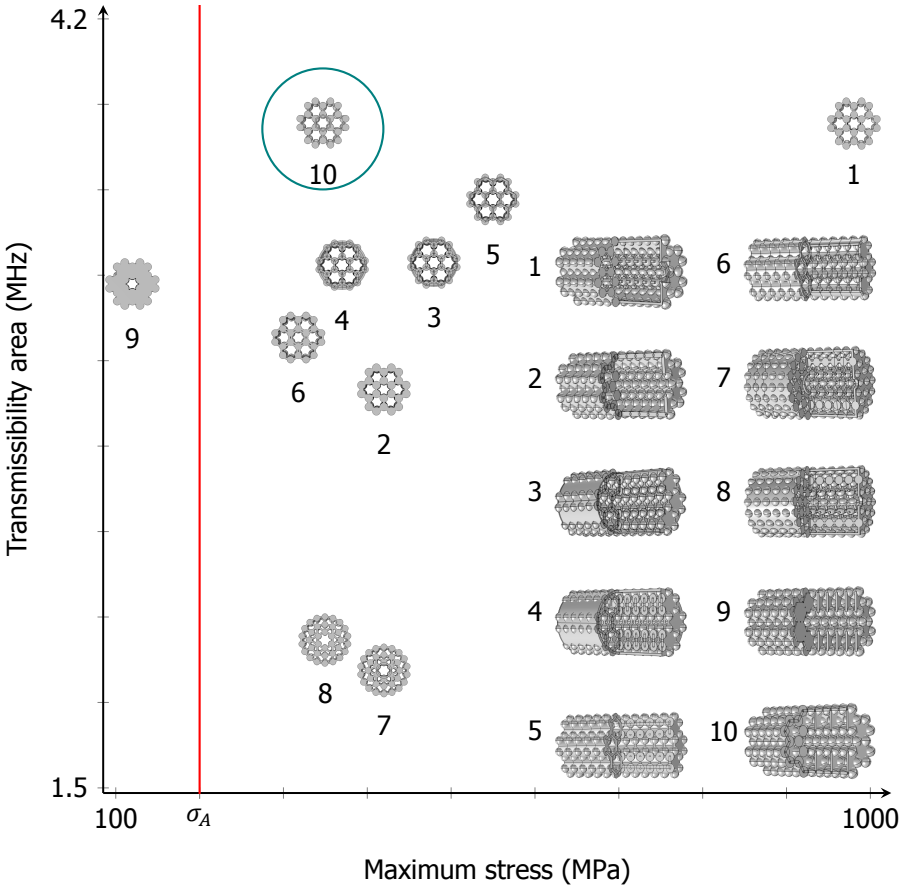

Figure 4.10: Transmissibility area vs. maximum von Mises stress for ten different initial designs. The cross-sectional view and 3D view of all designs are also provided in the plot. A desirable design should possess a higher transmissibility area and lower maximum stress. Thus, the design encircled with the ellipse (design 10) is selected, which is a closed hexagonal PnC waveguide with slabs in alternate layers perpendicular to the principal wave propagation direction.

transmissibility and static analyses, is represented as label 1 in the figure. Since the maximum stress is far greater than σ_A, we increase the outer enclosure thickness and the internal rib diameter, resulting in the design labeled 2. These modifications reduced the mechanical stress tremendously (from 983 MPa to 420 MPa). However, it also reduced the TA (from 3.83 MHz to 2.9 MHz); hence, it is not a favorable change. As cylindrical structures are ideal for pressure loads, designs featuring cylindrical inclusions were investigated. As such, in the designs labeled 3 and 4, the outer shell is replaced with different cylindrical enclosures, thereby decreasing the maximum stress to 480 MPa and 370 MPa, respectively. However, similar to the previous change, the TA also reduced (3.34 MHz for design 3 and 3.33 MHz for design 4); still, design 4 is better than the other three. We also use a different type

of cylindrical enclosures where instead of using one cylinder to enclose the waveguide, we add multiple overlapping cylinders to close the waveguide (see designs 5 and 6). Since a circular ring possesses higher strength than a hexagonal ring (a circular ring does not incur bending and has uniform stress for a pressure load), we replaced the straight ribs with curved ribs from design 5, as shown in the design labeled 6. As expected, designs 5 and 6 show superior mechanical performance. We also investigated the influence of combining a cylindrical enclosure and curved beams (see designs 7 and 8). Internal spheres were arranged cylindrically and connected with straight (design 7) and curved (design 8) ribs. Even though both showed improved mechanical strength, their TAs were drastically reduced, leaving them as the least-performing designs. Since all modifications/additions thus far have reduced one objective while improving the other, we need to find parameter(s) whose variations will have a lesser adverse effect on one objective while positively influencing the other. Thus, we introduced cross slabs perpendicular to the primary wave propagation direction. These slabs are subjected to radial loading when the pressure is applied, yielding a considerably lower stress since the radial stiffness is far greater than the bending stiffness. The design labeled 9 possesses slabs in every layer of the waveguide and thus has a maximum stress of 120 MPa, which is almost an order of magnitude lower than design 1 (same design without slabs). However, since all the ribs within the waveguide were replaced, the resulting TA was also reduced excessively. Thus, we propose design 10, where only alternate layers are replaced with slabs; this design possesses almost the same TA as design 1 with a significant reduction in maximum stress (347 MPa compared to 983 MPa of design 1). This exploitation of the design space also provides us with information about the variation in TA across different designs; thus, we choose the minimum required TA as $TA_{req} = 3.5$ MHz. We select design 10 as the preferred geometry, from which the parametric space is further explored.

4.3.4. **Step-4** – Parametric space survey

Using design 10, we further survey the parametric space to obtain designs that show superior performance for all requirements. To that end, we sweep the parameters within their respective ranges (see Table 4.1). We have updated the ranges for rib diameter ϕ and sphere diameter D after the PUC parametric sweep (see Figure 4.6). Additionally, the number of layers in the waveguide n (minimalistic model) was also selected from the transmissibility analysis (see Figure 4.8). However, even with this small number of parameters, exploring (and analyzing) each parameter is practically impossible since we have an infinite number of combinations within the design space. Although topology optimization has been used to maximize band gaps in PnCs as discussed in the introduction, the technique is only applicable to the design of a single unit cell [38]. And even for a single unit cell the computational requirements are further reduced by optimizing only on a fraction of the domain in pursuit of symmetric designs—thus enforcing the smallest irreducible Brillouin zone. The excessive computational demands associated with the design of a PnC-based structure composed of a finite number of unit cells preclude the use of topology optimization. In this work we circumvent this difficulty by trimming undesirable

regions of the design space by using different criteria, such as the minimum stress constraint, for which a diagonal sweep through the parametric space is used, as discussed next.

Diagonal sweeping

To understand the behavior of the objective functions in a portion of the design space, we vary all design parameters simultaneously (diagonal sweep). To that end, we define a non-dimensional parameter ξ whose ranges are provided in Table 4.1. As we already know the effects of variations of each parameter on the objectives, we define ξ such that its extreme values satisfy at least one objective. For instance, a small value of ϕ and a large value of D is desirable for maximizing the BG width; however, high values of t and h improve the mechanical strength immensely while reducing the transmissibility. Thus, we ensure that, with an increase in ξ, parameters ϕ, t, and h increase while D decreases.

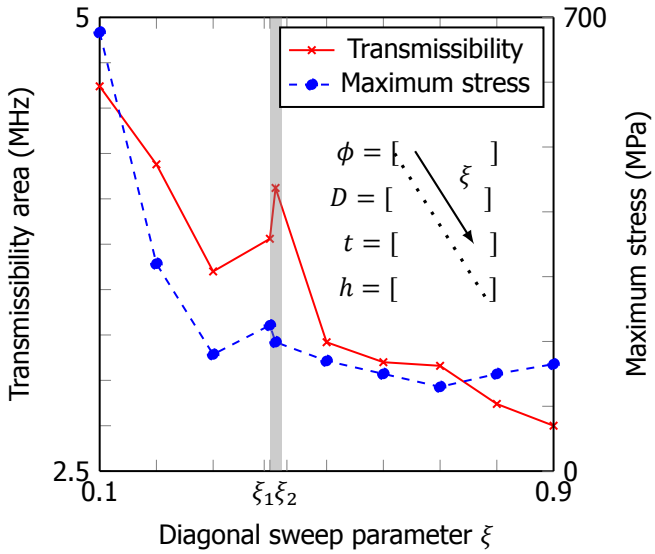

Figure 4.11: Variation of transmissibility and maximum stress of the finite waveguide corresponds to a change in the nondimensional parameter ξ. The shaded region shows a sudden response jump due to small variations in ξ ($\xi_1 = 0.4$ to $\xi_2 = 0.41$), indicating that the objective function space is rough in that neighborhood.

Figure 4.11 shows both objectives as a function of ξ; notice that the shaded region displays a sudden jump in both objectives. A minute variation in ξ (0.4 to 0.41) results in a considerable change in objectives, implying that the objective functions are highly nonlinear in that vicinity. Additionally, the TA has a steeper jump than the maximum stress. Since the objectives are conflicting, extreme values of ξ only satisfy one objective and thus are removed, resulting in a reduced design space. Additionally, we must select designs with appropriate trade-offs between objectives, which will allow us to trim down the design space further. Thus, instead of a diago-

nal sweep, we need to sweep through each parameter individually. However, since transmissibility analysis is computationally expensive, we develop surrogate models to reduce the computational cost. The first step is the minimalistic model (6 layer PnC waveguide) discussed in Section 4.3.3. We further reduce the computational cost of transmissibility analysis by starting with a coarser sample frequency step (e.g., 100 kHz instead of 10 kHz). If the TA of this transmissibility response is much lower than TA_{req}, we trim the design space. After selecting the surrogate model, we proceed to the parametric sweep of the PnC waveguide as described next.

PnC Waveguide's Parametric sweeping

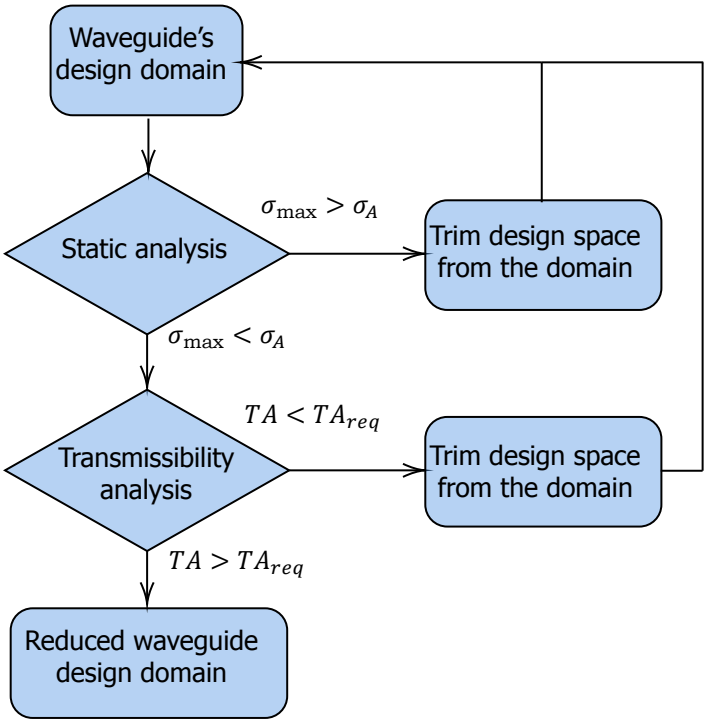

Figure 4.12: Flowchart showing the design procedure to trim down the waveguide's design space, including different analyses (static and transmissibility) and corresponding criteria. The order of analysis steps is selected based on their computational cost since, for instance, if a design does not qualify for the static analysis, we do not need to compute expensive transmissibility analysis.

Parametric sweeping of the waveguide is conducted by sweeping through all the design parameters of the waveguide (ϕ, D, t, and h) similarly to the PUC's parametric sweep discussed in Section 4.3.2. We construct PnC waveguides within this design space and check their performance using static and transmissibility analyses by following the flowchart in Figure 4.12. As the static analysis is the least expensive of the two, we first inspect the performance of the waveguide against pressure loading. We further trim the design space if the maximum stress in the PnC waveg-

uide $\sigma_{\max}$ is greater than σ_A. Additionally, if the difference between $\sigma_{\max}$ and σ_A is significantly high, we take larger steps in the parameter space before performing the static analysis again. If this sizable parameter step is sufficient to satisfy the static load requirement, we trim the intermediate portion of the design space and proceed to the transmissibility analysis. Otherwise, we choose a subsequent parameter step to create a waveguide design, which is analyzed via static analysis, and the resulting $\sigma_{\max}$ is compared against σ_A. The design that passes through this step is tested using the transmissibility analysis, whereby we compare its TA against TA_{req}, and if TA is much smaller than TA_{req}, we filter the design from the design domain and continue the process similar to the previous step (static analysis). Since both objectives are conflicting, by continuously trimming, we reach a reduced design space possessing designs with adequate trade-offs between both objectives. We see that designs with $\phi < 0.4\,\text{mm}$, $t < 0.8\,\text{mm}$, and $h < 0.8\,\text{mm}$ fail to satisfy the static load requirement; similarly, designs with $D < 1.6\,\text{mm}$ and $t > 1.2\,\text{mm}$ have low TA. Thus, the reduced design space is $\phi \subseteq \{0, 4, 0.54\}$, $D \subseteq \{1.6, 1.875\}$, $t \subseteq \{0.8, 1.2\}$, and $h \subseteq \{1, 1.4\}$. We then perform sensitivity analyses to improve the design further, zooming into the design space vicinities and moving towards a Pareto front of optimal designs.

4.3.5. Sensitivity analysis

Sensitivity analysis determines how an objective function is influenced by the rate of change of the design variable [59]. We use small (2%) and large (10%) variations to generate sensitivities of both objective functions for all the design parameters [60]. Using sensitivities, we zoom into the vicinity of a given design to explore whether further performance improvement is possible. By iteratively performing sensitivity analysis, we move in the direction of the Pareto front, beyond which one can only improve one objective by compromising the performance of the other.

After selecting the lowest bound design ($\phi = 0.4\,\text{mm}$, $D = 1.6\,\text{mm}$, $t = 0.8\,\text{mm}$, and $h = 1\,\text{mm}$) from the reduced design space, we increment each parameter and calculate objective functions. Noteworthy is that, here, TA has been replaced by the signal-to-noise ratio (SNR) since the former characterizes the PnC waveguide alone; in contrast, the latter incorporates details of the supplied input signal also (see Section 4.2). SNR is obtained by convoluting the PnC waveguide's transmissibility response with the input pulse. The time and frequency responses of the input pulse are provided in the supplementary material. Increasing all parameters except the wall thickness by 10% improved both SNR and rib center stress. After another iteration of a 10% increase in D and h, we arrive at the base design shown in Figure 4.13, which is the plot between the two objective functions for different designs and their sensitivities. We repeat the sensitivity analysis until the new sensitivities do not improve the performance of one objective without sacrificing the other. The encircled design from Figure 4.13 possesses an SNR of 75 dB with a rib center stress of 113 MPa, which are both desirable objectives. The design marked as a blue diamond could also be an appropriate design; however, its sphere diameter is slightly higher than the upper bound (1.887 mm>1.875 mm). Similarly, the slab thickness of the encircled design is also close to its upper limit; thus, further

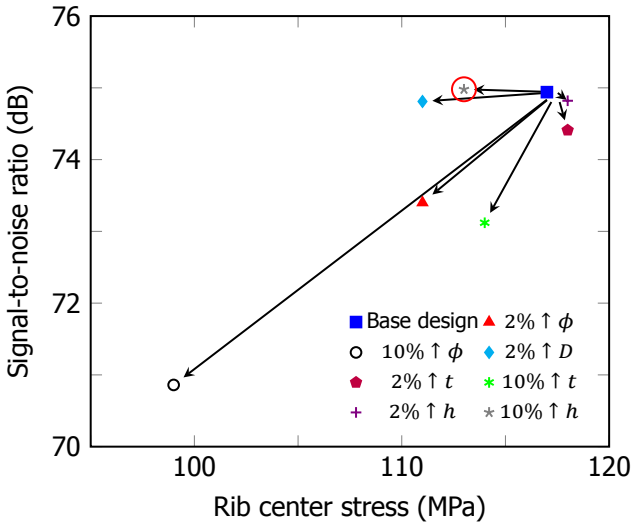

Figure 4.13: Sensitivity plot of signal-to-noise ratio and rib center stress corresponding to independent variations of all design parameters, where the desired design is encircled. 2% and 10% variations are used to capture local sensitivities, which are used to further advance the design towards an optimum. Note that we have not provided 10% variation for the sphere diameter D because its value is already close to its upper bound (1.875 mm for the base design) and cannot be increased further.

zooming in the vicinity of these two designs is difficult. Hence, the encircled design is selected as the desired final design with parameters: $\phi = 0.44$ mm, $D = 1.85$ mm, $t = 0.8$ mm, and $h = 1.4$ mm.

4.3.6. Inspection of the PnC waveguide fabricated via additive manufacturing

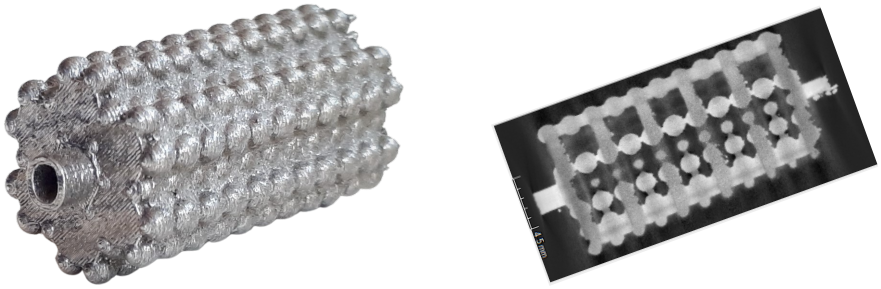

(a) (b)

Figure 4.14: (a) The photograph of a 3D PnC waveguide realized via metal additive manufacturing (selective laser sintering). (b) The CT scan of the longitudinal section through the center of the fabricated PnC waveguide shows the internal features. The difference in the feature sizes along the length is due to the orientation of the specimen in the micro-CT scanner, which distorted its view.

The final design's parameters are still difficult to realize using SS316 via available 3D printing technology (selective laser sintering) due to the high decimal precision (0.01 mm) used in the design process. Due to the intricacy of the design—i.e., multiple orientations of the ribs, large flat surfaces that are normal to the printing orientation, and the outer enclosure—currently available additive manufacturing technology cannot achieve the desired manufacturing tolerances. Thus, we fabricate a 3D PnC waveguide with slightly different design parameters, i.e., $\phi = 0.5\,\text{mm}$, $D = 1.8\,\text{mm}$, $t = 1\,\text{mm}$, and $h = 1\,\text{mm}$, whose photograph is shown in Figure 4.14(a). Noteworthy, these modifications will affect the waveguide's performance; however, they are not so significant since the waveguide still satisfies all design requirements. To compare the feature size and shape with the design, we performed a computed tomography (CT) scan of the specimen using a micro-CT scanner (Phoenix Nanotom). The rib diameter, sphere diameter, and wall thickness are consistent between the design and the printed part, with slight variations. However, the slab thickness experienced a 15 % average increase during manufacturing. The cross-sectional and longitudinal-sectional views of the PnC waveguide's CT scan with parameter measurements are provided in the supplementary material. The increase in the slab thickness could further improve the mechanical resistance. In addition, the outer surface of the waveguide is rough, as shown in Figures 4.14(a) and 4.14(b), which could influence its transmission behavior. Since a rough surface always creates more resistance to wave propagation than a smooth one, the increased surface roughness could be an advantage in reducing wave transmission. However, since we deal mainly with bulk rather than surface waves, this influence would also be minimal in the performance of the PnC waveguide.

4.4. Conclusions

In this paper, we presented a methodology for the design of a phononic crystal waveguide that maximizes wave attenuation while minimizing mechanical stress. We incorporated additional aspects to the design process, such as manufacturing considerations, domain size limitations, and industrial standards. Since various computationally expensive analyses were required, we used surrogate models, thereby minimizing analysis costs. By means of a parametric sweep we could explore the multi-dimensional design space in pursuit of an adequate design. Additionally, using sensitivity analysis, we obtained an adequate design that is part of a Pareto front, which satisfies all constraints. We realized that design via additive manufacturing and inspected using a micro-CT scanner.

Our concluding remarks are:

- For a single-phase 3D solid PnC, although the BG width increases with the contrast between the adjacent members' dimensions within the PUC, a maximum value exists beyond which any increase in dimensions decreases the BG width. This behavior is because, beyond the optimum value, any attempt to increase the contrast in properties (mass and/or stiffness) by changing the dimensions of the PUC's internal features results in a decrease in the mechanical impedance mismatch, thereby lowering the BG width;

- When attempting to maximize the performance of PnCs (or similar structures) to conflicting objectives, it is necessary to identify parameters whose variations do not influence the objectives adversely. In our case, we selected the thickness of slabs in alternate layers. Increasing this thickness improves mechanical strength tremendously while having little influence on wave attenuation behavior;
- While solving a multi-objective design problem within a design space consisting of several parameters (five in our case), it is necessary to trim the design space if associated analyses are computationally expensive. The trimming criteria can be derived from the design requirements and the objective functions' response to the parameters;

As a further step, we can generalize this design procedure to apply to other multi-objective problems having expensive and/or contradicting objectives with appropriate modifications in selecting the design parameters, analysis steps, and design space trimming criteria.

4.5. Appendix

4.5.1. Input pulse of the ultrasound transducer

The ultrasound transducer generates a high-frequency displacement pulse centered around 1 MHz, which is used for the flow measurement. Since the PnC waveguide needs to filter the signal from the transducer, we use the same signal as the input for the PnC waveguide. Figure 4.15a and 4.15b show the input pulse's time and frequency domain responses, where the displacement is plotted as functions of time (4.15a) and frequency (4.15b). The frequency corresponding to the peak displacement is marked as f_C' in Figure 4.15b whose value is 950 kHz, which is close to the central frequency ($f_c = 1$ MHz) used in the main document.

4.5.2. Micro CT images of the 3D printed PnC waveguide

After fabricating the 3D PnC waveguide via metal additive manufacturing using selective laser sintering, their internal features are measured by a micro CT scanner (Phoenix Nanotom). The cross-sectional and longitudinal sectional views of the waveguide are shown in Figure 4.16(a) and 4.16(b), respectively. We also measured all the design parameters (rib diameter, sphere diameter, wall thickness, and slab thickness) from the CT-scanned images. A list of measurements performed at different locations is provided in Figure 4.16(c), where we highlight the slab thickness measurements using a red box. The remaining parameters are close to their prescribed values, while the slab thickness experiences, on average, 15 % variation. This is due to the limitations in additive manufacturing while printing flat parts at 90°.

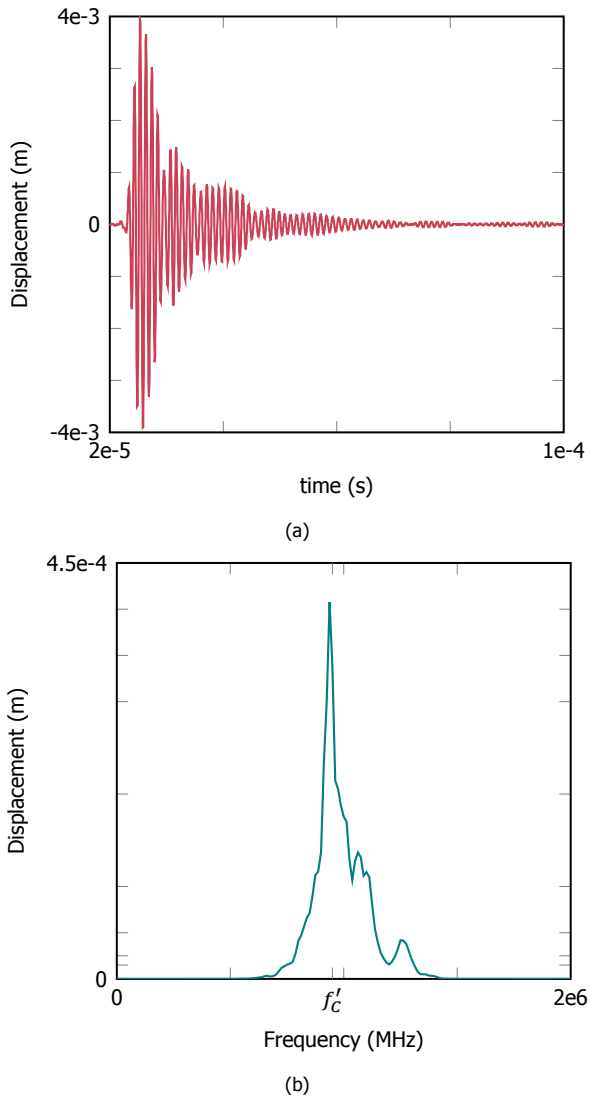

Figure 4.15: The input displacement signal is represented as functions of time (a) and frequency (b). The frequency corresponds to the peak displacement is marked as f_c' = 950 kHz in (b).

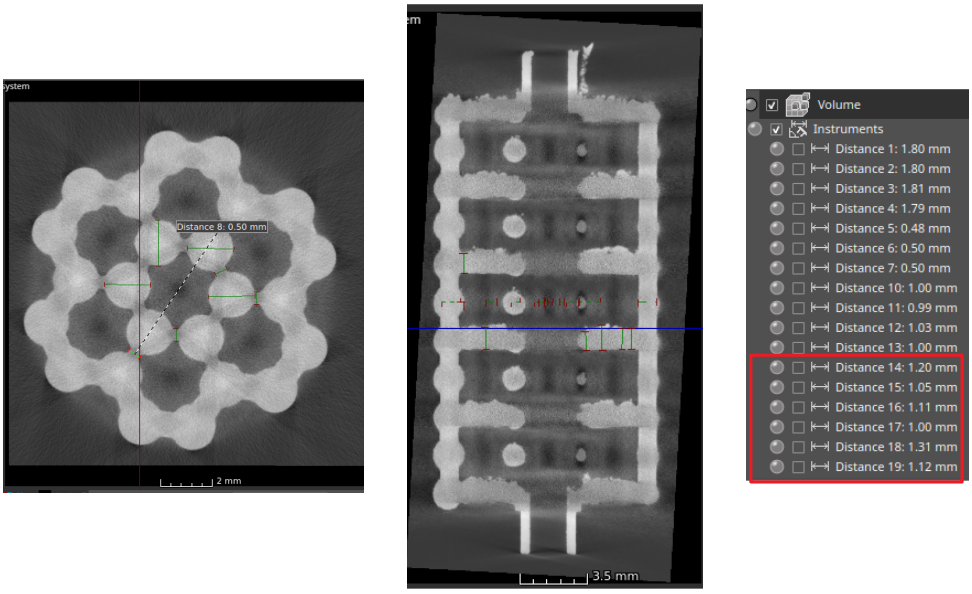

(a) (b) (c)

Figure 4.16: Cross-sectional (a) and longitudinal sectional (b) views of Micro CT images of the fabricated 3D hexagonal PnC waveguide. Measurements of various design parameters (ϕ, D, t, and h) are listed in (c), where the red box shows the slab thickness values. As evident from the measurements, the slab thickness shows, on average, 15 % variation to the required value. The remaining parameters are close to the prescribed values.

Bibliography

[1] Mahmoud Meribout et al. "Multiphase Flow Meters Targeting Oil & Gas Industries". In: *Measurement* 165 (2020), p. 108111. ISSN: 0263-2241. DOI: https://doi.org/10.1016/j.measurement.2020.108111. URL: https://shorturl.at/KauuH.

[2] Yong Chen, Yiyong Huang, and Xiaoqian Chen. "Acoustic propagation in viscous fluid with uniform flow and a novel design methodology for ultrasonic flow meter". In: *Ultrasonics* 53.2 (2013), pp. 595–606. ISSN: 0041-624X. DOI: https://doi.org/10.1016/j.ultras.2012.10.005. URL: https://www.sciencedirect.com/science/article/pii/S0041624X12002016.

[3] M. Kupnik et al. "Adaptive Pulse Repetition Frequency Technique for an Ultrasonic Transit-Time Gas Flowmeter for Hot Pulsating Gases". In: *IEEE Sensors Journal* 6.4 (2006), pp. 906–915. DOI: 10.1109/JSEN.2006.876042.

[4] H.-H. Eckstein et al. "Improvement of carotid blood flow after carotid endarterectomy Evaluation using intraoperative ultrasound flow measurement". In: *European Journal of Vascular and Endovascular Surgery* 25.2 (2003), pp. 168–174. ISSN: 1078-5884. DOI: https://doi.org/10.1053/ejvs.2002.1820. URL: https://www.sciencedirect.com/science/article/pii/S1078588402918204.

[5] Richard Smith et al. "A MEMS-Based Coriolis Mass Flow Sensor for Industrial Applications". In: *IEEE Transactions on Industrial Electronics* 56.4 (2009), pp. 1066–1071. DOI: 10.1109/TIE.2008.926703.

[6] Jankees Hogendoorn et al. "High viscosity hydrocarbon flow measurement: A challenge for Ultrasonic Flow Meters?" In: *27 th International North Sea Flow Measurement Workshop*. 2009.

[7] Pierre Ueberschlag, Andreas Berger, and Michal Bezdek. *Ultrasonic transducer for application in an ultrasonic, flow measuring device or in an ultrasonic, fill-level measuring device*. US Patent 10,620,026. Apr. 2020.

[8] Emanuel J Gottlieb et al. *Acoustically isolated ultrasonic transducer housing and flow meter*. US Patent 9,506,789. Nov. 2016.

[9] Jeroen Martin Van Klooster. *Flowmeter*. US Patent 6,799,475. Oct. 2004.

[10] A. Ramos, J.L. San Emeterio, and P.T. Sanz. "Improvement in transient piezoelectric responses of NDE transceivers using selective damping and tuning networks". In: *IEEE Transactions on Ultrasonics, Ferroelectrics, and Frequency Control* 47.4 (2000), pp. 826–835. DOI: 10.1109/58.852064.

[11] M. S. Kushwaha et al. "Acoustic band structure of periodic elastic composites". In: *Physical Review Letters* 71 (13 Sept. 1993), pp. 2022–2025. DOI: 10.1103/PhysRevLett.71.2022. URL: https://link.aps.org/doi/10.1103/PhysRevLett.71.2022.

[12] W. L. Bragg. "The Diffraction of Short Electromagnetic Waves by a Crystal". In: *Scientia* 23.45 (1929), p. 153.

[13] Caiyou Zhao et al. "Computational analysis of phononic crystal vibration isolators via FEM coupled with the acoustic black hole effect to attenuate railway-induced vibration". In: *Construction and Building Materials* 283 (2021), p. 122802. ISSN: 0950-0618. DOI: https://doi.org/10.1016/j.conbuildmat.2021.122802. URL: https://www.sciencedirect.com/science/article/pii/S0950061821005626.

[14] K. Petrover and A. Baz. "Finite element modeling of one-dimensional nonreciprocal acoustic metamaterial with anti-parallel diodes". In: *The Journal of the Acoustical Society of America* 148.1 (July 2020), pp. 334–346. ISSN: 0001-4966. DOI: 10.1121/10.0001625. eprint: https://pubs.aip.org/asa/jasa/article-pdf/148/1/334/15344454/334_1_online.pdf. URL: https://doi.org/10.1121/10.0001625.

[15] Kyung Hoon Lee et al. "Magnetoactive Acoustic Topological Transistors". In: *Advanced Science* 9.18 (2022), p. 2201204. DOI: https://doi.org/10.1002/advs.202201204. eprint: https://shorturl.at/TynZt. URL: https://shorturl.at/3cloL.

[16] Guobiao Hu et al. "Acoustic-elastic metamaterials and phononic crystals for energy harvesting: a review". In: *Smart Materials and Structures* 30.8 (July 2021), p. 085025. DOI: 10.1088/1361-665X/ac0cbc. URL: https://dx.doi.org/10.1088/1361-665X/ac0cbc.

[17] Hrishikesh Danawe et al. "Conformal gradient-index phononic crystal lens for ultrasonic wave focusing in pipe-like structures". In: *Applied Physics Letters* 117.2 (July 2020), p. 021906.

[18] Fuyin Ma et al. "Acoustic focusing and imaging via phononic crystal and acoustic metamaterials". In: *Journal of Applied Physics* 131.1 (Jan. 2022), p. 011103. ISSN: 0021-8979. DOI: 10.1063/5.0074503. eprint: https://pubs.aip.org/aip/jap/article-pdf/doi/10.1063/5.0074503/16454671/011103_1_online.pdf. URL: https://doi.org/10.1063/5.0074503.

[19] Craig W. Broadman et al. "Design of a one-dimensional underwater acoustic leaky wave antenna using an elastic metamaterial waveguide". In: *Journal of Applied Physics* 129.19 (May 2021), p. 194902. ISSN: 0021-8979. DOI: 10.1063/5.0044802. eprint: https://pubs.aip.org/aip/jap/article-pdf/doi/10.1063/5.0044802/15262282/194902_1_online.pdf. URL: https://doi.org/10.1063/5.0044802.

[20] Changqing Xu et al. "Multi-dimensional wave steering with higher-order topological phononic crystal". In: *Science Bulletin* 66.17 (2021), pp. 1740–1745. ISSN: 2095-9273. DOI: https://doi.org/10.1016/j.scib.2021.05.013. URL: https://www.sciencedirect.com/science/article/pii/S2095927321003509.

[21] Mahdiyeh Ghoreshi and Ali Bahrami. "Acoustic invisibility cloak based on two-dimensional solid-fluid phononic crystals". In: *Solid State Communications* 342 (2022), p. 114646. ISSN: 0038-1098. DOI: https://doi.org/10.1016/j.ssc.2021.114646. URL: https://www.sciencedirect.com/science/article/pii/S0038109821004221.

[22] Peng Chen, Michael R. Haberman, and Omar Ghattas. "Optimal design of acoustic metamaterial cloaks under uncertainty". In: *Journal of Computational Physics* 431 (2021), p. 110114. ISSN: 0021-9991. DOI: https://doi.org/10.1016/j.jcp.2021.110114. URL: https://www.sciencedirect.com/science/article/pii/S0021999121000061.

[23] Mohamed Farhat, Sebastien Guenneau, and Stefan Enoch. "Ultrabroadband elastic cloaking in thin plates". In: *Physical review letters* 103.2 (2009), p. 024301.

[24] Wen Kang Cao et al. "Tunable Acoustic Metasurface for Three-Dimensional Wave Manipulations". In: *Phys. Rev. Appl.* 15 (2 Feb. 2021), p. 024026. DOI: 10.1103/PhysRevApplied.15.024026. URL: https://link.aps.org/doi/10.1103/PhysRevApplied.15.024026.

[25] A-Li Chen et al. "Design of Acoustic/Elastic Phase Gradient Metasurfaces: Principles, Functional Elements, Tunability, and Coding". In: *Applied Mechanics Reviews* 74.2 (June 2022), p. 020801. ISSN: 0003-6900. DOI: 10.1115/1.4054629. eprint: https://asmedigitalcollection.asme.org/appliedmechanicsreviews/article-pdf/74/2/020801/6884767/amr_074_02_020801.pdf. URL: https://doi.org/10.1115/1.4054629.

[26] Kai Wu et al. "Metamaterial-based real-time communication with high information density by multipath twisting of acoustic wave". In: *Nature Communications* 13.1 (Sept. 2022), p. 5171. ISSN: 2041-1723. DOI: 10.1038/s41467-022-32778-z. URL: https://doi.org/10.1038/s41467-022-32778-z.

[27] Tinggui Chen, Wenting Li, and Dejie Yu. "A tunable gradient acoustic metamaterial for acoustic sensing". In: *Extreme Mechanics Letters* 49 (2021), p. 101481. ISSN: 2352-4316. DOI: https://doi.org/10.1016/j.eml.2021.101481. URL: https://www.sciencedirect.com/science/article/pii/S235243162100184X.

[28] Fabrice Lemoult, Mathias Fink, and Geoffroy Lerosey. "Acoustic Resonators for Far-Field Control of Sound on a Subwavelength Scale". In: *Phys. Rev. Lett.* 107 (6 Aug. 2011), p. 064301. DOI: 10.1103/PhysRevLett.107.064301. URL: https://link.aps.org/doi/10.1103/PhysRevLett.107.064301.

[29] Karl F Graff. *Wave motion in elastic solids*. Courier Corporation, 2012.

[30] Walter Benenson et al. *Handbook of physics*. Springer, 2002.

[31] István L Vér and Leo L Beranek. *Noise and vibration control engineering: principles and applications*. John Wiley & Sons, 2005.

[32] X.K. Han and Z. Zhang. "Bandgap design of three-phase phononic crystal by topological optimization". In: *Wave Motion* 93 (2020), p. 102496. ISSN: 0165-2125. DOI: https://doi.org/10.1016/j.wavemoti.2019.102496. URL: https://www.sciencedirect.com/science/article/pii/S0165212519302318.

[33] Atul Kumar Sharma et al. "Gradient-based topology optimization of soft dielectrics as tunable phononic crystals". In: *Composite Structures* 280 (2022), p. 114846. ISSN: 0263-8223. DOI: https://doi.org/10.1016/j.compstruct.2021.114846. URL: https://www.sciencedirect.com/science/article/pii/S026382232101285X.

[34] Qiangbo Wu et al. "Topology optimization of phononic crystal with prescribed band gaps". In: *Computer Methods in Applied Mechanics and Engineering* 412 (2023), p. 116071. ISSN: 0045-7825. DOI: https://doi.org/10.1016/j.cma.2023.116071. URL: https://www.sciencedirect.com/science/article/pii/S0045782523001950.

[35] Xiaopeng Zhang et al. "Narrow-band filter design of phononic crystals with periodic point defects via topology optimization". In: *International Journal of Mechanical Sciences* 212 (2021), p. 106829. ISSN: 0020-7403. DOI: https://doi.org/10.1016/j.ijmecsci.2021.106829. URL: https://www.sciencedirect.com/science/article/pii/S0020740321005531.

[36] Anna Dalklint et al. "Tunable phononic bandgap materials designed via topology optimization". In: *Journal of the Mechanics and Physics of Solids* 163 (2022), p. 104849. ISSN: 0022-5096. DOI: https://doi.org/10.1016/j.jmps.2022.104849. URL: https://www.sciencedirect.com/science/article/pii/S0022509622000631.

[37] Xing Zhang et al. "Design optimization of multifunctional metamaterials with tunable thermal expansion and phononic bandgap". In: *Materials & Design* 209 (2021), p. 109990. ISSN: 0264-1275. DOI: https://doi.org/10.1016/j.matdes.2021.109990. URL: https://www.sciencedirect.com/science/article/pii/S026412752100544X.

[38] Sanne J. van den Boom et al. "A level set-based interface-enriched topology optimization for the design of phononic crystals with smooth boundaries". In: *Computer Methods in Applied Mechanics and Engineering* 408 (2023), p. 115888. ISSN: 0045-7825. DOI: https://doi.org/10.1016/j.cma.2023.115888. URL: https://www.sciencedirect.com/science/article/pii/S0045782523000117.

[39] Ole Sigmund and Jakob Søndergaard Jensen. "Systematic design of phononic band–gap materials and structures by topology optimization". In: *Philosophical Transactions of the Royal Society of London. Series A: Mathematical, Physical and Engineering Sciences* 361.1806 (2003), pp. 1001–1019.

[40] Maximilian Wormser et al. "Design and Additive Manufacturing of 3D Phononic Band Gap Structures Based on Gradient Based Optimization". In: *Materials* 10 (2017). ISSN: 1996-1944. DOI: 10.3390/ma10101125. URL: https://www.mdpi.com/1996-1944/10/10/1125.

[41] Weibai Li et al. "Topological design of 3D phononic crystals for ultra-wide omnidirectional bandgaps". In: *Structural and Multidisciplinary Optimization* 60.6 (2019), pp. 2405–2415.

[42] Claudio Quaglia et al. "An endoscopic capsule robot: a meso-scale engineering case study". In: *Journal of Micromechanics and Microengineering* 19.10 (Sept. 2009), p. 105007. DOI: 10.1088/0960-1317/19/10/105007. URL: https://doi.org/10.1088/0960-1317/19/10/105007.

[43] Sabiju Valiya Valappil, Johannes F. L. Goosen, and Alejandro M. Aragón. "Phononic Crystals for Suppressing Crosstalk in Ultrasonic Flowmeters". In: *IEEE Transactions on Instrumentation and Measurement* 72 (2023), pp. 1–11. DOI: 10.1109/TIM.2023.3284960.

[44] Joseph L. Rose. "A Baseline and Vision of Ultrasonic Guided Wave Inspection Potential ". In: *Journal of Pressure Vessel Technology* 124.3 (July 2002), pp. 273–282. ISSN: 0094-9930. DOI: 10.1115/1.1491272. eprint: https://asmedigitalcollection.asme.org/pressurevesseltech/article-pdf/124/3/273/5656578/273_1.pdf. URL: https://doi.org/10.1115/1.1491272.

[45] J Yin et al. "Band structure and transmission characteristics of complex phononic crystals by multi-level substructure scheme". In: *International Journal of Modern Physics B* 29.04 (2015), p. 1550013.

[46] Q Aumann, M Miksch, and G Müller. "Parametric model order reduction for acoustic metamaterials based on local thickness variations". In: *Journal of Physics: Conference Series* 1264 (July 2019), p. 012014. DOI: 10.1088/1742-6596/1264/1/012014. URL: https://doi.org/10.1088/1742-6596/1264/1/012014.

[47] Zian Jia et al. "Designing Phononic Crystals with Wide and Robust Band Gaps". In: *Phys. Rev. Applied* 9 (4 Apr. 2018), p. 044021. DOI: 10.1103/PhysRevApplied.9.044021. URL: https://link.aps.org/doi/10.1103/PhysRevApplied.9.044021.

[48] Ahmed Mehaney and Hussein A. Elsayed. "Hydrostatic pressure effects on a one-dimensional defective phononic crystal comprising a polymer material". In: *Solid State Communications* 322 (2020), p. 114054. ISSN: 0038-1098. DOI: https://doi.org/10.1016/j.ssc.2020.114054. URL: https://www.sciencedirect.com/science/article/pii/S0038109820305585.

[49] William E Frazier. "Metal additive manufacturing: a review". In: *Journal of Materials Engineering and performance* 23.6 (2014), pp. 1917–1928.

[50] Y.S Liao, J.T Huang, and Y.H Chen. "A study to achieve a fine surface finish in Wire-EDM". In: *Journal of Materials Processing Technology* 149.1 (2004). 14th Interntaional Symposium on Electromachining (ISEM XIV), pp. 165–171. ISSN: 0924-0136. DOI: https://doi.org/10.1016/j.jmatprotec.2003.10.034. URL: https://www.sciencedirect.com/science/article/pii/S0924013604001463,%20keywords%20=%20%7BWire-EDM,%20Finish,%20Pulse-generating%20circuit,%20Surface%20roughness%7D,.

[51] Charles Kittel and Paul McEuen. *Kittel's Introduction to Solid State Physics*. John Wiley & Sons, 2018.

[52] Felix Bloch. "Quantum mechanics of electrons in crystal lattices". In: *Z. Phys* 52 (1928), pp. 555–600.

[53] A Bedford and DS Drumheller. "Elastic wave propagation". In: *John Wileg g Sons* (1994), pp. 151–165.

[54] L. D'Alessandro et al. "Modeling and experimental verification of an ultra-wide bandgap in 3D phononic crystal". In: *Applied Physics Letters* 109.22 (2016), p. 221907. DOI: 10.1063/1.4971290. eprint: https://doi.org/10.1063/1.4971290. URL: https://doi.org/10.1063/1.4971290.

[55] Thomas JR Hughes. *The finite element method: linear static and dynamic finite element analysis*. Courier Corporation, 2012.

[56] JE Shigley, CR Mischke, and RG Budynas. *Mechanical Engineering Design. 7, vol. 4*. 2007.

[57] Mingming Ma et al. "Control of shape and performance for direct laser fabrication of precision large-scale metal parts with 316L Stainless Steel". In: *Optics & Laser Technology* 45 (2013), pp. 209–216. ISSN: 0030-3992. DOI: https://doi.org/10.1016/j.optlastec.2012.07.002. URL: https://rb.gy/nk9hz5.

[58] *Ductile iron pipes, fittings, accessories and their joints for water applications, volume = 2000, address = Geneva, CH, institution = International Organization for Standardization*. Standard. Dec. 2009.

[59] Saman Razavi and Hoshin V. Gupta. "What do we mean by sensitivity analysis? The need for comprehensive characterization of "global" sensitivity in Earth and Environmental systems models". In: *Water Resources Research* 51.5 (2015), pp. 3070–3092. DOI: https://rb.gy/nk9hz5. eprint: https://shorturl.at/DFAyQ. URL: https://shorturl.at/kTVzL.

[60] Jérôme Morio. "Global and local sensitivity analysis methods for a physical system". In: *European Journal of Physics* 32.6 (Oct. 2011), pp. 1577–1583. DOI: 10.1088/0143-0807/32/6/011. URL: https://doi.org/10.1088/0143-0807/32/6/011.

5

Phononic crystals' band gap manipulation via displacement modes

Phononic crystal band gaps (BGs), which are realized by Bragg scattering, have a central frequency and width related to the unit cell's size and the impedance mismatch between material phases. BG tuning has generally been performed by either trial and error or by computational tools such as topology optimization. In either case, understanding how to systematically change the design for a particular band structure is missing. This letter addresses this by closely studying the displacement modes within the wavebands that are responsible for the BG. We look at the variation in different displacement modes due to the changes in the geometry and correlate these changes to their corresponding band structures. We then use this insight to design the unit cell for a particular application, for instance, for generating partial BGs.

5.1. Introduction

Phononic crystals (PnCs) are artificial materials that rely on the periodicity of scatterers in a matrix to derive unusual properties, such as band gaps (BGs), which are frequency ranges where mechanical waves are attenuated [1, 2]. These BGs are generated because of the destructive interference of waves due to Bragg scattering at material interfaces of the periodic unit cell (PUC) [3]. As a result, PnCs are currently being explored in various applications, such as vibration isolation [4], energy harvesting [5, 6], wave steering [7, 8], and acoustic cloaking [9, 10], among others [11, 12].

Parts of this chapter have been published in Solid State Communications **361**, p. 115061 (2023).

BGs can be identified by means of the PnCs band structure (or dispersion relation) [13], which is obtained by solving a series of eigenvalue problems that are derived by considering a finite set of wave vectors along the irreducible Brillouin zone (IBZ) [14] and prescribing their corresponding Bloch-Floquet periodic boundary conditions [15]. The achieved band structure relates the frequency to the wave vector and provides us with the wave speeds of different wavebands (frequency bands present in the band structure) and BGs. An example is shown in Figure 5.1 with the PUC, its IBZ (marked inside the first Brillouin zone), and the band structure with the BG (shaded region).

For designing PnCs, it is essential to understand how changing the geometric features of the PUC affects the band structure. As BGs in PnCs are generated due to Bragg scattering, the BG central frequency is related to the dimensions of the PUC (Bragg's law of diffraction [3]). As a result, scaling the PUC geometry allows us to shift the BG in the frequency domain. Moreover, the BG width is directly related to the impedance mismatch between the material phases within the PUC. Hence, changing this feature allows tuning of the BG width. Band structure manipulation, in general, is conducted either by trial and error or by using existing designs with specific known BG properties that can be subjected to minor changes—for instance, tuning partial BGs (PBGs) of topological PnCs [16]. PBGs are intriguing features because unlike a complete BG, PBGs possess directional aspects, *i.e.,* using PBGs, we can control the propagation direction of incoming waves. PBGs are used in applications including directional waveguiding [17] and medical imaging [18]. However, to obtain PBGs, one needs to break the spatial symmetry in the structure, thus making the design process more intricate. Hence sophisticated computational tools such as topology optimization [19] have also been used for designing PnCs with PBG. Nevertheless, the relation between different wavebands, variations of wavebands with regard to the PUC geometry, and other factors affecting their changes have not fully been explored.

We propose a design approach to make informed changes to the PUC geometry to achieve the desired BG based on the displacement modes associated with specific points in the band structure. We apply this approach to design 2D PnCs possessing PBGs from an initial design having a BG.

5.2. Analysis of a 2D solid phononic crystal

Consider a single phase 2D PnC composed of a solid material as shown in Figure 5.1(a) where the geometric parameters, a, w, and t, are marked using arrows. The particular shape of this initial design is irrelevant since the only objective of this design is to possess a BG, which can be achieved by various means. For instance, a two-phase design where a spherical (or any other shaped) scatterer in a substrate structure would also possess a BG and can be used as the initial design. However, a single-phase design is easier to manufacture at smaller scales than a two-phase design. The interior of the PUC (Figure 5.1(a)) is considered to be void, and thus the wave propagation through this geometry is governed by the elastic wave equation:

$$\rho \ddot{\boldsymbol{u}} = (\lambda + 2\mu)\Delta \boldsymbol{u} - \mu \nabla \times \nabla \times \boldsymbol{u}, \tag{5.1}$$

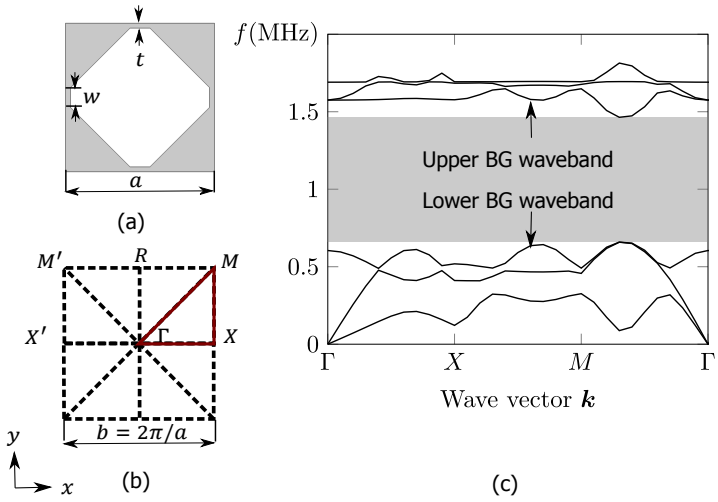

Figure 5.1: Schematic of a 2D PnC: (a) the PUC where the lattice length $a = 0.75\,\text{mm}$, width and thickness of the thin sections, $w = 0.1\,\text{mm}$, and $t = 0.025\,\text{mm}$, respectively, are marked, (b) the complete Brillouin zone (dashed lines) with the dimension b and the triangular IBZ (solid lines), (c) corresponding band structure with the shaded region representing the BG bounded by upper and lower wavebands.

where, $\boldsymbol{u}(\boldsymbol{r})$ and $\ddot{\boldsymbol{u}}(\boldsymbol{r})$ are the spatial displacement field and acceleration, respectively, and $\boldsymbol{r}$ is the position vector. ρ represents the density of the material, and λ and μ are the Lamé coefficients, whereas Δ and $\nabla\times$, respectively, are 2D Laplacian and curl operators. We consider polysulfone (PSU) to be the preferred material for the analysis with $\rho = 1350\,\text{kg/m}^3$, elastic modulus, $E = 5.18\,\text{GPa}$, and Poisson's ratio, $\nu = 0.37$.

We apply the Bloch-Floquet periodic boundary condition [15] while sweeping the wave vector through the IBZ (highlighted using solid lines in the Brillouin zone from Figure 5.1(b), where $\boldsymbol{\Gamma} = 0$) to obtain the band structure response as shown in Figure 5.1(c). The equation takes the following form:

$$\boldsymbol{u}_{n+1}(\boldsymbol{r}) = e^{i\boldsymbol{k}\cdot\boldsymbol{a}_i}\boldsymbol{u}_n(\boldsymbol{r}), \tag{5.2}$$

where n is the PUC's index, $\boldsymbol{k} = (\boldsymbol{k}_x, \boldsymbol{k}_y)$ is the wave vector in 2D [20], $\boldsymbol{a}_i = (\boldsymbol{a}_x, \boldsymbol{a}_y)$ is the lattice vector, where $\|\boldsymbol{a}_x\| = \|\boldsymbol{a}_y\| = a$, and i is the complex number. The upper and lower wavebands bounding the BG are also marked in Figure 5.1(c). Starting from the given PUC, we would like to design another PUC that possesses PBGs (BGs only in specific ranges of the wave vector) instead. In that case, we need to influence these bounding modes and create localized changes in the band structure. Since geometry changes to the PUC may break its symmetry, we may also need to change the IBZ and sweep through more branches to obtain a complete band structure [21]. We instead use a half Brillouin zone (HBZ) from the beginning, as any change in the geometry can be accommodated by the band structure without modifying the HBZ [21]. Figure 5.2(b) shows the same PUC from Figure 5.1(a),

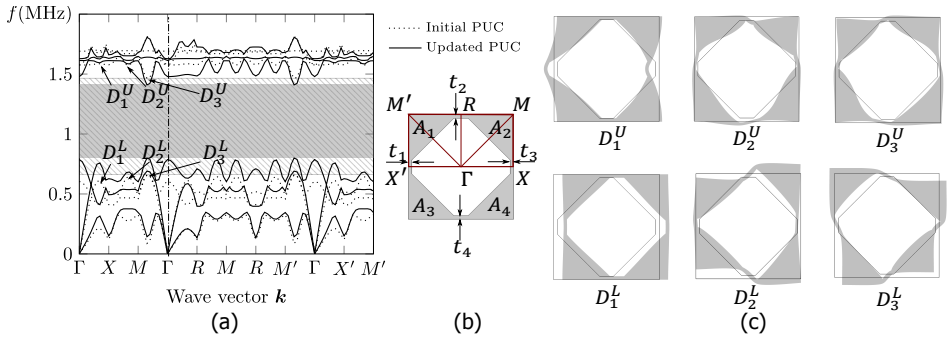

Figure 5.2: Schematic showing (a) band structures of initial and updated PUCs with hatched and shaded regions showing corresponding BGs, (b) Initial PUC with HBZ, and (c) relevant displacement modes. The PUC has been segmented into different portions such as thicknesses of ribs (t_1 through t_4) and areas of triangular shapes (A_1 through A_4). D_1 through D_3 are three displacement modes from the first three branches of the HBZ corresponding to the BG. Superscripts L and U respectively represent lower and upper BG wavebands.

5

with an HBZ, and Figure 5.2(a) shows the corresponding band structure represented using dotted curves. Figure 5.2(c) also shows a few displacement modes (marked with arrows in Figure 5.2(a)), which are selected at the HBZ's first three branches' midpoints. The band structure and displacement modes are obtained via the $\omega(\boldsymbol{k})$ approach using finite element analysis [22] by solving the wave equation (5.1) subjected to Bloch-Floquet periodic boundary condition (5.2). The superscripts L and U represent points on the lower and upper BG wavebands (bounding bands) within the band structure. To tune the band structure locally, we make necessary modifications to the geometry, changing the corresponding displacement mode by locally changing the stiffness or mass using concepts from basic mechanics. Noteworthy is that the modifications in the geometry are not particular to the initial design since the changes are based on displacement modes that can be applied to any selected initial design. Take, for instance, t_1 through t_4 and A_1 through A_4 as design parameters (refer Figure 5.2(b)). These can be considered as springs and masses with the associated behaviors. Increasing thicknesses t_2 and t_4, in turn, increases stiffnesses (and, in effect, frequencies) of D_1^L and D_3^L more than D_2^L since the latter is a combination of axial and bending modes, which turns to a bending dominated mode because of the asymmetries introduced (see the transition of the 3rd waveband in Figure 5.2(a)). Similarly, for masses, removing material from the center of rotation has minimal effect on rotating modes (*e.g.,* D_2^U) while having a substantial effect on translational modes (*e.g.,* D_1^U). The effect of local changes can then be visualized by regenerating the band structure, as we have done in Figure 5.2(a).

5.3. Partial band gap generation by manipulating displacement modes

Our objective is to obtain the topology of the PUC for the desired band structure. As an example, we want to create a geometry with a band structure possessing PBGs,

which allow the propagation of waves with short wavelengths closer to $\boldsymbol{k} = \boldsymbol{\Gamma}$ while attenuating the rest of the waves (refer Figure 5.3(b)). This peculiar property would allow the PnC structure to act as a polarizer/filter for shear (S) waves, *i.e.,* it permits the propagation of S waves while suppressing pressure (P) waves in the same direction. Consider, for instance, the initial PUC and the band structure (Figure 5.2). We need to manipulate the bounding bands (3rd and 4th bands) such that they intersect at a particular position (in the current case at $\boldsymbol{k} = \boldsymbol{\Gamma}$). So we increased the thicknesses t_2 and t_4, which resulted in an increase in stiffness (as mentioned already); therefore, corresponding points (from 3rd band) in the band structure moved up. To further locally tune the band structure, we introduced additional asymmetries by supplying t_1 through t_4 with linearly variable thicknesses, thus moving only the points of the lower BG waveband near $\boldsymbol{k} = \boldsymbol{\Gamma}$ up. Further, A_1 and A_4 were increased (thus increasing the corresponding masses), which resulted in shifting down the 4th band closer to $\boldsymbol{\Gamma}$. We repeated this process for a few more steps and obtained PBGs in the band structure. Figure 5.3(a) shows the initial and modified band structures, where we can see the shifting of the upper and lower BG wavebands till they intersect. Figure 5.3(b) and (c) respectively represent the corresponding PUC geometry

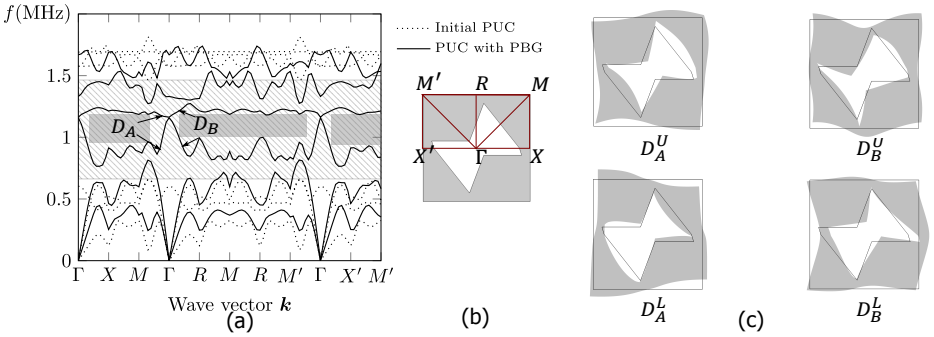

Figure 5.3: Schematic representing (a) Band structures of the initial and modified PUCs where hatched and shaded regions respectively show the initial BG and updated PBGs, (b) modified PUC with HBZ, and (c) corresponding displacement modes. D_A and D_B are displacement modes close to the separation of two BGs by a transmission region. Their locations in the bandstructure are marked in (a).

and displacement modes. All design steps, together with their corresponding PUCs, band structures, and selected displacement modes, are provided in the supplementary material. It should be noted that the redistribution of the material reduced the contrast in the stiffness and mass between the adjacent phases within the PUC, thus reducing the BG width. A transmission analysis is performed on an 8×8 PnC waveguide array to verify the band structure, whose geometry and the result are also provided in the supplementary material. Transmission of S waves shows more than two orders of magnitude compared to P waves traveling in the same direction; thus, we can infer that the obtained PnC design is an S wave polarizer.

5.4. Introducing resonator modes to create partial band gaps

Instead of making local changes to the PUC, a PBG could also be obtained by introducing a resonator. These resonators can produce BGs (due to local resonance), as in the case of an acoustic metamaterial [23, 24]. By tuning the frequency and the spatial orientation of the resonator, PBGs can be generated at a given frequency range in the original band structure (without the resonator). However, the introduction of the resonator changes the PUC topology, which may result in drastic changes in the existing band structure depending upon the level of coupling between the modes of the resonator and the remaining PUC. Adding a resonator at a 45° to the PUC from Figure 5.2 results in strong coupling between their modes because the resonator is connected to the stiffer portion of the PUC. Thus we cannot create a localized change in the band structure. Therefore no PBGs can be created (the geometry, band structure, and relevant displacement modes are available in the supplementary material). Hence, to obtain a PBG, we need to have a weak coupling between these modes (in the current case, modes from the lower BG waveband and the adjacent waveband introduced by the resonator), such that changes in the desired resonator mode have limited influences to the rest of the band structure.

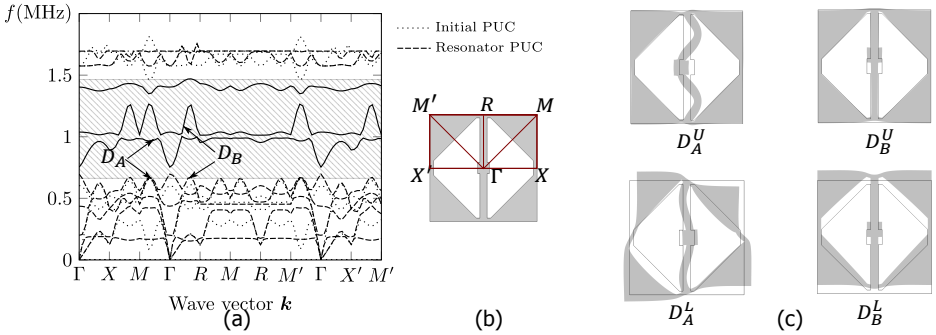

Figure 5.4: (a) comparison of band structures between initial and resonator PUCs where the resonator introduced wavebands are shown using solid curves, while the hatched region represents the former's BG, (b) schematic of the PUC with a vertical resonator and its HBZ, and (c) relevant displacement modes.

For instance, by adding a resonator connected vertically to the PUC of Figure 5.2(a) (see Figure 5.4(b)), we could introduce additional bands within the BG of the initial PUC (as represented by solid curves in Figure 5.4(a)). D_A^L and D_B^L From Figure 5.4(c) are displacement modes corresponding to the points of the lower BG waveband of the PUC. Since this band and corresponding displacement modes are similar to the original PUC from Figure 5.2 (although D_B^L shows 90° rotation to that of D_1^L because the corresponding wave vector experiences the same rotation), we can state that the resonator and the remaining PUC modes have a weak coupling. Because, in the vertical orientation, the resonator is connected to the flexible region of the PUC, thus, reducing their interactions. However, both D_A^U and D_B^U are almost

exclusively resonator modes; hence, we can tune the corresponding band locally by changing these modes (D_A^U and D_B^U) with minimal effects on the rest of the band structure.

To create the PBG, we can bring this resonator-dominant waveband closer to the lower BG waveband by reducing its frequency. For instance, by increasing the area of the central square of the resonator, as shown in Figure 5.5(b), we could increase its mass to bring down the frequency of the upper waveband. Figure 5.5(a) shows the band structures of the PUC with the resonator and the PUC with an updated resonator where the upper and lower wavebands are connected at $\boldsymbol{k} = \boldsymbol{\Gamma}$ to form partial BGs. The corresponding displacement modes (see Figure 5.5(c)) are virtually identical to that of the initial resonator (see Figure 5.4(c)), implying that the changes in the resonator did not modify the modes. In comparison with the previous case (tuning existing bands to obtain the desired band structure behavior), a resonator allows placing additional wavebands at desired locations in the band structure. Moreover, the changes in the resonator have very localized effects on the band structure (they affect the resonator wavebands). This can also be verified by the fact that the lower waveband, where BG begins, experienced few changes due to the introduction and modification of the resonator (see Figure 5.4(a) and Figure 5.5(a)). Similar to the previous case described in Section 5.3, a transmis-

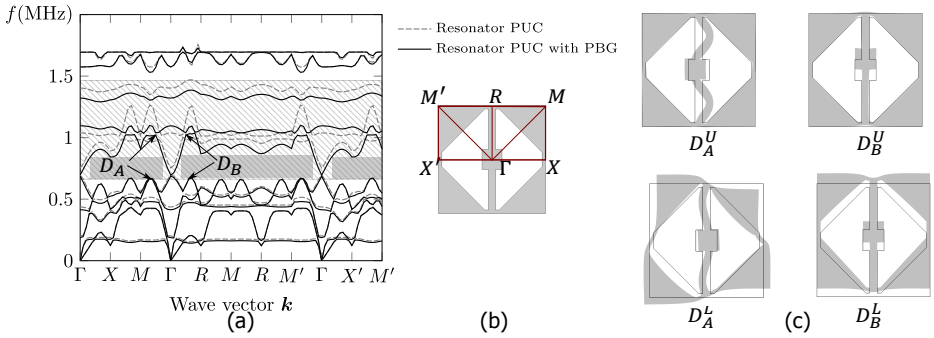

Figure 5.5: (a) Band structure comparison between PUC with a resonator and the PUC with the modified resonator, where hatched and shaded regions are the BG of the initial PUC, and PBGs of the PUC with modified resonator, (b) schematic of the resonator PUC with HBZ, and (c) relevant displacement modes.

sibility analysis can be performed on a finite PnC waveguide based on the PUC (Figure 5.5(b)) geometry. Since the procedure is the same as described in the supplementary material, we avoid it for brevity.

5.5. Conclusion

In this work, we proposed an approach to understand the link between PUC geometry and the band structure effectively, and we showed that it can be used to make predictable changes to the band structure by locally tuning the PUC by either changing the geometry or by introducing a resonator. These local modifications follow from straightforward mechanics' principles. Starting from a given PUC

geometry and its corresponding band structure, we showed that PBGs could be generated by following this approach, resulting in a new geometry by tuning the relevant displacement modes. We also demonstrated that we can manipulate the band structure further by introducing resonators with particular resonance frequencies and spatial orientations. By tuning distinct resonator modes after studying their influence on the band structure, we effectively generated PBGs. Thus, we conclude that this displacement mode-based approach is a useful tool for BG manipulation and tuning the band structure for PnCs and PnC-inspired components. Moreover, we could use the results of this approach as initial designs for further tuning by systematic computational tools such as topology optimization.

5.6. Appendix

5.6.1. Tuning the BG wave bands to obtain a partial BG

From the initial PUC (refer to the Figure 5.2 of the main document) that shows a broad complete BG, we have selected the relevant displacement modes (D_1^L through D_3^L and D_1^U through D_3^U) for tuning. To increase the eigenfrequencies of D_1^L and D_3^L modes (to move them up in the waveband), we increased their stiffnesses by increasing thicknesses of t_2 and t_4, and the resulting band structure is shown in Figure 5.6(a). By comparing the band structures of the initial PUC with this PUC, we can observe a shifting up of the lower BG waveband that brought it closer to the upper band. Simultaneously the upper waveband also moved down, which is obvious from the corresponding displacement modes. The resulting relevant displacement modes are shown in Figure 5.6(c). From the changes in the band structure, we see that multiple modes get affected by the uniform variation in thickness; thus, in order to locally move BG wavebands closer at $\boldsymbol{k} = \boldsymbol{\Gamma}$, we need to introduce further asymmetries. Additionally, D_A^L from Figure 5.6(c) is a combination of axial (tension-compression) and bending modes that might have a higher stiffness compared to a bending-dominated mode. To reduce the stiffness of this mode, while increasing the stiffness of D_B^L (to locally move the lower BG waveband up), we introduced non-uniform thicknesses to all ribs. The resulting geometry with HBZ, band structure, and displacement modes are shown in Figure 5.7.

By linearly varying all thicknesses (t_1 through t_4), we were able to make D_A^L a bending mode, thus reducing the corresponding stiffness (and frequency). From Figure 5.7(a), we see that the corresponding point shifted down along with other similar peaks from the lower BG waveband, letting points close to $\boldsymbol{k} = \boldsymbol{\Gamma}$ shift up. This change had a negligible effect on the upper waveband, meaning the modification had a localized effect on the lower BG waveband. However, we still need to move the bands closer to create a PBG. Thus, we increased the areas of triangles A_1 and A_4 (see Figure 5.8(b)), thereby increasing the variation in thickness of the ribs, while shifting the upper BG waveband down (due to the increase in the mass of the corresponding portions of the PUC). The resulting band structure and displacement modes are shown in Figure 5.8.

The effect of increasing areas of A_1 and A_4 are captured in the band structure from Figure 5.8(a), where we see that the points of lower and upper BG wavebands

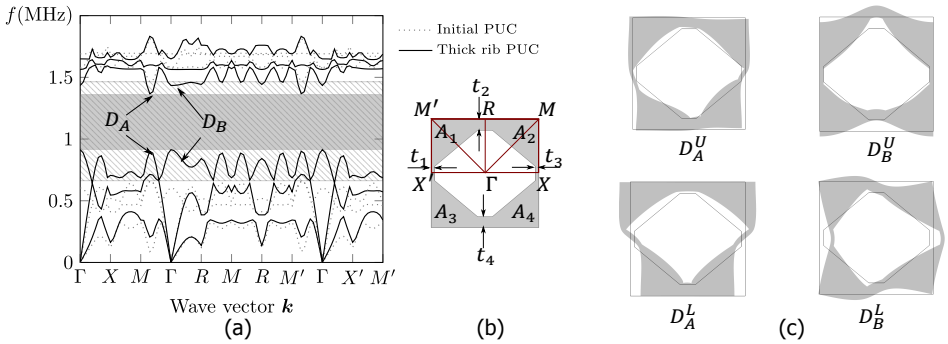

Figure 5.6: Schematic of (a) band structures of initial PUC and the PUC with thicker rib where hatched and shaded regions respectively represent the BGs of initial and updated PUCs, (b) PUC with thicker t_2 and t_4 with HBZ (c) relevant displacement modes.

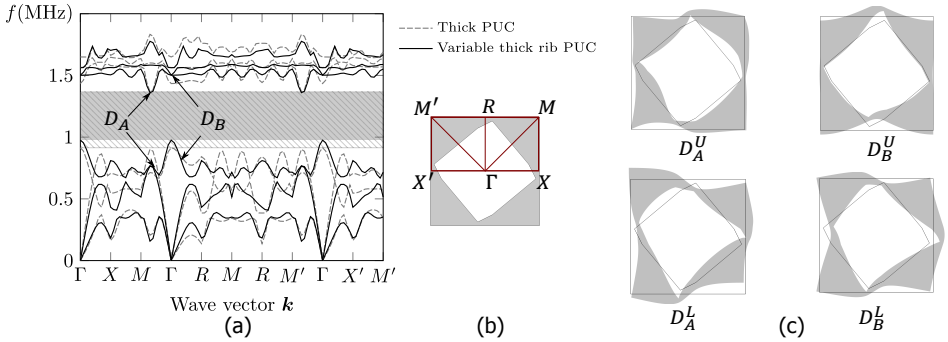

Figure 5.7: Schematic of (a) band structures and corresponding BGs of thick rib PUC and variable thick rib PUCs, (b) PUC with variable thick rib with its HBZ, and (c) relevant displacement modes.

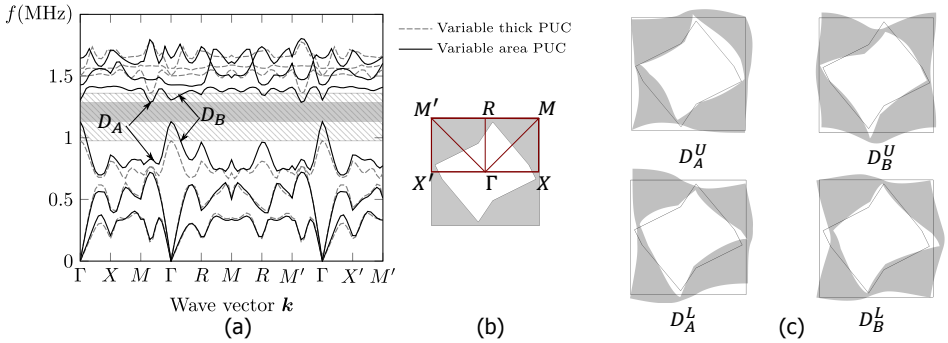

Figure 5.8: Schematic of (a) band structures and corresponding BGs of variable rib thick PUC and variable area PUC, (b) PUC with variable area with its HBZ, and (c) relevant displacement modes.

close to $\boldsymbol{k} = \boldsymbol{\Gamma}$ are getting nearer while the points away experience less shifting. Additionally, the modes do not experience drastic changes compared to the previous

iteration. Thus, we continued to implement similar changes (increasing areas of A_1 and A_4 while keeping a significant variation in thickness of ribs) and obtained the PUC that has PBGs as shown in Figure 5.3 of the main document.

5.6.2. Creating propagation mode within the BG using a resonator

As discussed already, the resonator introduces additional resonance modes to the band structure (refer Figure 5.9(a)). By aligning the resonator at a 45° angle with the PUC, we were able to create a strong coupling between the modes of the resonator to the rest of the PnC. Hence, we introduced traveling waves into the band structure (within the BG) for a specific frequency range. We can shift this frequency range by tuning the resonator properties.

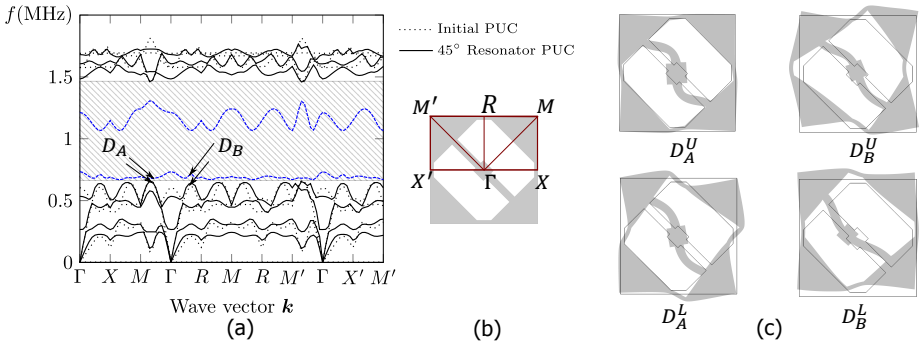

Figure 5.9: Schematic of (a) band structures of the initial design and the design with 45° oriented resonator and the BG of initial PUC (hatched), (b) geometry of the PUC with the 45° resonator and its HBZ, (c) relevant displacement modes. The resonator-introduced bands are shown using dashed lines in (a).

Figure 5.9 shows the PUC with a half BZ, its band structure with additional traveling waves (represented with blue dashed lines), and relevant displacement modes. In contrast to the case where the resonator was vertically aligned, here, all displacement modes are global (refer to Figure 5.9(c)). *i.e.,* the entire PUC gets deformed along with the resonator. Thus, we can state that the resonator modes are strongly coupled with the rest of the PUC in this orientation.

5.6.3. Transmissibility relation of partial BG PnC waveguide

Transmissibility relation provides the propagation/attenuation characteristics of a finite PnC waveguide at a particular frequency. We supply the Dirichlet boundary condition at the location $\boldsymbol{l}$ of the PnC waveguide shown in Figure 6.7(a). Dirichlet boundary condition takes the following form:

$$\boldsymbol{u}(\boldsymbol{l}) = \bar{\boldsymbol{u}} e^{i\omega\tau}, \tag{5.3}$$

where $\bar{\boldsymbol{u}}$ is the constant displacement imposed at one end (left end), ω is the applied frequency, τ is the time, and $\boldsymbol{l}$ represents position vectors of the line marked

on the left edge of the waveguide (Figure 6.7(a)). This waveguide is composed of 8×8 array of the PUC from Figure 5.3 of the main document. Two sets of transmissibility analysis are performed, wherein in the first case, the displacement ($\boldsymbol{u}_x$) is applied perpendicular to the surface generating a P wave, while in the second, the displacement ($\boldsymbol{u}_y$) is applied parallel to the surface producing an S wave. The low-reflective boundary condition is imposed along the rest of the boundary of the waveguide to limit the reflections. In both cases, the output displacement is measured at the probe location (marked on the right edge of the waveguide using an arrow in Figure 6.7(a)). The transmissibility relation is calculated for the frequency

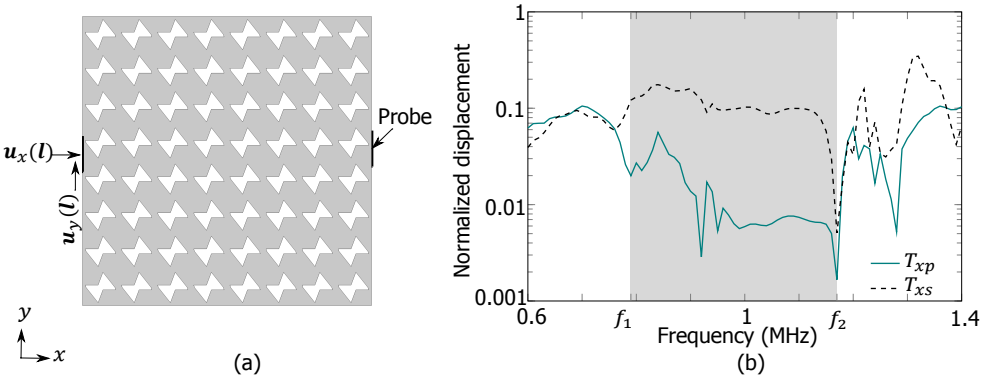

Figure 5.10: Schematic of (a) PnC waveguide possessing 8×8 array of PUCs, where Dirichlet boundary condition and probing locations are marked using arrows. $\boldsymbol{u}_x$ and $\boldsymbol{u}_y$ are displacements towards x- and y- directions, respectively. (b) Transmissibility response where the BG obtained from the band structure is shaded in gray, which is bounded by f_1 = 0.8 MHz and f_2 = 1.2 MHz. The transmissibility towards x-direction (Tx_P) is a P wave, whereas the transmission in the y-direction (Tx_S) is an S wave.

range from 0.6 MHz to 1.4 MHz with 10 kHz frequency step, where the BG bounded by f_1 and f_2 are shaded in gray. From the normalized displacement (ratio of output to the input displacement) within the BG frequency range, it is evident that S waves with longer wavelengths experience much less resistance compared to the P waves that have shorter wavelengths for the same frequency. Thus the proposed design can act as a P wave filter or polarizer.

Bibliography

[1] M. S. Kushwaha et al. "Acoustic band structure of periodic elastic composites". In: *Physical Review Letters* 71 (13 Sept. 1993), pp. 2022–2025. DOI: 10.1103/PhysRevLett.71.2022. URL: https://link.aps.org/doi/10.1103/PhysRevLett.71.2022.

[2] M. S. Kushwaha et al. "Theory of acoustic band structure of periodic elastic composites". In: *Phys. Rev. B* 49 (4 Jan. 1994), pp. 2313–2322. DOI: 10.1103/PhysRevB.49.2313. URL: https://link.aps.org/doi/10.1103/PhysRevB.49.2313.

[3] W. L. Bragg. "The Diffraction of Short Electromagnetic Waves by a Crystal". In: *Scientia* 23.45 (1929), p. 153.

[4] Matthew Reynolds and Stephen Daley. "An active viscoelastic metamaterial for isolation applications". In: *Smart Materials and Structures* 23.4 (2014), p. 045030.

[5] Kyung Ho Sun et al. "Sound energy harvesting using a doubly coiled-up acoustic metamaterial cavity". In: *Smart Materials and Structures* 26.7 (2017), p. 075011.

[6] Shu Zhang, Leilei Yin, and Nicholas Fang. "Focusing ultrasound with an acoustic metamaterial network". In: *Physical review letters* 102.19 (2009), p. 194301.

[7] J Xu and J Tang. "Tunable prism based on piezoelectric metamaterial for acoustic beam steering". In: *Applied Physics Letters* 110.18 (2017), p. 181902.

[8] Zhaojian He, Feiyan Cai, and Zhengyou Liu. "Guiding acoustic waves with graded phononic crystals". In: *Solid State Communications* 148.1 (2008), pp. 74–77. ISSN: 0038-1098. DOI: https://doi.org/10.1016/j.ssc.2008.07.007. URL: https://www.sciencedirect.com/science/article/pii/S0038109808003906.

[9] Shu Zhang, Chunguang Xia, and Nicholas Fang. "Broadband acoustic cloak for ultrasound waves". In: *Physical Review Letters* 106.2 (2011), p. 024301.

[10] Mahdiyeh Ghoreshi and Ali Bahrami. "Acoustic invisibility cloak based on two-dimensional solid-fluid phononic crystals". In: *Solid State Communications* 342 (2022), p. 114646. ISSN: 0038-1098. DOI: https://doi.org/10.1016/j.ssc.2021.114646. URL: https://www.sciencedirect.com/science/article/pii/S0038109821004221.

[11] A.A. Maznev, A.G. Every, and O.B. Wright. "Reciprocity in reflection and transmission: What is a 'phonon diode'?" In: *Wave Motion* 50.4 (2013), pp. 776–784. ISSN: 0165-2125. DOI: https://doi.org/10.1016/j.wavemoti.2013.02.006. URL: https://www.sciencedirect.com/science/article/pii/S016521251300036X.

[12] Osama R. Bilal, André Foehr, and Chiara Daraio. "Bistable metamaterial for switching and cascading elastic vibrations". In: *Proceedings of the National Academy of Sciences* 114.18 (2017), pp. 4603–4606. ISSN: 0027-8424. DOI: 10.1073/pnas.1618314114. eprint: https://www.pnas.org/content/114/18/4603.full.pdf. URL: https://www.pnas.org/content/114/18/4603.

[13] Karl F Graff. *Wave motion in elastic solids*. Courier Corporation, 2012.

[14] Hendrik J. Monkhorst and James D. Pack. "Special points for Brillouin-zone integrations". In: *Phys. Rev. B* 13 (12 June 1976), pp. 5188–5192. DOI: 10.1103/PhysRevB.13.5188. URL: https://link.aps.org/doi/10.1103/PhysRevB.13.5188.

[15] Felix Bloch. "Quantum mechanics of electrons in crystal lattices". In: *Z. Phys* 52 (1928), pp. 555–600.

[16] Ze-Guo Chen and Ying Wu. "Tunable Topological Phononic Crystals". In: *Phys. Rev. Applied* 5 (5 May 2016), p. 054021. DOI: 10.1103/PhysRevApplied.5.054021. URL: https://link.aps.org/doi/10.1103/PhysRevApplied.5.054021.

[17] Bo Yuan et al. "Broadband directional acoustic waveguide with high efficiency". In: *Applied Physics Letters* 101.4 (2012), p. 043503. DOI: 10.1063/1.4739081. eprint: https://doi.org/10.1063/1.4739081. URL: https://doi.org/10.1063/1.4739081.

[18] Xiasheng Guo et al. "Modeling and optimization of an acoustic diode based on micro-bubble nonlinearity". In: *The Journal of the Acoustical Society of America* 133.2 (2013), pp. 1119–1125. DOI: 10.1121/1.4773256. eprint: https://doi.org/10.1121/1.4773256. URL: https://doi.org/10.1121/1.4773256.

[19] Jingjie He and Zhan Kang. "Achieving directional propagation of elastic waves via topology optimization". In: *Ultrasonics* 82 (2018), pp. 1–10. ISSN: 0041-624X. DOI: https://doi.org/10.1016/j.ultras.2017.07.006. URL: https://www.sciencedirect.com/science/article/pii/S0041624X17300045.

[20] A Bedford and DS Drumheller. "Elastic wave propagation". In: *John Wileg g Sons* (1994), pp. 151–165.

[21] Florian Maurin et al. "Probability that a band-gap extremum is located on the irreducible Brillouin-zone contour for the 17 different plane crystallographic lattices". In: *International Journal of Solids and Structures* 135 (2018), pp. 26–36. ISSN: 0020-7683. DOI: https://doi.org/10.1016/j.ijsolstr.2017.11.006. URL: https://www.sciencedirect.com/science/article/pii/S0020768317305103.

[22] L. D'Alessandro et al. "Modeling and experimental verification of an ultra-wide bandgap in 3D phononic crystal". In: *Applied Physics Letters* 109.22 (2016), p. 221907. DOI: 10.1063/1.4971290. eprint: https://doi.org/10.1063/1.4971290. URL: https://doi.org/10.1063/1.4971290.

[23] Steven A Cummer, Johan Christensen, and Andrea Alù. "Controlling sound with acoustic metamaterials". In: *Nature Reviews Materials* 1.3 (2016), p. 16001.

[24] Guancong Ma and Ping Sheng. "Acoustic metamaterials: From local resonances to broad horizons". In: *Science Advances* 2.2 (2016), e1501595. DOI: 10.1126/sciadv.1501595. eprint: https://www.science.org/doi/pdf/10.1126/sciadv.1501595. URL: https://www.science.org/doi/abs/10.1126/sciadv.1501595.

6

Partial band gap phononic structures for attenuating crosstalk in clamp-on ultrasonic flowmeters

Clamp-on ultrasonic flowmeters suffer from crosstalk—i.e., measurement errors due to the interference of signals generated in solid regions and solid-fluid interfaces with the required signal from the fluid. Although several approaches have been proposed to alleviate crosstalk, they only work in specific ranges of flow rates and pipe diameters, and some also introduce additional issues. We propose a novel clamp-on system design where the transmitting and receiving wedges are embedded with directional noise filtering mechanisms based on phononic crystals (PnCs) possessing partial band gaps (PBGs). PnCs are artificial materials consisting of periodic structures arrayed in a matrix medium exhibiting band gaps—i.e., frequency ranges where waves are attenuated—due to Bragg scattering. PBGs enable PnCs to propagate waves in specific directions while suppressing them in other directions. By guiding the input signal through the transmitting wedge to the wall, we minimize the generation of noise signals due to secondary reflections within the wedge. Similarly, by using the directionality of the PBG PnC in the receiver, we limit the effects of noise signals (that arrive in different directions) in the receiver. We numerically verify the PBG PnC embedded wedges' performance by comparing wave propagation aspects of the PnC embedded clamp-on system with a standard clamp-on device. To that end, we develop accurate wave propagation models based on the Discontinuous Galerkin finite element method. By incorporating PBG PnCs into the wedges, we obtain

Parts of this chapter is under review at Mechanical Systems and Signal Processing.

about 20 dB *increase in the signal-to-noise ratio compared to the clamp-on system with standard wedges.*

6.1. Introduction

Flow metering is a quintessential process in many industries to ensure quality and smooth operation, and its market size is predicted to reach $12.99 billion by 2028 [1]. Flow meters are used in various applications, such as pharmaceutical [2], oil and natural gas [3], automotive [4], aerospace [5], and medical diagnostics [6], among others. They are classified as variable area type, pressure-based, optical, magnetic type, Coriolis, and ultrasonic devices [7]. Ultrasonic flowmeters (UFs) can be further divided into in-line and clamp-on devices, which provide accurate measurements since they can be used without disrupting the flow. Additionally, they are very versatile as we can use them with a wide range of pipe sizes and various types of fluids. Despite all these advantages, in-line UFs are difficult to install since, for an accurate measurement, it is necessary to know the arrangement of transducers, for which the manufacturer needs to know *a priori* the size of the pipeline and the properties of the flowing fluid. These parameters are not always known. Moreover, the flow needs to be temporally interrupted to install these flowmeters, which may lead to pressure drops, fouling, and leakage [8].

Clamp-on flowmeters do not have these limitations since they are portable devices that can be installed to a pipe wall effortlessly without disrupting the flow and without introducing additional pipe sections. Moreover, they offer measurement in wide flow ranges and are less expensive than their in-line counterparts [9]. Since the device is not directly in contact with the measuring fluid, the maintenance cost is practically negligible [10]. Clamp-on UFs operate based on the transit-time principle as shown in Figure 6.1. In a clamp-on UF, the ultrasound signal generated by

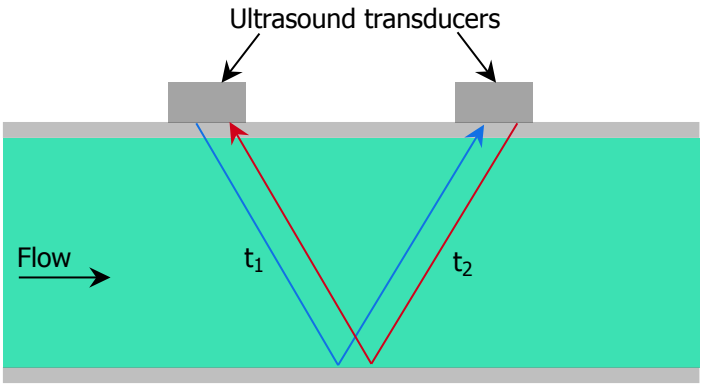

Figure 6.1: Schematic representation of the operation of a clamp-on UF, where t_1 and t_2, respectively, represent the upstream (towards the flow direction) and downstream (against the flow direction) travel times whose difference is proportional to the flow rate.

a piezoelectric transducer (piezo) is transmitted to the pipe wall, which then enters into the fluid in contact. After traveling through the fluid, this wave is transmitted

back to the pipe wall and is received by the receiving piezo (blue line from the figure). The exact process is repeated in the opposite direction (red line in the figure), and the difference in the travel time between these two signals provides us with information about the flow rate of the fluid. However, the input signal also excites other types of parasitic waves, such as pressure (P) waves and Lamb waves in the pipe wall [11], which interact with the required signal through the fluid, resulting in crosstalk between these signals. Due to crosstalk, the flowmeter experiences measurement issues such as a reduction in accuracy or the loss of the necessary signal.

Several solutions have been proposed to reduce these interactions in the clamp-on UFs, thereby improving the measurement accuracy. Sanderson and Yueng proposed a design where an absorbing layer is placed around the pipe wall between the transducers that attenuates the interfering Lamb waves [8]. However, in many cases, the pipe may be covered by materials for heat protection, thus limiting access to the pipe wall and making this approach less viable. Tezuka et al. modified the wedge angle that couples the transducer to the pipe wall to minimize the generation of Lamb waves [12]. Nevertheless, modifications in the wedge angle would require manual adjustment of transducers, thereby making the process operator-dependent. Wang et al. used metallic wedges made of stainless steel instead of polymer (which are commonly used) and excited the wedges' shear modes, which in turn induce shear waves in the pipe wall, thereby reducing the P wave generation [13]. However, the additional interfaces (to produce a shear wave in the wedge) introduce multiple reflections, which inherently induce various waves in the pipe wall that could interfere with the required signal, further reducing measurement accuracy.

Array-based sensors can circumvent the usage of wedges, thereby avoiding manual calibration and reducing multiple wave interactions, thus improving the measurement accuracy [10]. They consist of an array of piezoelectric sensors that are wrapped around the pipe, and the flow rate is measured using array processing techniques [14]. These sensors possess high accuracy and repeatability. Moreover, since no coupling compound (generally applied between wedges and the pipe wall) is needed, no maintenance is required. Nevertheless, the flow rate should be greater than 0.9 m/s, they have long start-up time, and they put restrictions on the pipe diameter (which should be greater than 5 cm) [10]. Another type of transducer array, known as a matrix transducer array, has been used to minimize the Lamb waves in the pipe wall while maintaining the required beam shape in the fluid with a flat wave front [15]. Unlike the previously mentioned sensor arrays, the matrix transducer array uses spatially arranged small-sized piezo elements with a much smaller spatial footprint than the array-based sensors (sub-millimeter) separated by air [16]. By using electronic beam steering techniques, matrix arrays can adjust the angle and the shape of the wavefront [17], enabling them to produce multiple beams in different directions, thereby improving the measurement accuracy. However, the steering and focusing are only possible in the near field, and a larger aperture is required otherwise. Another significant issue is the generation of electric crosstalk caused by the deficiency of electromagnetic shielding, the capacitive

effects between the elements, or close electric connections [18]. This crosstalk can deteriorate the directivity of the ultrasonic beam and accidental excitation of a piezo element by the adjacent element, reducing the capacity to control the beam.

A solution to reduce the interference of waves from the pipe wall and the fluid, without introducing additional crosstalk, could be attained by using phononic crystals (PnCs) [19, 20]. PnCs are artificial periodic structures possessing unusual dynamic characteristics, such as band gaps (BGs), which are frequency ranges where the propagation of mechanical waves is attenuated. These BGs are generated due to destructive interference of waves when the unit cell dimensions are comparable to the incoming wavelength, similarly to Bragg scattering of electromagnetic waves [21]. PnCs are employed in various applications such as vibration isolation [22], frequency steering [23], acoustic cloaking [24], energy harvesting [25], and super/hyper lens [26, 27], among others. We have previously used PnC structures in an in-line UF to improve its measurement accuracy by minimizing the crosstalk levels [28]. They have also been applied in non-invasive ultrasonic transducers to enhance the sensitivity of liquid sensors [29, 30]. Other similar applications of PnCs in a clamp-on setting include enhancing sensing capabilities of gasoline property detection systems [31, 32], improving transducer's accuracy during non-destructive evaluation [33, 34], and aiding in structural health monitoring [35–37]. To the best of our knowledge, PnCs have yet to be used in a clamp-on UF to improve measurement accuracy by minimizing the interference of waves between the pipe and the fluid.

In this study, we investigate the feasibility of using PnCs with directional wave propagation behavior because of the presence of partial band gaps (PBGs) to improve the measurement accuracy of clamp-on UFs. We first build accurate wave propagation models of the complete clamp-on system based on the discontinuous Galerkin finite element method (DG FEM) [38]. Further, we develop standard finite element models of PnC structures, which possess partial BGs that enable wave propagation only through specific directions. Using the band structure and transmissibility analyses, we evaluate the performance of the PnC structures. The PnC waveguide is incorporated into the wedge section of the clamp-on system to steer the incoming waves to desired directions while minimizing the transmission of waves in other directions, thereby reducing the undesirable wave generation in the pipe wall. The performance of the PnC-incorporated transducer is compared against a standard transducer via transient analysis using DG FEM models.

6.2. Clamp-on ultrasonic flowmeter: operation and noise generation

We begin by defining the clamp-on UF geometry and material parameters. The clamp-on system consists of a fluid-filled pipe, an acoustic transmitter, and a receiver, as shown in the schematic Figure 6.2(a). The pipe is made of stainless steel, while the fluid used is water. Additionally, the wedges used in the clamp-on flowmeter are generally constructed from polysulfone (PSU), a high-performance thermoplastic with superior corrosion resistance [39]. The relevant properties of

these materials are listed in Table 6.1. These properties are used to calculate the signal path through the clamp-on system.

Material	Density (kg/m^3)	Pressure wave speed (m/s)	Shear wave speed (m/s)
Polysulfone	1350	1958.84	1183.38
Stainless steel	7800	4935.5	3102.9
Water	998.2	1481.4	–

Table 6.1: Material properties of various parts of the clamp-on system. Polysulfone is used in the wedge region, whereas the pipe wall is made of stainless steel, and the measuring fluid is water.

6.2.1. Clamp-on ultrasonic flowmeter characteristics

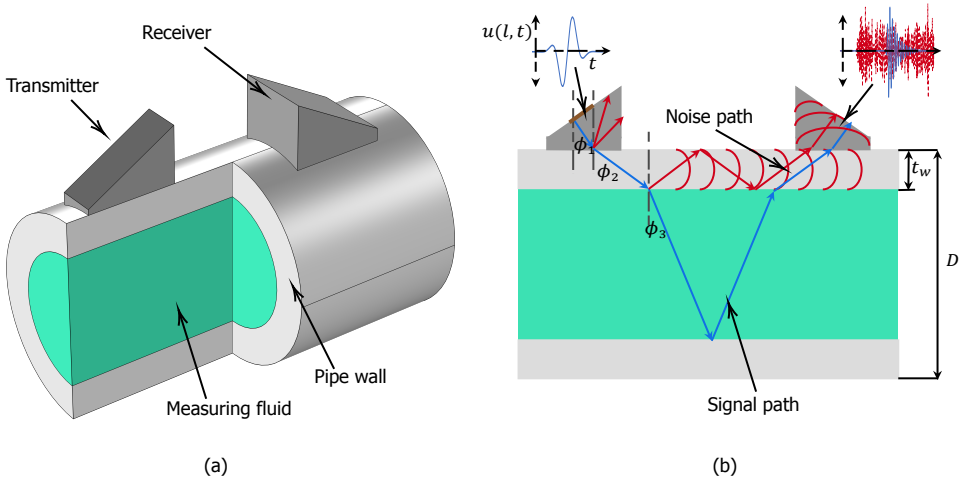

Figure 6.2: Schematic of the clamp-on system. (a) 3D view where transmitting and receiving wedges, the pipe wall, and the internal fluid are marked with arrows. (b) 2D view of the center plane with different signal and noise paths, refraction angles, pipe diameter D, and wall thickness t_w. Blue arrows represent the required signal path, whereas red arrows and curves constitute noise paths. $\boldsymbol{l}$ represents the location on the wedge where the input displacement $\boldsymbol{u}$ is applied (marked in (b)). Input displacement's time response $\boldsymbol{u}(\boldsymbol{l},t)$ is shown above the left wedge, while a schematic of the output displacement (signal and noise) is displayed above the right wedge.

Figure 6.2(b) shows the 2D sectional view (through the center of the pipe along its length) of the clamp-on UF, where signal and noise paths and various angles are marked. Commonly used clamp-on UF has a target central frequency of 1 MHz, which we select for the input pulse. Schematics of an input signal and the resulting output pulse that includes both the signal via the fluid and the noise are also illustrated in the figure. During the operation of the clamp-on UF, the input electric signal is converted to an ultrasound pulse by piezoceramic elements (not shown in the figure) that are attached to wedges. This ultrasound signal generates a P

wave in the transmitting wedge, which then travels to the wedge-pipe wall interface, where part of it reflects back to the wedge while another part transmits to the pipe wall. This transmitted signal then travels through the pipe wall-fluid interface and, similarly to the previous case, experiences reflection and refraction; thus, part of it enters the fluid domain. After traveling through the fluid, this signal enters the receiving wedge via the pipe wall, where the attached piezoceramic elements convert the acoustic wave to an electric signal to provide the travel time that aids in determining the flow rate. Noteworthy, the signal path is affected by the orientation of the wedges, operational frequency, and pipe diameter. Thus, the fluid signal can travel in an inclined line, a V-shape (used here), or a W-shape, depending on which the number of fluid-solid interfaces can vary.

The angles that determine the signal path, ϕ_1, ϕ_2, and ϕ_3, respectively, are the angle of incidence of the ultrasonic signal from the piezo, the refraction angle at the wedge-pipe wall interface, and the refraction angle to the fluid. These angles are calculated using ray acoustics since, at high frequencies, such as in the current situation, ray approximation can provide accurate predictions of refraction angles using Snell's law [40]:

$$\frac{\sin\phi_1}{c_1} = \frac{\sin\phi_2}{c_2}, \tag{6.1}$$

where c_1 and c_2, respectively, are the sound speeds of medium 1 (where the incoming wave comes from) and medium 2 (where the wave travels to). ϕ_1 is the incident angle in medium 1, while ϕ_2 is the refraction angle in medium 2. ϕ_1 is equivalent to the angle of the wedge, which is 30° (market standard for clamp-on UFs). From the material properties in Table 6.1 and using Equation (6.1), we get $\phi_2 = 52.4°$, and $\phi_3 = 22.2°$, respectively. Since the wedge-pipe wall is a solid-solid interface, an incoming P wave would refract a P wave and a shear (S) wave at this interface. This results in multiple signals in the measuring fluid and pipe wall, leading to difficulties in the measurement process. To avoid this complication, the wedge is designed such that ϕ_1 is always larger than the first critical angle so that P waves experience total internal reflection; therefore, only S waves are present in the pipe wall. Additionally, to ensure S waves are always present, ϕ_1 is always kept lower than the second critical angle (critical angle for S waves). The dimensions of the wedge (36 mm base and 22.5 mm height), and the pipe (diameter $D = 80$ mm and wall thickness $t = 4$ mm) are selected from a commercially used clamp-on UF (Krohne OPTISONIC 6300). These dimensions and the aforementioned angles can provide the signal path length, which determines the exact location of the receiving wedge for precise detection of the measuring signal. We call signals constituting this wave path the primary signals (marked using blue arrows in Figure 6.2(b)); we discuss below various other signals and their paths. Although we can obtain the primary signal path accurately by using ray tracing (via ray acoustics), the noise path is more complicated due to the presence of different types of waves (P, S, and Rayleigh), their interactions, and the presence of multiple wavefronts (planar and cylindrical) and boundaries. To investigate the influence of these aspects in the measurement process, we study wave propagation through different domains of the clamp-on system.

6.2.2. Wave propagation through the clamp-on flow meter

Wave propagation in the clamp-on device shown in Figure 6.2 is governed by elastic and acoustic wave equations. Since at 1 MHz constructing high-fidelity 3D wave propagation models is challenging because of the enormous computational cost associated, we analyze the entire system in 2D (as shown in Figure 6.2(b)). Thus, we use the 2D elastic wave equation to describe the wave propagation through the wedges and the pipe wall:

$$\rho_s \ddot{\boldsymbol{u}} = (\lambda_s + 2\mu_s)\Delta \boldsymbol{u} - \mu_s \nabla \times \nabla \times \boldsymbol{u}, \tag{6.2}$$

where, $\boldsymbol{u}(\boldsymbol{x}, t)$ and $\ddot{\boldsymbol{u}}(\boldsymbol{x}, t)$ are, respectively, the planar ($x - y$ plane) displacement and acceleration at the spatial coordinate $\boldsymbol{x}$ and time t. ρ_s represents the density, λ_s, and μ_s are the Lamé coefficients of the solid material, whereas Δ and $\nabla\times$, respectively, represent the Laplacian and curl vector operators. The stresses and strains within the solid domains are related by the following constitutive equation, $\boldsymbol{\sigma} = \boldsymbol{C} : \boldsymbol{\epsilon}$, where $\boldsymbol{\sigma}$ and $\boldsymbol{\epsilon}$ are, respectively, the Cauchy stress tensor, and the strain tensor (both 2$^{\text{nd}}$ order), while $\boldsymbol{C}$ is the 4$^{\text{th}}$ order elasticity tensor. Similarly, the wave propagation through the fluid domain can be represented using a 2D acoustic wave equation. As two wave fields (pressure and velocity) are present in the fluid domain, we can use either to represent wave propagation:

$$\Delta p = \rho_f \beta \ddot{p}, \qquad \Delta \boldsymbol{v} = \rho_f \beta \ddot{\boldsymbol{v}}, \tag{6.3}$$

where $p(\boldsymbol{x}, t)$ and $\boldsymbol{v}(\boldsymbol{x}, t)$, respectively, represent the pressure and velocity fields, while β is the compressibility of the fluid and ρ_f its density. We use interface conditions to connect different domains. The wedge-pipe wall interface is defined using a solid-solid contact pair, which dictates that the displacements and tractions across the interface should be the same for both regions:

$$\boldsymbol{u}_1 = \boldsymbol{u}_2, \qquad \boldsymbol{\sigma}_1 \cdot \boldsymbol{n}_1 = \boldsymbol{\sigma}_2 \cdot \boldsymbol{n}_2, \tag{6.4}$$

where 1 and 2, respectively, are the solid region 1 and region 2 in contact, and $\boldsymbol{n}$ is the unit outward normal vector along the interface. Coupling the pipe-fluid interface is more complicated since the field variables are different in both domains. We couple elastic and acoustic wave equations using a kinematic interface condition that ensures the continuity of normal components of the velocity along the interface as follows:

$$\boldsymbol{n} \cdot \nabla p = -\rho_s \boldsymbol{n} \cdot \ddot{\boldsymbol{u}}, \tag{6.5}$$

where ∇ is the gradient operator. Additionally, we need a dynamic interface condition to ensure the continuity of the traction along the interface:

$$-p\boldsymbol{n} = \mu_s \frac{\partial \boldsymbol{u}}{\partial \boldsymbol{n}} + (\lambda_s + \mu_s)(\nabla \cdot \boldsymbol{u})\boldsymbol{n}. \tag{6.6}$$

The details of these interface conditions can be found in [41]. We still require boundary conditions (BCs) for the wave propagation analysis. We supply a Dirichlet BC (prescribed displacement) along the boundary of the transmitting wedge where

the piezo is attached (marked using a brown-thick solid line in the left wedge of Figure 6.2(b)) while keeping the remaining outer boundaries traction free (homogeneous Neumann BC). The former BC takes the form

$$\boldsymbol{u}(\boldsymbol{l},t) = \bar{\boldsymbol{u}}g(t), \quad \text{applied at} \quad \underline{x} = \underline{l}, \tag{6.7}$$

where $\bar{\boldsymbol{u}}$ is the constant displacement amplitude that is multiplied by the function $g(t)$, which determines the time response. We use a sinusoidal pulse to represent $g(t)$ (the function $\boldsymbol{u}(\boldsymbol{l},t)$ is shown in Figure 6.2(b) above the left wedge). The input signal in the frequency domain is a Gaussian pulse having a central frequency of 1 MHz with a −6 dB bandwidth of 1 MHz (the explanation of the frequency-domain pulse is provided in the Section 0.1 of the supplementary material). By using the wave equations (6.2) and (6.3), interface conditions (6.4), (6.5), and (6.6), and the boundary condition (6.7), we have everything to set up the numerical analyses required to obtain information about various traveling waves in the clamp-on flowmeter.

Wave propagation analysis using DG FEM

We select DG FEM to analyze the wave propagation since this approach is suitable for arbitrary time-dependent sources and fields. The method is adequate for modeling elastic and acoustic wave propagation over large distances relative to the wavelength, such as in the present case, where the signal path length is 220 mm, while the smallest wavelength is 0.8 mm (signal wavelength of 1.5 MHz (highest signal frequency) in the PSU wedge.) The Comsol implementation uses a time-explicit solver and is memory efficient as compared to standard FEM [42]. Additionally, DG FEM allows non-conformal mapping along interfaces. In other words, we can mesh different sections of the domains with dissimilar mesh densities with non-matching interfaces, which is particularly beneficial since the minimum element sizes vary across different domains. The polynomials used for interpolation in DG FEM are also higher order (4^{th} to 6^{th} order), resulting in smaller models (i.e., fewer degrees of freedom as compared to standard FE models).

The DG FEM method solves the elastic wave equation in velocity-strain formulation rather than the standard displacement field described in Equation (6.2). Thus, to obtain the displacement field, we have to integrate the velocity field with respect to time. In DG FEM, the governing equations for elastic wave propagation in the absence of body forces (equivalent to Equation (6.2)) take the form

$$\begin{aligned} \rho_s \frac{\partial \boldsymbol{v_s}}{\partial t} - \nabla \cdot \boldsymbol{\sigma} &= 0, \\ \frac{\partial \boldsymbol{\epsilon}}{\partial t} - \frac{1}{2}\left[\nabla \boldsymbol{v_s} + (\nabla \boldsymbol{v_s})^{\mathsf{T}}\right] &= 0, \end{aligned} \tag{6.8}$$

where $\boldsymbol{v_s}$ is the particle velocity. In the fluid domain, linearized Euler equations (continuity and momentum equations) are solved, where the dependent variables are the fluid pressure and the particle velocity (also called acoustic velocity perturbation). The acoustic wave equation in the absence of body forces takes the

form

$$\frac{1}{\rho_f c_f^2}\frac{\partial p_t}{\partial t} + \nabla \cdot \boldsymbol{v_f} = 0,$$
$$\rho_f \frac{\partial \boldsymbol{v_f}}{\partial t} + \nabla \cdot (p_t \boldsymbol{I}) = 0, \tag{6.9}$$

where p_t is the total acoustic pressure, $\boldsymbol{v_f}$ is the total acoustic velocity, c_f is the speed of sound in the fluid, and $\boldsymbol{I}$ is the identity matrix. The interface conditions are similar to Equations (6.4) –(6.6) (continuity in displacement, velocity, and normal stresses across interfaces), while the boundary condition is also similar to Equation (6.7), where the displacement $\boldsymbol{u}$ is replaced by the velocity $\boldsymbol{v_s}$, i.e., $\boldsymbol{v_s}(\boldsymbol{l}, t) = \bar{\boldsymbol{v}}_s g(t)$.

Using DG FEM, we perform time-dependent analyses on the clamp-on system geometry shown in Figure 6.2(b) to identify different wave profiles. The wave interactions in the complete clamp-on system are very complex, so it is difficult to distinguish different types of waves and their interactions throughout the domain. Thus, we characterize these waves by segmenting the clamp-on geometry into different sections, such as wedge-pipe wall and pipe wall-fluid portions. Additionally, the pipe wall is a thin region compared to the wedge and the water domains in contact, which makes it challenging to visualize the wavefield in the pipe wall. Thus, we modify the geometry (only for identifying the wavefields) as shown in Figure 6.3(a), where the pipe wall dimensions are comparable to the wedge (width of 36 mm and height of 22.5 mm). We apply Dirichlet BC on the slant face of the wedge along the brown dashed line as shown in the same figure (similar to Figure 6.2(b)). Since the incident pulse is a P wave, we prescribe the velocity normal to the edge and perform the time-dependent analysis. We select the time step as $t_s = T/15$, where $T = 1/f$ is the time period of the input signal ($f = 1$ MHz), while we set the total simulation time $20 \times T$. Figure 6.3(a) shows the velocity profile of the wedge-pipe wall system at approximately $t = 12 \times T$, where we can see the reflected and transmitted pulses with plane wavefronts and additional waves with circular wavefronts.

Similarly, we conduct the time-dependent analysis of the pipe wall-fluid system, where the same time step ($T/15$) is used, while the total simulation time is modified to $15 \times T$ to reduce reflections from free edges. As in the case of the wedge-pipe wall system, we modify the pipe wall-fluid system's geometry for better visualization of the waves present (refer to Figure 6.3(d)). Here both the solid and fluid domains are 50 mm wide, while the fluid region is 30 mm high, whereas the pipe wall has a 31.3 mm height. Additionally, the edge of the pipe wall where the incoming signal comes from (left edge in Figure 6.3(d)) is also modified to match the angle of the incoming S wave (52.4°). Then we prescribe the Dirichlet BC along the brown dashed line, where the direction of the velocity is parallel to the edge (to match the behavior of the S wave). The resulting velocity profile shown in Figure 6.3(d) displays both the S wave in the pipe wall (reflected from the pipe wall-fluid interface) and the P wave transmitted to the fluid. Using these two velocity profiles, we can measure the reflection and transmission angles of the wedge-pipe wall and pipe wall-fluid interfaces, which can be compared against the theoretical predictions (angles ϕ_1, ϕ_2, and ϕ_3 discussed in Section 6.2.1).

6.2.3. Comparison between ray tracing and DG FEM

To verify the accuracy of the DG FEM models in predicting the wave propagation behavior of the clamp-on UF, the propagating angles are compared with theoretical (ray tracing) predictions. These DG FEM models also allow us to investigate the presence of additional waves in the clamp-on UF, which is not possible via ray tracing. Since the time-domain analysis provides us with a resultant field (velocity in the solid domain and velocity/pressure in the fluid region), it would be insightful to discriminate the wave behavior into S and P waves. To that end, we use a wavefield decomposition method.

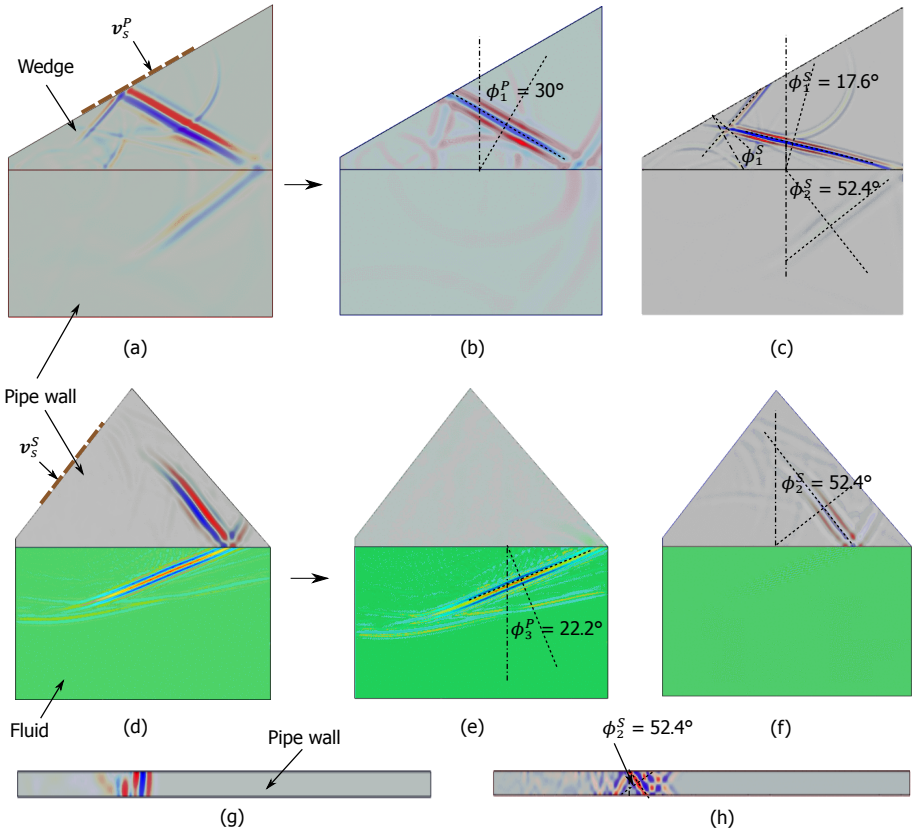

Figure 6.3: Decomposition of the wave field into P and S waves. (a) and (d) are, respectively, velocity fields of the wedge-pipe wall and pipe wall-fluid interfaces. The former is a solid-solid interface, while the latter is a solid-fluid interface where the incident prescribed velocity BCs (v_s^P and v_s^S) are marked using brown dashed lines. (b) and (e) are the corresponding P wavefields, where ϕ_1^P represents the angle of reflection of the incident P wave from the interface and ϕ_3^P is the transmission angle to the fluid. (c) and (f) are S wavefields of (a) and (d), respectively, where ϕ_1^S and ϕ_2^S are the reflected S wave angle to the wedge and the transmitted S wave angle to the pipe wall. ϕ_1^S marked close to the slant face of the wedge is the secondary reflected S wave due to the reflected P wave. (g) and (h), respectively, represent the P and S wavefield of the pipe wall for the entire simulation (150 cycles) where ϕ_2^S is the same as in (f) and (c). As shown in (g), no specific angles are present for P waves in the pipe wall.

Wavefield decomposition

We perform the wavefield decomposition whereby the resultant velocity field is decomposed into a scalar (for P waves) and a vector (for S waves) field. This decomposition is carried out by wave-type separation using dilation and rotation calculations, where the wavefield is represented as a combination of irrotational (curl-free) and solenoidal (divergence-free) fields [43]. Although there are other methods, such as Helmholtz decomposition [44], which preserve the amplitude and dimension of the field variables, they are more complicated to implement. As spatial derivatives are used in the process, the separated field contains one less spatial dimension than the original one. In other words, a velocity field with the dimension m/s transforms to a field with a dimension of 1/s. However, we are interested only in the different types of waves, their propagation angles, and their wavefronts' shapes, and not in the exact amplitude of the waves; a qualitative analysis such as the wave-type separation is sufficient.

For the separation of fields, we consider a velocity field $\boldsymbol{v}(\boldsymbol{x}, t) \in \mathbb{R}^2$, where $\boldsymbol{v}$ can be written as:

$$\boldsymbol{v} = -\nabla\psi + \nabla \times \boldsymbol{A}, \tag{6.10}$$

where ψ is the scalar potential and $\boldsymbol{A}$ is the vector potential. Since P waves are irrotational, the curl of $\boldsymbol{v}$ removes them and produces only S waves. Similarly, S waves are solenoidal, and the divergence of $\boldsymbol{v}$ provides only P waves. We apply wave-type separation to all segments of the clamp-on system, as described next.

Wedge-pipe wall interface

The first section of the clamp-on UF that we compare (between ray tracing and DG FEM) is the wedge-pipe wall interface (transmitter side) – left wedge from Figure 6.2(b), where the plane incident P wave interacts with the solid-solid interface to produce a transmitted P wave, and two reflected (P and S) waves. From the resultant wavefield (Figure 6.3(a)), it is not instantly apparent that S waves are also reflected, which can be clearly visualized in the decomposed field (see Figure 6.3(c)). In the separated fields (Figures 6.3(b) and 6.3(c)), we have also marked angles of different plane waves along with their polarization. The reflected P wave travels back to the wedge at the incident angle ($\phi_1^P = \phi_1 = 30°$), while the reflected S wave is at $\phi_1^S = 17.6°$. The S wave transmitting to the pipe wall is marked in Figure 6.3(c) as $\phi_2^S = \phi_2 = 52.4°$. Since ϕ_1 is greater than the first critical angle, we do not expect any P waves in the pipe wall. Figure 6.3(b) shows that, indeed there are no plane P waves traveling through the pipe wall. All the aforementioned angles (ϕ_1^P, ϕ_1^S, ϕ_2^S) are consistent with Snell's law predictions.

Figures 6.3(a)–(c) also show additional waves that ray tracing could not predict because of its inherent limitations (plane wavefront in a semi-infinite domain). For instance, when the incident angle is larger than the critical angle, waves do not propagate through the second medium according to the ray approximation. However, we can see in Figure 6.3(b) an evanescent P wave traveling along the wedge-pipe wall interface that enters the pipe wall with a cylindrical wavefront. Additionally, the reflected P wave proceeds towards the free surface of the wedge, which then reflects back into the wedge, resulting in several P waves with cylindrical wavefronts.

Similarly, many S waves with cylindrical wavefronts are also present, as can be seen in Figure 6.3(c). These are generated due to the point-source nature of the edges of the plane wavefront. In addition, the P waves with the cylindrical wavefront that are reflected from the interface towards the slant edge of the wedge reflect to form another S wave with a plane wavefront. This new plane S wave is also at ϕ_1^S angle with the normal to the slant edge, which travels to the wedge-pipe wall interface at an angle $2 \times \phi_1^S$. All the aforementioned signals and noise of both P and S type travel to the pipe wall, and some portions of their energy enter the measuring fluid.

Pipe wall-fluid interface

The next section of the clamp-on system is the pipe wall-fluid interface, which is a solid-fluid interface and has a more complicated wave propagation behavior than the solid-solid interface. This is because waves can travel through solid, fluid, and their interface. The resultant velocity field, along with its decomposition (in P and S waves), are provided in Figures 6.3(d)–(f). At the pipe wall-fluid interface, the incoming primary S wave (at $\phi_2^S = 52.4°$) generates the required P wave in the fluid (at $\phi_3^P = 22.2°$) that has a plane wavefront as marked in Figure 6.3(e). This S wave is also reflected through the wall to become the first noise signal that also has a plane wavefront (except for the edges with circular wavefront) as shown in Figure 6.3(f)).

Similar to the previous section, we can observe several S waves with cylindrical wavefronts in the pipe wall that transmit energy to the fluid at different intervals. Also, noise signals are present in the fluid domain (P-type) at different angles generated due to the point source nature of the wavefront's edges. Noteworthy, the different noise waves entering from the wedge-pipe wall section are not shown here since prescribing all those disturbances as BCs is nearly impossible. However, all these waves are present in the complete clamp-on UF simulation performed for the actual geometry (Figure 6.2(b).)

Snapshots of P and S waves in the pipe wall from a complete clamp-on system simulation are, respectively, shown in Figures 6.3(g) and 6.3(h). The pipe wall's length is selected as 140 mm and the total simulation time as $t_S = 150 \times T$. We used the same time step ($T/15$) as in previous simulations for the clamp-on model. As shown in Figure 6.3(h), the primary S wave travels through the pipe wall with a planar wavefront at an angle ϕ_2^S, while some noise S waves travel without any specific angle. All P waves propagate with a cylindrical wavefront (the small lateral dimension of the pipe wall makes it look like a flat wavefront), as shown in Figure 6.3(g). The superposition of the P and S wavefields provides the total wavefield in the pipe wall, which looks similar to the schematic representation of the wavefield in the pipe wall region of Figure 6.2(b). All the animations (traveling waves) corresponding to Figure 6.3(a) – 6.3(h) are provided in the supplementary material, Section 0.2. The complete simulation of the clamp-on UF also shows that noise signals (P and S) are present throughout the simulation time, which must be removed to distinguish the required signal from the fluid. To that end, we need to understand all waves in the clamp-on UF and categorize them based on their wavefront shape and behavior, discussed in the next section.

6.2.4. Types of waves present in the clamp-on system: Ideal *vs.* non-ideal waves

We have seen previously in Figure 6.3 that P and S waves are present in the wedge, pipe wall, and their interface, while the fluid contains only P waves. We have also observed that some of these waves have planar wavefronts while others possess cylindrical wavefronts, so we categorize them according to their behavior and origin. The waves with planar wavefronts that propagate with the angles predicted by Snell's law (ray acoustics), such as primary P and S waves in the wedge, are *ideal waves*: their travel time and direction can be calculated straightforwardly (for a pipe with a static fluid). However, for Snell's law to be completely valid, the media at either side of the interface must be semi-infinite, or the wavelength should be very small compared to the characteristic length. Since none of the domains (wedge, pipe wall, and water) are semi-infinite, there will always be portions of the wave energy that do not follow Snell's law, such as the curvatures at the ends of the plane wavefronts. These waves with cylindrical wavefronts are generated due to the point-source nature of the source and interactions of oblique waves with multiple interfaces; we call them *non-ideal waves*. For instance, the secondary P wave with the cylindrical wavefront in the wedge is a non-ideal wave with no specific direction of propagation (see Figure 6.3(b)). These non-ideal waves are present predominantly in the pipe wall region, which is a thin section with relatively high impedance where the incoming wavelength is comparable to the wall thickness. This is further aggravated due to the presence of both solid-solid (wedge-pipe wall) and solid-fluid (pipe wall-fluid) interfaces. As non-ideal waves are present throughout the simulation, determining their arrival time or direction is cumbersome. Additionally, since these waves can interact with the ideal waves, they could produce more unpredictable disturbances in the measurement process.

Similarly to the wedge and pipe wall, the primary wave (working signal) in the fluid region is an ideal wave, as represented using blue arrows in Figure 6.2(b). Since the primary S wave reflected from the pipe wall-fluid interface travels through the pipe wall to reach the receiving wedge with a plane wavefront, it is also an ideal wave. Since the working signal has to travel through the pipe wall from the fluid, it also transforms into an S wave, which travels at the same angle ($\phi_2 = 52.4°$) as the primary S wave in the pipe wall (as represented using blue and red arrows in the receiving wedge in Figure 6.2(b)). Since these two ideal waves (working signal and primary S wave in the pipe wall) have the same incident angle, polarization, and frequency, it becomes difficult to distinguish them based on the aforementioned aspects. However, the reflected primary S wave has a higher wave speed (refer Table 6.1) and shorter travel distance than the working signal, so it reaches the receiver much earlier than the P wave from the fluid. Similar to the working signal, we can accurately determine the arrival time of this S wave for a clamp-on UF with a static fluid setting. However, this primary S wave can reflect back to the pipe wall from the receiver, which can take multiple paths traveling around the pipe wall, resulting in a "ringing" that adds more noise to the measurement. The non-ideal signals in the fluid are generated due to multiple interactions between the waves in the pipe wall and the fluid and have several wave paths. Since they also possess

the same frequencies as the working signal, it is difficult to distinguish them.

All signals (ideal and non-ideal, P and S) that reach the receiving piezo transducer are represented using a time series, where voltages (corresponding to the displacements) are recorded for a definite time period. Since we can predict the travel time of the working signal and primary noise signal (ideal S wave through the pipe wall), we can mark them in the time series and filter the latter by time-windowing. However, as the non-ideal waves are present throughout the time spectrum, we cannot filter them *a posteriori* by standard means, such as using frequency band filtering or time windowing. Additionally, as the working signal and noise signals are coming through the same interface, it is virtually impossible to apply conventional vibration isolation systems at the receiver to remove the noise, as it will affect both the working signal and noise equally. So, we need to develop a noise mitigation mechanism that can alleviate these non-ideal noise signals from the output time series to distinguish the working signal and improve the measurement accuracy. To that end, we need a filtering mechanism that can minimize the generation of noise signals and is sensitive to specific directions and frequencies that align with the working signal. In addition, both wedges should ensure optimal energy transfer and maintain the shape of the wavefront since a distorted wavefront will lose the plane wave nature and directionality and thus disturb the measurement and may not be detected by the receiver. Moreover, as the arrival time of the working signal is relevant in the clamp-on system, the filters should particularly attenuate noise close to the required signal in the time domain. We can potentially achieve these by using PnCs.

6.3. Phononic crystals for noise attenuation

Since PnCs have been used for wave manipulation (wave suppression, steering, focusing, and cloaking), we explore their capabilities in mitigating noise for the clamp-on UF. Figure 6.4(a) shows the schematic of a single phase 2D PnC's periodic unit cell (PUC) comprised of solid material, with its irreducible Brillouin zone (IBZ) $\Gamma - X - M - \Gamma - M'$ and lattice vectors $\boldsymbol{a}_i$, $i = \{1, 2\}$. The PUC is the repeating unit of the PnC, whereas the IBZ is the smallest section that can represent the Brillouin zone that is obtained by transforming the PUC from direct lattice (Bravais lattice) to the reciprocal lattice [45]. The wave propagation behavior of the PnC's PUC is characterized using a band structure as discussed next.

The band structure or dispersion relation [46] is the relation between the applied frequency and the wave vector $\boldsymbol{k}$ (whose amplitude is the reciprocal of the wavelength and whose direction is the direction of wave propagation [46]). The band structure can be used to reveal a complete or partial bandgap as described in Figure 6.4(b), which shows the schematic of a band structure. In this figure, different bands (curves) describe traveling waves, while the slopes of these bands capture their propagation speed. The teal-shaded region, where wavebands are absent, indicates a complete BG, where waves experience omnidirectional attenuation for all wave vector values. The gray-shaded regions in the same figure show PBGs, which do not span the entire IBZ. In other words, for the same frequency range, wavebands are present in the $M - \Gamma$ branch; thus, waves propagate for $\boldsymbol{k}$

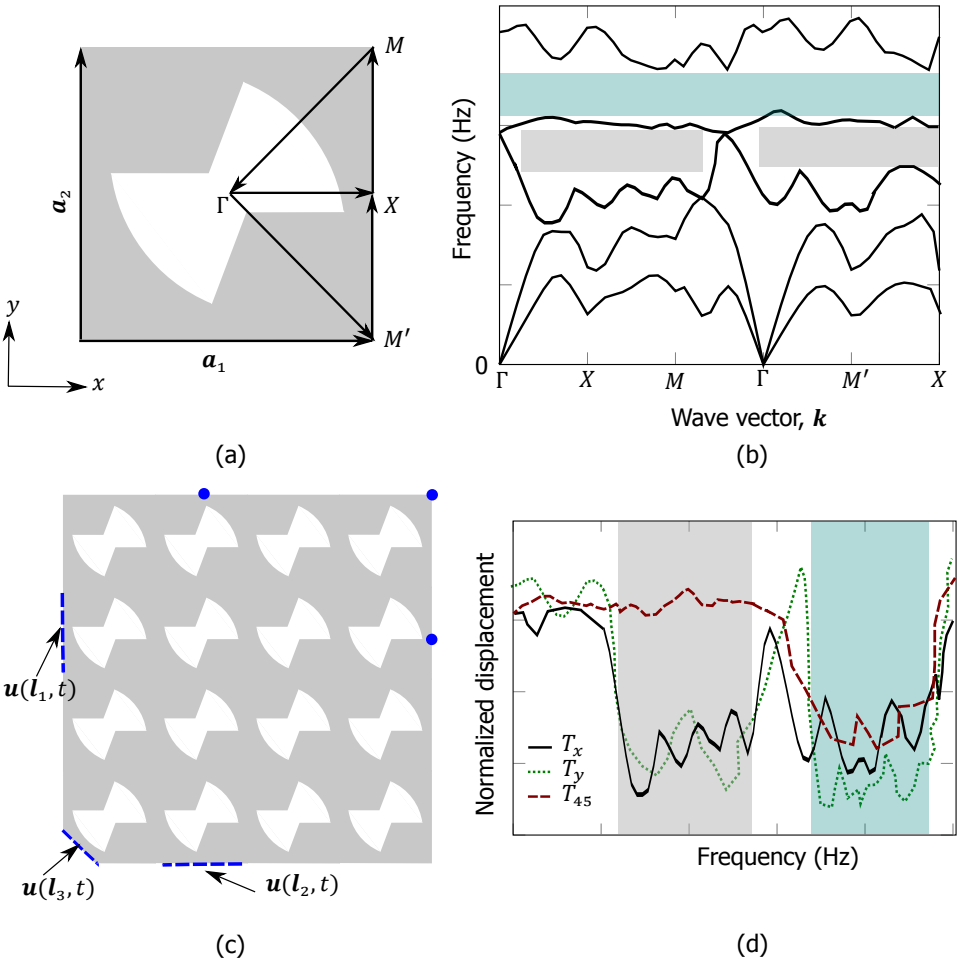

Figure 6.4: (a) Schematic of a PUC of the 2D PnC with its IBZ; (b) Band structure of the PUC, i.e., frequency as a function of the wave vector, where the teal-shaded region shows a complete BG and gray-shaded regions represent partial BGs. (c) waveguide composed of a 4X4 array of the PUC, where Dirichlet BCs are prescribed on the edges using blue dashed lines while output displacements are measured at blue dots. (d) transmissibility relations (along x, y, and 45°) represented as the ratio of the output displacement (measured at the opposite side of the prescribed displacement) to the prescribed input displacement as a function of the supplied frequency, where partial and complete BGs are shaded using gray and teal regions.

corresponding to 45° orientation while they are attenuated for $\boldsymbol{k}$ along x and y directions due to lack of wavebands in those IBZ branches. Since we want to design a structure that allows waves to propagate in certain directions while suppressing them in other directions, we explore possibilities of using devices possessing PBGs. PBGs are generally not present in a PUC with a complete symmetry (8-fold symmetry in 2D that has a triangular IBZ) because of the presence of symmetric modes;

thus, we need to introduce asymmetries in the band structure by tuning the PUC geometry. Hence, the PUC in Figure 6.4(a) has a 4-fold symmetry thereby possessing more IBZ branches (5 branches in total) than a completely symmetric PUC (IBZ with 3 branches). This leads to the increased computational cost for the band structure analysis. In the following, we discuss the different analyses used to design PnCs with PBGs that can act as directional wave filters for the clamp-on system.

6.3.1. Analysis of PnCs with PBGs

For the waveguiding application in clamp-on flowmeters, we consider a single phase 2D PnC composed solely of solid material, so we can use the same elastic wave Equation (6.2) to describe the wave propagation through the PnC. We still need to provide appropriate BCs to the boundary value problems (BVPs); we study two BCs as discussed next.

BVP1: Band structure analysis

The first analysis we perform is the band structure analysis obtained by conducting a set of eigenvalue analyses of the PUC after applying Bloch-Floquet periodic boundary conditions (BFPBCs) [47] and sweeping the wave vector through the vertices of the IBZ as shown in Figure 6.4(a). The BFPBC takes the form:

$$\boldsymbol{u}(\boldsymbol{x} + \boldsymbol{a}_i, t) = e^{i\boldsymbol{k}.\boldsymbol{a}_i}\boldsymbol{u}(\boldsymbol{x}, t), \tag{6.11}$$

where i is the imaginary number. The magnitudes of the lattice parameters (Figure 6.4(a)) are equal for the square PUC, i.e.,

$$\|\boldsymbol{a}_1\| = \|\boldsymbol{a}_2\| = a, \tag{6.12}$$

where a is the magnitude of the lattice vector in both directions. Although the band structure analysis reveals the presence of BGs and PBGs (frequency and wave vector ranges), it does not provide actual wave propagation behavior of the PnC structure comprised of a finite number of PUCs. This is because the band structure analysis assumes an infinite medium due to the application of BFPBCs. Thus, we conduct a transmissibility analysis over a finite PnC waveguide to obtain its performance.

BVP2: Transmissibility analysis

Transmissibility analysis or harmonic frequency sweep analysis [48] is the steady-state frequency response analysis of the finite PnC waveguide from Figure 6.4(c) after applying essential (or Dirichlet) BCs [49] for the range of applied frequencies. For a given frequency, the transmissibility relation provides the transmission amplitude of the traveling wave in the finite PnC waveguide. We perform three transmissibility analyses by providing Dirichlet BCs along three different directions, as shown in the figure, to investigate the wave propagation at 0°, 90°, and 45° orientations. These BCs are similar to the one defined in Equation (6.7), except that in PnC analyses, we assume a time-invariant harmonic response. The expressions take the form:

$$\boldsymbol{u}(\boldsymbol{l}_1, t) = \bar{u}_1 e^{i\omega t}\underline{e}_1 \quad \boldsymbol{u}(\boldsymbol{l}_2, t) = \bar{u}_2 e^{i\omega t}\underline{e}_2 \quad \boldsymbol{u}(\boldsymbol{l}_3, t) = \bar{u}_3 e^{i\omega t}\left(\underline{e}_1 + \underline{e}_2\right), \tag{6.13}$$

where $\bar{u}_1$, $\bar{u}_2$, and $\bar{u}_3$ are constant displacement amplitudes applied along $\boldsymbol{x} = \boldsymbol{l}_1$, $\boldsymbol{x} = \boldsymbol{l}_2$, and $\boldsymbol{x} = \boldsymbol{l}_3$, respectively, while ω is the applied angular frequency in rad/s. $\underline{e}_1$ and $\underline{e}_2$ are the unit vectors in x and y directions, respectively. The displacements in the three orientations are measured at the blue dots in the figure, opposite to the Dirichlet BC region, and are divided by incident displacement amplitudes to obtain transmissibilities T_x, T_y, and T_{45}. Since the waves are suppressed within the BG, the displacement amplitude there would be significantly lower than outside the BG. When the PnC waveguide possesses a PBG, depending upon the direction of the wave propagation (given by the Dirichlet BC as shown in Figure 6.4(c)), the transmissibility shows either an attenuation, propagation, or combination response thereof. Figure 6.4(d) shows the schematic of the transmissibility relations T_x, T_y, and T_{45}, where the complete (teal) and partial (gray) BGs from the band structure (Figure 6.4(b)) are also shown. We can observe that T_{45} experiences little attenuation within the PBG frequency range while T_x and T_y are immensely suppressed, corroborating the directional propagation property of the PnC waveguide. Additionally, since the transmissibility analysis provides the attenuation rate within the BG, we can select the number of PUCs in the PnC waveguide, depending on the required wave attenuation (more PUCs along the propagation direction lead to a higher reduction in amplitude). In addition, as the transmissibility response can be obtained for different locations, we can determine an adequate arrangement pattern of the PUCs within the PBG PnC waveguide for its optimal performance in the clamp-on flowmeter application.

6.3.2. Design of the partial BG PnC's periodic unit cell and waveguide

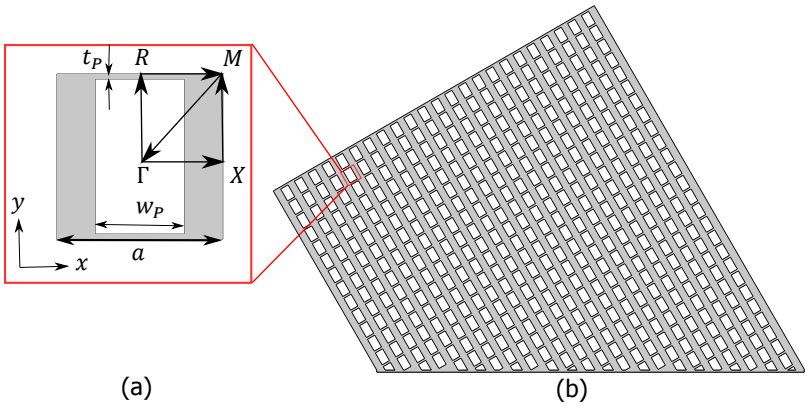

Figure 6.5: (a) 2D partial BG PUC with IBZ $\Gamma - X - M - \Gamma - R - M$, where a is its lattice vectors' length, and the two additional parameters w_P and t_P defining the geometry. (b) the design of the PnC wedge with 492 PBG PUCs, whose edges are also reshaped to reduce wave reflections to the measuring region.

Using the aforementioned analysis techniques, we design the PUC and the waveguide of the partial BG PnC. Since the BG is generated by Bragg scattering, the

magnitude of the lattice vector a is related to the applied frequency via the Bragg law of diffraction [21]. We select PSU (the wedge material) for the PnC as well, and we calculate a using PSU's wave speeds from Table 6.1 and the required frequency (1 MHz) as:

$$n\lambda = 2a\cos\theta, \qquad \lambda = c/f, \tag{6.14}$$

where n is an integer (generally $n = 1$), λ is the wavelength of the applied wave in the material, θ is the angle of incidence of the wave to the normal of the surface, and f is the applied frequency. Supplying the aforementioned values to Equation (6.14) provides us with $a = 0.75$ mm. Since we need to introduce asymmetries to generate PBGs, we employ an anisotropic material distribution in the PUC (as shown in Figure 6.5(a)), thereby increasing the stiffness and mass towards the y direction more than in the x direction. Further, we follow the displacement-mode-based analysis discussed in our previous work [50], whereby the desired band structure is achieved by modifying the relevant displacement modes bounding the wavebands via tuning the PUC geometry. Thus, we arrive at a PUC design possessing a partial BG in the x-direction in Figure 6.5(a). The dimensions of the PUC are also marked in the figure, where the thickness of the thinnest section is $t_P = 0.05$ mm, and the width of the void region is $w_P = 0.4$ mm. As apparent from the PUC geometry, the thickness of each layer in the y-direction is 3.5 times larger than that of the x-direction. Therefore, waves traveling in the y-direction experience less resistance than in the x-direction.

After designing the PUC with partial BGs in the required frequency range and direction, we develop the PnC waveguide in the form of a wedge similar to the wedge from the initial clamp-on flowmeter (Figure 6.2) to create the transmitter and receiver. Since the vertical edge of this wedge (a free surface) can reflect waves back to the measuring region, we reshape the wedge to induce a larger reflection angle, thereby guiding the noise signals away from the measuring domain. Similarly, the portion of the wedge opposite to the vertical edge is a small region in contact with the pipe wall and can also contribute more noise to the system; hence, it is also modified. Then, the PnCs are added to the modified wedge to transmit the required signal in the desired direction by rotating the PnC waveguide 30° (wedge angle) from the y-axis as shown in Figure 6.5(b). The resulting PnC wedge is a trapezium with 24 PUCs arrayed between its parallel edges (along the local x-axis), while the short and long sides have 14 and 27 PUCs, respectively. Thus, in total, the wedge has 492 partial BG PUCs. We use the same geometry for transmitting and receiving wedges to allow the reciprocity necessary for the transit-time flow measurement application. Further, we verify the performance of the PUC and waveguide by band structure and transmissibility calculations.

Band structure response of partial BG PnC

We obtain the band structure of the 2D square PUC in Figure 6.5(a) by using the $\omega(\boldsymbol{k})$ approach, whereby the frequencies are calculated as a function of $\boldsymbol{k}$ values sampled through the IBZ [51]. Recall that since BFPBCs are applied, the band structure analysis assumes an infinite material. We consider the square PUC with a

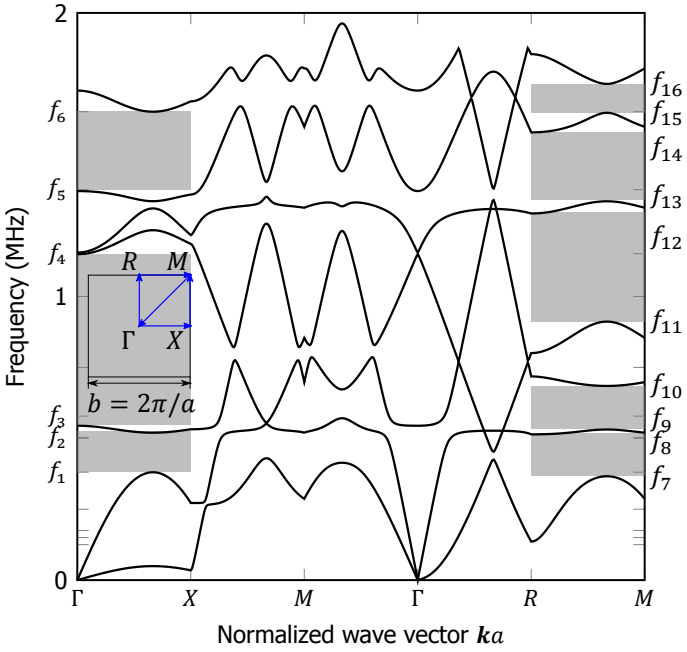

(a)

PBG (MHz)	Bands	IBZ branch
$[f_1, f_2]$ = [0.38,0.523]	2-3	$\Gamma - X$
$[f_3, f_4]$ = [0.548,1.15]	3-4	$\Gamma - X$
$[f_5, f_6]$ = [1.38,1.6]	6-7	$\Gamma - X$
$[f_7, f_8]$ = [0.366,0.517]	1-2	$R - M$
$[f_9, f_{10}]$ = [0.535,0.685]	2-3	$R - M$
$[f_{11}, f_{12}]$ = [0.9,1.3]	4-5	$R - M$
$[f_{13}, f_{14}]$ = [1.34,1.58]	5-6	$R - M$
$[f_{15}, f_{16}]$ = [1.65,1.75]	6-7	$R - M$

(b)

Figure 6.6: (a) Band structure of the 2D PnC PUC with the inset showing a square BZ of the dimension $b = 2\pi/a$ where the IBZ is marked with blue arrows and the shaded regions represent PBGs. (b) Table listing the partial BG frequency ranges, their enclosing wavebands, and the IBZ branches, which shows that BGs are only present in $\Gamma - X$ and $R - M$ branches.

4-fold symmetry; thus, the shape of the IBZ is a square with one diagonal (both PUC and the IBZ are shown in Figure 6.5(a)). Figure 6.6(a) shows the band structure of the PUC with shaded partial BGs. The inset in the figure shows the Brillouin zone and the IBZ of the PUC. The normalized wave vector shown in the x-axis is obtained after multiplying the wave vector $\boldsymbol{k}$ with the lattice length a. There are six wavebands present in the band structure between 0 and 2 MHz that span five

branches of the IBZ, and we use 500 wave vector steps (100 steps per branch) to represent these branches. The partial BGs bounding frequencies f_1 through f_{16} are also marked in the figure.

Figure 6.6(b) shows a tabular description of the partial BG frequency ranges, their bounding wavebands, and corresponding IBZ branches. It shows that partial BGs are only present in the $\Gamma - X$ and $R - M$ branches of the IBZ. For the remaining branches ($X-M$, $M-\Gamma$, and $\Gamma-R$), wavebands are present throughout the frequency range, implying the absence of BGs for waves traveling towards the y-direction and 45° orientation (both local to the PUC coordinate system). We can also observe that more BGs are present in the $R - M$ branch, and corresponding wavebands experience a larger spread compared to the $\Gamma - X$ branch. This is because the first IBZ branch contains only wave vectors in x-direction while the latter also possesses a non-zero y component; thus, more waves are allowed to propagate through the $R - M$ branch. Once we obtain the PBG frequency ranges and corresponding IBZ branches, we move towards the transmissibility analysis to attain the performance of the finite PnC waveguide.

Transmissibility response of the finite PnC waveguide

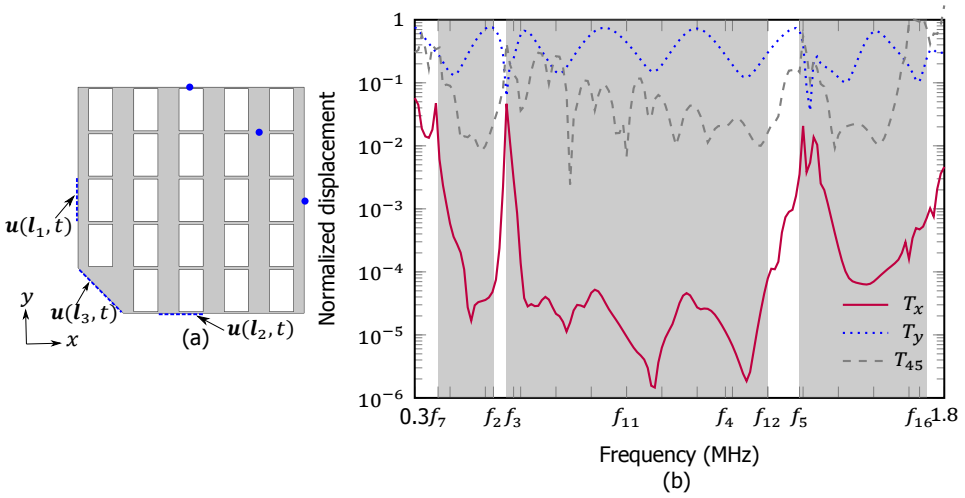

Figure 6.7: Transmissibility relation of the 2D PnC waveguide for different directions, where (a) the PnC waveguide geometry marked with Dirichlet BCs and probing points. (b) the transmissibility response: the normalized displacement (in log scale) as a function of the applied frequency in MHz, where BGs predicted by the band structure are shaded (marked with f_7, f_2, f_3, f_4, f_{11}, f_{12}, f_5, and f_{16}). Transmissibility in x-direction, T_x is represented using the solid red curve that has a low amplitude (average 10^{-5}), while the blue dotted curve shows the transmissibility in y-direction and its amplitude is close to 1. Transmissibility along 45°, T_{45} is shown using green dashed line and is between T_x and T_y.

Transmissibility analyses are performed for the PnC waveguide after applying Dirichlet BCs, as shown in Figure 6.7(a), where the waveguide is composed of a 5×5 PUC array. Noteworthy, the PUC at the left bottom of the waveguide is replaced by a 45° wedge to provide the essential BC $\boldsymbol{u}(\boldsymbol{l}_3, t)$ at 45°. The analyses are

conducted for the frequency range 300 kHz to 1.8 MHz (the range includes all PBGs) with a frequency step of 10 kHz and an input amplitude of 1 µm. A low-reflective BC is applied along the remaining edges of the waveguide to minimize reflections from free edges. As discussed in Section 6.3.1, output displacements are measured opposite to the prescribed BC (blue dots), and transmissibility responses are obtained towards x, y, and 45° directions and shown in Figure 6.7(b). Noteworthy, we positioned the probing point corresponding to the 45° to keep consistent the distance between the location of the BC to the probing point (distance of 3.75 mm) for all three transmissibility cases.

In Figure 6.7(b), T_x, T_y, and T_{45}, respectively, represent the transmissibility towards x, y, and 45° directions. The shaded regions in the plot show overlapped BG frequency ranges predicted by the band structure analysis along the $\Gamma - X$ and $R - M$ branches of the IBZ (no BGs are present in other IBZ branches). Within the BG frequency range, towards x-direction, waves experience an immense attenuation with an average attenuation rate of 10^{-5} (see red solid curve), while towards y-direction, the waveguide exhibits a smooth transmission similar to the wave propagation through a uniform structure such as a bar or a beam (see blue dotted curve); thus we can say that the waves traveling in y-direction experience negligible attenuation. Wave propagation towards 45° (green dashed curve) is close to T_y but does not exhibit the same response. This is because it is nearly impossible to excite the PnC waveguide at 45° without influencing modes in x and y directions. Thus we observe a moderate attenuation (average 2×10^{-2}) in the 45° direction.

Since we want to guide the input signal through a specific path via the wedge to the pipe wall while minimizing noise generation, we incorporate the PnC waveguide to the wedge as shown in Figure 6.5(b). As mentioned before, we orient the waveguide such that the vertical side of the PUC ($X - M$ branch of the IBZ) aligns with the desired P wave propagation angle of 30° to the wedge, thus allowing a complete transmission of the input signal. This orientation also ensures that waves traveling in other directions are attenuated, and only a small fraction enters the pipe wall. After performing the transmissibility analysis of the PnC waveguide and designing the wedge, we proceed to the analysis of the complete clamp-on UF.

6.3.3. Comparison of clamp-on system with and without partial band gap PnC

Noise levels in the pipe wall, the time response at the receiving wedge, and the frequency content of the receiving signal are compared between the standard clamp-on system and the one possessing partial BG PnC wedges to check the performance of the added PnC structure. In the 2D model of the clamp-on system, the standard wedges of the existing clamp-on geometry from Figure 6.2(b) are replaced with the PnC wedges from Figure 6.5(b). Wave propagation analysis through the updated clamp-on system is carried out similarly to the standard one (refer to Section 6.2.2).

Since the different media of the clamp-on flowmeter have different field variables, to compare the performances of the PnC-embedded clamp-on design with the standard one, we select the pressure profile of the complete system and displacement at the center of the receiving wedge's slant face as parameters. The

former provides information about the traveling waves, including the required signal and noise in the entire system, whereas the latter shows the influence of the PnC waveguide in the signal and noise amplitudes at the receiver.

Pressure profile and displacement comparison

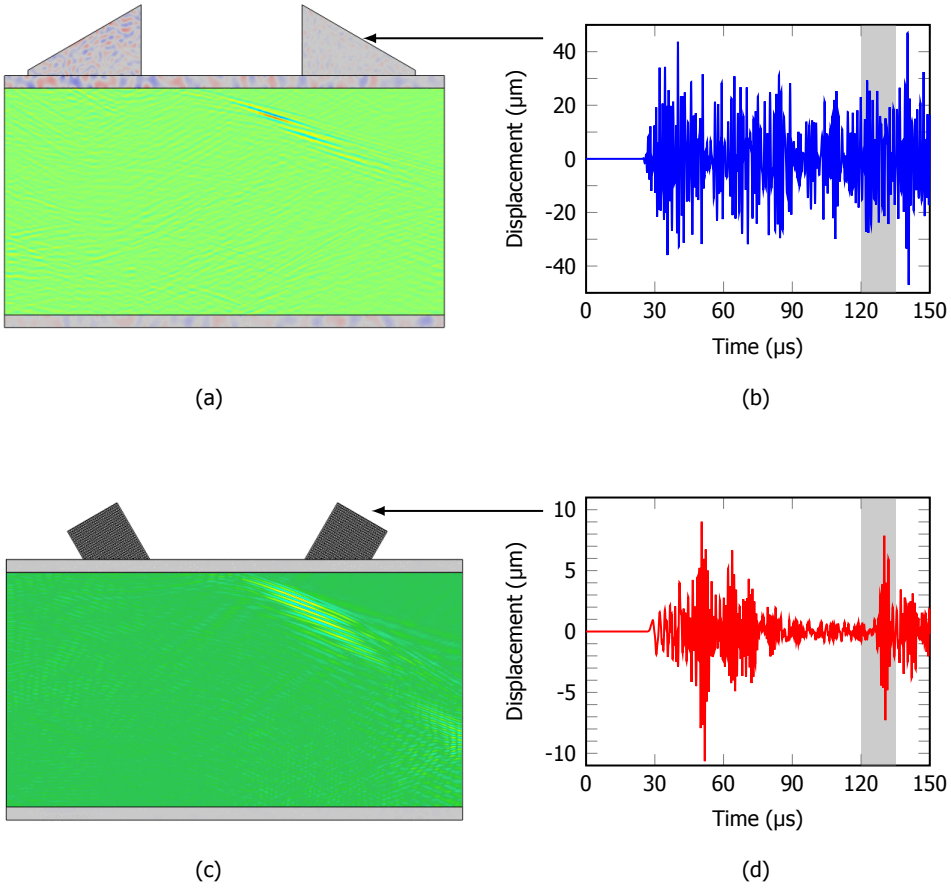

Figure 6.8: Comparison of pressure and displacement responses of a clamp-on system with a standard wedge (top) and partial BG PnC embedded wedge (bottom). (a) and (c) are snapshots of the pressure profile of the standard clamp-on system and the clamp-on system with PnC-embedded wedges, respectively, for the time instance when the signal from the fluid is about to impinge the pipe wall (t = 120 μs). (b) and (d) are the corresponding displacements (in μm) as functions of time (in μs) at the receiving wedges at the locations marked with arrows. Shaded regions in (b) and (d) show the time range corresponding to the arrival time of the signal from the fluid.

Figure 6.8 displays the comparison between the original (top) and PnC (bottom) versions. Figures 6.8(a) and (c) show snapshots of pressure profiles corresponding to the time (120 μs) when the resulting signal from the fluid is about to impinge the pipe wall. This time interval is particularly relevant because this is the time for which

we need to minimize the noise amplitude to get an accurate measurement. From pressure profiles, we observe a considerable amount of noise in the pipe wall of the clamp-on system with the standard wedge as compared to the PnC counterpart. In addition, the fluid region of the standard clamp-on design also exhibits higher wave scattering than the one with PnC-embedded wedges, implying that the noise signals from the pipe wall induce more noise in the fluid. Thus, we can state that the PnC waveguide is filtering most of the noise signals from the pipe wall and the fluid, consequently aiding in identifying the required signal at the receiver.

The displacement response on a point along the slant edge of the receiving wedge, as marked in Figures 6.8(a) and (c), is compared next. Since the independent variable in DG FEM analysis is velocity, we extract velocities in x and y directions, which are then integrated to obtain their corresponding displacements. Then, by using the component addition, the resultant displacement normal to the edge of the wedge is

$$u_{res} = \left(\int_0^{T_{\max}} v_x dt\right) \sin\left(\frac{\pi}{6}\right) + \left(\int_0^{T_{\max}} v_y dt\right) \cos\left(\frac{\pi}{6}\right), \tag{6.15}$$

where u_{res} is the magnitude of the resultant displacement normal to the slant edge of the receiving wedge, v_x and v_y, respectively, are the velocity components in x and y directions, $T_{\max}$ is the maximum time or total time of the simulation, and $\pi/6$ rad is the wedge angle. Figures 6.8(b) and (d), respectively, show displacements as functions of time measured at points on the receiving wedges of the standard clamp-on device and the PnC-embedded clamp-on device. These responses are calculated for 150 µs with a time step of 66.67 ns. The shaded regions in these figures represent the time interval when the required signal reaches the receiver. As apparent in the figures, although the maximum amplitude in the PnC-embedded system is four times lower than that of the standard system, the latter has displacement peaks throughout the simulation time, making it difficult to identify the fluid's required signal. On the contrary, we can clearly distinguish the required signal from the displacement plot of the PnC-embedded clamp-on system.

Comparison of signal-to-noise ratio

To further inspect the quality of the receiving signal, we use signal-to-noise ratio (SNR) [52], which for a time series is obtained by

$$\text{SNR(dB)} = 10 \log_{10}\left(\frac{P_s}{P_N}\right), \tag{6.16}$$

where P_s and P_N, respectively, are the power levels of the signal and noise pulses. We use the square of the displacement signal at the receiving wedge (refer to Figures 6.8(b) and (d)) to calculate P_s and P_N, where we select the peak corresponding to the fluid pulse's arrival time for signal and an adjacent peak for noise. For the system with standard wedges, we obtain the SNR to be 0.83 dB, whereas, for the system with PnC embedded wedges, the SNR turned out to be 20.4 dB, which is 19.6 dB higher than that of the standard wedge system. Thus, the quality of the receiving signal has drastically improved due to the addition of PnC structures.

Spectrogram comparison

To further check the influence of PnCs on the frequency spectrum of the output signal, we use a spectrogram, which visually represents the signal in time and frequency domains [53]. In this way, we can observe the signal strength at different frequencies and its variation over time. The time series is bundled into different overlapping time buckets, and their frequency responses are obtained via a short-time Fourier transform [53].

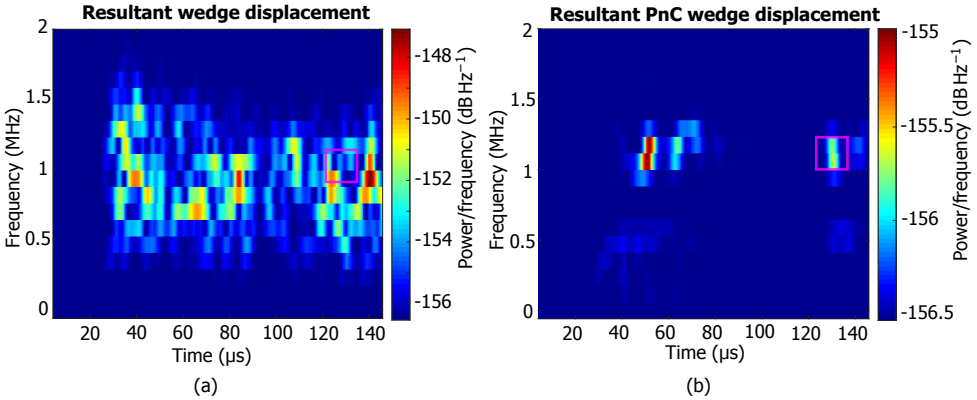

Figure 6.9: Spectrograms for the standard wedge (a) and the PnC-embedded wedge (b) corresponding to the displacement response from Figure 6.8. The abscissa is the total time in μs, the ordinate is the frequency in MHz, and the color code represents the power distribution of the signal per frequency shown using dB/Hz. Purple squares in both plots display the region of interest in time and frequency domains, where we can see the clamp-on system with PnC-embedded wedge is less noisy.

Figures 6.9(a) and 6.9(b), respectively, show spectrogram representations of the displacement time series from Figures 6.8(b) and (d). Here, the abscissa represents time (μs), the ordinate describes frequency (MHz), and the color spectrum shows the signal strength in terms of power per frequency (dB/Hz). The regions marked by purple squares in both plots show the region of interest in both time and frequency domains, i.e., f close to 1 MHz and t from 120 μs to 130 μs. Similarly to the displacement plots (Figures 6.8(b) and (d)), the signal strength is lower for the clamp-on system with PnCs as compared to the standard one. However, from Figure 6.9 it is apparent that the displacement signal from the standard wedge close to the required time (time of arrival of the signal through the fluid) is noisy in both time and frequency. In other words, the signal has many higher- and lower-order frequency components close to 1 MHz that span nearly the required time, making it difficult to detect the signal. Conversely, in the case of the clamp-on system with PnCs, the displacement signal close to the required time is relatively clean in both time and frequency domains, making it easier to identify the signal. Additionally, while using the clamp-on system with PnC-embedded wedges for flow measurement, we may be able to avoid using other filters, such as a frequency filter, since the receiving transducer already has less noise. However, one may need to improve this signal strength for better detection, which can be easily done using a low-noise

amplifier.

6.4. Summary and Conclusions

To alleviate crosstalk in clamp-on ultrasonic flowmeters, we proposed a novel wedge design comprised of phononic crystals possessing partial band gaps. Using band structure and transmissibility analyses, we performed the forward design of the PnC structures to match the required frequency and wave vector ranges. The performance of the clamp-on ultrasonic flowmeter with PnC-embedded wedges was compared against a standard clamp-on system using wave propagation analysis, and we observed an enormous reduction in noise levels in the pipe wall. We also showed that by using the new wedges, we could obtain an improvement of 19.6 dB in signal-to-noise ratio as compared to a standard wedge. We conclude that

- To remove acoustic/elastic noise from the clamp-on system, it is beneficial to understand the type (P or S wave) and behavior (ideal or non-ideal) of the signal, along with the frequency. This provides us additional information to target a particular signal type separately and eliminate them effectively;

- When there are multiple interfaces in the wave propagation system, waveguiding can effectively reduce the noise generated due to multiple reflections at various interfaces. By limiting these interactions through waveguiding in specific directions, we can prevent noises from entering the system, which can tamper with measurements;

- Current wave filtration methods rely on time by identifying the signal in time and slicing the required time window and frequency; they remove low and high-frequency signals with band-pass or other types of filters. Therefore, they could be less effective when the receiving signal and noise are of similar frequencies and arrival times. Thus, we proposed a new kind of wave filtration method based on directionality. We can filter the noise close to the required signal by using directional waveguides that allow only the required signal to pass through, although the noise has the same frequency and time of arrival.

Our investigation shows that partial band gap phononic crystals can considerably improve clamp-on ultrasonic flowmeters' performance by mitigating the noise signals traveling through the solid and fluid regions. The directional filter concept we developed using the partial BG PnC structures could be applied in various fields of non-destructive evaluation to obtain noise-free measurements. Additionally, this method could be used with the existing filtration (time and frequency) techniques to augment the accuracy of sensing devices further. Noteworthy, introducing partial band gap phononic crystals reduces the overall signal strength, and depending on the detection system, one may need to amplify the output signal. The future step is to realize such a partial band gap phononic wedge and validate experimentally in a clamp-on setting.

6.5. Appendix

6.5.1. Input pulse of the clamp-on ultrasonic flowmeter

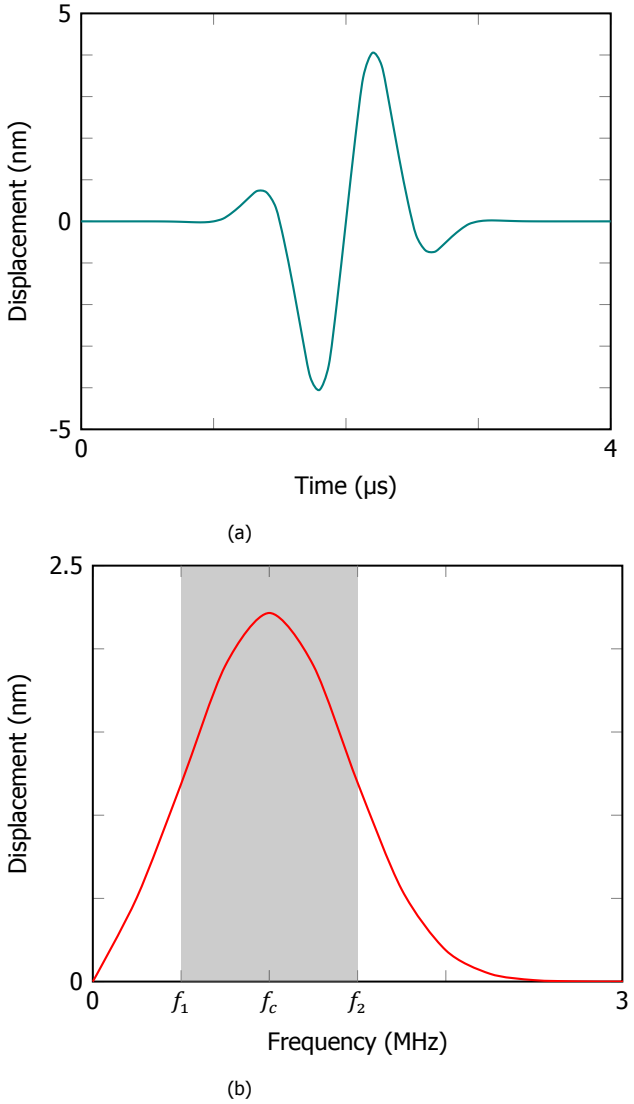

Figure 6.10: The input displacement signal is represented as functions of time (a) and frequency (b). The frequencies correspond to the peak displacement (f_c = 1 MHz), the lower (f_1 = 0.5 MHz) and upper (f_2 = 1.5 MHz) bounds of the bandwidth are also marked in (b).

Figures 6.10a and 6.10b, respectively, show the time- and frequency-domain description of the input signal from Figure 2 of the main document. The central frequency of the Gaussian pulse f_c = 1 MHz and the full-width half maximum band-

width bounded by $f_1 = 0.5$ MHz and $f_2 = 1.5$ MHz are also marked in Figure 6.10b.

6.5.2. Animations of traveling waves in the clamp-on system

All animations of the wedge-pipe wall, pipe wall-fluid, and the pipe wall of the clamp-on system discussed in Section 2.3 and Figure 3 of the main document are provided as GIF files along with this PDF. Additionally, the animations of the complete clamp-on system with and without partial BG PnC waveguides discussed in Section 3.3 and shown in Figure 8 are also included as GIF files. Table 6.2 connects the file names with the description. Within the description, the figures in the main document that correspond to these animations are also provided in parenthesis.

File name	Description
2D_solid_solid_resultant_velocity	Resultant velocity field of the wedge-pipe wall interface (Fig. 3(a))
2D_solid_solid_P_velocity	Pressure velocity field of the wedge-pipe wall interface (Fig. 3(b))
2D_solid_solid_S_velocity	Shear velocity field of the wedge-pipe wall interface (Fig. 3(c))
2D_solid_fluid_resultant_velocity	Resultant velocity field of the pipe wall-fluid interface (Fig. 3(d))
2D_solid_fluid_P_velocity	Pressure velocity field of the wedge-pipe wall interface (Fig. 3(e))
2D_solid_fluid_S_velocity	Shear velocity field of the wedge-pipe wall interface (Fig. 3(f))
2D_pipe_wall_clamp_on_P	Pressure velocity of the pipe wall of clamp-on system (Fig. 3(g))
2D_pipe_wall_clamp_on_S	Shear velocity of the pipe wall of clamp-on system (Fig. 3(h))
2D_pipe_clamp_on_standard_wedge	Resultant velocity of the clamp-on system with standard wedge (Fig. 8(a))
2D_pipe_clamp_on_PnC_wedge	Resultant velocity of the clamp-on system with PnC wedge (Fig. 8(c))

Table 6.2: List of animation files corresponding to the wave propagation through solid-solid, solid-fluid, and complete clamp-on systems.

Bibliography

[1] *Global flow meter market size report, 2021-2028*. 2020. URL: https://www.grandviewresearch.com/industry-analysis/flow-meters-market.

[2] Richard Smith et al. "A MEMS-Based Coriolis Mass Flow Sensor for Industrial Applications". In: *IEEE Transactions on Industrial Electronics* 56.4 (2009), pp. 1066–1071. DOI: 10.1109/TIE.2008.926703.

[3] Mahmoud Meribout et al. "Multiphase Flow Meters Targeting Oil & Gas Industries". In: *Measurement* 165 (2020), p. 108111. ISSN: 0263-2241. DOI: https://doi.org/10.1016/j.measurement.2020.108111. URL: https://shorturl.at/KauuH.

[4] M. Kupnik et al. "Adaptive Pulse Repetition Frequency Technique for an Ultrasonic Transit-Time Gas Flowmeter for Hot Pulsating Gases". In: *IEEE Sensors Journal* 6.4 (2006), pp. 906–915. DOI: 10.1109/JSEN.2006.876042.

[5] Yong Chen, Yiyong Huang, and Xiaoqian Chen. "Acoustic propagation in viscous fluid with uniform flow and a novel design methodology for ultrasonic flow meter". In: *Ultrasonics* 53.2 (2013), pp. 595–606. ISSN: 0041-624X. DOI: https://doi.org/10.1016/j.ultras.2012.10.005. URL: https://www.sciencedirect.com/science/article/pii/S0041624X12002016.

[6] H.-H. Eckstein et al. "Improvement of carotid blood flow after carotid endarterectomy Evaluation using intraoperative ultrasound flow measurement". In: *European Journal of Vascular and Endovascular Surgery* 25.2 (2003), pp. 168–174. ISSN: 1078-5884. DOI: https://doi.org/10.1053/ejvs.2002.1820. URL: https://www.sciencedirect.com/science/article/pii/S1078588402918204.

[7] R.C. Baker. *Flow Measurement Handbook*. Flow Measurement Handbook: Industrial Designs, Operating Principles, Performance, and Applications. Cambridge University Press, 2016. ISBN: 9781107045866. URL: https://books.google.nl/books?id=D4-5DAAAQBAJ.

[8] M.L Sanderson and H Yeung. "Guidelines for the use of ultrasonic non-invasive metering techniques". In: *Flow Measurement and Instrumentation* 13.4 (2002), pp. 125–142. ISSN: 0955-5986. DOI: https://doi.org/10.1016/S0955-5986(02)00043-2. URL: https://www.sciencedirect.com/science/article/pii/S0955598602000432.

[9] Furio Cascetta. "Application of a portable clamp-on ultrasonic flowmeter in the water industry". In: *Flow Measurement and Instrumentation* 5.3 (1994), pp. 191–194. ISSN: 0955-5986. DOI: https://doi.org/10.1016/0955-5986(94)90019-1. URL: https://www.sciencedirect.com/science/article/pii/0955598694900191.

[10] Americo Zuzunaga and Bob Maron. "A survey of non-invasive and semiinvasive flow meters for mining applications: Understanding and selecting the right technology for the application". In: *CiDRA Minerals Processing, Wallingford, USA* (2013).

[11] IA Viktrov. "Rayleigh and Lamb waves: physical theory and applications". In: *Chapter II* (1967).

[12] Kenichi TEZUKA et al. "Analysis of Ultrasound Propagation in High-Temperature Nuclear Reactor Feedwater to Investigate a Clamp-on Ultrasonic Pulse Doppler Flowmeter". In: *Journal of Nuclear Science and Technology* 45.8 (2008), pp. 752–762. DOI: 10.1080/18811248.2008.9711476. eprint: https://www.tandfonline.com/doi/pdf/10.1080/18811248.2008.9711476. URL: https://www.tandfonline.com/doi/abs/10.1080/18811248.2008.9711476.

[13] Chuangnan Wang et al. "Wedge design for high-temperature ultrasonic flow rate measurement". In: *Sensors and Actuators A: Physical* 298 (2019), p. 111585. ISSN: 0924-4247. DOI: https://doi.org/10.1016/j.sna.2019.111585. URL: https://www.sciencedirect.com/science/article/pii/S0924424719312622.

[14] Simon Haykin and KJ Ray Liu. *Handbook on array processing and sensor networks*. John Wiley & Sons, 2010.

[15] Jack Massaad et al. "Suppression of Lamb wave excitation via aperture control of a transducer array for ultrasonic clamp-on flow metering". In: *The Journal of the Acoustical Society of America* 147.4 (2020), pp. 2670–2681. DOI: 10.1121/10.0001135. eprint: https://doi.org/10.1121/10.0001135. URL: https://doi.org/10.1121/10.0001135.

[16] Jack Massaad et al. "Design and Proof-of-Concept of a Matrix Transducer Array for Clamp-On Ultrasonic Flow Measurements". In: *IEEE Transactions on Ultrasonics, Ferroelectrics, and Frequency Control* 69.8 (2022), pp. 2555–2568. DOI: 10.1109/TUFFC.2022.3186170.

[17] Jack Massaad et al. "Acoustic Design of a Transducer Array for Ultrasonic Clamp-on Flow Metering". In: *2019 IEEE International Ultrasonics Symposium (IUS)*. 2019, pp. 1133–1136. DOI: 10.1109/ULTSYM.2019.8925680.

[18] A. Bybi et al. "Reducing crosstalk in array structures by controlling the excitation voltage of individual elements: A feasibility study". In: *Ultrasonics* 53.6 (2013), pp. 1135–1140. ISSN: 0041-624X. DOI: https://doi.org/10.1016/j.ultras.2013.02.009. URL: https://www.sciencedirect.com/science/article/pii/S0041624X13000553.

[19] M. S. Kushwaha et al. "Acoustic band structure of periodic elastic composites". In: *Physical Review Letters* 71 (13 Sept. 1993), pp. 2022–2025. DOI: 10.1103/PhysRevLett.71.2022. URL: https://link.aps.org/doi/10.1103/PhysRevLett.71.2022.

[20] M. S. Kushwaha et al. "Theory of acoustic band structure of periodic elastic composites". In: *Phys. Rev. B* 49 (4 Jan. 1994), pp. 2313–2322. DOI: 10.1103/PhysRevB.49.2313. URL: https://link.aps.org/doi/10.1103/PhysRevB.49.2313.

[21] W. L. Bragg. "The Diffraction of Short Electromagnetic Waves by a Crystal". In: *Scientia* 23.45 (1929), p. 153.

[22] Matthew Reynolds and Stephen Daley. "An active viscoelastic metamaterial for isolation applications". In: *Smart Materials and Structures* 23.4 (2014), p. 045030.

[23] J Xu and J Tang. "Tunable prism based on piezoelectric metamaterial for acoustic beam steering". In: *Applied Physics Letters* 110.18 (2017), p. 181902.

[24] Shu Zhang, Chunguang Xia, and Nicholas Fang. "Broadband acoustic cloak for ultrasound waves". In: *Physical Review Letters* 106.2 (2011), p. 024301.

[25] Kyung Ho Sun et al. "Sound energy harvesting using a doubly coiled-up acoustic metamaterial cavity". In: *Smart Materials and Structures* 26.7 (2017), p. 075011.

[26] Choon Mahn Park et al. "Amplification of Acoustic Evanescent Waves Using Metamaterial Slabs". In: *Phys. Rev. Lett.* 107 (19 Nov. 2011), p. 194301. DOI: 10.1103/PhysRevLett.107.194301. URL: https://link.aps.org/doi/10.1103/PhysRevLett.107.194301.

[27] Gang Yong Song et al. "Broadband focusing acoustic lens based on fractal metamaterials". In: *Scientific reports* 6 (2016), p. 35929.

[28] Sabiju Valiya Valappil, Johannes F. L. Goosen, and Alejandro M. Aragón. "Phononic Crystals for Suppressing Crosstalk in Ultrasonic Flowmeters". In: *IEEE Transactions on Instrumentation and Measurement* 72 (2023), pp. 1–11. DOI: 10.1109/TIM.2023.3284960.

[29] Ralf Lucklum and Nikolay Mukhin. "Enhanced sensitivity of resonant liquid sensors by phononic crystals". In: *Journal of Applied Physics* 130.2 (2021), p. 024508. DOI: 10.1063/5.0046847. eprint: https://doi.org/10.1063/5.0046847. URL: https://doi.org/10.1063/5.0046847.

[30] Nikolay Mukhin et al. "Narrow Band Solid-Liquid Composite Arrangements: Alternative Solutions for Phononic Crystal-Based Liquid Sensors". In: *Sensors* 19.17 (2019). ISSN: 1424-8220. DOI: 10.3390/s19173743. URL: https://www.mdpi.com/1424-8220/19/17/3743.

[31] A. Oseev, M. Zubtsov, and R. Lucklum. "Octane Number Determination of Gasoline with a Phononic Crystal Sensor". In: *Procedia Engineering* 47 (2012). 26th European Conference on Solid-State Transducers, EUROSENSOR 2012, pp. 1382–1385. ISSN: 1877-7058. DOI: https://doi.org/10.1016/j.proeng.2012.09.414. URL: https://www.sciencedirect.com/science/article/pii/S1877705812044773.

[32] A. Oseev, M. Zubtsov, and R. Lucklum. "Gasoline properties determination with phononic crystal cavity sensor". In: *Sensors and Actuators B: Chemical* 189 (2013). Selected Papers from the 26th European Conference on Solid-State Transducers, pp. 208–212. ISSN: 0925-4005. DOI: https://doi.org/10.1016/j.snb.2013.03.072. URL: https://www.sciencedirect.com/science/article/pii/S0925400513003535.

[33] M. Miniaci et al. "Proof of Concept for an Ultrasensitive Technique to Detect and Localize Sources of Elastic Nonlinearity Using Phononic Crystals". In: *Phys. Rev. Lett.* 118 (21 May 2017), p. 214301. DOI: 10.1103/PhysRevLett.118.214301. URL: https://link.aps.org/doi/10.1103/PhysRevLett.118.214301.

[34] Elizabeth J. Smith and Kathryn H. Matlack. "Metal additively manufactured phononic materials as ultrasonic filters in nonlinear ultrasound measurements". In: *The Journal of the Acoustical Society of America* 149.6 (2021), pp. 3739–3750. DOI: 10.1121/10.0004995. eprint: https://doi.org/10.1121/10.0004995. URL: https://doi.org/10.1121/10.0004995.

[35] Geoffrey Roger Sherwood et al. "3D-printed phononic crystal waveguide transducers for nonlinear ultrasonic damage detection". In: *NDT & E International* 121 (2021), p. 102456. ISSN: 0963-8695. DOI: https://doi.org/10.1016/j.ndteint.2021.102456. URL: https://www.sciencedirect.com/science/article/pii/S0963869521000554.

[36] Menglong Liu et al. "Applications of a nanocomposite-inspired in-situ broadband ultrasonic sensor to acousto-ultrasonics-based passive and active structural health monitoring". In: *Ultrasonics* 78 (2017), pp. 166–174. ISSN: 0041-624X. DOI: https://doi.org/10.1016/j.ultras.2017.03.007. URL: https://www.sciencedirect.com/science/article/pii/S0041624X16302414.

[37] Minoo Kabir, Amir Mostavi, and Didem Ozevin. "Noise isolation with phononic crystals to enhance fatigue crack growth detection using acoustic emission". In: *Journal of Civil Structural Health Monitoring* 8.3 (July 2018), pp. 529–542.

[38] Fang Q. Hu, M.Y. Hussaini, and Patrick Rasetarinera. "An Analysis of the Discontinuous Galerkin Method for Wave Propagation Problems". In: *Journal of Computational Physics* 151.2 (1999), pp. 921–946. ISSN: 0021-9991. DOI: https://doi.org/10.1006/jcph.1999.6227. URL: https://www.sciencedirect.com/science/article/pii/S0021999199962277.

[39] J.B. Rose. "Preparation and properties of poly(arylene ether sulphones)". In: *Polymer* 15.7 (1974), pp. 456–465. ISSN: 0032-3861. DOI: https://doi.org/10.1016/0032-3861(74)90111-6. URL: https://rb.gy/nk9hz5.

[40] Daniel Royer and Eugene Dieulesaint. *Elastic waves in solids I: Free and guided propagation*. Springer Science & Business Media, 1999.

[41] Gang Bao, Yixian Gao, and Peijun Li. "Time-Domain Analysis of an Acoustic–Elastic Interaction Problem". In: *Archive for Rational Mechanics and Analysis* 229.2 (Aug. 2018), pp. 835–884. ISSN: 1432-0673. DOI: 10.1007/s00205-018-1228-2. URL: https://doi.org/10.1007/s00205-018-1228-2.

[42] COMSOL. "Acoustics Module User's Guide". In: *COMSOL Multiphysics* 6.16 (2022), pp. 354–370.

[43] J. Dellinger and J. Etgen. "Wave-field separation in two-dimensional anisotropic media". In: *GEOPHYSICS* 55.7 (1990), pp. 914–919. DOI: 10.1190/1.1442906. URL: https://doi.org/10.1190/1.1442906.

[44] Hejun Zhu. "Elastic wavefield separation based on the Helmholtz decomposition". In: *Geophysics* 82.2 (Feb. 2017), S173–S183. ISSN: 0016-8033. DOI: 10.1190/geo2016-0419.1. eprint: https://pubs.geoscienceworld.org/geophysics/article-pdf/82/2/S173/4052999/geo-2016-0419.1.pdf. URL: https://doi.org/10.1190/geo2016-0419.1.

[45] Charles Kittel and Paul McEuen. *Introduction to solid state physics*. John Wiley & Sons, 2018.

[46] Karl F Graff. *Wave motion in elastic solids*. Courier Corporation, 2012.

[47] Felix Bloch. "Quantum mechanics of electrons in crystal lattices". In: *Z. Phys* 52 (1928), pp. 555–600.

[48] István L Vér and Leo L Beranek. *Noise and vibration control engineering: principles and applications*. John Wiley & Sons, 2005.

[49] Thomas JR Hughes. *The finite element method: linear static and dynamic finite element analysis*. Courier Corporation, 2012.

[50] Sabiju Valiya Valappil, Alejandro M. Aragón, and Hans Goosen. "Phononic crystals' band gap manipulation via displacement modes". In: *Solid State Communications* 361 (2023), p. 115061. ISSN: 0038-1098. DOI: https://doi.org/10.1016/j.ssc.2022.115061. URL: https://www.sciencedirect.com/science/article/pii/S0038109822003854.

[51] L. D'Alessandro et al. "Modeling and experimental verification of an ultra-wide bandgap in 3D phononic crystal". In: *Applied Physics Letters* 109.22 (2016), p. 221907. DOI: 10.1063/1.4971290. eprint: https://doi.org/10.1063/1.4971290. URL: https://doi.org/10.1063/1.4971290.

[52] Don H Johnson. "Signal-to-noise ratio". In: *Scholarpedia* 1.12 (2006), p. 2088.

[53] Wenkai Lu and Fangyu Li. "Seismic spectral decomposition using deconvolutive short-time Fourier transform spectrogram". In: *GEOPHYSICS* 78.2 (2013), pp. V43–V51. DOI: 10.1190/geo2012-0125.1. eprint: https://doi.org/10.1190/geo2012-0125.1. URL: https://doi.org/10.1190/geo2012-0125.1.

7

A semi-analytical approach to characterize high-frequency 3D wave propagation through a clamp-on flowmeter

*Wave propagation analysis at high frequencies is quintessential for applications involving ultrasound waves such as in clamp-on ultrasonic flowmeters. However, it is extremely challenging to perform a 3D transient analysis of a clamp-on flowmeter using standard tools such as finite element analysis (FEA) due to the enormous computational cost associated. In this study, we separate the clamp-on flowmeter into different domains and analyze them separately. Wave propagation in the fluid domain is analyzed via FEA at low frequencies (*100 kHz*, 200 kHz, and* 500 kHz*) and using ray tracing at high frequencies (*1 MHz*). The behavior in the solid domain (wedges and pipe wall) is analytically characterized via geometric projection. All these individual analyses provide us with different scaling factors with which the waves in the respective domains scale when 3D effects are considered. The complete clamp-on system is then analyzed in 2D via the Discontinuous Galerkin (DG) finite element method to obtain the response at the receiver. This receiving signal is then scaled using the aforementioned scaling factors to accurately capture the wave propagation behavior of the clamp-on system in 3D. The output signal from the 2D analysis then becomes much clearer and we can easily identify the fluid signal, which would be nearly impossible otherwise.*

Parts of this chapter are to be submitted for publication.

7.1. Introduction

Ultrasound waves, because of their substantial power density, short wavelength, and non-invasive nature compared to electromagnetic waves, have been immensely applied in bio-imaging [1–3], flowrate measurement [4, 5], distance and velocity measurement [6, 7], temperature measurement [8], and non-destructive evaluation [9, 10], among others. The global ultrasound device market size was valued $9.3 billion in 2022 and expected to grow till $15.4 billion by 2032 [11]. To effectively design ultrasound devices for different applications, it is necessary to characterize their behavior. However, experiments are generally expensive and time-consuming; thus, several analytical and numerical methods have been proposed.

Analytical solutions, although computationally efficient, exist only for simplified geometries such as cylinders and spheres [12–14]. For more complicated systems, numerical methods such as the finite element method (FEM) [15] or boundary element method (BEM) [16] are used. The former solves the governing equations after discretizing the domain in a finite number of interconnected elements of simple (usually linear) behavior, whereas the latter transforms the equations to integral form and solves them over the boundary. Although resulting in a small system size due to discretizing only the boundary, BEM's implementation is complex and has fully dense asymmetric matrices, in contrast to FEM's sparse banded symmetric matrices. FEM is generally used to solve wave propagation in solids and fluids because of its versatility in discretizing complex geometries [17]. However, the computational cost increases with an increase in frequency to account for the spatial and temporal accuracy (as a rule of thumb eight linear finite elements are required per wavelength) [18]. BEM and FEM have also been combined to leverage their respective advantages in analyzing wave propagation through a fluid-filled cylindrical shell, where a coupled vibration analysis is performed [19].

The wave propagation analysis becomes particularly challenging when dealing with ultrasound devices such as clamp-on ultrasonic flowmeters operating at high frequencies (in MHz range) and in far-field (where characteristic length is much higher than the acoustic wavelength). This is because the total number of degrees of freedom (DOFs) becomes enormous due to the large domain compared to the mesh size. Additionally, the time step required for the evaluation becomes very small at high frequencies (at least ten steps per period), leading to vast computational demands. In addition, in the case of time-harmonic wave solutions, the accuracy of the numerical solution drastically decreases with the increase in wave number [20, 21]. For transient wave propagation, such as the case of the clamp-on flowmeter, the solution can exhibit spurious oscillations due to Gibb's phenomenon (the oscillatory behavior of the Fourier series of a piecewise continuously differentiable periodic function around a jump discontinuity) [22], and dispersion and dissipation errors due to numerical period elongation and amplitude decay [23]. When high-frequency waves travel long distances the cumulative error becomes large and the inaccuracy in the numerical solution rapidly increases [24]. Additionally, the computed wave velocities may depend on the propagation direction due to the mesh, which causes waveform distortions, leading the model to behave anisotropically even in an isotropic medium.

Several approaches have been proposed to address the aforementioned challenges of FEM. In particular, the spectral method, which uses harmonic functions in the solution space, can obtain numerical solutions very close to exact solutions [25]. However, the spectral method is difficult to implement for complex geometries since the method uses global basis functions. An extension of the spectral method was proposed where high-order Lagrangian-based finite elements along with a special integration scheme (Gauss-Lobatto-Legendre) were used. The method has low numerical dispersion compared to standard FEM [26] and is effective in explicit time integration. However, it still lacks the means to model complex geometries, which was addressed in parts by combining the spectral method with FEM—spectral finite element method [27, 28].

A second method to overcome the challenges of FEM is by means of the higher-order Discontinuous Galerkin (DG) method, which leads to block-diagonal mass matrices [29, 30]. The higher order is essential here since the wave equations produce parasitic waves, which should be suppressed by using penalty terms that are dissipative. Thus, DG possess low numerical dissipation and dispersion [31]. Moreover, DG is also capable of avoiding the Runge phenomenon—oscillations at the edges of an interval when using higher-order polynomial approximations along equispaced points [32]. DG also facilitates non-conformal discretizations allowing a flexible meshing schemes for fluid and solid domains [33]. In other words, due to the discontinuous interpolation space and the use of higher-order shape functions (4^{th} to 6^{th} polynomial order), we can have non-matching interfaces and use a significantly smaller number of elements (as a rule of thumb 1.5 to 2 elements per wavelength). DG has been used in linear and non-linear ultrasound simulations including elastic and acoustic waves [34–37]. However, even with DG the 3D transient analysis of a clamp-on ultrasonic flowmeter is still computationally very intensive due to the different types of wave interactions between large-sized domains. To the best of our knowledge, there are no known methods that can characterize elastic and acoustic wave propagation through a large system such as a clamp-on flowmeter in 3D at high frequencies.

In this study, we propose an approach that combines DG, ray tracing, and geometric projection methods to provide an accurate interpretation of the complete wave propagation through a clamp-on flowmeter. We perform 3D DG analysis only for the fluid domain at low to medium frequencies (100 kHz, 200 kHz, and 500 kHz). The behavior at high frequencies is obtained qualitatively via 3D ray tracing, which provides a scaling factor. The spread of the acoustic field on the pipe wall is then evaluated by the geometric projection. Combining these three responses with a 2D model of the complete clamp-on system provides us with its full wave propagation behavior.

7.2. Problem definition

In this section, we discuss the different types of waves present in a clamp-on ultrasonic flowmeter, the wave interactions, and the resulting wavefields. The properties and operation of the clamp-on ultrasonic flowmeter are discussed in detail in Section 2 of Chapter 6. We take the geometric and material properties from

there as listed in Table 7.1. Polysulfone was selected as the wedge material, stain-

Pipe properties			
$D_o = 80\,\text{mm}$	$t_p = 4\,\text{mm}$ $c_{pp} = 4935.5\,\text{m/s}$	$L_p = 140\,\text{mm}$ $c_{ps} = 3102.9\,\text{m/s}$	$\rho_p = 7800\,\text{kg/m}^3$
Wedge properties			
$b_w = 36\,\text{mm}$	$h_w = 22.5\,\text{mm}$ $c_{wp} = 1958.84\,\text{m/s}$	$t_w = 30\,\text{mm}$ $c_{ws} = 1183.38\,\text{m/s}$	$\rho_w = 1350\,\text{kg/m}^3$

Table 7.1: Geometric and material properties of the pipe and wedge, where D_o, t_p, and L_p respectively, are the outer diameter, the wall thickness, and the length of the pipe. b_w, h_w, and t_w are the base, height, and thickness of the wedge, respectively. ρ_p, c_{pp}, and c_{ps}, respectively, are the density, pressure, and shear wave speeds of the pipe, while ρ_w, c_{wp}, and c_{ws} are the corresponding material properties of the wedge.

less steel for the pipe, and water (density, $\rho_f = 998.2\,\text{kg/m}^3$ and sound speed, $c_f = 1481.4\,\text{m/s}$) for the fluid. Figure 7.1 shows a schematic representation of the

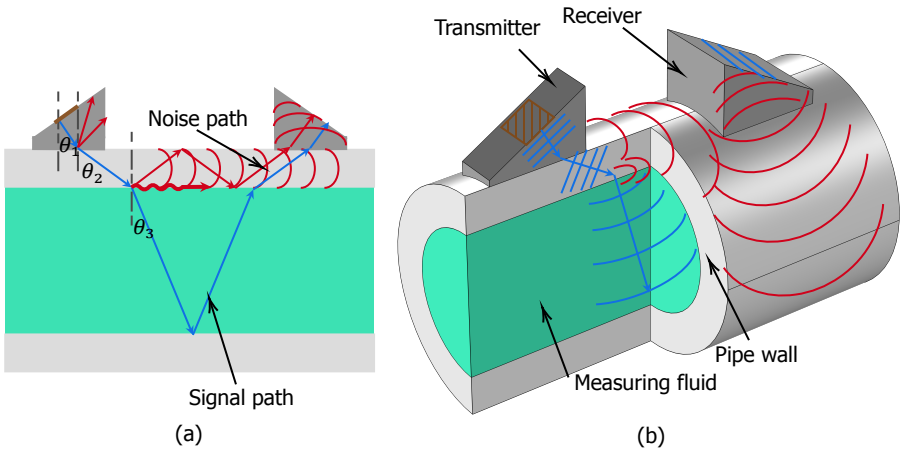

Figure 7.1: Schematic representation of the wave propagation through a clamp-on ultrasonic flowmeter (a) 2D view with signal (blue) and noise (red) paths along with different refraction angles. The incoming angle $\theta_1 = 30°$, refraction angle at the wedge-pipe wall interface $\theta_2 = 52.4°$, and transmission angle from the pipe to fluid $\theta_3 = 22.2°$ are also marked here (b) The 3D representation of the wavefield from (a), where different components of the clamp-on ultrasonic flowmeter are labeled. The brown hatched region is the location of the input signal (prescribed displacement). Schematics of 3D representations of the wavefields in the fluid, solid, and interface are also provided here.

different wave paths and the possible wavefields of a fluid-filled cylinder excited by an oblique source of ultrasound pulse. It is similar to the clamp-on flowmeter geometry shown in Figure 2 from Chapter 6.

In Figure 7.1(a), the blue arrows show the required signal path, while the red arrows and curves represent the noise generated along different interfaces. The

2D wave propagation through the clamp-on system is also discussed in detail in Section 2 of Chapter 6. Here, we emphasize the aspects the 2D analysis cannot comprehend, for instance, due to its intrinsic restriction, the 2D model cannot predict the radial expansion of the wavefield in the fluid domain as represented in Figure 7.1(b). The figure also shows a more detailed representation of signal and noise paths.

The input signal in the transmitter is assumed to be a plane wave, which is a fair approximation as the pulse is coming from a piezoelectric crystal attached to the transmitting wedge (see the brown hatched region in the figure). The incoming plane wave experiences several reflections and refractions generating multiple signals before reaching the receiver. Due to the cylindrical shape of the pipe and fluid, the primary signal (blue) entering the fluid domain expands radially before impinging the opposite pipe wall. This signal then converges on a region within the fluid domain before arriving at the receiver. Similarly, the primary noise signal traveling via the pipe wall also spreads around the wall before reaching the receiver as shown in Figure 7.1(b). Additionally, the ringing down of waves among the wedges, and interference between different noise pulses and the required signal also experience the influence of the 3rd dimension and will scale accordingly. Thus, we explore different methods to analyze the 3D wave propagation through the clamp-on system as discussed next.

7.3. Methods for high-frequency wave propagation analysis in a clamp-on flowmeter

As the high-frequency analysis of the clamp-on flowmeter is incredibly complex, we segment the geometry into different domains and analyze them separately. To that end, we select multiple methods, investigate their pros and cons, and possibilities to combine their responses as below.

7.3.1. Geometric acoustics

Ray tracing is a geometric acoustic method that can compute trajectories, phase, and intensity of acoustic rays, which is valid in the high-frequency limit where the acoustic wavelength is much smaller than the characteristic length of the geometry [38]. Using the trajectory, we can obtain the arrival time and location of the acoustic pulse at the receiver. We can also calculate the scattering and absorption of the traveling waves using ray tracing. Additionally, it provides the focal location within the medium with a curved boundary (such as the current situation). Nonetheless, ray tracing assumes the waves to be straight lines traveling without any distortions, resulting in variations when dealing with complex geometries, dispersive environments, and wave interference. Thus we can apply ray tracing to the fluid domain, which has a more uniform geometry and acoustic response compared to the solid domain. The equation that governs the ray acoustics takes the following form:

$$\frac{d\boldsymbol{k}}{dt} = \frac{\partial \omega}{\partial \boldsymbol{x}} \qquad \frac{d\boldsymbol{x}}{dt} = -\frac{\partial \omega}{\partial \boldsymbol{k}}, \tag{7.1}$$

where $\boldsymbol{k}$ is the wave vector, ω is the circular frequency (in rad/s), $\boldsymbol{x}$ is the spatial coordinate vector, and t is the time coordinate. The boundary condition (BC) necessary to solve the system of equations is provided by a prescribed wave vector as follows:

$$\boldsymbol{k}(\boldsymbol{x}_0) = k_0 \frac{\boldsymbol{L}_0}{|\boldsymbol{L}_0|}, \tag{7.2}$$

where k_0 is the magnitude of the wave vector prescribed at $\boldsymbol{x}_0$ and $\frac{\boldsymbol{L}_0}{|\boldsymbol{L}_0|}$ is the unit ray direction vector. Using the ray equation (7.1) and boundary condition (7.2) we can set up the analysis to obtain the wave propagation characteristics in the fluid domain.

Within the solid domain, the wedge mostly has straight boundaries except for the interface with the pipe wall, which in most cases can also be assumed straight due to the significant dimensional difference between the two (the width and thickness of the wedge are considerably smaller than the diameter of the pipe). Hence the primary pulse traveling through the wedge accurately follows Snell's law and can be characterized analytically. The secondary reflections and refractions at the wedge-pipe wall interface can be precisely analyzed via 2D FEA as discussed in Section 2.3 of Chapter 6. Thus, we do not need additional methods to characterize the wedge. On the contrary, the pipe wall allows radial expansion of the acoustic waves, and hence by projecting the expanding wave field from a cylinder to a plane, we determine the proportion of energy reaching the receiver. The assumptions here are that the pipe wall is non-dispersive and non-dissipative, which is fairly valid considering the pipe is made of stainless steel. The proportion factor is then used to scale the acoustic signal from the primary noise extracted at the receiver using the 2D FEA. To obtain a better understanding of the traveling waves in the clamp-on system, we also try to analyze it using 3D FEA as discussed next.

7.3.2. 3D finite element analysis

As the 3D FEA of the complete clamp-on system at 1 MHz is computationally demanding even within a high-performance computing cluster, we reduce the complexities by removing the solid domain. Additionally, by performing the acoustic analysis at low frequencies (100 kHz, 200 kHz, and 500 kHz), we can obtain the 3D acoustic response within the fluid medium. Figure 7.2 shows the geometry of the fluid domain with the necessary BCs used to perform the 3D FEA. Since the domain is symmetric to the $y-z$ plane, we only need to analyze half of the domain allowing us to reduce the computational cost further. Thus the design shown in the figure is a semi-circular cylinder with two wedges on top to mimic the transmitter and receiver. As the incoming pressure wave enters the fluid from the pipe wall at an angle θ_3 (refer Figure 7.1(a)), we modify the geometry to accommodate for the same (both transmitter and receiver). We perform a time-domain analysis using DG FEM with Comsol to characterize the wave propagation in the fluid domain for which the linearized Euler equations are solved. The acoustic wave equation in the

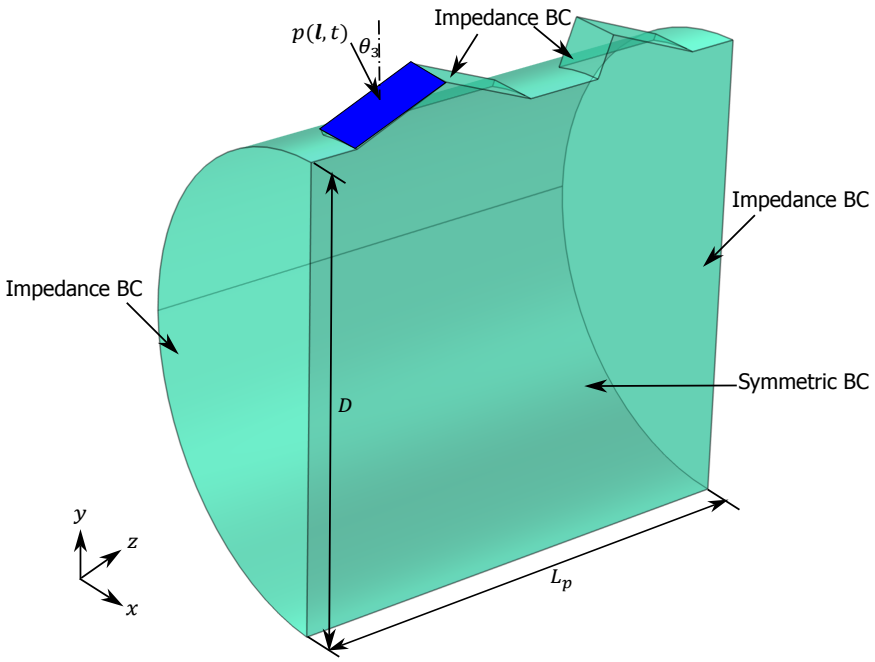

Figure 7.2: 3D model of the fluid domain with necessary BCs. $p(\boldsymbol{l},t)$ is the prescribed pressure applied at an angle θ_3 while impedance and symmetric BCs are provided on the flat surfaces of the fluid domain except for transmitter and receiver locations. The inner diameter of the pipe $D = D_o - 2 \times t_p = 72\,\text{mm}$ and length $L_p = 140\,\text{mm}$ are also marked here.

absence of body forces takes the form

$$\begin{aligned} \frac{1}{\rho_f c_f^2}\frac{\partial p_t}{\partial t} + \nabla \cdot \boldsymbol{v}_f &= 0, \\ \rho_f \frac{\partial \boldsymbol{v}_f}{\partial t} + \nabla \cdot (p_t \boldsymbol{I}) &= 0, \end{aligned} \tag{7.3}$$

where p_t is the total acoustic pressure, $\boldsymbol{v}_f$ is the total acoustic velocity, $\boldsymbol{I}$ is the identity matrix, and $\nabla\cdot$ is the 3D vector divergence operator. We still need to supply the necessary BCs to solve this boundary value problem. We provide a Dirichlet BC (prescribed pressure) along the boundary of the fluid domain shaded using a blue quadrilateral in Figure 7.2, which takes the form

$$p(\boldsymbol{l},t) = \bar{p}g(t), \quad \text{applied at} \quad \underline{x} = \underline{l}, \tag{7.4}$$

where, $\bar{p}$ is the constant pressure amplitude that is multiplied by $g(t)$, which is a broadband Gaussian pulse. The two flat surfaces of the fluid domain normal to the z axis are supplied with impedance BCs, which mimic a low-reflective boundary allowing the waves to escape through those boundaries. The impedance BC takes the form

$$\boldsymbol{n} \cdot \boldsymbol{v}_f = \frac{p_t}{Z_i}, \tag{7.5}$$

where $\boldsymbol{n}$ is the unit outward normal vector on the surface and $Z_i = \rho_f c_f$ is the acoustic impedance of the fluid medium. We also provide impedance BCs to the flat surfaces of the wedges except for the input (blue-shaded plane) and output (similar plane on the receiver) surfaces. We further apply a symmetric BC on the flat surface along the z axis, which takes the form

$$\boldsymbol{n}.\boldsymbol{v}_f = 0. \tag{7.6}$$

The curved surface of the water domain and the flat surface of the receiver that is at θ_3 to z axis are left free allowing the waves a complete reflection from those boundaries. The details of these BCs are available in Comsol documentation [39]. Using wave equation (7.3) and BCs (7.4), (7.5), and (7.6), we can set up the numerical analysis to obtain the wave propagation behavior of the fluid domain. These responses can then be compared against the ray acoustics and 2D FEA results to determine the 3D scaling factor.

However, to apply all the aforementioned scaling factors effectively, we need to know the arrival times of each of these signals in the receiver. Arrival times of the required signal, primary noise, and ring-down noise can be determined by their travel distance and sound speeds in different materials. The arrival times of noise produced by the interference of different waves within the wall and the wall-fluid interface are more challenging and can only be obtained accurately via a 3D analysis of the entire geometry. This is out of the scope of this study and hence omitted from further investigation. By performing these analyses on the clamp-on geometry, we calculate various responses of the clamp-on system as discussed next.

7.4. Results

7.4.1. Ray tracing response of the fluid medium

Ray tracing analysis is performed using Comsol multiphysics' ray acoustics module, for the geometry shown in Figure 7.3. Here, we assume no attenuation of the waves within the domain and that the boundaries have specular reflections, i.e., the waves impinging the boundaries reflect at the same angle [40]. The acoustic source selected here is a plane wave oriented at $\theta_3 = 22.2°$ to the normal, which is the transmission angle of the pressure pulse across pipe wall-fluid interface (as described in Figure 7.1(a)). The diameter $D = 72\,\text{mm}$ and the length of the fluid domain L_p (same as the pipe) are marked in the figure. Since at 1 MHz the acoustic wavelength in water $\lambda = c_w/f = 1.5\,\text{mm}$ is much smaller than D, ray acoustics is valid for this situation. We perform the analysis for 120 µs with a time step of 0.2 µs and the resulting ray trajectories are studied.

Figure 7.4 shows different instances of the ray trajectories where we can clearly see the focusing and diverging effects of the waves within the cylindrical domain. The source is described as a grid with 121 points (11 points per side of a square), each of which travels at the same speed within the domain. The color of the dots represents the sound pressure level (SPL) in dB. When the rays are traveling from the source to the opposite wall, they have the same SPL and are within the same plane as shown in Figures 7.4(a) to 7.4(d). However, they impinge the curved wall

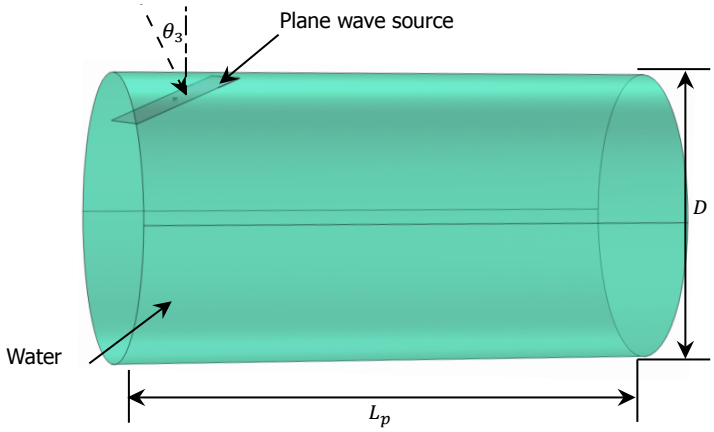

Figure 7.3: Water domain geometry used in the ray tracing analysis where the inclined plane shows the wave source at an angle θ_3 to the normal. The diameter D and length L_p of the fluid domain are labeled here.

at different times as shown in Figure 7.4(d) where some points have touched the wall while others have not. This results in a change in their wavefront shape from a plane to concave (see Figure 7.4(f)). Since a curved wavefront keeps on expanding/contracting to maintain the energy, this concave wavefront shrinks to focus on a small region as represented in Figure 7.4(e). After focusing, the wavefront changes its shape to convex and expands during its travel to the wall as can be seen in Figures 7.4(g) and 7.4(h). Noteworthy, due to the focusing effect, some dots within the wavefront possess higher SPL compared to the rest as evident from the same figures. Additionally, we can also see that after the expansion some parts of the wavefront impinge on the upper wall and travel back to the fluid domain. These rays can interact with the outer wall and also interfere among themselves creating more noise. However, since they have lower SPL and arrive after the required signal, they can be identified and filtered out from the output signal.

From the ray trajectory, we can estimate the approximate location of the focal region to the source as described in Figure 7.5. Here two instances of the ray projection are shown; Figure 7.5(a) the start of the simulation when the rays have not started propagating yet, and Figure 7.5(b) when the rays are focusing after reflecting from the bottom wall. The left-top corner of the pipe wall is selected as the reference coordinate represented using a maroon cross in both figures. For simplicity, we track the movement of the first row of dots (sources) to estimate the focal region. The coordinates of the selected source points in the $y-z$ plane measured in mm are (1.81, 15.04), while the coordinates of the focal point are (32.66, 54.62). Thus the distance between the source and the focal point for the first raw of dots is 50.2 mm. Noteworthy, with respect to the source's location, the position of the focal region changes. However, since the orientation of the source is consistent (kept to θ_3), the relative position between the source and the focal region follows this prediction.

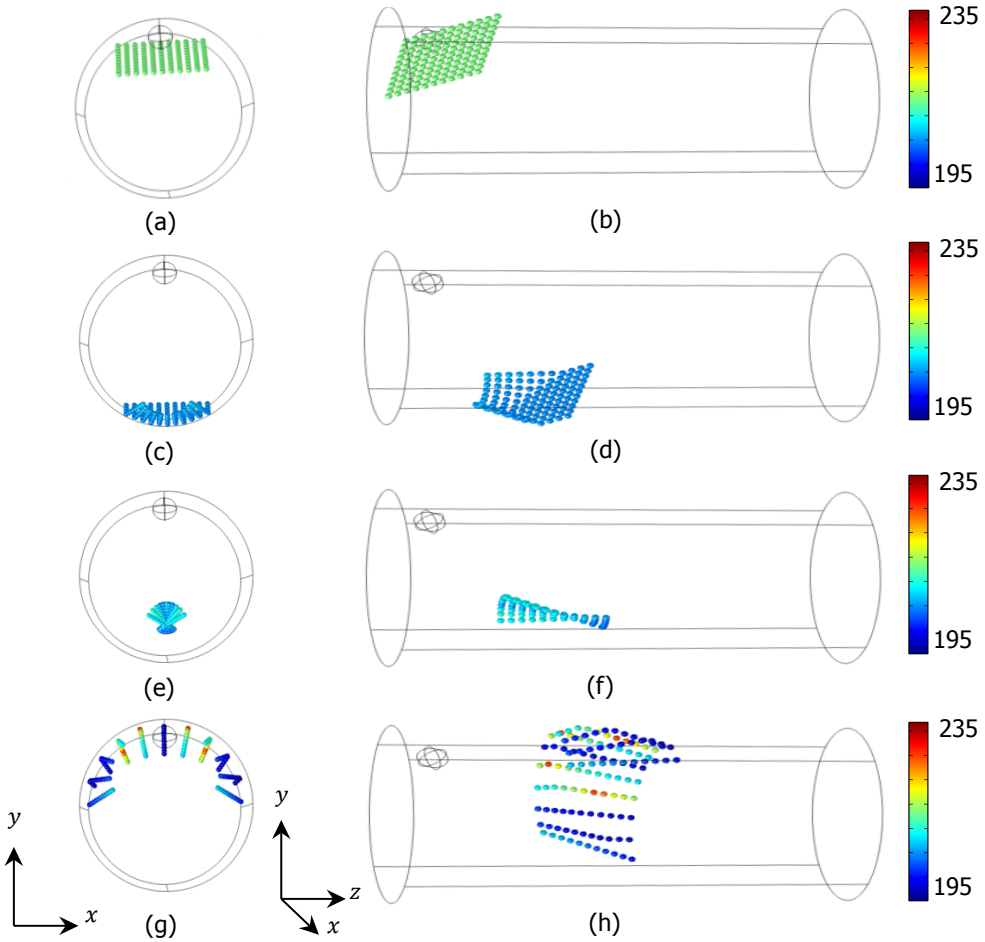

Figure 7.4: Ray trajectories through the water domain with an oblique plane source. The cross-sectional views of the domain correspond to (a) the start of the simulation, (c) when the rays impinge the opposite wall and start to reflect, (e) the rays focus within the medium, and (g) when the rays reach the upper boundary (close to the receiver). (b), (d), (f), and (h), respectively, are the corresponding longitudinal-sectional views. The color of the dots indicates the sound pressure level in dB at that instance.

Using this ray acoustics model, we can also qualitatively estimate the energy of the signal at the receiver by counting the number of dots that reached the receiver and convoluting them with the corresponding SPLs. For instance, here approximately 50 out of 121 dots have reached the receiver location as highlighted by the red box in Figure 7.6, which shows the top view of the ray trajectory. From the number of dots alone, we can see that the total energy decreases by a factor $f_1 = 2.4$. Their SPLs are in the range of 196 dB to 214 dB (refer to the color bar from the same figure). Calculating the sum of each dot's SPL values and subtracting from the average SPL of the center raw provides the change in SPL within the enclosure

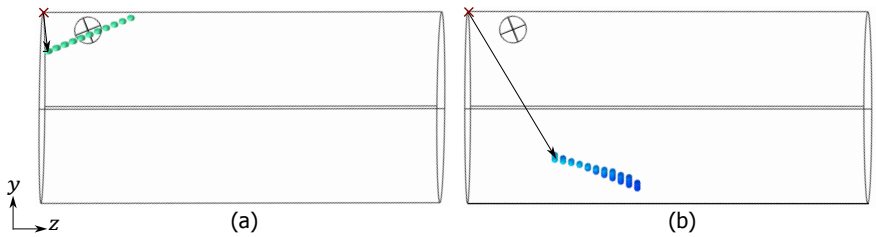

Figure 7.5: Side views of ray trajectories for (a) the start of the simulation and (b) when the rays are focusing in the fluid medium. The maroon cross is the reference point in both (a) and (b), while the arrows indicate the distance from the reference to the beginning of (a) source and (b) focal region.

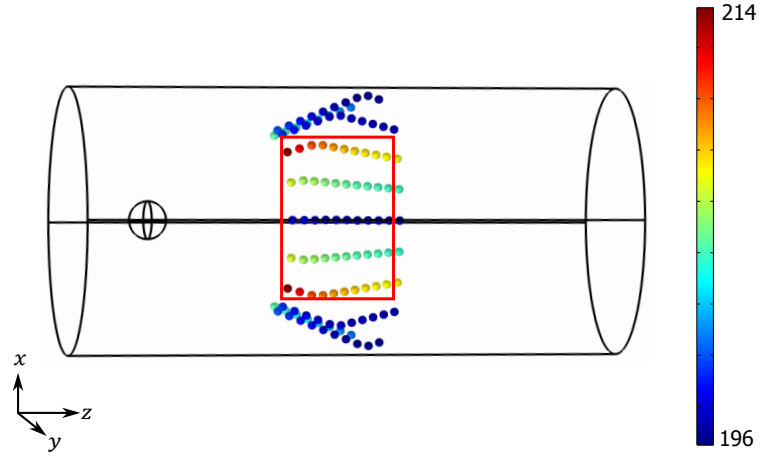

Figure 7.6: Top view of the ray trajectory when the rays impinge the top wall where the red rectangle represents the area of the receiver. The color chart captures the SPL of each ray in dB.

to be ΔSPL=7.7 dB. This factor can be incorporated into the aforementioned scaling factor f_1 to obtain the influence of radial expansion, focusing, and divergence of the acoustic field within the fluid domain. To that end, we convert the relative SPL value to the pressure ratio using the following expression

$$\text{SPL} = 20 \log p_r, \qquad p_r = 10^{(\text{SPL}/20)}, \tag{7.7}$$

and we get $p_r = 2.42$. By dividing p_r by f_1, we obtain an approximate scaling factor, $SF_f = 1.01$. In other words, the output signal at the receiving location should be scaled in magnitude by the factor SF_f if the effects of 3D are not considered in the analysis. We further analyze the fluid domain through 3D FEA to compare the responses between ray tracing and FEA.

7.4.2. 3D finite element analysis of the fluid domain

3D FEA in the time domain is performed on the geometry shown in Figure 7.2 for three different central frequencies, 100 kHz, 200 kHz, and 500 kHz frequencies. A

time step of $T/10$, where T is the time period corresponding to the center frequency of the incoming pulse is used throughout the analysis. Since it takes about 120 µs for the pulse to travel from the transmitter to the receiver in a non-dispersive situation (sound speed independent of the frequency), we select the total simulation time for all three cases to be 125 µs. We compare the pressure profile, arrival time, amplitude, and signal spread (in time) between these analyses to obtain the acoustic behavior of the fluid domain in low and medium frequencies.

Pressure profile comparison between different frequencies

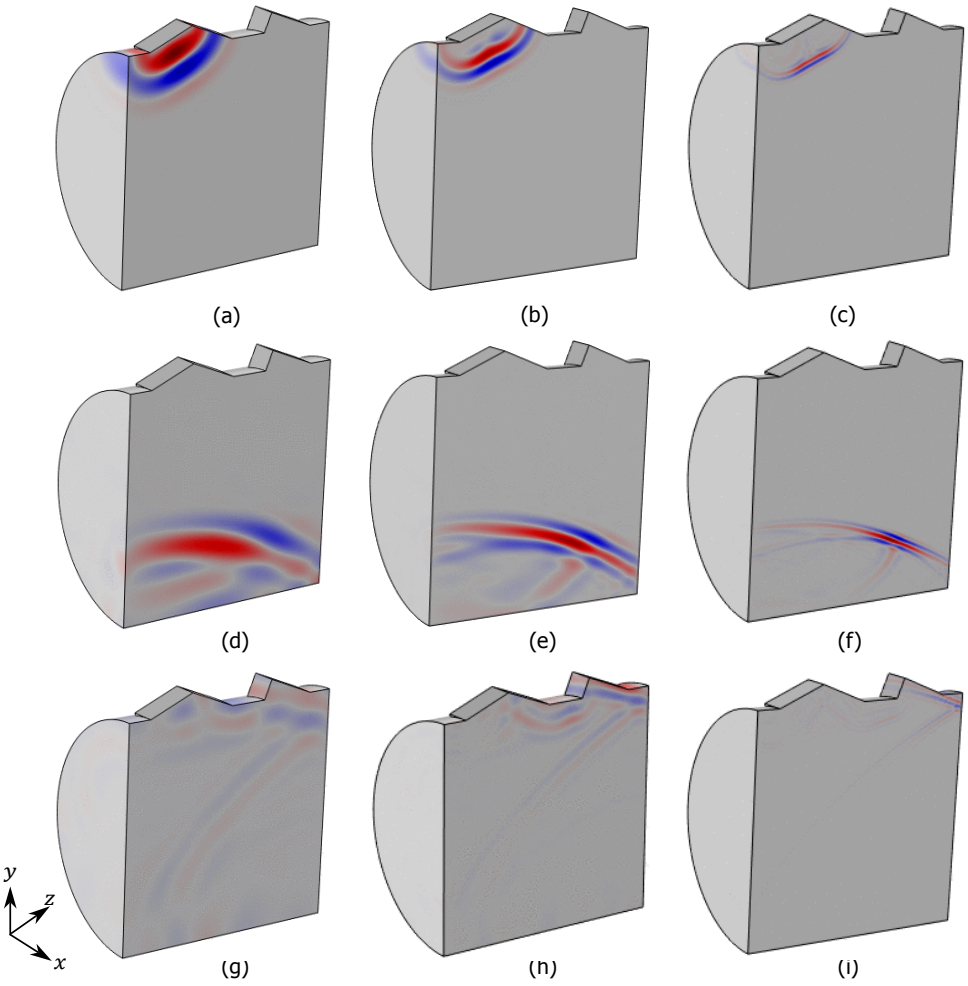

Figure 7.7: Pressure profiles at different instances for 3D wave propagation in water at different frequencies. (a), (d), and (g), respectively, represent the start of the wave propagation, when the acoustic waves focus within the domain, and when it reaches the receiver at 100 kHz. (b), (e), and (h) are the corresponding behavior at 200 kHz, whereas (c), (f), and (i), respectively, are the behavior at 500 kHz.

Figure 7.7 shows the comparison of the total pressure of the fluid domain at different instances corresponding to 100 kHz, 200 kHz, and 500 kHz. The instances shown here include the starting of the simulation (Figures 7.7(a), 7.7(b), and 7.7(c)), when the waves focus within the domain (Figures 7.7(d), 7.7(e), and 7.7(f)), and when the pulse arrives at the receiver (Figures 7.7(g), 7.7(h), and 7.7(i)). As we know, a low-frequency pulse experiences a larger spread due to diffraction [41], we see that the signal spread is higher for 100 kHz from the beginning of the simulation as compared to the other two cases (see Figures 7.7(a), 7.7(b), and 7.7(c)). The 200 kHz case although spreads relatively less, it still focuses on a larger region (7.7(e)), leading to loss of energy when reaching the receiver. On the contrary, the 500 kHz signal experiences little spread while traveling through the fluid and focuses on a smaller region and reaches the receiver as shown in Figures 7.7(c), 7.7(f), and 7.7(i). This is also the reason, high frequency signals are preferred during the measurement process. To further investigate the signal response, we measure the output pulse at the receiving location of the fluid domain and compare them, as follows.

Figure 7.8 shows the normalized pressure (receiver pressure divided by the input pressure) as a function of time measured at the center of the receiver for the three frequencies. Since the curved surface is a free boundary, some waves travel

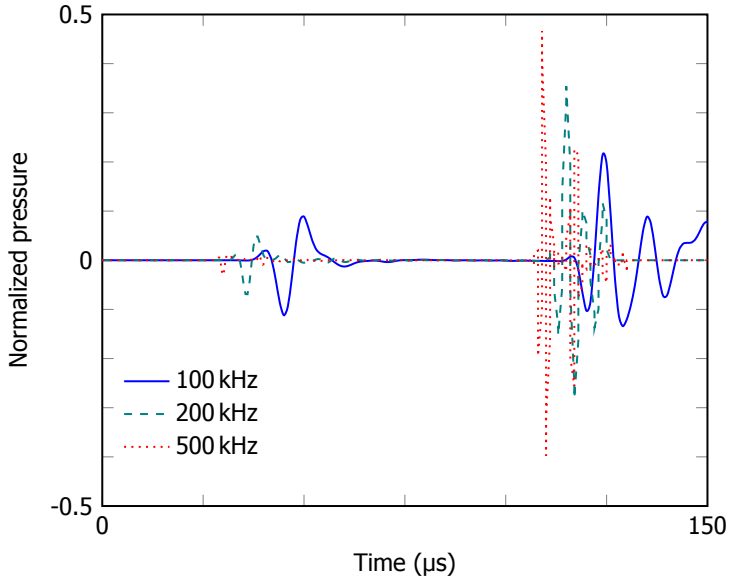

Figure 7.8: Normalized pressure response as a function of time at the receiver location of the fluid domain for 100 kHz (solid blue), 200 kHz (dashed teal), and 500 kHz (dotted red) frequencies.

through that surface to the receiver. As this travel distance is much smaller than the actual wave path (through the domain), the pulse through the surface reaches much earlier than the bulk waves as can be seen in the figure. However, their amplitudes are much smaller than the actual signal and can be discarded. The

figure also shows that with the increase in the frequency, the bulk signal's amplitude increases whereas its spread decreases. This is expected since a high-frequency signal has a high energy and low diffraction. Additionally, although the signals arrive at different times, the difference in the arrival time is very small compared to the total travel time and hence it can be neglected. We compare this wave behavior with a corresponding 2D model to investigate the effect of the 3rd dimension on wave propagation in the fluid domain, as discussed next.

Comparison between 3D and 2D FEA

The 2D FEA model is built based on the geometry from Figure 7.2, where only its central plane (with height D and length L_p) is used. The incoming pressure is from a line source at an angle θ_3 (similar to the plane source from Figure 7.2), while the same time step (T/10) and total time (125 µs) as in the 3D model are used here for consistency. We conducted the simulation for 100 kHz, 200 kHz, 500 kHz, and 1 MHz. Figure 7.9 compares the pressure profile between the 2D and the 3D analysis at 500 kHz for the same three instances discussed in Section 7.4.2. From

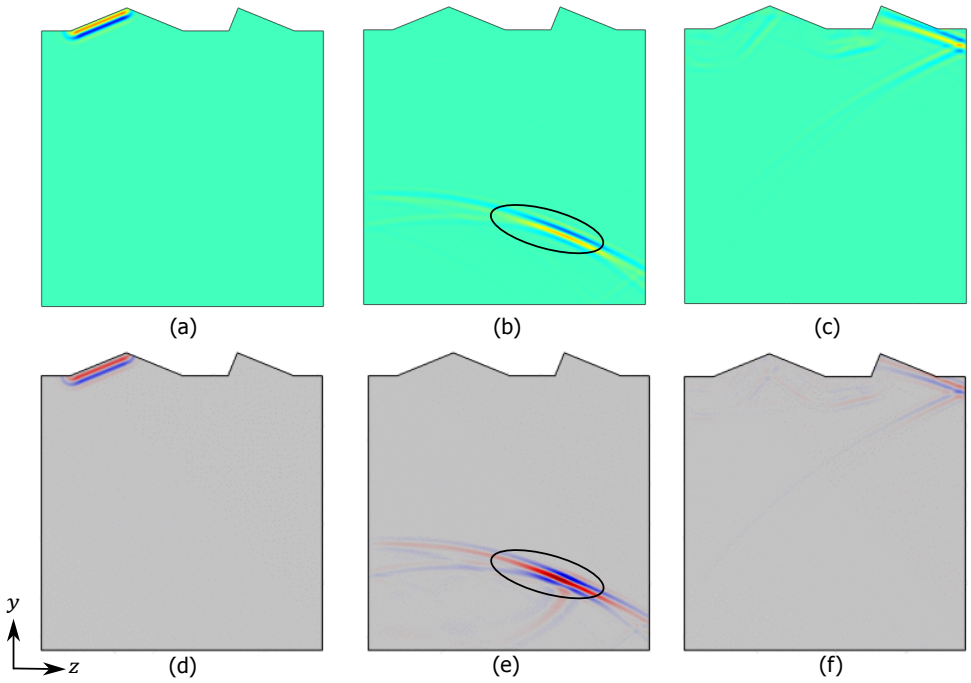

Figure 7.9: Pressure profiles comparison between 2D and 3D at different instances at 500 kHz. The behavior is similar for 2D and 3D at the start of the wave propagation (a) and (d), and when the signal reaches the receiver (c), (f). However, as highlighted with black ellipses in (b) and (e), the wavefield during focusing is considerably different between 2D and 3D as the former cannot capture the focusing effect.

Figures 7.9(a) and 7.9(d), we can see that the wavefronts are very similar between 2D and 3D at the beginning of the simulation. However, the signal traveling back

to the medium after impinging at the opposite side still shows a uniform wavefront in 2D, whereas in 3D we observe a focusing effect. This difference is highlighted in Figures 7.9(b) and 7.9(d) using a black ellipse. The signals arriving at the receiver as shown in Figures 7.9(c) and 7.9(f) show similar shapes meaning the focusing had little effect on the receiving signal's wavefront shape. To quantify the focusing and spreading effects on the signal amplitude, we compare the time response at the receiver between the 2D and 3D models.

Pressure at the receiver comparison between 2D and 3D

Normalized pressure at the receiver is calculated for the 2D models similar to the 3D case. Figure 7.10a and 7.10b show the comparison of the normalized pressure between 2D and 3D for 200 kHz and 500 kHz, respectively. While the pulse shape at 200 kHz is considerably different between 2D and 3D, the response at 500 kHz is very close. This is also due to the lower diffraction at high frequencies. From this behavior, we can predict that at 1 MHz, the variation between 2D and 3D will be even smaller and we will be able to use the 2D model to obtain the arrival time and the signal spread through the fluid medium with a nominal accuracy. The maximum amplitude of the signal is lower for the 3D model compared to the 2D because of the expansion in the third dimension. Additionally, we can see that this variation decreases with the increase in frequency as we discuss in detail next.

Parametric response and dispersion relation

Similar to the ray tracing discussed in Section 7.4.1, we can obtain the scaling factor that determines the variation in pressure amplitude in the fluid domain due to 3D via FEA. To that end, we need to determine the dispersion relation of the domain in addition to the time response shown in Figures 7.10a and 7.10b. The dispersion relation relates the frequency with the wave vector (reciprocal of the wavelength), whose slope provides the wave speed [42]. If the wave speed varies with the frequency, then the medium is dispersive. Since the domain for all these three frequency cases is the same, the travel distance remains constant. The arrival time is then obtained from the time response (Figure 7.10b), which is used to calculate the sound speed and the magnitude of the wave vector within the medium as follows

$$v_m = \frac{L_{tot}}{t_a}, \qquad \lambda = \frac{v_m}{f}, \qquad k = \frac{2\pi}{\lambda}, \tag{7.8}$$

where, l_{tot} is the total distance from the source to the receiver, t_a is the arrival time of the pulse, v_m is the calculated sound speed within the domain, λ is the wavelength, and k is the magnitude of the wave vector also called a wave number. Figure 7.11a shows the comparison of the dispersion relation between 2D and 3D FEA, which are linear and very similar. In other words, the fluid medium can be considered non-dispersive and the additional dimension does not have a significant influence on the dispersion relation of the medium.

Figure 7.11b shows the relation between the pressure ratio for different applied frequencies, which is calculated by dividing the peak pressure values of 3D with 2D obtained from the corresponding time response plots. We see that the pressure ratio increases with frequency and the slope between 100 kHz and 200 kHz is

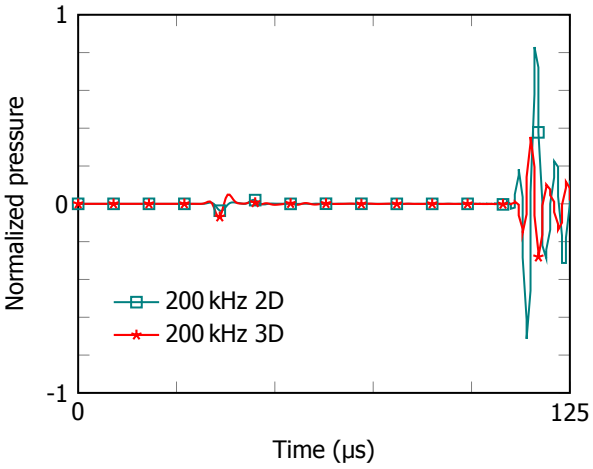

(a)

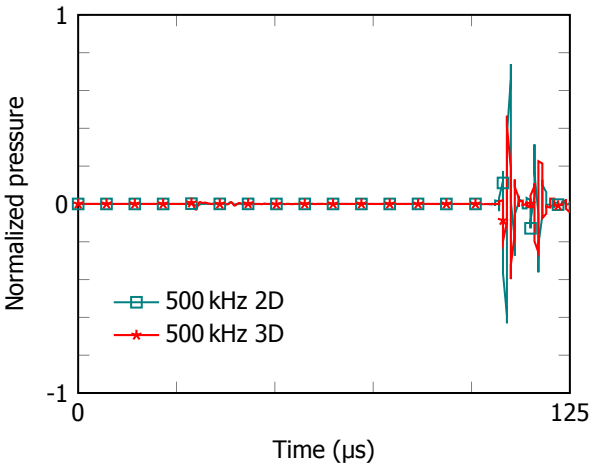

(b)

Figure 7.10: Comparison of the normalized pressure at the receiver between 2D (teal line with square marker) and 3D (red line with asterisk marker) for (a) 200 kHz and (b) 500 kHz frequencies. The pulse shape and amplitudes are considerably different between 2D and 3D at 200 kHz while they tend to be closer at 500 kHz.

larger than the slope between 200 kHz and 500 kHz because at lower frequencies due to higher diffraction, the signal experiences larger spread and thus the losses increases. At higher frequencies, the behavior would be more linear due to the lower loss. Additionally, the sound pressure within the fluid is directly related to the sound speed and frequency, where the former can be considered constant due to the non-dispersive behavior. Thus, we can linearly extrapolate the pressure ratio in Figure 7.11b from 500 kHz to 1 MHz, and its value is 0.973. Recall that we esti-

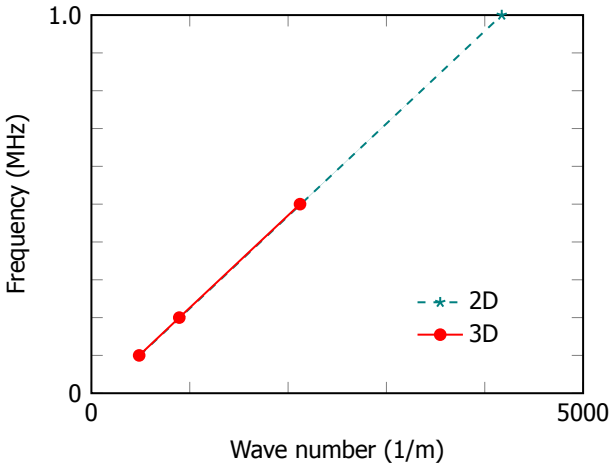

(a)

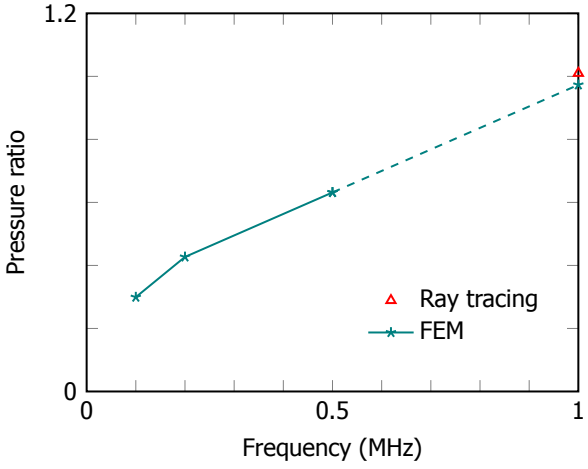

(b)

Figure 7.11: (a) Dispersion relation (b) Pressure ratio comparison between 2D and 3D. The dispersion relations for 2D and 3D are linear (non-dispersive) and closely matching. The pressure ratio increases with frequency and at low frequencies the variation is higher due to high diffraction. The variation at high frequencies would be more linear and proportional to frequency. The extrapolated pressure ratio at 1 MHz predicted by FEM (teal asterisk) is close to the ray acoustic estimation shown using a red triangle (3.6 % variation).

mated the pressure ratio from ray tracing to be 1.01 (marked using a red triangle in the figure), which is only 3.6 % higher than the FEA prediction. We proceed to determine the scaling factor for the pipe wall using the geometric projection method, as discussed next.

7.4.3. Geometric projection of the pipe wall

Geometric projection is carried out by unwrapping the cylindrical pipe wall to a plane and measuring the area of the expanding semi-circle when reaching the receiver as shown in Figure 7.12. The pipe with the outer diameter D_o and length L_p is

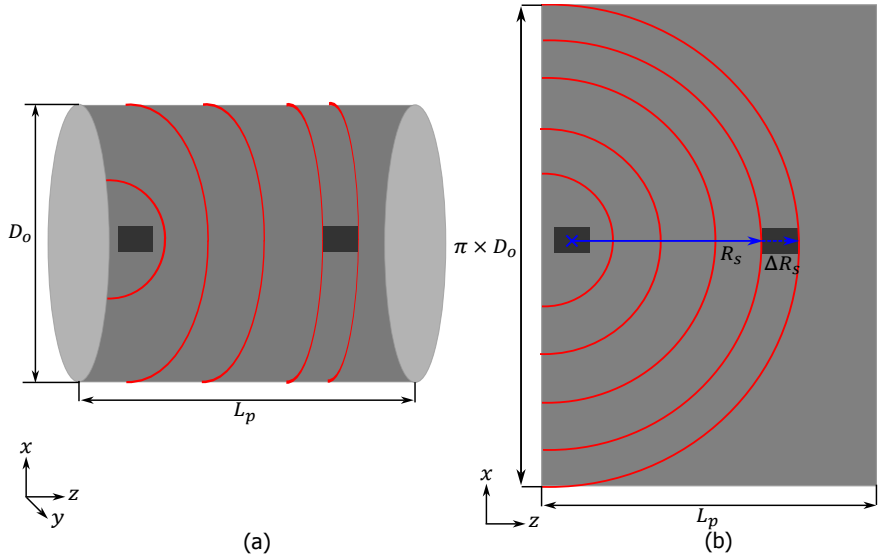

Figure 7.12: Geometric projection of waves traveling in the pipe wall (a) top view of the pipe wall with wedges where D_o and L_p are marked. It shows cylindrical waves traveling from the transmitter to the receiver. (b) projection of the pipe to a plane where its width is the same as the length of the pipe (L_p), while its height is the circumference of the pipe ($\pi \times D_o$). The wavefield is represented using concentric circles and the blue arrow with length R_s shows the radius of the field when the waves impinge the receiver. ΔR_s is the change in the radius of the wavefield from the start to the end of the receiver that is equivalent to b_w.

projected to a rectangle with width L_p and height $\pi \times D_o$ as shown in the figure. The expanding cylindrical wavefield can be represented as concentric circles in the planar domain, which is shown using red semi-circular rings in Figure 7.12(b). The blue arrow of length R_s is the radius of the expanding circle when reaching the receiver and ΔR_s is its variation from the start to the end of the receiver (along z direction).

On the pipe wall, solid waves are present, whose energy is directly related to the area of the circle. We use the area of the receiver and the total area of the circular strip enclosing the receiver to obtain the area ratio as follows:

$$A_w = b_w \times t_w, \qquad A_s = \pi \times \left[(R_s + \Delta R_s)^2 - R_s^2\right], \qquad A_r = A_w / A_s, \tag{7.9}$$

where A_w is the area of the receiver, A_s is the area of the strip encircling the receiver, and A_r is the area ratio, which is equivalent to the energy ratio. For the current geometry, $R_s = 70\,\text{mm}$ and $\Delta R_s = 36\,\text{mm}$ resulting in $A_r = 0.05426$. As energy is related to the square of the displacement (in the solid domain), the displacement

ratio $d_r = \sqrt{A_r} = 0.233$ on the pipe wall. In other words, all waves traveling on the pipe wall from the transmitter to the receiver (with cylindrically expanding wavefield), experience a reduction in amplitude with the factor d_r when the effect of the 3rd dimension is incorporated into the 2D analysis. We now apply scaling factors in both fluid and solid to the output signal from the clamp-on flowmeter. To that end, we use the complete 2D clamp-on model discussed in Section 3.3 of Chapter 6, as follows.

7.4.4. 2D wave propagation of the clamp-on flowmeter

The 2D time-domain analysis of the complete clamp-on flowmeter is performed using dG FEM and the results are provided in Figure 7.13. Figure 7.13(a) shows the

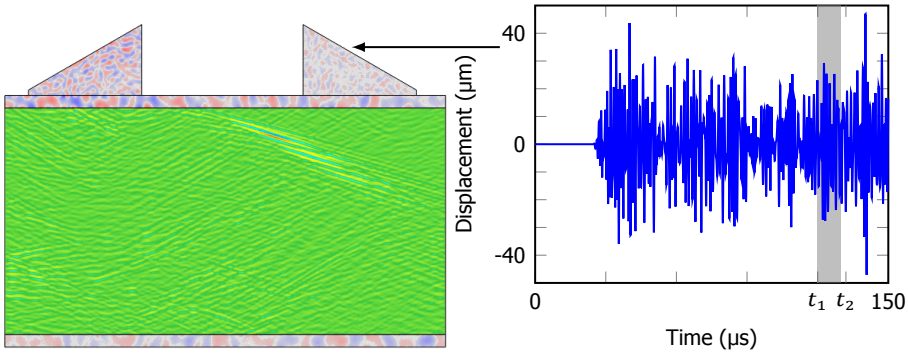

Figure 7.13: 2D clamp-on flowmeter response (a) snapshot of the pressure profile when the fluid signal is about to impinge the pipe wall (b) the displacement (in micro/meter) at the receiver as a function of time (in micro/second). The gray shaded region corresponds to the arrival time of the fluid signal bounded by $t_1 = 120\,\mu s$ and $t_2 = 130\,\mu s$, while the teal shaded parts correspond to the ringing within the transmitting wedge and between wedges.

pressure profile of the clamp-on flowmeter when the signal from the fluid domain is about to impinge the pipe wall. Here, we can see that the wedge, pipe wall, and fluid are very noisy, as can be seen by the output displacement measured on the receiver shown in Figure 7.13(b). The noise in the output signal is majorly contributed by the multiple ringing effects from the transmitting wedge, i.e., the input pulse after reflecting from the wedge-pipe wall interface travels back to the wedge. This pulse then reflects from other free surfaces (of the wedge) back to the pipe wall and travels through the wall as noise signals. This process repeats until the amplitude diminishes to the device's noise floor. Another noise source is the ringing of waves between the transmitter and the receiver. Since the distance between the wedges is fixed (52 mm), the time difference between these ringing can be easily calculated using the sound speed in the pipe wall and the travel distance (twice the distance between the wedges). The ringing interval is obtained as 21.1 μs for P waves whereas 33.5 μs for S waves. However, since these signals tend to overlap, it would be challenging to separate them solely based on these arrival times. To that

end, we provide certain modifications to the 2D FEA of the clamp-on flowmeter as discussed next.

Output signal separation of the clamp-on ultrasonic flowmeter

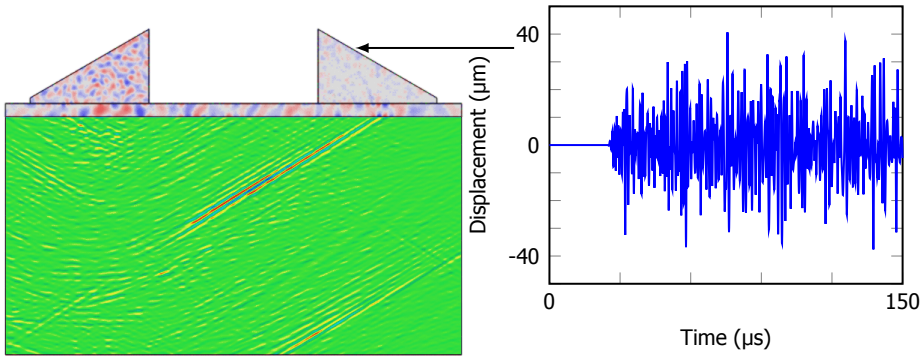

Figure 7.14: Response of the clamp-on flowmeter model without the bottom pipe wall (a) snapshot of the pressure profile for the same time instance as Figure 7.13(a), (b) the receiving wedge's displacement as a function of time also measured at the same location as Figure 7.13(b).

The bottom pipe wall of the 2D FEM model is replaced by an impedance BC to ensure that the required signal from the fluid domain does not reach the receiver. The pressure profile shown in Figure 7.14(a) is at the same instance as in Figure 7.13(a) where we can clearly see that no signal arrives at the receiver from the fluid. The corresponding time response is also extracted at the top of the wedge (same location as the response from Figure 7.13(b)) and plotted in Figure 7.14(b). Since we assume linearity throughout the modeling and we kept all other factors (geometry, simulation settings, and solver settings) unchanged, we can safely assume that the difference between the signal from the clamp-on model and the model without the bottom pipe wall will provide the required fluid signal as shown in Figure 7.15a. Here, we can see that when the influences of the solid portion and the solid-fluid interaction (of the top pipe wall-fluid interface) are removed, the signal from the fluid is clearly visible and as predicted it is between 120 µs and 130 µs. Additionally, the signal amplitude is also diminished by a factor of two due to the lack of waves from the solid domain. This also implies that the waves traveling in the solid domain possess higher energy than the required signal from the fluid. We can also observe an additional signal just after the required signal, which is due to the secondary reflection from the transmitting wedge.

We apply the different scaling factors derived in previous sections to these two (noise and required signals) and add them together to obtain the complete output response of the clamp-on ultrasonic flowmeter. To that end, the signal from the fluid is scaled with the pressure ratio $p_r = 1.01$ and the signal from the solid region is scaled with the displacement ratio $d_r = 0.233$. The assumption here is that, since we already consider the area of the receiving wedge while determining p_r

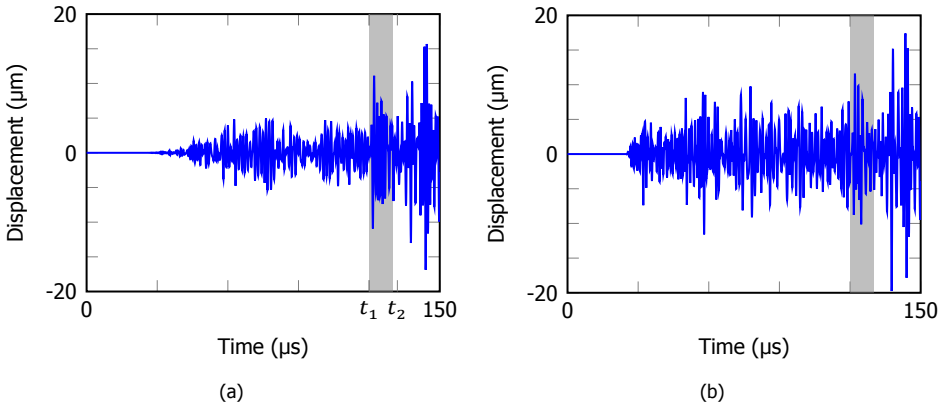

Figure 7.15: (a) Displacement response of the signal traveling through the fluid domain calculated by subtracting the signal from the solid domain (Figure 7.14(b)) from the time response of the clamp-on flowmeter (Figure 7.13(b)), where the shaded region represents the working signal bounded by t_1 and t_2. (b) The displacement at the receiver was obtained after scaling the solid domain's signal by $d_r = 0.233$, and the fluid domain's signal by $p_r = 1.01$ and combining both. The gray-shaded region is the same as (a).

(from ray acoustics), the scaling factor stays the same when the fluid signal travels through the pipe wall and then to the wedge because of the short travel time. In other words, the displacement scaling factor for the fluid signal is equal to p_r. The resulting displacement response of the receiving wedge is shown in Figure 7.15b. Although the working signal can be identified, the signals from the solid portion and multiple solid-fluid interactions are still present. These are not spurious signals since due to the multiple solid-fluid interfaces these signals can be generated in a clamp-on ultrasonic flowmeter. However, in most commercially used clamp-on ultrasonic flowmeters, plastic wedges are used to transmit and receive signals. They possess damping due to viscoelastic behavior that enables them to minimize the secondary reflections and ringing between the wedges. Incorporating this complex behavior needs the complete viscoelastic characterization of the wedge materials, which is out of the scope of this study. However, compared to Figure 7.13(b), the response of the clamp-on ultrasonic flowmeter is better captured here due to incorporating the influence of 3D via different scaling factors.

7.5. Summary and Conclusion

To characterize the wave propagation through a complex media such as a clamp-on ultrasonic flowmeter, we proposed a semi-analytical approach combining 2D and 3D FEA, ray tracing, and geometric projection. Since the complete 3D transient analysis of the clamp-on flowmeter at high frequency is computationally extremely intensive and as we cannot rely on frequency-domain analyses because they do not represent the physical reality, we analyzed the clamp-on system using 2D transient FEA. We then separated the geometry into different domains, where we characterized the fluid domain with 3D FEA and ray tracing, and the solid domain via the geometric

projection. We determined scaling factors that account for the effects of 3D for waves traveling in different domains. Using these scaling factors, we scale the output response at the receiver from the 2D analysis allowing us to distinguish the fluid signal from the surrounding noise, which was impossible otherwise. We conclude that:

- To represent the wave propagation through a clamp-on flowmeter accurately, it is beneficial to separate the domain into different sub-domains and analyze them individually. This aids in reducing the overall computational cost and allows us to section the output signal into different parts;
- Dispersion relation and the wave envelope shape are comparable between 2D and 3D FEA at low frequencies implying that low-frequency models could provide reasonable predictions and allow us to forecast the wave propagation behavior of the fluid domain at high frequencies by extrapolation;
- Ray tracing assumes a particle-like behavior and hence can provide accurate descriptions at high frequencies. For an isotropic solid domain without dispersion and damping, depending on the type of wavefield, geometrical projection based on analytical expressions can be used to characterize the wave propagation behavior. We can use these two approaches in conjunction with 2D FEA to represent the wave propagation through clamp-on flowmeters accurately;

The proposed method lacks the means to model the solid-fluid interface in 3D, so we cannot properly characterize the interfacial waves; however, with the 2D analysis, we can partially get the interface behavior. Since in the selected clamp-on flowmeter, the influence of the interface waves was not as prominent as the solid and fluid waves, we can ignore them. Additionally, the viscoelastic damping behavior of the plastic wedges is also not included in the proposed model, which influences its accuracy. Thus, the next step could be to characterize the viscoelastic behavior of the wedge materials and include them in the wave propagation model. Another possible direction could be to accurately model the solid-fluid interface and generalize the approach for more complex systems' wave propagation behavior at high frequencies.

Bibliography

[1] Nabilah Ibrahim, Hideyuki Hasegawa, and Hiroshi Kanai. "Detection of Arterial Wall Boundaries Using an Echo Model Composed of Multiple Ultrasonic Pulses". In: *Japanese Journal of Applied Physics* 52.7S (June 2013), 07HF03. DOI: 10.7567/JJAP.52.07HF03. URL: https://dx.doi.org/10.7567/JJAP.52.07HF03.

[2] P. Abolmaesumi et al. "Image-guided control of a robot for medical ultrasound". In: *IEEE Transactions on Robotics and Automation* 18.1 (2002), pp. 11–23. DOI: 10.1109/70.988970.

[3] Jeff Powers and Frederick Kremkau. "Medical ultrasound systems". In: *Interface focus* 1.4 (2011), pp. 477–489.

[4] D. L. Franklin et al. "A Pulsed Ultrasonic Flowmeter". In: *IRE Transactions on Medical Electronics* ME-6.4 (1959), pp. 204–206. DOI: 10.1109/IRETME.1959.5007965.

[5] Pamela I Moore, Gregor J Brown, and Brian P Stimpson. "Ultrasonic transit-time flowmeters modelled with theoretical velocity profiles: methodology". In: *Measurement Science and Technology* 11.12 (Nov. 2000), pp. 1802–1811. DOI: 10.1088/0957-0233/11/12/321. URL: https://doi.org/10.1088/0957-0233/11/12/321.

[6] D. Marioli, E. Sardini, and A. Taroni. "Ultrasonic distance measurement for linear and angular position control". In: *IEEE Transactions on Instrumentation and Measurement* 37.4 (1988), pp. 578–581. DOI: 10.1109/19.9817.

[7] P Boltryk et al. "An ultrasonic transducer array for velocity measurement in underwater vehicles". In: *Ultrasonics* 42.1 (2004). Proceedings of Ultrasonics International 2003, pp. 473–478. ISSN: 0041-624X. DOI: https://doi.org/10.1016/j.ultras.2003.12.036. URL: https://www.sciencedirect.com/science/article/pii/S0041624X03002592.

[8] Takahiro Motegi, Koichi Mizutani, and Naoto Wakatsuki. "Simultaneous Measurement of Air Temperature and Humidity Based on Sound Velocity and Attenuation Using Ultrasonic Probe". In: *Japanese Journal of Applied Physics* 52.7S (July 2013), 07HC05. DOI: 10.7567/JJAP.52.07HC05. URL: https://dx.doi.org/10.7567/JJAP.52.07HC05.

[9] James Helal, Massoud Sofi, and Priyan Mendis. "Non-destructive testing of concrete: A review of methods". In: *Electronic Journal of Structural Engineering* 14.1 (2015), pp. 97–105.

[10] Sylvain Chatillon et al. "Ultrasonic non-destructive testing of pieces of complex geometry with a flexible phased array transducer". In: *Ultrasonics* 38.1 (2000), pp. 131–134. ISSN: 0041-624X. DOI: https://doi.org/10.1016/S0041-624X(99)00181-X. URL: https://www.sciencedirect.com/science/article/pii/S0041624X9900181X.

[11] Allied Market Research. *Ultrasound Devices Market Size, Share, Competitive Landscape and Trend Analysis Report by Product, 2023-2032*. 2022. URL: https://www.alliedmarketresearch.com/ultrasound-devices-market.

[12] Marilyn J. Berliner and Roman Solecki. "Wave propagation in fluid□loaded, transversely isotropic cylinders. Part I. Analytical formulation". In: *The Journal of the Acoustical Society of America* 99.4 (Apr. 1996), pp. 1841–1847. ISSN: 0001-4966. DOI: 10.1121/1.415365. eprint: https://pubs.aip.org/asa/jasa/article-pdf/99/4/1841/15273869/1841_1_online.pdf. URL: https://doi.org/10.1121/1.415365.

[13] Marilyn J. Berliner and Roman Solecki. "Wave propagation in fluid□loaded, transversely isotropic cylinders. Part II. Numerical results". In: *The Journal of the Acoustical Society of America* 99.4 (Apr. 1996), pp. 1848–1853. ISSN: 0001-4966. DOI: 10.1121/1.415366. eprint: https://pubs.aip.org/asa/jasa/article-pdf/99/4/1848/15273883/1848_1_online.pdf. URL: https://doi.org/10.1121/1.415366.

[14] Edward W. Peterson. "Acoustic wave propagation along a fluid□filled cylinder". In: *Journal of Applied Physics* 45.8 (Oct. 2003), pp. 3340–3350. ISSN: 0021-8979. DOI: 10.1063/1.1663783. eprint: https://pubs.aip.org/aip/jap/article-pdf/45/8/3340/7422992/3340_1_online.pdf. URL: https://doi.org/10.1063/1.1663783.

[15] Xiaotang Gu and Frederic Cegla. "The Effect of Internal Pipe Wall Roughness on the Accuracy of Clamp-On Ultrasonic Flowmeters". In: *IEEE Transactions on Instrumentation and Measurement* 68.1 (2019), pp. 65–72. DOI: 10.1109/TIM.2018.2834118.

[16] António J.B. Tadeu and Paulo F.A. Santos. "3-D wave propagation in fluid-filled irregular boreholes in elastic formations". In: *Soil Dynamics and Earthquake Engineering* 21.6 (2001), pp. 499–517. ISSN: 0267-7261. DOI: https://doi.org/10.1016/S0267-7261(01)00016-1. URL: https://www.sciencedirect.com/science/article/pii/S0267726101000161.

[17] A. Van Pamel et al. "Finite-element modelling of elastic wave propagation and scattering within heterogeneous media". In: *Proceedings of the Royal Society A: Mathematical, Physical and Engineering Sciences* 473.2197 (2017), p. 20160738. DOI: 10.1098/rspa.2016.0738. eprint: https://royalsocietypublishing.org/doi/pdf/10.1098/rspa.2016.0738. URL: https://royalsocietypublishing.org/doi/abs/10.1098/rspa.2016.0738.

[18] Joseph L Rose. "A baseline and vision of ultrasonic guided wave inspection potential". In: *Journal of pressure vessel technology* 124.3 (2002), pp. 273–282.

[19] X.M. Zhang, G.R. Liu, and K.Y. Lam. "Coupled vibration analysis of fluid-filled cylindrical shells using the wave propagation approach". In: *Applied Acoustics* 62.3 (2001), pp. 229–243. ISSN: 0003-682X. DOI: https://doi.org/10.1016/S0003-682X(00)00045-1. URL: https://www.sciencedirect.com/science/article/pii/S0003682X00000451.

[20] F. Ihlenburg and I. Babuška. "Finite element solution of the Helmholtz equation with high wave number Part I: The h-version of the FEM". In: *Computers & Mathematics with Applications* 30.9 (1995), pp. 9–37. ISSN: 0898-1221. DOI: https://doi.org/10.1016/0898-1221(95)00144-N. URL: https://www.sciencedirect.com/science/article/pii/089812219500144N.

[21] Arnaud Deraemaeker, Ivo Babuška, and Philippe Bouillard. "Dispersion and pollution of the FEM solution for the Helmholtz equation in one, two and three dimensions". In: *International Journal for Numerical Methods in Engineering* 46.4 (1999), pp. 471–499. DOI: https://doi.org/10.1002/(SICI)1097-0207(19991010)46:4<471::AID-NME684>3.0.CO;2-6. eprint: https://rb.gy/nk9hz5. URL: https://rb.gy/nk9hz5.

[22] David Gottlieb and Chi-Wang Shu. "On the Gibbs Phenomenon and Its Resolution". In: *SIAM Review* 39.4 (1997), pp. 644–668. DOI: https://10.1137/S0036144596301390. eprint: https://rb.gy/9lzus3. URL: https://rb.gy/9lzus3.

[23] K. J. Bathe and E. L. Wilson. "Stability and accuracy analysis of direct integration methods". In: *Earthquake Engineering & Structural Dynamics* 1.3 (1972), pp. 283–291. DOI: https://doi.org/10.1002/eqe.4290010308. eprint: https://onlinelibrary.wiley.com/doi/pdf/10.1002/eqe.4290010308. URL: https://onlinelibrary.wiley.com/doi/abs/10.1002/eqe.4290010308.

[24] A. V. Idesman, M. Schmidt, and J. R. Foley. "Accurate finite element modeling of linear elastodynamics problems with the reduced dispersion error". In: *Computational Mechanics* 47.5 (May 2011), pp. 555–572. ISSN: 1432-0924. DOI: 10.1007/s00466-010-0564-3. URL: https://doi.org/10.1007/s00466-010-0564-3.

[25] David Gottlieb and Steven A Orszag. *Numerical analysis of spectral methods: theory and applications*. SIAM, 1977.

[26] Anthony T Patera. "A spectral element method for fluid dynamics: Laminar flow in a channel expansion". In: *Journal of Computational Physics* 54.3 (1984), pp. 468–488. ISSN: 0021-9991. DOI: https://doi.org/10.1016/0021-9991(84)90128-1. URL: https://www.sciencedirect.com/science/article/pii/0021999184901281.

[27] Srinivasan Gopalakrishnan, Massimo Ruzzene, and Sathyanarayana Hanagud. "Spectral Finite Element Method". In: *Computational Techniques for Structural Health Monitoring*. London: Springer London, 2011, pp. 177–217. ISBN: 978-0-85729-284-1. DOI: 10.1007/978-0-85729-284-1_5. URL: https://doi.org/10.1007/978-0-85729-284-1_5.

[28] A. Chakraborty and S. Gopalakrishnan. "A Spectral Finite Element Model for Wave Propagation Analysis in Laminated Composite Plate". In: *Journal of Vibration and Acoustics* 128.4 (Feb. 2006), pp. 477–488. ISSN: 1048-9002. DOI: 10.1115/1.2203338. eprint: https://asmedigitalcollection.asme.org/vibrationacoustics/article-pdf/128/4/477/5538988/477_1.pdf. URL: https://doi.org/10.1115/1.2203338.

[29] Jan S Hesthaven and Tim Warburton. *Nodal discontinuous Galerkin methods: algorithms, analysis, and applications*. Springer Science & Business Media, 2007.

[30] J. S. Hesthaven and C. H. Teng. "Stable Spectral Methods on Tetrahedral Elements". In: *SIAM Journal on Scientific Computing* 21.6 (2000), pp. 2352–2380. DOI: 10.1137/S1064827598343723. eprint: https://doi.org/10.1137/S1064827598343723. URL: https://doi.org/10.1137/S1064827598343723.

[31] Lucas C. Wilcox et al. "A high-order discontinuous Galerkin method for wave propagation through coupled elastic–acoustic media". In: *Journal of Computational Physics* 229.24 (2010), pp. 9373–9396. ISSN: 0021-9991. DOI: https://doi.org/10.1016/j.jcp.2010.09.008. URL: https://www.sciencedirect.com/science/article/pii/S0021999110005024.

[32] J. S. Hesthaven. "From Electrostatics to Almost Optimal Nodal Sets for Polynomial Interpolation in a Simplex". In: *SIAM Journal on Numerical Analysis* 35.2 (1998), pp. 655–676. DOI: 10.1137/S003614299630587X. eprint: https://doi.org/10.1137/S003614299630587X. URL: https://doi.org/10.1137/S003614299630587X.

[33] Marcus J. Grote, Anna Schneebeli, and Dominik Schötzau. "Discontinuous Galerkin Finite Element Method for the Wave Equation". In: *SIAM Journal on Numerical Analysis* 44.6 (2006), pp. 2408–2431. DOI: 10.1137/05063194X. eprint: https://doi.org/10.1137/05063194X. URL: https://doi.org/10.1137/05063194X.

[34] Markus Muhr, Barbara Wohlmuth, and Vanja Nikolić. "A discontinuous Galerkin coupling for nonlinear elasto-acoustics". In: *IMA Journal of Numerical Analysis* 43.1 (Nov. 2021), pp. 225–257. ISSN: 0272-4979. DOI: 10.1093/imanum/drab089. eprint: https://academic.oup.com/imajna/article-pdf/43/1/225/49059561/drab089.pdf. URL: https://doi.org/10.1093/imanum/drab089.

[35] Ching-Shan Chou et al. "Local Discontinuous Galerkin Methods for the Khokhlov–Zabolotskaya–Kuznetzov Equation". In: *Journal of Scientific Computing* 73.2 (Dec. 2017), pp. 593–616. ISSN: 1573-7691. DOI: 10.1007/s10915-017-0502-z. URL: https://doi.org/10.1007/s10915-017-0502-z.

[36] James F. Kelly et al. "Linear and nonlinear ultrasound simulations using the discontinuous Galerkin method". In: *The Journal of the Acoustical Society of America* 143.4 (Apr. 2018), pp. 2438–2448. ISSN: 0001-4966. DOI: 10.1121/1.5032196. eprint: https://pubs.aip.org/asa/jasa/article-pdf/143/4/2438/15331981/2438_1_online.pdf. URL: https://doi.org/10.1121/1.5032196.

[37] James F. Kelly et al. "Nonlinear ultrasound simulations using a time-explicit discontinuous Galerkin (DG) method". In: *2017 IEEE International Ultrasonics Symposium (IUS)*. 2017, pp. 1–4. DOI: 10.1109/ULTSYM.2017.8092235.

[38] Allan D. Pierce. "Ray Acoustics". In: *Acoustics: An Introduction to Its Physical Principles and Applications*. Cham: Springer International Publishing, 2019, pp. 427–486. ISBN: 978-3-030-11214-1. DOI: 10.1007/978-3-030-11214-1_8. URL: https://doi.org/10.1007/978-3-030-11214-1_8.

[39] COMSOL. "Acoustics Module User's Guide". In: *COMSOL Multiphysics* 6.16 (2022), pp. 354–370.

[40] Heinrich Kuttruff. *Room acoustics*. Crc Press, 2016. ISBN: 978-1-315-27485-0. DOI: 10.1201/9781482266450. URL: https://doi.org/10.1201/9781482266450.

[41] Allan D. Pierce. "Scattering and Diffraction". In: *Acoustics: An Introduction to Its Physical Principles and Applications*. Cham: Springer International Publishing, 2019, pp. 487–581. ISBN: 978-3-030-11214-1. DOI: 10.1007/978-3-030-11214-1_9. URL: https://doi.org/10.1007/978-3-030-11214-1_9.

[42] Karl F Graff. *Wave motion in elastic solids*. Courier Corporation, 2012.

8

Manufacturing aspects of phononic crystals

Phononic crystals (PnCs) have been extensively explored in several applications due to their unusual dynamic characteristics such as band gaps (BGs). Although we can design PnCs with high accuracy, their progress is limited by manufacturing, especially in mesoscales, due to their complicated geometry and small internal feature sizes. Here, we discuss the fabrication of various PnCs applied in ultrasonic flowmeters for mitigating crosstalk. We manufacture 3D cubic PnC waveguides in stainless steel via selective laser sintering to apply them to suppress crosstalk from in-line ultrasonic flowmeters. The distortions of the waveguide's internal features due to overhang angles are addressed by modifying the geometry and printing orientations. We further realize 3D hexagonal PnC waveguides possessing broad BG and resistance against mechanical loading by the same method. We also fabricate PnC waveguides in plastic that possess partial BGs for steering acoustic waves and avoiding crosstalk in a clamp-on ultrasonic flowmeter via polyjet printing. Here, the challenge with the small feature size is addressed by replacing thin elements with soft (rubbery) materials possessing low acoustic impedance. After implementing the desired changes, the fabricated PnC structures are consistent with their design.

8.1. Introduction

Periodic structures such as phononic crystals (PnCs) have found tremendous applications in various fields of mechanics, acoustics, and instrumentation, as their bulk properties can be influenced by tuning the periodic unit cell (PUC) [1]. Additionally, they possess characteristics such as negative Poisson's ratio [2] or acoustic band gaps [3] owing to their structural arrangement, which is unusual to natural materials. Thus, PnCs are used in vibration isolation [4], energy harvesting [5], acoustic

focusing and steering [6], non-destructive evaluation [7], and super/hyper lens [8] among others. However, most of the progress in these periodic structures is still in the proof of concept stage, which has not reached the level of a real product.

The major bottleneck in the progress of PnCs is the limitations in manufacturing. While the computational tools needed for their analysis and design have undergone tremendous advancements, the fabrication processes are still lacking. Especially in the mesoscale (ranging from sub-millimeter to a few centimeters), the available manufacturing processes for realizing periodic structures with complex geometry are limited. The two suitable processes are wire electric discharge machining (wire-EDM) [9] and additive manufacturing [10]. Although the former possesses high precision and surface finish, it is a subtractive manufacturing process (removes material from a block), restricting its ability to realize complex geometries. Additive manufacturing uses a layer-by-layer deposition to add materials in 3D and can create complex geometries with small feature sizes. However, the accuracy, repeatability, and surface roughness are still challenges to be addressed.

Here, we discuss the fabrication of various PnCs applied in ultrasonic flowmeters via additive manufacturing. We further explore the challenges in their realization and how to circumvent them.

8.2. 3D cubic PnC waveguides

We start by discussing the fabrication of 3D cubic PnC waveguides, which are used as wave rejection mechanisms to mitigate crosstalk from in-line ultrasonic flowmeters discussed in Chapter 4. Since they needed to be metallic (constructed from stainless steel 316), we fabricated them via selective laser sintering (SLS) [11]. SLS is a type of powder bed fusion technology where a laser beam is used to melt and fuse metallic powder in multiple passes to develop the desired product. After a powder layer has been melted, a new layer of powder is spread to continue the process. Figure 8.1 shows two types of 3D PnC waveguides fabricated via SLS, where 8.1(c) has spherical internal features and 8.1(d) possesses triangular features. The corresponding PUC designs are shown in 8.1(a) and 8.1(b), respectively. As evident from the photographs, the spherical features underwent certain distortions during printing, resulting in a poor surface finish. This is due to the significant overhanging angle of the sphere close to the center of the unit cell (the tangent to the sphere is parallel to the base). Additionally, the lower and side edges of the waveguide have rough surfaces due to the sticking of powder particles with the melt pool.

The issue with the overhang angle is resolved during the fabrication of the PnC waveguide with triangular features (Figure 8.1(d)) by providing two modifications. Firstly, we replace the spheres with isosceles right triangles, which ensure a constant overhang angle along the slant edges of the triangular features. Secondly, the printing orientation is also modified, i.e., in the case of spherical PnC, the axial direction of the waveguide is aligned towards the printing direction. We rotated the triangular PnC waveguide such that its axial direction is aligned 45° to the printing direction, ensuring all overhang angles to be 45°, which is its upper limit. Although this orientation requires additional support structures, they can be effectively removed during the post-processing. Thus, the triangular PnC has a better surface

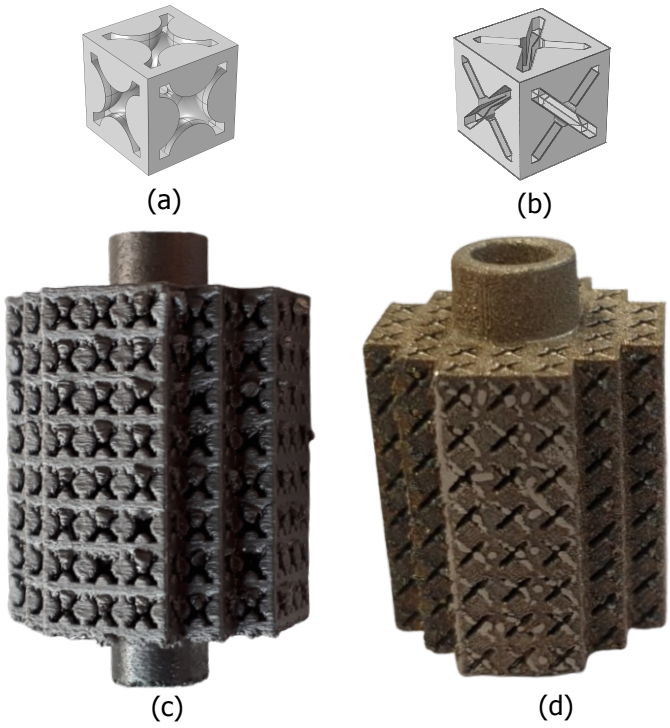

Figure 8.1: Photographs of 3D printed cubic PnC waveguides with (c) spherical and (d) triangular features fabricated via selective laser sintering, where (a) and (b), respectively, are corresponding PUCs.

finish and more consistent internal features compared to the spherical PnC, hence should perform nominally.

8.3. 3D hexagonal PnC waveguide

We move to the manufacturing of 3D hexagonal PnC waveguide discussed in Chapter 5. In addition to alleviating the crosstalk, this structure should withstand a tremendous pressure load from the surrounding fluid (15 MPa). Thus, the PnC waveguide has a hexagonal arrangement of unit cells, an outer wall, and internal slabs in alternate layers. The same fabrication method used in the cubic PnC waveguide (SLS) is also employed here, and the printed waveguide is shown in Figure 8.2(a). The realized waveguide possesses a nominal surface finish, and we can see that the external spheres are undistorted, unlike in the previous case (see Figure 8.1(c)). It is because the spheres in the hexagonal PUC are moved to its corners (see Figure 8.2(b)) instead of the centers of connecting ribs as in the cubic case (refer Figure 8.1(a)). This modification ensures the reduction of overhang angles, thus improving the overall quality of the print. Since the hexagonal waveguide is a closed structure, we cut it along different directions to investigate the quality of the internal features, as discussed next.

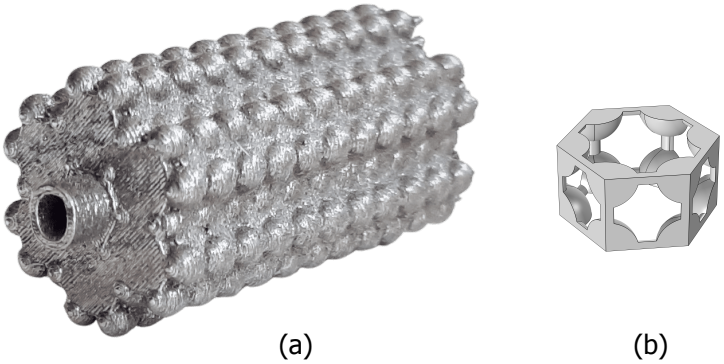

Figure 8.2: (a) The photograph of a 3D printed hexagonal PnC waveguide fabricated via selective laser sintering and (b) the corresponding PUC.

Figure 8.3 shows different sectional views of the 3D hexagonal waveguide from Figure 8.2. Figures 8.3(a) and 8.3(c) display the cross-sectional view of the PnC waveguide where we can see that the internal spheres have not experienced any distortions. On the contrary, the surface beneath the spheres is rough and inconsistent. It is because of the limitation in the SLS process while printing a flat surface 90° to the printing direction. In other words, more powder is deposited in the unprinted region due to the large overhang angles and gravity.

Figures 8.3(b) and 8.3(d) show the inclined sectional views of the PnC waveguide, where the outer wall and the ribs connecting the internal spheres are coherent with the corresponding design (no distortions). The walls where the spheres are connected also are smooth, unlike the flat slabs. So, the overall 3D hexagonal PnC waveguide fabricated via SLS is close to the required design except for the internal slabs. One way to circumvent this distortion is to add adequate support structures to the slab structures in the design phase. However, in this case, due to the intricacy of the PnC design, it is challenging to add those structures without creating additional problems. For instance, the new support structures may produce new connections between the internal features, reducing the PnC's wave propagation performance. Nevertheless, as explained in Chapter 5, thicker internal slabs have negligible effects on the performance of the PnC waveguide; thus, this variation is acceptable and the waveguide should perform adequately.

8.4. PnC wedge with partial band gaps

In Chapter 6, we have designed a PnC wedge possessing partial BGs for guiding ultrasound pulse through a specific path while filtering noise generated at different interfaces, as shown in Figure 8.4(a). Since the wedge is composed of plastic material, we use a polyjet printing (PJP) process (Stratasys 3D printer) for its fabrication [12]. PJP is an additive manufacturing process where photoreactive resins or casting wax materials are deposited layer by layer. These layers are then cured by means of ultraviolet (UV) light, providing a smooth and accurate part. Since

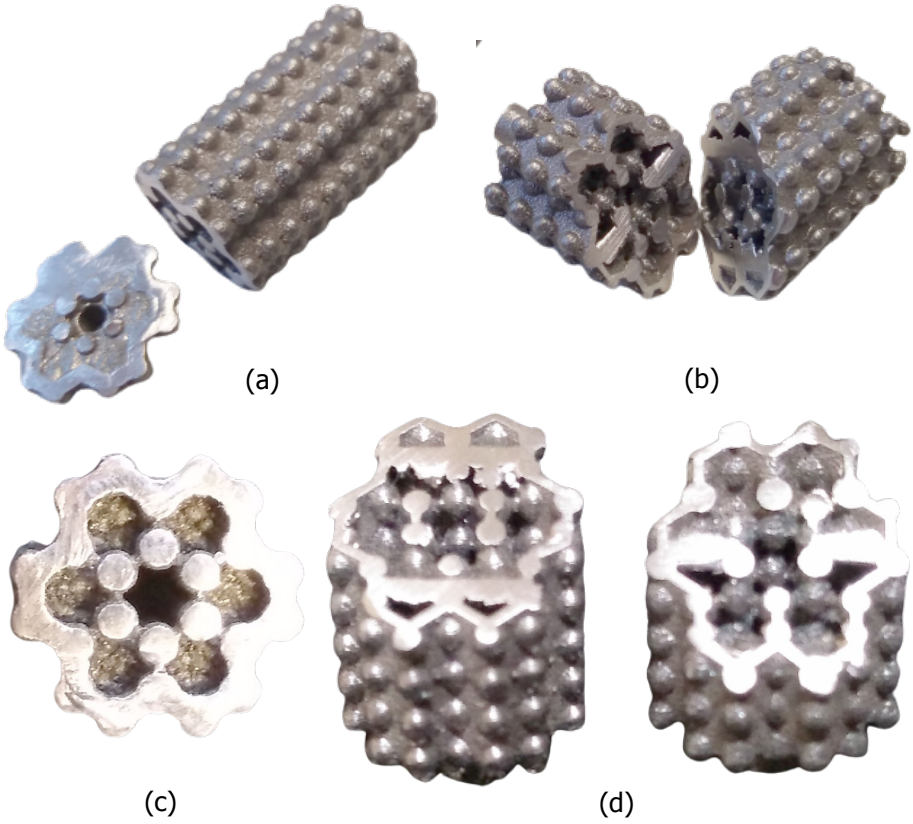

Figure 8.3: The photographs of sectional views of 3D hexagonal PnC waveguide (a) Cross-sectional view where the section plane is perpendicular to the printing orientation, (b) Oblique section where the section plane is at 45° to the printing direction. (c) and (d), respectively, are the close-up views of cross- and oblique-sections.

the smallest feature size of the wedge is 100 µm, it is challenging to manufacture although it is still within the fabrication tolerance. This is because the thin structure is also free-standing and does not have adequate support and hence will break down during the addition of the successive layer. Thus, we modify the design by creating the PUC with two different materials as shown in Figure 8.4(b). In this design, the thin structures are replaced with soft materials (casting wax and Agilus 30) having substantially lower acoustic impedance compared to the adjacent plastic layer (VeroCyan). Figures 8.4(c) and 8.4(d), respectively, show the fabricated PnC wedges, where the soft material in the former is casting wax while in the latter, it is Agilus 30.

Although the feature sizes, shapes, surface texture, and orientations were accurate, the wedge with the casting wax has some distortions as visible from Figure 8.4(c). This is because the wax material is easy to remove with force and is water-soluble limiting its performance in long runs. In contrast, the wedge with plas-

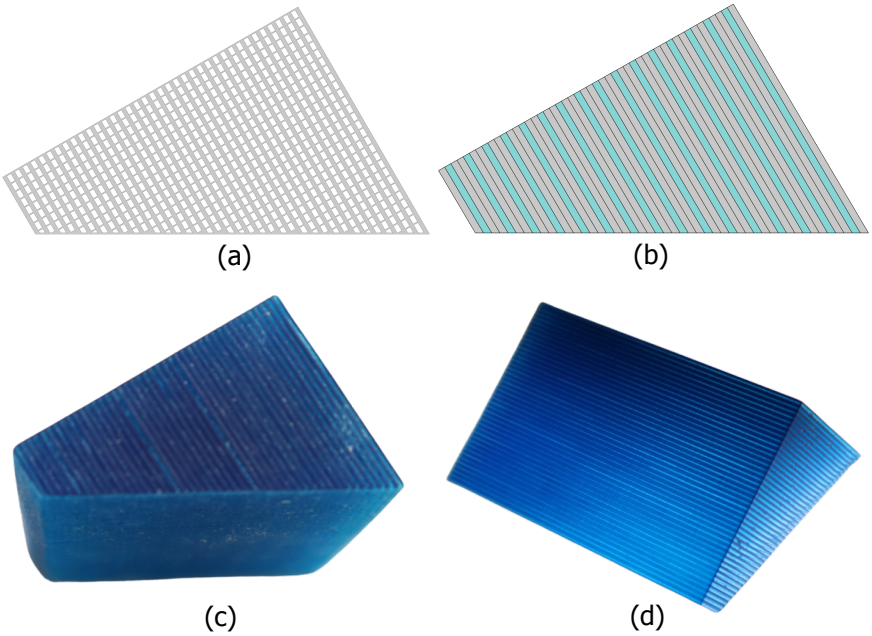

Figure 8.4: 2D geometries of a clamp-on flowmeter's wedge with partial band gaps designed from (a) single material and (b) two materials. The wedge is fabricated via multijet printing, where (c) plastic with wax and (d) plastic with a rubbery material.

tic and elastomer (see Figure 8.4(d)) is more stable and resistant to environmental conditions, thus, should perform adequately.

8.5. Summary and Conclusion

We discussed the fabrication of different types of phononic crystals via additive manufacturing, applied in in-line and clamp-on ultrasonic flowmeters to mitigate crosstalk. Although we can design phononic crystals with great performance, they may not have adequate manufacturability. Thus, certain tuning in the design is needed to realize them. Additionally, incorporating manufacturing aspects such as the overhang angles or the minimum feature size during the early design stage, greatly improves the quality during the fabrication.

Bibliography

[1] P.A. Deymier. *Acoustic Metamaterials and Phononic Crystals*. Springer Series in Solid-State Sciences. Springer Berlin Heidelberg, 2013. ISBN: 9783642312328. URL: https://books.google.nl/books?id=8eg%5C_AAAAQBAJ.

[2] Roderic S. Lakes. "Negative-Poisson's-Ratio Materials: Auxetic Solids". In: *Annual Review of Materials Research* 47.1 (2017), pp. 63–81. DOI: 10.1146/annurev-matsci-070616-124118. eprint: https://doi.org/10.1146/annurev-matsci-070616-124118. URL: https://doi.org/10.1146/annurev-matsci-070616-124118.

[3] A. Khelif et al. "Complete band gaps in two-dimensional phononic crystal slabs". In: *Phys. Rev. E* 74 (4 Oct. 2006), p. 046610. DOI: 10.1103/PhysRevE.74.046610. URL: https://link.aps.org/doi/10.1103/PhysRevE.74.046610.

[4] Matthew Reynolds and Stephen Daley. "An active viscoelastic metamaterial for isolation applications". In: *Smart Materials and Structures* 23.4 (2014), p. 045030.

[5] Kyung Ho Sun et al. "Sound energy harvesting using a doubly coiled-up acoustic metamaterial cavity". In: *Smart Materials and Structures* 26.7 (2017), p. 075011.

[6] J Xu and J Tang. "Tunable prism based on piezoelectric metamaterial for acoustic beam steering". In: *Applied Physics Letters* 110.18 (2017), p. 181902.

[7] Ralf Lucklum and Nikolay Mukhin. "Enhanced sensitivity of resonant liquid sensors by phononic crystals". In: *Journal of Applied Physics* 130.2 (2021), p. 024508. DOI: 10.1063/5.0046847. eprint: https://doi.org/10.1063/5.0046847. URL: https://doi.org/10.1063/5.0046847.

[8] Gang Yong Song et al. "Broadband focusing acoustic lens based on fractal metamaterials". In: *Scientific reports* 6 (2016), p. 35929.

[9] Y.S Liao, J.T Huang, and Y.H Chen. "A study to achieve a fine surface finish in Wire-EDM". In: *Journal of Materials Processing Technology* 149.1 (2004). 14th Interntaional Symposium on Electromachining (ISEM XIV), pp. 165–171. ISSN: 0924-0136. DOI: https://doi.org/10.1016/j.jmatprotec.2003.10.034. URL: https://www.sciencedirect.com/science/article/pii/S0924013604001463,%20keywords%20=%20%7BWire-EDM,%20Finish,%20Pulse-generating%20circuit,%20Surface%20roughness%7D,.

[10] Ian Gibson et al. *Additive manufacturing technologies*. Vol. 17. Springer, 2021.

[11] William E Frazier. "Metal additive manufacturing: a review". In: *Journal of Materials Engineering and performance* 23.6 (2014), pp. 1917–1928.

[12] N. Muthuram et al. "A review of recent literatures in poly jet printing process". In: *Materials Today: Proceedings* 68 (2022). 4th International Conference on Advances in Mechanical Engineering, pp. 1906–1920. ISSN: 2214-7853. DOI: https://doi.org/10.1016/j.matpr.2022.08.090. URL: https://www.sciencedirect.com/science/article/pii/S2214785322052464.

9

Discussion and Conclusions

This thesis aimed to develop devices based on phononic crystals (PnCs) to mitigate crosstalk in ultrasonic flowmeters (UFs), which severely affects their measurement accuracy. To that end, two different cases were investigated: In **Case-1**, we developed a mechanical wave filter based on PnC waveguides that can attenuate high-frequency broadband waves traveling through the solid region thereby alleviating crosstalk in inline UFs. Therefore, we investigated the feasibility of PnCs to possess adequate band gap (BG) widths and methods to accurately characterize them. Thus, in Chapter 2, a low-cost analytical model based on the spectral element method (SEM) was proposed to analyze the dynamic response of viscoelastic metamaterials. Then in Chapter 3, we developed a PnC waveguide capable of mitigating crosstalk at 1 MHz, which is extended to include additional mechanical performance in Chapter 4. In **Case-2**, we designed a PnC-based wave steering mechanism to transmit the incoming signal through a required wave path while redirecting/suppressing the remaining waves in clamp-on UFs. To that end, we proposed a PnC waveguide with partial BGs (PBGs) in Chapter 6, which was designed using a novel analysis procedure based on displacement modes discussed in Chapter 5. Since the 3D analysis of the clamp-on UF was prohibitively computationally expensive, we proposed a method to incorporate the effects of 3D in the wave propagation analysis using combinations of different analytical and numerical methods in Chapter 7. All these investigations yielded several interesting findings, which are concluded below.

The PnC wave filter developed for the inline UF is the first of its kind, which demonstrated a 40 dB noise reduction in a broad bandwidth, which can be used in a multitude of vibration isolation applications. Additionally, unlike most PnC devices discussed in the literature that are fabricated in plastic, this waveguide is realized in stainless steel 316 (SS316), a very relevant material used across several industries. This further enhances the wave filter's potential in fields where the application of plastic is limited, for instance, in the case of non-destructive evaluation at extreme temperature or pressure situations. In addition, the design procedure proposed

for incorporating multiple conflicting objectives into the PnC wave filter design is a generic process that can be applied to the multi-objective design of similar periodic structures with adequate changes in the design space and parameters. Besides, the wave steering mechanism proposed for the clamp-on UF is also a novel concept since most PnC-based wave-guiding systems described in the literature use PnC waveguides with defects for controlling the wave propagation direction. In other words, the unit cells in the desired direction are replaced by homogeneous materials (usually composed of the matrix material) thereby introducing a new wave path for the waves to travel. Although these can maintain the direction of wave propagation, this approach has dire consequences on the wavefront shape and the pulse duration. Thus they are not useful in situations where the signal arrival time and the wave envelope are significant such as in a clamp-on UF. Our innovative wave steering mechanism addresses these challenges by allowing wave propagation without resistance towards the desired direction due to the presence of propagation modes along the branches of the irreducible Brillouin zone (IBZ) that align with the required direction. Since the waveguide also has BGs in the remaining IBZ branches, the waves traveling in those directions are attenuated. The PnC structures with PBGs can be used to improve the performance of devices used in other similar situations where the wave travel duration is important, such as pulse-echo measurements. Despite these exciting capabilities, there are still some challenges to the application of PnCs in the crosstalk mitigation in UFs as discussed further.

The foremost limitation is the difficulty in manufacturing the PnC waveguides. Since the target frequency and material requirements pushed the desired structure to *mesoscale* (unit cell in mm with sub-mm internal features), where fabrication is incredibly challenging. Thus in the present cases, some simplifications were applied to realize the PnC waveguides. For instance, the 3D PnC waveguide with the outer enclosure design (developed for **Case-1**) was tuned slightly because the manufacturing process (selective laser sintering) could not handle the precision required for the design. Similarly, the wedge used for wave steering was designed for a single material; however, was modified to a two-material design since the thinnest parts of the design lacked stability during the fabrication using polyjet printing. Thus, the manufacturability still needs improvement in accuracy, repeatability, and capabilities in handling complex geometries with small feature sizes, before PnCs could be exploited for other real-world applications.

Another challenge these PnCs face is the enormous computational cost during their analysis. Since various designs discussed in this thesis have complex geometries, high operational frequency, and deal with multi-physics situations, their analysis is computationally very demanding. Although several approaches were proposed to address this problem, they have inherent limitations. For instance, SEM-based models can avoid meshing leading to low analysis costs; however, they can only deal with simple geometries, and extending them to complex situations needs geometric approximations. These approximations affect the accuracy and the response is valid only for specific frequency ranges. Similarly, finite element models are very costly and take several hours or days of computational time to provide accurate solutions. Additionally, the clamp-on UF analysis needed to be performed in the

time domain, which is much more expensive than the frequency domain analysis (generally used for PnC analysis). Thus, for applying PnCs to complex situations, the challenges with the computational cost need to be addressed or inexpensive approximate models should be developed. A drawback regarding the 3D PnC design approach developed to address multiple conflicting objectives is that the design might get stuck in a local optimum before reaching a global optimum design due to the parametric sweeping. Instead, a more systematic process such as topology optimization might provide better-performing designs. However, it is noteworthy that as the various analyses involved in the design problem were computationally expensive limiting the possibility of standard topology optimization. It is clear that the design process can be improved when the challenges with the computational cost are addressed.

Some assumptions were made during the design, analysis, and realization of the PnC waveguides. 3D waveguides developed for the inline UF were assumed to possess no damping since it was realized in SS316. However, the manufacturing process introduced some form of dissipation, increasing the wave attenuation and enhancing performance. However, this is not always necessary, and depending upon the application the damping can have adverse effects, thus the influence of damping should be studied to further apply the PnCs in different practical scenarios. Similarly, due to the lack of available data such as viscoelastic material properties, and the limitation of the modeling approach, damping was also excluded during the time-domain analysis of the clamp-on UF with PnC wedges. Since the wedges are composed of polymeric materials, their viscoelastic behavior should be characterized accurately and incorporated into the design to improve the accuracy of the model and further extend its applications.

9.1. Recommendations for further research

The future development of this work presents numerous exciting and relevant directions. The displacement mode-based PnC design method can be extended to create other periodic structures, such as acoustic metamaterials with additional band gaps due to the local resonance of the resonators. Tuning the wavebands introduced by these resonators via displacement modes can provide the required response. Furthermore, this method can be applied to photonic crystals (PCs) that are optical analogs to PnCs. Although the governing equations and parameters are different, both PnCs and PCs derive band structure using eigenvalue analysis of the periodic unit cell after applying Bloch-Floquet periodic boundary conditions and sweeping the wave vector through the IBZ. Additionally, PnCs with PBGs have significant potential in isolating and localizing waves without removing them, making them suitable for signal amplification while retaining the source waveform.

The PnCs discussed here can also be applied in other industries where ultrasound transducers are used. Depending on the frequency range, the PnC design may need up/downscaling. For instance, in medical imaging, the PnCs could help improve the performance of ultrasonic devices used to image the fetus inside the uterus or detect tumors, where multiple interfaces between the transmitter and receiver present similar challenges to those of clamp-on ultrasound transducers.

Acknowledgements

Although the front cover only bears my name, the completion of this thesis was possible due to the support and encouragement of several people, within and outside the office. I wish to thank everyone who supported and guided me in finishing this thesis.

Firstly, I want to express my gratitude to my supervisors, *Fred*, *Alejandro*, and *Hans* for providing me with the opportunity and bearing me throughout the Ph.D. journey. *Fred*, thanks for all the insights and critical remarks, which paved the keystones for this thesis. *Alejandro*, I cannot stress enough the acknowledgment I have for all the guidance and encouragement you have provided, especially, the extra effort you put to train me in writing scientific articles. I am certain this will help me throughout my career. *Hans*, although you joined the project late, your knowledge and insight in various aspects became quintessential to the successful completion of the project and this thesis. Additionally, I immensely enjoyed our discussions on different topics (related or unrelated to the project).

I wish to thank the collaborators from Krohne (project sponsor), for providing not just financial but technical support throughout the project. Thanks *Jankees*, *Jeroen*, *Rogier*, and *Ari* for all your insight throughout the update meetings. I also want to thank *Anastasiia* for the collaborative work validating my spectral element models, resulting in a nice article. Thank you also for your patience and kindness throughout our collaboration. I hope to continue to work with you in the future.

I would also like to thank my former colleagues from PME, *Jian*, *Dongyu*, *Ana*, *Tomas*, *Satadal*, *Xianfeng* (AKA *Vincent*), *Prabhat*, *Rajit*, *Vibhas*, *Sanne*, *Emiel*, *Max*, *Stijn*, *Arnoud*, *Andrea*, *Minxing*, *Gurhan*, *Lidan*, *Hanqing* (AKA *Curry*), *Ata*, *Ali*, *Yuhang*, and *Yong* with whom I spent a lot of time in office and attending courses and conferences. Thanks, everyone for providing ample support during the course of my Ph.D. I also want to extend my gratitude towards my colleagues from ImPhys with whom I have been spending time for the last couple of years. Especially to *Djalma*, *Xiufeng*, *Fabian*, *Agis*, *Boudewien*, *Ayda*, and *Eleonora* who provided a safe group to let me express my extreme pessimism without judging. Thanks, everyone.

I am extremely grateful for the amount of support and encouragement I received from my friends, *Renil*, *Parvathi*, *Gokul*, *Desiree*, *Divya*, *Eldho*, *Sarah*, *Rajesh*, *Sneha*, *Imaya*, *Viswajeet*, *Geethika*, *Deepak*, *Aravind*, *Krishnapriya*, *Arun*, *Irene*, and *Jonathan*.

I also want to thank my family for their support. Finally, I want to express my utmost appreciation to my wife *Namitha*, and daughter *Sanvi*. *Namitha*, your role in keeping my sanity intact, helping me to prepare for presentations, and providing me emotional support throughout is immeasurable. I know it is not easy to handle my character, but you have done a wonderful job for which I am extremely grateful. Owing to the fact that it is from you I have learned a great deal of soft skills, which

I am sure will always be useful. *Sanvi*, you blessed us with your grace at the peak of COVID-19 when everything was in turmoil. You managed to mitigate the stress we had and taught us several things. Our life has been much sweeter from the day I hold you in my arms for the first time. Thank you very much for that.

Curriculum Vitæ

Sabiju Valiya Valappil

13-07-1989 Born in Taliparamba, Kerala, India.

Education

2018–2022 PhD. Mechanical Engineering
Delft University of Technology, Delft
Thesis: Phononic crystal-based devices for improving the accuracy of ultrasonic flowmeters
Promotor: Prof. dr. ir. A. van Keulen
Dr. A. M. Aragón
Co-Promotors: Dr. ir. J. F. L. Goosen

2012–2014 Master of Technology in Mechanical Systems Design
Indian Institute of Technology, Kharagpur,
Kharagpur, West Bengal, India

2007–2011 Bachelor of Technology in Mechanical Engineering
Government College of Engineering, Kannur,
Kannur, Kerala, India

Professional experiences

2022–present Postdoctoral researcher, Delft University of Technology, Delft, Netherlands.

2017–2018 Research Associate, Oklahoma State University, Stillwater, Oklahoma, USA.

2014–2017 Associate Engineer, Caterpillar INC, Chennai, India.

List of Publications

Journal Publications

7. **S. V. Valappil**, A. M. Aragón, and J. F. L. Goosen, *A semi-analytical approach to characterize high-frequency three-dimensional wave propagation through a clamp-on flowmeter*, In preparation.

6. **S. V. Valappil**, A. M. Aragón, and J. F. L. Goosen, *Partial band gap phononic structures for attenuating crosstalk in clamp-on ultrasonic flowmeters*, Mechanical Systems and Signal Processing (under review).

5. A. C. A. Vasconcelos, **S. V. Valappil**, D. Schott, J. Jovanova, and A. M. Aragón, *A metamaterial-based interface for the structural resonance shielding of impact-driven offshore monopiles.*, Engineering Structures 300, p. 117261 (2024).

4. **S. V. Valappil**, J. F. L. Goosen, and A. M. Aragón, *Multi-objective design of 3D phononic crystal waveguide by design space trimming*, Materials & Design 237, p. 112594 (2024).

3. **S. V. Valappil**, A. O. Krushynska, and A. M. Aragón, *Analytical characterization of the dynamic response of viscoelastic metamaterials*, Computational Materials Science 229, p. 112385 (2023).

2. **S. V. Valappil**, J. F. L. Goosen, and A. M. Aragón, *Phononic crystals for suppressing crosstalk in ultrasonic flowmeters*, IEEE Transactions on Instrumentation and Measurement 72, pp. 1-11, (2023).

1. **S. V. Valappil**, A. M. Aragón, and J. F. L. Goosen *Phononic crystals' band gap manipulation via displacement modes*, Solid State Communications 361, p. 115061 (2023).

Patent

1. A. M. Aragón, **S. V. Valappil**, and C. J. Hogendoorn *Ultrasonic Transducer and Ultrasonic Flowmeter*, United State patent application, 18/048, 774 (2023).

Conference Proceedings

3. **S. V. Valappil**, A. van Keulen, J. F. L. Goosen, and A. M. Aragón *Phononic structures for enhancing the accuracy of ultrasonic flowmeters*, 15th World Congress on Computational Mechanics (Virtual Edition, 31 July–5 August 2022).

2. **S. V. Valappil**, A. van Keulen, and A. M. Aragón *Analytical models for dynamic analysis of 1D damped acoustic metamaterials*, 14th World Congress on Computational Mechanics (Virtual Edition, 11-15 January 2021).

1. **S. V. Valappil**, A. van Keulen, and A. M. Aragón *Analysis of 1D damped acoustic metamaterials using spectral element method*, 5th International Conference on Phononic Crystals/Metamaterials, Phonon Transport & Topological Phononics (02-07 June 2019).